

# **The Development of On-Chip THz Time-Domain Spectroscopy**

Manoj Kumar (M.Tech)

*Submitted in accordance with the requirements for the degree of  
Doctor of Philosophy*

The University of Leeds  
School of Electronic and Electrical Engineering

May 2016



*The candidate confirms that the work submitted is his own, except where work which has formed part of jointly authored publications has been included, and that appropriate credit has been given where reference has been made to the work of others.*

The carrier lifetime measurement discussed in Chapter 3 was published in the article:

*“Study of the effect of annealing temperature on low-temperature-grown-GaAs photomixers”*. Siddhant Chowdhury, Joshua R. Freeman, Mark C. Rosamond, Reshma A. Mohandas, Manoj Kumar, Lianhe Li, Paul Dean, A. Giles Davies and Edmund H. Linfield. *UK Semiconductor 2015*, 2015-07-01 – 2015-07-02, Sheffield, UK.

Manoj Kumar was responsible for on-chip measurement setup and aligning the laser beams focused onto the test sample. Autocorrelation measurements were performed by Siddhant Chowdhury and Manoj Kumar. Other authors were responsible for fabrication, annealing temperature recipe and supervision work.

*This copy has been supplied on the understanding that it is copyright material and that no quotation from the thesis may be published without proper acknowledgement.*

© 2016 The University of Leeds and Manoj Kumar

*The right of Manoj Kumar to be identified as Author of this work has been asserted by him in accordance with the Copyright, Designs and Patents Act 1988.*





*This thesis is dedicated to my loving wife  
Suman Bala*



*The mind is restless and difficult to restrain, but it is subdued by practice.*

- *Bhagavad Gita*



# Acknowledgements

It is with immense gratitude that I acknowledge the guidance and support of my supervisors, Prof. John Cunningham, Prof. A. Giles Davies and Prof. Edmund H. Linfield throughout the course of this project. Without their continuous optimism concerning this work, encouragement and help this study would hardly have been completed.

Also, I would like to acknowledge Dr. Chris Wood and Dr. Andrew Burnett for their valuable suggestions during supervisory meetings.

I would like to express my deepest appreciation to my colleague Dr. Nicholas Hunter for providing useful guidance, assistance and helping hand in the cleanroom.

I owe a special thank you to Dr. Siddhant Chowdhury for giving me constant motivation for all these years and assistance with free space THz-TDS measurements.

I would also like to show my gratitude to Dr. Chris Russell for giving me useful guidance in on-chip spectroscopic measurements.

Finally, I would like to thank all the staff and students at Institute of Microwave and Photonics, School of Electronic and Electrical Engineering, University of Leeds. I owe my deepest gratitude to Govt. of India for their financial support.

I am indebted to my parents for being there and for believing in me for all these years.



# Abstract

Since the development of efficient THz sources, THz-TDS has been proved to be a promising tool to probe directly the intermolecular modes, rotational motion and intermolecular vibrations of molecules in a variety of chemicals capable of extracting useful spectroscopic information. In this thesis, an on-chip spectroscopy system based on coplanar waveguide (CPW) technology has been designed, optimised and tested, in order to probe spectral features of overlaid polycrystalline materials. As proof of principle, this system was used to recover the THz spectra of  $\alpha$ -lactose monohydrate, observing spectral features at  $\sim 0.53$  THz and  $\sim 1.37$  THz. A significant frequency shift in the 1.37 THz feature was observed when the on-chip spectroscopy measurements were performed over a variable temperature range of ( $\sim 6$ -293 K). Spectral features obtained from the on-chip system were also compared to those obtained from a free-space THz-TDS system to highlight the benefits of using an on-chip system over free space THz-TDS.

A theoretical model developed using Ansoft HFSS tool was then used to optimise device design parameters in the second generation of CPW devices. In doing so, the bandwidth of the system was enhanced from  $\sim 0.42$  to 1.6 THz and a much higher frequency resolution of ( $\sim 2$  GHz) was obtained compared to that of the first-generation CPW devices ( $\sim 55$  GHz) with the modified device design of second generation devices. Branching waveguide systems (THz Y-splitter and coupler) were also simulated, fabricated and measured in order to investigate THz pulse splitting in branching waveguides. These systems allow the measurement of both a sampled and reference pulse. During these measurements, the splitting of the THz pulses propagating in an on-chip THz system was also demonstrated for the first time.





# Table of Contents

<b>Acknowledgements .....</b>	<b>i</b>
<b>Abstract.....</b>	<b>iii</b>
<b>List of Figures .....</b>	<b>x</b>
<b>List of Tables .....</b>	<b>xxiii</b>
<b>Abbreviations .....</b>	<b>xxiv</b>
<b>Chapter 1 .....</b>	<b>1</b>
<b>Fundamentals of THz Time-Domain Spectroscopy.....</b>	<b>1</b>
1.1 Introduction .....	1
1.2 Sources of THz generation and detection: An overview.....	2
1.3 Free-space THz generation and detection .....	3
1.3.1 THz generation by photoconductive switch .....	3
1.3.2 THz generation by optical rectification.....	8
1.3.3 THz detection by photoconductive switch.....	9
1.3.4 THz detection by an Electro-optic crystal.....	10
1.4 Free-space THz time-domain spectroscopy .....	11
1.4.1 THz-TDS of polycrystalline lactose monohydrate .....	14
1.4.2 Differential THz-TDS system.....	18
1.5 On-chip THz generation and detection .....	21
1.5.1 Free-standing waveguide system.....	21
1.5.2 On-chip waveguide system .....	24
1.6 Thesis structure.....	26
<b>Chapter 2 .....</b>	<b>28</b>
<b>Transmission Line Theory and Modelling of On-Chip Waveguides using HFSS .....</b>	<b>28</b>
2.1 Introduction .....	28
2.2 Transmission line theory.....	29
2.2.1 Lossless transmission line .....	32
2.2.2 Distortionless transmission line .....	32
2.2.3 Reflection Coefficient .....	33
2.2.4 Different load conditions .....	34
2.3 Planar transmission lines .....	35
2.3.1 Slotline.....	36

2.3.2	Microstrip.....	36
2.3.3	Goubau line .....	37
2.3.4	Stripline.....	38
2.3.5	Coplanar waveguide.....	39
2.3.6	Coplanar waveguide discontinuities.....	42
2.4	Quasi-static analysis of coplanar waveguide.....	44
2.4.1	Conformal mapping.....	45
2.4.2	Quasi-TEM parameters of coplanar waveguide.....	47
2.4.3	Losses in coplanar waveguide .....	52
2.4.4	Discontinuous (series coupling gap) coplanar waveguide .....	55
2.5	Electromagnetic simulations using High-Frequency Structure Simulator (HFSS) .....	59
2.5.1	Finite Elements Method and adaptive meshing .....	59
2.5.2	S-parameters .....	62
2.5.3	CPW simulation setup and results.....	65
2.5.4	Simulation results (discontinuous CPW) .....	70
2.6	Series and Shunt Capacitances.....	73
2.7	Conclusion.....	75
<b>Chapter 3</b>	.....	<b>77</b>
<b>Conventional and Differential On-Chip THz Systems: Device Design, Fabrication and Measurements</b>	.....	<b>77</b>
3.1	Introduction.....	77
3.2	Fabrication of the first generation CPW device on LT-GaAs substrate .....	78
3.3	First generation CPW device design.....	79
3.3.1	PCB layout .....	81
3.4	On-chip measurements of the first generation CPW device (LT-GaAs substrate) .....	82
3.4.1	Experimental setup: Two beams (pump-probe) on-chip system.....	82
3.4.2	Annealing temperature and carrier lifetime of LT-GaAs material..	84
3.4.3	Characterisation of the first generation CPW device (LT-GaAs substrate).....	88
3.4.4	Switch Characterisation .....	88
3.4.5	Input pulse detection .....	90
3.4.6	Output pulse detection .....	94
3.4.7	THz Pulse velocity (GaAs substrate) .....	97

3.4.8	Mode excitations.....	99
3.5	On-chip measurements of the first generation CGAP-CPW device (LT-GaAs substrate) .....	102
3.5.1	Experimental setup: Three-beam on-chip system.....	103
3.5.2	Characterisation of the first generation CGAP-CPW (LT-GaAs substrate).....	104
3.5.3	Switch Characterisation .....	104
3.5.4	Knife edge experiment to determine the spot size.....	106
3.5.5	Input pulse detection.....	109
3.5.6	Output pulse detection.....	110
3.5.7	Mode excitation .....	112
3.6	First generation CPW devices on quartz substrate.....	115
3.6.1	Fabrication of the first generation CPW on quartz substrate .....	116
3.6.2	Characterisation of the first generation CPW (quartz substrate)...	120
3.6.3	Switch Characterisation .....	120
3.6.4	Input pulse detection.....	122
3.6.5	Output pulse detection.....	124
3.6.6	Pulse velocity (quartz substrate) .....	126
3.6.7	Excitation of odd (co-planar) mode.....	127
3.6.8	Excitation of even (slot-line) mode.....	128
3.7	Theoretical modelling of coupling gap.....	129
3.7.1	Photo-conductance .....	129
3.8	On-chip measurements of the first generation CGAP-CPW device on quartz substrate .....	132
3.8.1	Switch characterisation .....	132
3.8.2	Detection of input and output pulse .....	133
3.8.3	Co-planar mode (Odd mode) .....	137
3.8.4	Coupling loss .....	139
3.9	On-chip differential THz pulse measurement using CGAP-CPW (quartz substrate).....	140
3.9.1	Experimental setup.....	140
3.9.2	Generation and detection of differential THz pulse .....	141
3.9.3	Mode testing .....	145
3.10	Conclusion .....	148

<b>Chapter 4</b> .....	<b>149</b>
<b>On-Chip Measurements of Second Generation CPW Devices</b> .....	<b>149</b>
4.1 Introduction.....	149
4.2 Second generation CPW device design .....	150
4.3 PCB layout.....	151
4.4 Characterisation of the second generation CPW device (quartz substrate) 151	
4.4.1 Switch characterisation.....	152
4.4.2 Input pulse detection .....	152
4.4.3 Output pulse detection .....	154
4.4.4 Pulse velocity (quartz substrate).....	157
4.4.5 Coplanar mode (Odd mode) .....	157
4.4.6 Slot line mode (Even mode) .....	158
4.5 THz Y-splitter and coupler.....	159
4.5.1 Device Design.....	160
4.5.2 Simulation model of Y-splitter and coupler.....	162
4.6 On-chip measurements of Y-splitter CPW (LT-GaAs substrate).....	165
4.6.1 Input pulse detection .....	165
4.6.2 Pulse detection for a split output .....	166
4.7 On-chip measurements of Y-splitter CPW (quartz substrate).....	169
4.7.1 Input pulse detection .....	169
4.7.2 Output (split) pulse detection .....	170
4.7.3 Pulse velocity.....	172
4.8 On-chip measurements of Y-coupler CPW (quartz substrate) .....	173
4.8.1 Detection of the output (split) pulses .....	173
4.8.2 THz pulse detection using coupling switch modulation .....	175
4.8.3 Initial spectroscopy measurement using Y-coupler CPW device..	176
4.9 Conclusion.....	178
<b>Chapter 5</b> .....	<b>180</b>
<b>On-Chip THz-TDS of Lactose Monohydrate using Conventional and CGAP-CPW     Devices at Low-Temperature</b> .....	<b>180</b>
5.1 Introduction.....	180
5.2 Slot gap width optimisation and estimation of extent of evanescent field 181	
5.2.1 Theoretical modelling of slot gap width W.....	181

5.2.2	HFSS simulations to find the extent of evanescent field .....	183
5.2.3	Improvements in signal bandwidth by optimising transmission length.....	186
5.2.4	Experimental Results: Initial testing of optimised CPW device ....	187
5.3	Variable temperature on-chip measurements using microstat.....	191
5.3.1	Measurement set up .....	191
5.3.2	PCB Design for back-side excitation of PC switches.....	192
5.3.3	Sample preparation .....	193
5.3.4	Initial spectroscopy measurement using the first generation CGAP CPW device.....	195
5.3.5	Low-temperature measurement using second generation CPW ...	197
5.4	Conclusion .....	209
<b>Chapter 6</b>	.....	<b>211</b>
<b>Conclusions and Future Work</b>	.....	<b>211</b>
6.1	Conclusions.....	211
6.1.1	First generation CPW devices.....	211
6.1.2	Second generation CPW devices .....	212
6.1.3	Y-splitter/coupler.....	213
6.2	Future Work.....	213
6.2.1	Bandwidth enhancement .....	214
6.2.2	Implementation of tunable filters in CPW .....	215
6.2.3	Future spectroscopic measurements using Y-splitter/coupler.....	217

# List of Figures

Figure 1.1 Diagram showing the THz region of the electromagnetic spectrum. ....	1
Figure 1.2 An illustration of THz generation a) A photoconductive switch illuminated with NIR fs laser pulses. b) The motion of photo-charge carriers in energy bands on the application of NIR laser beam. c) Generation of a temporal transient current pulse. d) Transient current pulse leads to the emission of THz field (taken from Ref. [18]). ....	4
Figure 1.3 An illustration of THz emission in both forward and backward direction from a photoconductive switch. ....	6
Figure 1.4 THz generation from a non-linear electro-optic crystal due to difference frequency mixing. ....	9
Figure 1.5 Detection of the THz field using a photoconductive switch, where an average current mapped by time-delayed probe beam is measured by lock-in amplifier connected in series with a metal electrode. ....	10
Figure 1.6 Detection of THz field using EO crystal as a relative change in field components of NIR laser beam (Image reproduced from Ref. [17]). ....	11
Figure 1.7 Free-space THz-TDS system consisting of femtosecond laser source, motorised optical delay stage, a mechanical chopper, guiding mirrors, a 50:50 beam splitter, mechanical chopper, EO crystal and balanced photodiodes for THz detection. ....	13
Figure 1.8 Free-space THz-TDS of lactose monohydrate a) A comparison of spectral features obtained from three different samples of lactose monohydrate. b) Calculated refractive index and absorption coefficient. c) A comparison of absorption coefficients calculated from three separate samples of lactose monohydrate. ....	15
Figure 1.9 A comparison of spectral features obtained from free-space THz-TDS with on-chip THz-TDS a) A comparison of sampled and reference pulses measured from free-space THz-TDS. b) A comparison of sampled and reference pulses measured from On-chip THz-TDS. c) A comparison of FFT spectra with and without zero padding (free-space THz-TDS). d) A comparison of spectral features of lactose monohydrate obtained from free space and On-chip THz-TDS. ....	17
Figure 1.10 A differential THz-TDS system (free-space) consisting of femtosecond laser source, motorised optical delay stage, a mechanical chopper, guiding mirror, a 50:50 beam splitter, mechanical chopper, EO crystal and a mechanical vibrator to move the sample in and out. ....	19
Figure 1.11 An illustrative representation of the THz field passing through the blank substrate ( $E_{ref}$ ) and biological cell ( $E_{film}$ ), where the difference of $E_{ref}$ and $E_{film}$ will generate a differential THz pulse. ....	20

Figure 1.12 a) A comparison of a conventional difference signal (measured without using mechanical vibrator) with a differential THz signal (measured when the sample was moving in and out). b) Amplitudes of reference (through the blank substrate) and the differential signal (with sample moving in and out) are compared (taken from Ref. [56]).	20
Figure 1.13 a) An illustration of free standing metal wire waveguide in which THz field is coupled to metal wire tip. b) Time-domain pulses measured with metal wire of different diameters. c) Normalised amplitudes.	23
Figure 1.14 An illustration of a ribbon dielectric waveguide coupled with THz field in THz-TDS system using Si lenses.	24
Figure 1.15 a) Photoconductive switches along with transmission region patterned on the LT-GaAs substrate. b) Photoconductive switches patterned on LT-GaAs overlaid onto quartz substrate (selectively etched by epitaxial lift-off technique).	24
Figure 1.16 An illustration of on-chip waveguide system for THz generation and detection in which photoconductive switches are embedded with a metal waveguide in order to transmit THz pulse from the emitter to detector. Components: a femtosecond laser source, motorised optical delay stage, a mechanical chopper, guiding mirrors, beam splitter, and a lock-in amplifier.	25
Figure 2.1 A two-wire transmission line and its distributed network model.	29
Figure 2.2 A two conductor transmission line represented as a lumped element model.	30
Figure 2.3 Transmission line terminated into a load $Z_L$ .	34
Figure 2.4 Planar transmission lines with electric field distribution shown in red a) Slot line. b) Microstrip. c) Goubau line. d) Strip line. e) Conductor-backed coplanar waveguide. f) Coplanar waveguide.	35
Figure 2.5 Schematic of CPW and its field distribution: a) A CPW geometry with spacing (S+2W) between two ground planes. b) The field distribution in coplanar mode (odd mode). c) The field distribution in slot line mode (even mode).	40
Figure 2.6 Function $f(z) = w$ transforms a region in z-plane into w-plane.	45
Figure 2.7 Mapping between a circle in z-plane and a line segment in w-plane [78].	46
Figure 2.8 The Schwarz-Christoffel transformation: a) z-plane. b) $\zeta$ -plane.	46
Figure 2.9 Schematics of CPW showing line capacitances above and below of metallization plane.	47
Figure 2.10 Geometric transformation of CPW a) Schematic of a CPW showing dimensions. b) Cross section of CPW with metallisation plane of zero thickness. c) Schwarz-Christoffel mapping of a CPW with zero thickness into a parallel plate capacitor.	48

Figure 2.11 Plot of calculated characteristic impedance of CPW as a function of modulus $k$ on a) GaAs substrate (plotted in red). b) Quartz substrate (plotted in black). .....	51
Figure 2.12 Skin depth of gold (Au) plotted against frequency of operation.....	53
Figure 2.13 Calculated conductor loss for gold (Au), CPW on both GaAs and quartz substrates plotted against modulus $k$ (ratio of CPW dimensions). .....	54
Figure 2.14 Schematic of CGAP-CPW a) Showing line capacitances above and below of metallisation plane. b) Electric field distribution in discontinuity region. c) Equivalent capacitive $\pi$ -model of coupling discontinuity. ....	56
Figure 2.15 Schwarz-Christoffel transformation of a planar CGAP-CPW into parallel plate capacitor [132]. .....	57
Figure 2.16 The series and shunt capacitances of a CPW as function of coupling gap length a) GaAs substrate with dielectric constant $\epsilon_r = 12.9$ . b) Quartz substrate with dielectric constant $\epsilon_r = 3.78$ .....	58
Figure 2.17 A large volume of a 3D structure of a CPW decomposed into small elements (tetrahedrons). E-field valued are calculated at vertices and edges of a single tetrahedron.....	59
Figure 2.18 Adaptive mesh refinement process based on solution frequency value. ....	60
Figure 2.19 Flow chart showing HFSS's 3D-field solving steps. ....	61
Figure 2.20 A schematic of the two-port network with reflection and transmission coefficients. Incident and reflected waves at port-1 and port-2 are $v_1 +$ , $v_2 +$ and $v_1 -$ , $v_2 -$ .....	63
Figure 2.21 3D model of CPW with excitation modes: a) An air box surrounding a CPW on a dielectric substrate. b) Electric field vectors are showing odd mode excitation in waveport. c) Electric field vectors are showing even-mode excitation in waveport.....	66
Figure 2.22 $S_{21}$ parameter for both CPW <sub>GaAs</sub> and CPW <sub>quartz</sub> plotted as a function of frequency. ....	67
Figure 2.23 Frequency dependent effective permittivity plotted as a function of frequency a) CPW <sub>GaAs</sub> . b) CPW <sub>quartz</sub> Phase constant for quasi-TEM mode and the first higher mode is plotted. c) CPW <sub>GaAs</sub> . d) CPW <sub>quartz</sub> .....	68
Figure 2.24 EM field's distribution above and below the metallisation plane a) EM field at 300 GHz in CPW <sub>GaAs</sub> . b) EM field at 600 GHz in CPW <sub>GaAs</sub> . c) EM field at 600 GHz in CPW <sub>quartz</sub> . d) EM field at 900 GHz in CPW <sub>quartz</sub> . ....	69
Figure 2.25 a) Attenuation in both CPW <sub>GaAs</sub> and CPW <sub>quartz</sub> b) Loss factor in both CPW <sub>GaAs</sub> and CPW <sub>quartz</sub> calculated from S-parameters. ....	70
Figure 2.26 Schematic of 3D simulation model a) CGAP-CPW. b) EM fields at low-frequency c) EM fields at a higher frequency.....	71
Figure 2.27 High pass filter a) Circuit diagram. b) The frequency response of high pass filter.....	71



Figure 2.28 <b>S21</b> parameter obtained from HFSS simulation for a) CPW <sub>GaAs</sub> and CGAP-CPW <sub>GaAs</sub> with varying gap length. b) CPW <sub>quartz</sub> and CGAP-CPW <sub>quartz</sub> with varying gap length and a frequency shift in resonance feature at 920 GHz is shown in inset graph. ....	73
Figure 2.29 a) A capacitive pi-circuit model of coupling gap discontinuity. b) An equivalent pi-model represented in terms of Y-parameters.....	74
Figure 2.30 Capacitance of CGAP-CPW plotted a function of frequency a) Series capacitance (GaAs substrate). b) Shunt capacitance (GaAs substrate). c) Series capacitance (quartz substrate). d) Shunt capacitance (quartz substrate).....	75
Figure 3.1 Fabrication steps for first generation CPW on a LT-GaAs substrate a) Deposition of photoresist. b) UV exposure through photo-mask. c) A chlorobenzene soak process. d) Resist development process e) Metal (Ti/Au) deposition process f) A lift-off process.....	78
Figure 3.2 Photoconductive switch layout with dimensions. b) A magnified view of the photoconductive switch region. ....	80
Figure 3.3 a) PCB layout compatible for room temperature measurements. b) A portable PCB layout compatible with both room and low-temperature measurements. ....	81
Figure 3.4 a) A schematic of an on-chip THz measurement system consisting of femtosecond laser source, motorised optical delay stage, a 50:50 beam splitter, guiding mirrors for beam alignment, neutral density filters (NDFs) to control laser beam intensity, a pair of lenses ( $f = 10\text{cm}$ ), CCD camera, Keithely source meter for DC bias, a mechanical chopper and lock-in amplifier to measure amplitude and phase of THz pulse. b) A magnified view of pump/probe beam alignment using a pair of lenses. c) An illustration of the THz pulse sampled by the probe beam, where an average THz current pulse is mapped out by collecting sampled data points at discrete time intervals.....	83
Figure 3.5 a) An autocorrelation measurement setup. b) Bandwidth and carrier lifetime are plotted as a function of increasing annealing temperature (taken from Ref. [138, 139]).....	85
Figure 3.6 A schematic representation of an on-chip system for autocorrelation measurement.....	86
Figure 3.7 a) Correlated photocurrent measured while pump and probe beam were of same polarisation. b) Normalised photocurrent with exponential fit to the falling edge of the pulse shown in inset graph. c) Correlated photocurrent measured while pump and probe beam were of different polarisation (orthogonal). d) Carrier lifetime plotted as function of increasing bias voltage. ....	87
Figure 3.8 IV sweep characteristic with varying laser power and bias of all four switches a) S1 b) S2 c) S3 and d) S4. ....	89
Figure 3.9 Schematic of the input pulses generation/detection in an on-chip CPW device, where the origins of reflections are indicated as A, B and C.....	91

Figure 3.10 Trace of an input THz pulse in a time-window of 60 ps, where reflections are pointed out by red dots and calculated FWHM is shown in the inset graph. ....	92
Figure 3.11 An input THz pulse trace a) As a function of varying bias. b) As a function of varying laser power. Peak amplitude is linear fitted, and FWHM is non-linear curve fitted in the inset graphs. ....	93
Figure 3.12 Schematic of an output pulse detection in an on-chip CPW device, where origins of reflections are indicated as A and B. ....	94
Figure 3.13 Trace of a THz output pulse in a time-window of 60 ps, where reflections are pointed out by red dots and calculated FWHM is shown in inset graph. .	95
Figure 3.14 An output THz pulse trace a) As a function of varying bias. b) As a function of varying laser power. Peak amplitude is fitted by a straight line as a guide to the eye, and the .....	96
Figure 3.15 FFT spectra of an output pulse detected at switch S2, where the noise floor is indicated by red dotted line to distinguish useful bandwidth present in the signal. ....	97
Figure 3.16 Schematic of input-output pulse detection in the same time-window by moving probe beam between switches S2 and S3. ....	98
Figure 3.17 Forward and reverse detection of output pulses a) Pulse generation-detection at S1 and S3 respectively. b) Pulse generation-detection at S3 and S1 respectively by swapping biasing and probing connections. c) Traces of two output pulses detected in the same time-window. d) Traces of input and out pulses detected in the same time-window. ....	99
Figure 3.18 Excitation of the symmetric odd mode by optical excitation of a pair of switches S1 and S2 in which the pump beam is defocused to cover both switch regions. ....	100
Figure 3.19 Detection of an output pulse at switch S3 and S4 (in two consecutive scans) in odd mode excitation. Lorentz fit to main pulse and FFT spectra of output pulse are shown in inset graphs. ....	101
Figure 3.20 Detection of an output pulse at switch S3 and S4 (in two consecutive scans) in even-mode excitation. Lorentz fit to main pulse and FFT spectra of output pulse are shown in inset graphs. ....	102
Figure 3.21 Schematic of the three-beams on-chip system, where the third beam split from pump beam is used to illuminate coupling switch. A and B indicates the position of the mechanical chopper while performing conventional and differential pulse measurements respectively. ....	103
Figure 3.22 IV characteristics of photoconductive switches a) S1. b) S3. ....	105
Figure 3.23 Coupling switch IV and slot gap leakage current. ....	106
Figure 3.24 Knife-edge experiment: a surgical scalpel blade mounted on an XYZ manual translation stage. ....	107

- Figure 3.25 Laser beam spot size measurement. a) Average beam power measured and its first derivative plotted as a function of knife edge position in X-axis b) FWHM of Gaussian beam profile plotted as a function of knife edge position in z-axis c) Intensity of Gaussian beam by taking the first derivative of average power plotted as function of knife edge in x and z-axes d) An example of beam spot size calculation for the FWHM of the Gaussian profile.....108
- Figure 3.26 A schematic showing generation-detection of an input pulse in a CGAP-CPW device. ....109
- Figure 3.27 A trace of an input pulse, where the main pulse followed by three reflections is shown in a 50 ps time-window.....110
- Figure 3.28 Multiple traces of an input pulse taken by varying bias applied across switch S1, where a linear dependence is obtained by fit to the pulse amplitudes. ....110
- Figure 3.29 Output pulse detection in a CGAP-CPW device, where third beam (not chopped) is focused onto coupling switch. ....111
- Figure 3.30 A trace of an output pulse detected at photoconductive switch S2 and multiple traces shown in inset graph, taken while coupling switch is illuminated by the third beam. ....112
- Figure 3.31 A schematic representation of odd/even mode excitation in a CGAP-CPW device by defocusing pump in order to excite a pair of switches (S1 and S2) while coupling switch is illuminated by the third beam. ....112
- Figure 3.32 a) An odd mode excited output pulse detected at switch S3 and multiple scans of odd mode pulse taken while coupling switch was illuminated by the third beam are shown in inset graph. b) An output THz pulse and its first derivative plotted as a function of time delay. ....113
- Figure 3.33 An illustration of conversion of a Gaussian THz pulse into monocycle pulse by performing differentiation operation.....114
- Figure 3.34 Traces of an output pulse measured at S3 and S4 respectively by exciting an even mode at switch S1 and S2, FFT spectra and Bigaussian fit to main are shown in inset graph. ....115
- Figure 3.35 Transfer process for thin LT-GaAs layers on to quartz substrates in CPW device fabrication: a) LT-GaAs layer on SI-GaAs separated by AlAs layer. b) LT-GaAs covered with black wax. c) Removal of wax from outer edges. d) AlAs layer etched away by HF. e) Sample placed onto quartz chip f) Black wax removed from LT-GaAs. ....116
- Figure 3.36 a) A good quality LT-GaAs transfer b) LT-GaAs lifted-off after an etching and sample cleaning process. ....118
- Figure 3.37 CPW lithography on a quartz substrate a) Deposition of bilayer resist on quartz. b) UV exposure through device mask. c) Development of resist in developer MF319 d) LOR development. e) Deposition of Ti/Au in metallisation process. f) Lift-off process. ....118

Figure 3.38 A schematic representation of LT-GaAs transfer on quartz substrate followed by CPW metallisation process. ....	119
Figure 3.39 IV characteristics of switch S1 and S4 with varying bias and laser power. ....	120
Figure 3.40 a) A pair of photoconductive switches fabricated by epitaxial lift-off of LT-GaAs. b) Switches damaged by electrostatic discharge. c) A small patch of LT-GaAs is forming a coupling switch. d) A damaged coupling switch. ....	121
Figure 3.41 A trace of input THz pulse consisting of the main pulse at zero ps followed by secondary reflections. FWHM calculated by Lorentz fit to the main pulse is shown in inset graph. ....	122
Figure 3.42 Input THz pulse a) A linear bias dependence shown by linear fit in inset graph. b) A linear power dependence shown by linear fit in inset graph. ....	123
Figure 3.43 A trace of an output pulse, where the main pulse occurred at zero time delay is followed by two secondary reflections occurred at 21.81 ps and 26.12 ps respectively and Lorentz fit to the main pulse is shown in inset graph. ....	124
Figure 3.44 Traces of output pulse taken at different bias and laser powers showing a linear dependence by a linear fit to pulse amplitude shown in inset graph. ....	125
Figure 3.45 An average of ten FFT spectra plotted against standard deviation to reveal noise level present in the signal. ....	126
Figure 3.46 Traces of two output pulse detected at switch S1 and S3 respectively, where zero time delay represents the origin of input pulse generation. ....	127
Figure 3.47 An average of ten FFT spectra of an “odd mode-output pulse” plotted against standard deviation to reveal noise level present in the signal. ....	128
Figure 3.48 Trace of an “even mode-output pulse” detected at switch S3 and S4 in two consecutive scans. ....	128
Figure 3.49 a) A capacitive pi-equivalent circuit model of coupling gap discontinuity, where a photoconductance $G(t)$ is added in parallel to coupling capacitor under illumination condition b) Photoconductance plotted as function of gap length. ....	131
Figure 3.50 An illustration of ultra-fast fs pulses with a repetition rate of 80 MHz and pulse width of 110 fs. ....	131
Figure 3.51 IV sweep characteristics of a) Photoconductive switch S1. b) Photoconductive switch S3. ....	133
Figure 3.52 A waterfall model of input pulse trace measured from four CGAP-CPW devices (10, 20, 30 and 40 $\mu\text{m}$ coupling gap), where a relative change in peak amplitude of secondary reflection is demonstrated by increasing third beam power from 0 to 13 mW. ....	134
Figure 3.53 Normalised input pulse traces for 10, 20, 30 and 40 $\mu\text{m}$ gap devices, where the relative amplitude of the first reflection compared at 0 and 13 mW power of the third beam. ....	135

Figure 3.54 Traces of output pulse detected at switch S3 in a CGAP-CPW device with coupling gap length of 10 and 20 $\mu\text{m}$ .....	136
Figure 3.55 Traces of output pulse in odd mode excitation in a CGAP-CPW device a) 10 $\mu\text{m}$ gap device. b) 20 $\mu\text{m}$ gap device. c) 30 $\mu\text{m}$ gap device. d) 40 $\mu\text{m}$ gap device.....	138
Figure 3.56 dB values obtained from FFT performed on $S_{\text{on}}$ and $S_{\text{off}}$ output pulses obtained under dark and illumination condition, plotted as a function of the frequency of operation. ....	139
Figure 3.57 An average of ten FFT spectra plotted against standard deviation to reveal noise level present in the signal. ....	140
Figure 3.58 An illustration of three-beam measurement setup .....	141
Figure 3.59 a) A schmatic showing differential pulse measurement using three-beam measurement system. b) A trace of detected differential pulse in the time-window of 40 ps.....	142
Figure 3.60 a, b) Differential (modulated) and conventional pulse measurement setup. c) A comparison of conventional and differential pulse. d) A comparison of FFT spectra obtained from differential and conventional pulses. ....	143
Figure 3.61 a) A comparison of “Odd mode” output pulses under dark and with laser illumination. b) A difference signal $S_{\text{on}}-S_{\text{off}}$ was obtained by subtracting $S_{\text{off}}$ from $S_{\text{on}}$ c) A comparison of difference and differential pulses d) A comparison of FFT spectra obtained from difference and differential pulses. ....	144
Figure 3.62 a) A schematic in which odd/even modes are launched by biasing a pair of switches and illumination with defocused pump beam b) A coupling switch filters out even mode componenet of field from the hybrid mode launched from switch S1 c) Output pulses measured from both measurement configurations are compared and FFT spectra of output pulses are compared in inset graph. ....	146
Figure 3.63 a) A comparison of differential pulses measured from CGAP-CPWs of different gap lengths (10, 20, 30 and 40 $\mu\text{m}$ ) b) A comparison of FFT spectra. ....	147
Figure 4.1 The second generation CPW device a) A magnified view of the parasitic region. b) A four photoconductive switch layout with parasitic regions. c) A magnified view of photoconductive switch regions. ....	150
Figure 4.2 A PCB layout for the second generation CPW device and mounting PCB compatible with both room and low-temperature operation. ....	151
Figure 4.3 IV characteristics of switch S2 and S4 with varying bias and laser power. ....	152
Figure 4.4 a) Magnified view of transmission region in which a reflection coming from the photoconductive switch region S3-S4 is shown by the blue dashed line. b) Overall schematic of input pulse detection for the second generation CPW device. In Figure a,.....	153

- Figure 4.5 Trace of an input pulse in a time-window of 120 ps, in which the main pulse is followed by a secondary reflection occurring at 11.2 ps after the main pulse and a Lorentz fit to the main pulse is shown in inset graph. .... 153
- Figure 4.6 Traces of the input pulse in a time-window of 60 ps a) Amplitude of input pulse as a function of varying bias. b) The amplitude of input pulse as a function of varying the laser power and a Lorentz fit to peak amplitude is shown in inset graphs. .... 154
- Figure 4.7 A trace of an output pulse, in which the main pulse is occurring at zero time delay is followed by a minor reflection occurred at 126 ps and Lorentz fit to the main pulse is shown in inset graph. .... 155
- Figure 4.8 A trace of an output pulse detected in a time-window of 500 ps and an average of ten FFT spectra plotted against standard deviation in inset graph. .... 156
- Figure 4.9 Traces of output pulses a) A linear bias dependence shown by a linear fit to peak amplitude in inset graph. b) A linear power dependence shown by a linear fit to peak amplitude. .... 156
- Figure 4.10 Traces of two output pulses detected at switch S2 and S4 respectively, where zero time delay represents the origin of input pulse generation. .... 157
- Figure 4.11 Detection of an output pulse at switch S3 and S4 (in two consecutive scans) in odd mode excitation. Lorentz fit to main pulse and FFT spectra of output pulse are shown in inset graphs. .... 158
- Figure 4.12 Detection of an output pulse at switch S3 and S4 (in two consecutive scans) in even-mode excitation. Lorentz fit to main pulse and FFT spectra of output pulse are shown in inset graphs. .... 159
- Figure 4.13 An illustration of THz pulse splitting (sampled and reference pulses) in an on-chip spectroscopy measurement a) Y-splitter loaded with SUT. b) Y-coupler loaded with SUT. .... 160
- Figure 4.14 A schematic representation of THz Splitter device design. .... 161
- Figure 4.15 a) Schematic representation of a Y-coupler fabricated on a quartz substrate. b) Detail, in which free standing LT-GaAs switches are pointed as S1, S2, S3, S4, and Sc. .... 162
- Figure 4.16 a) 3D simulation model of a Y-splitter. b) Scattering parameters obtained from Y-splitter on a GaAs substrate. c) Scattering parameters obtained from Y-splitter on a quartz substrate. .... 163
- Figure 4.17 EM-field a) An equal EM-field splitting between  $Y_A$  and  $Y_B$  shown in the Y-splitter, simulation model. b) A weak coupling between straight CPW and  $Y_A$  of EM-field shown in a Y-coupler simulation model. c) Scattering parameters **S21** and **S31** obtained from port 2 and port 3 respectively in a Y-coupler.... 164
- Figure 4.18 Input pulse detection a) A schematic representation of generation and detection of an input pulse in Y-splitter waveguide. b) Trace of an input pulse, in which the main pulse is followed by two secondary reflections occurring at 34.6 and 41.3 ps after the main pulse. .... 165

- Figure 4.19 Traces of the input pulse measured from a Y-splitter waveguide a) Traces of input pulse as a function of varying bias. b) Traces of input pulse as a function of varying laser power, a linear fit to peak amplitude is shown in inset graphs. ....166
- Figure 4.20 An output pulse detection in a Y-splitter (LT-GaAs substrate) a) A schematic representation of detection of split THz pulses in the Y-splitter waveguide. b) Traces of output pulses, in which the main pulse is followed by secondary reflections occurring at 26.54, 34.01 and 41.26 ps after the main pulse. c) Traces of input and output pulses with a relative time difference of  $\sim 19.38$  ps measured in the same time-window ( $\sim 70$  ps). ....167
- Figure 4.21 Traces of output pulses measured from a Y-splitter a) As a function of varying bias. b) As a function of varying laser power; a linear fit to peak amplitude is shown in the inset graphs. ....168
- Figure 4.22 FFT spectra of input (shown in red) and output pulses (shown in blue and green) measured from the Y-splitter on GaAs substrate. ....168
- Figure 4.23 A trace of an input pulse, in which the main pulse is occurring at zero time delay is followed by secondary reflections occurred at 22.13 and 25.8 ps. ....170
- Figure 4.24 Output pulse detection in a Y-splitter a) Traces of split THz pulses detected at S3 and S4 b) Traces of input and output pulses with a relative time difference of 12.67 measured in the same time-window of 40 ps. ....171
- Figure 4.25 FFT spectra of the input and output pulses plotted on a dB scale. ....172
- Figure 4.26 Traces of the output pulses detected at S3 and S4 detected in the same time-window of 120 ps, where zero time delay represents the generation of an input pulse. ....172
- Figure 4.27 a) Detection of the input and output pulses with a relative time difference of 12.67 in the same time-window of 40 ps. b) A comparison of output pulses under dark and illuminated conditions. ....174
- Figure 4.28 a) Detection of an output pulse in Y-coupler while coupling switch is illuminated by the third beam. b) FFT spectra of input and output pulses plotted on a dB scale. ....174
- Figure 4.29 Schematic representation of differential pulse measurement in a Y-coupler using three beams on-chip system, where the mechanical chopper was moved to position B in order to modulate coupling switch Sc. ....175
- Figure 4.30 Detection of conventional and modulated THz pulses in branching waveguides  $Y_A$  and  $Y_B$  respectively in a time-window of 60 ps. FWHM and FFT spectra of conventional and modulated THz pulses are compared in inset graphs. ....176
- Figure 4.31 A schematic representation of on-chip spectroscopy of overlaid lactose monohydrate on branching waveguide  $Y_A$  in a Y-coupler using three beams on-chip system. ....177

Figure 4.32 a) Reference and sampled output pulses in time-domain. b) A comparison of FFT spectra of the reference and sampled pulses. ....	178
Figure 5.1 Electric field lines are shown in coplanar mode (blue) and slot-line mode (red). ....	181
Figure 5.2 a) Attenuation coefficient is plotted w.r.t slot gap width. b) Characteristic impedance and effective permittivity are plotted w.r.t gap width. ....	183
Figure 5.3 A 3D model of a CPW in HFSS, where electric field plotted against a polyline in blue. ....	184
Figure 5.4 Electric field intensity for different gap widths is plotted against a polyline in the perpendicular direction, and field intensity also plotted against gap widths for data clarity in inset graph. ....	185
Figure 5.5 E-field intensities plots are normalised from 0 to 1 to emphasise the depth of penetration of the field into both air and the substrate. ....	186
Figure 5.6 <b>S<sub>21</sub></b> scattering parameter plotted on a dB scale against frequency. ....	187
Figure 5.7 A magnification of PC switches region of the second generation CPW device with slot gap width 10 $\mu\text{m}$ and transmission length of 750 $\mu\text{m}$ . ....	188
Figure 5.8 A schematic of the second generation CPW showing the origin of first and second reflections in pulse detection. ....	189
Figure 5.9 Comparison of the input and output THz pulses detected at switches S2 and S4 respectively. The output pulse is offset by 20 nA for clarity. ....	190
Figure 5.10 A comparison of the bandwidth of output pulses measured from CPWs (10 $\mu\text{m}$ and 20 $\mu\text{m}$ slot gaps). ....	190
Figure 5.11 Schematic of variable temperature setup consisting of; Oxford Instruments Microstat, Helium Dewar, transfer tube to transfer helium, ports for electrical connection and temperature sensor (EC and TC). ....	192
Figure 5.12 (a) PCB for on-chip spectroscopy with a window for optical access. b) A CPW device is placed on the top of the optical window for backside illumination. ....	193
Figure 5.13 a) Compressed lactose pellet in a copper ring. b) Lactose sample overlaid onto a CPW device. ....	194
Figure 5.14 a) A concentrated solution of lactose monohydrate in DI water. b) Lactose monohydrate drop cast onto a CPW device. ....	194
Figure 5.15 A schematic of a first-generation CPW device with gap loaded with lactose monohydrate for differential modulated pulse spectroscopy measurement using the three-beam on-chip system in which coupling switch (Sc) is illuminated by 3 <sup>rd</sup> beam. ....	196
Figure 5.16 a) Time-domain differential (modulated) output pulses (reference and sample). Reflections in the output pulse are shown in inset graph. b) A comparison of FFT spectra of the reference and sample. ....	196



- Figure 5.17 a) Normalised time-domain input pulses measured at different temperatures ranging from 6 to 292 K. b) Normalised output pulses measured for different temperatures. c) FWHM of the input and output pulses plotted against temperature. d) Lorentz fit of the input and output pulses (at room temperature), with FWHM of 1.32 ps and 1.41 ps respectively. ....198
- Figure 5.18 a) Averaged FFT spectra of 10 scans at room temperature plotted against standard deviation (shown in red). Time-domain signal is shown in the inset graph. b) Averaged FFT spectra of 10 scans at 6 K with standard deviation is shown in red. Time-domain signal is shown in the inset graph. ....199
- Figure 5.19 Image of drop-casted lactose onto transmission line of the second generation CPW device. The device is mounted on a PCB attached to the cold finger.....200
- Figure 5.20 FFT Spectra of lactose monohydrate at room temperature (red) and low temperature (6 K, in blue). The temperature result is compared with FFT spectra obtained by free space THz-TDS (black). Plots are offset for clarity. 200
- Figure 5.21 FFT Spectra of lactose monohydrate at room (red) and low (6 K in blue) temperature. FWHM of 0.53 THz absorption feature is compared in the inset graph.....202
- Figure 5.22 a) Absorption spectra of purine at 4, 54, 105, 204, 253, and 295 K (from top to bottom). b) Temperature dependence of the resonance frequency centred at 1.68 THz (at 4K). Open circles are experimental data, and the solid line is calculated by fitting Equation 5-6. The inset shows the best-fitting parameters in units of THz, K. (All plots taken from [182])......202
- Figure 5.23 FFT spectra of subsequent measurements at room temperature, 6 K and temperatures ranging from 70 – 220 K in 50 K increments are plotted on a reciprocal (1/amplitude) scale against frequency.....203
- Figure 5.24 a) The FWHM of the absorption feature at 1.41 THz plotted against temperature. Lorentz fit of absorption feature is shown in inset graph. b) Shift in absorption dip (1.41 THz) plotted against temperature and centre frequency of high-frequency absorption feature is determined by curve fitting using Equation 5-6. ....204
- Figure 5.25 HFSS simulation results for varying interaction lengths (100 – 800  $\mu\text{m}$ ) a) **S21** parameters. b) Absorption spectra obtained for a PGL (planar Goubau line) loaded with lactose monohydrate. Simulation results are taken from [90].....205
- Figure 5.26 a) Differential-THz output pulse measurement (second generation gap CPW) using three-beam on-chip system. b) Conventional output pulse measurement (second generation continuous CPW) using the two-beam on-chip system.....206
- Figure 5.27 a) A comparison of output pulses measured using two- and three-beam on-chip systems. Pulses are offset for clarity. FWHM of output pulses are compared in the inset graph. b) A comparison of the FFT spectra of output pulses from the different techniques.....207

Figure 5.28 A schematic of second generation gap CPW loaded with lactose monohydrate for differential spectroscopy measurement using the three-beam on-chip system.....	208
Figure 5.29 a) FFT spectra of 10 scans at room temperature plotted against standard deviation (shown in red). Differential time–domain signal is shown in the inset graph. b) FFT spectra of 10 scans at 6 K with standard deviation is shown in red. Differential time –domain signal is shown in the inset graph. ....	208
Figure 6.1 a) A comparison of scattering parameters obtained from HFSS simulations performed on CPWs with 5 and 10 $\mu\text{m}$ slot gaps. b) Normalised field intensity for gap widths 5 and 10 $\mu\text{m}$ plotted against a ployline perpendicular to CPW plane. ....	214
Figure 6.2 Implementation of tunable filters in CPW a) A stop band filter formed by series short stub b) A pass-band filter formed by series open stub c) A schematic of proposed CPW device design. ....	215
Figure 6.3 a) A stop band with resonant frequency 460 GHz b) A pass band with centre frequency 275 GHz, followed by a stop band with resonant frequency 920 GHz. c) EM field simulation of stop band filter showing resonance field around stub region d) Em field simulations of pass-band filter shwoing two resonances corresponding to pass-band and stop-band. ....	216
Figure 6.4 An illustration of Y-splitter used as a multiplexer/combiner in order to study interference pattern.....	217
Figure 6.5 An illustration of 1×4 Y-splitter comprising cascaded 1×2 Y-splitters with arc-shaped branching waveguides in which three branching waveguides are loaded with samples under test and the remaining branching waveguide is used to measure a reference signal. ....	218

# List of Tables

Table 1-1 An overview of different electronic and optoelectronic THz sources (taken from Ref. [17]) .....	3
Table 1-2 Characteristics of photoconductive materials suitable for THz generation and detection (taken from Ref. [24]). .....	7
Table 2-1 Essential coplanar waveguide discontinuities and their equivalent circuits (Images are reproduced from Ref. [99]). .....	42
Table 2-2 Fundamental filter elements realised in coplanar waveguide technology (Images are reproduced from Ref. [99]). .....	43
Table 2-3 Values of voltage and power ratios against roll off values of signal amplitude in dB. ....	64
Table 5-1 Comparing the bandwidth of various transmission lengths. ....	187

# Abbreviations

BCB	Benzocyclobutene
BWP	Backward-Wave Oscillator
CBCPW	Conductor-backed Coplanar Waveguide
CPW	Coplanar Waveguide
CGAP-CPW	Coupling Gap CPW
DC	Direct Current
DFG	Difference Frequency Generation
EM	Electromagnetic Waves
EO	Electro-Optic
FDM	Finite Difference Method
FEM	Finite Element Method
FDTD	Finite Difference Time Domain
FFT	Fast Fourier Transform
fs	Femtosecond
FWHM	Full Width Half Maximum
GaAs	Gallium Arsenide
HEMT	High Electron Mobility Transistor
HFSS	High-Frequency Structure Simulator
HPF	High Pass Filter
LT-GaAs	Low-Temperature Gallium Arsenide
MBE	Molecular Beam Epitaxy
MIM	Metal Insulator Metal
ND	Neutral-Density

NIR	Near Infra-red
PC	Photoconductive
PCB	Printed Circuit Board
ps	Pico-second
PTFE	Polytetrafluoroethylene
QCL	Quantum Cascade Laser
SNR	Signal-to-Noise Ratio
SOS	Silicon-on-Sapphire
SUT	Sample Under Test
TDS	Time-Domain Spectroscopy
TEM	Transverse Electromagnetic
THz	Terahertz
UWB	Ultra Wide Band
UV	Ultraviolet



# Chapter 1

## Fundamentals of THz Time-Domain Spectroscopy

### 1.1 Introduction

The Terahertz (THz) spectrum, which is located between the microwave and mid-infrared frequency bands of the electromagnetic spectrum has been less developed compared to its neighbouring frequency ranges and has therefore, sometimes been referred to as the “Terahertz-Gap” [1, 2]. Modern THz technology, also referred as millimeter-wave technology (as spanning between 3 and 0.03 mm) arguably began with the development of THz sources over three decades ago. A major breakthrough in technology came with the development of broadband THz sources using ultra-fast femtosecond lasers to excite photoconductive switches.

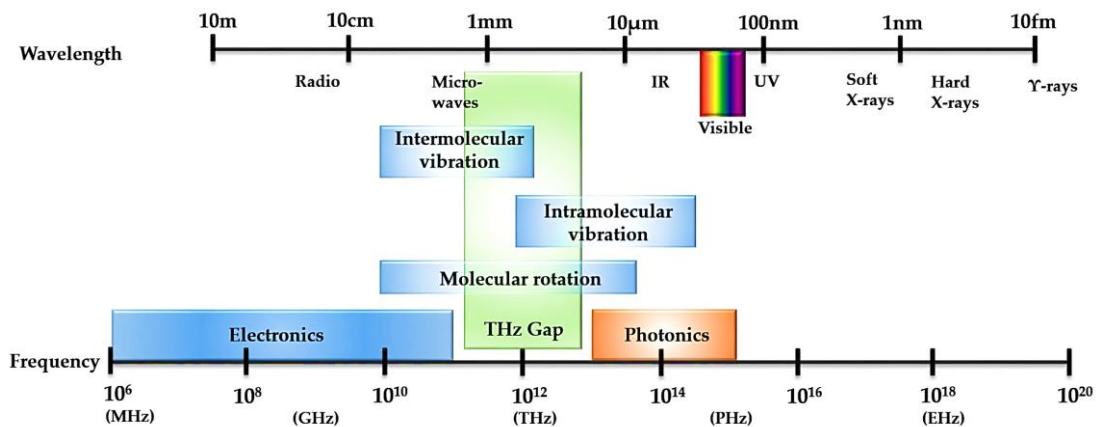


Figure 1.1 Diagram showing the THz region of the electromagnetic spectrum.

The THz spectrum can be broadly defined as between 0.1 and 10 THz in the frequency domain, [3] so bridging the gap between millimetre (electronic) and sub-

millimetre (photonic) wave technologies. Since the advent of THz spectroscopy in the 1980s, great attention has been paid to THz frequency range due to its potential in time-domain spectroscopy and imaging of a wide variety of chemicals (including water, paper, plastic, ceramics, wood, biological tissue, carbon mono-oxide, glucose, lactose and methanol to name a few), since strong frequency-dependent absorption features can often clearly be seen in this range [4].

Due to the non-ionising and non-destructive properties of THz radiation, prospective applications for THz technology are identified in the fields of security[5], Spectroscopy [6, 7], pharmaceutical drugs [8] and investigation of condensed matter systems [9].

## **1.2 Sources of THz generation and detection: An overview**

This section covers a brief introduction to different THz sources with a greater emphasis on optical THz sources, which will be used in this project. Sources of THz generation and detection can primarily be divided into the three categories such as electronic, laser and optically driven sources as shown in Table 1-1.

The backward-wave oscillator (BWO), an electron vacuum diode, has been used as a THz source for spectroscopic measurements [10, 11], covering a frequency range of 0.1 to 1.5 THz. However, several BWOs are needed in order to cover full THz range because BWOs can only be tuned  $\pm 30\%$  of its centre frequency [12, 13]. In a Gunn diode, with a negative differential resistance region, a high CPW bias leads to current fluctuations, which eventually become coherent oscillations in the frequency range of THz[14]. Gunn diodes with output power  $\sim 100$  mW have been used for THz generation up to frequencies of operation around 3 THz. Quantum cascade lasers (QCL) yield a relatively high power of up to be 1-Watt at cryogenic temperatures [15]. A limitation with QCLs is that they have a maximum operating temperature of 199.5 K[16]. On the other hand, photoconductive switches can efficiently be used for both room and cryogenic temperatures for THz generation and detection. The term photoconductive



switch was first coined by D.H Auston and therefore, photoconductive switches also known as Auston switches.

Sources	Generation	Detection
Electronic	<ul style="list-style-type: none"> <li>• Backward-wave oscillator</li> <li>• Gunn diode</li> <li>• Resonant tunnelling diode</li> </ul>	<ul style="list-style-type: none"> <li>• Schottky diode</li> <li>• Backward diode</li> <li>• HEMT transistor</li> <li>• Bolometer (<math>\sim 4</math> K)</li> <li>• Golay Cell</li> <li>• Pyroelectric detector</li> </ul>
Laser	<ul style="list-style-type: none"> <li>• Quantum cascade laser</li> <li>• p-type germanium laser</li> <li>• Free electron laser</li> </ul>	QCLs by self-mixing
Optical	<ul style="list-style-type: none"> <li>• Photoconductive switch</li> <li>• Optical rectification</li> </ul>	<ul style="list-style-type: none"> <li>• Photoconductive switch</li> <li>• Electro-optic sampling</li> </ul>

**Table 1-1** An overview of different electronic and optoelectronic THz sources (taken from Ref. [17])

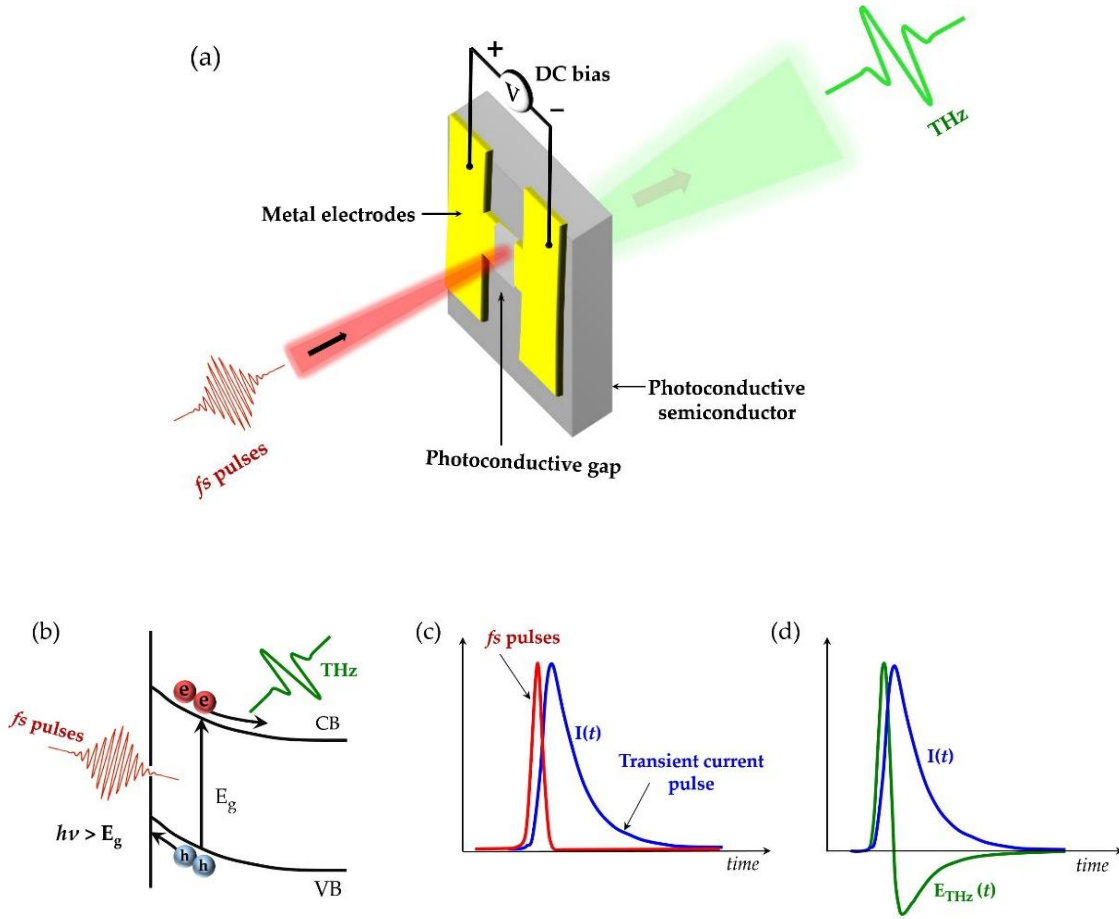
## 1.3 Free-space THz generation and detection

In the previous section, it was discussed that photoconductive switches can be used for THz generation and detection. This section discusses the working principle of the photoconductive switch to give an insight into underlying physics of THz generation and detection.

### 1.3.1 THz generation by photoconductive switch

In a photoconductive switch, THz radiation is generated by exploiting the photoconductive properties of semiconductor material. In doing so, a direct band-gap semiconductor such as Gallium Arsenide (GaAs) is first DC biased using metal electrodes. The Inter-electrode gap (often called as a photoconductive gap) is

illuminated by near infra-red (NIR) laser pulses with photon energy greater than that of the band gap of semiconductor material (shown in Figure 1.2 b) which promotes electrons from the valence band into the conduction band, creating holes in the valence band.



**Figure 1.2** An illustration of THz generation a) A photoconductive switch illuminated with NIR fs laser pulses. b) The motion of photo-charge carriers in energy bands on the application of NIR laser beam. c) Generation of a temporal transient current pulse. d) Transient current pulse leads to the emission of THz field (taken from Ref. [18]).

The generated photo-charge carriers are then accelerated by the external field provided by a DC bias, resulting in transient current pulses (shown in Figure 1.2 c). If the generated transient current pulses vary on a picosecond time-scale, the radiating electromagnetic field will be in the THz regime.

The radiating field  $E_{THz}$  is proportional to the rate of change of the total photocurrent density  $J_{ph}$  in the inter-electrode gap [19] and is given by:

$$E_{THz}(t) \propto \frac{dJ_{ph}(t)}{dt} \quad 1-1$$

Where, total photocurrent density  $J_{ph}$  is contributed due to both charge carriers (i.e. electrons and holes) and therefore is given as [20]:

$$J_{ph} = J_e + J_h = e(nv_e + pv_h) \quad 1-2$$

Where,  $v_e$  and  $v_h$  are the drift velocities of electron and holes respectively,  $n$  and  $p$  denote the carrier densities of electron and hole respectively and  $e$  is the charge of an electron.

The time-derivative of the total photocurrent density  $dJ_{ph}(t)/dt$ , which is proportional to the radiating THz field  $E_{THz}$  can be expressed as [21]:

$$\frac{dJ_{ph}(t)}{dt} = e \left[ v_e \frac{dn}{dt} + v_h \frac{dp}{dt} + n \frac{dv_e}{dt} + p \frac{dv_h}{dt} \right] \quad 1-3$$

Therefore, the THz field  $E_{THz}(t)$  is given by:

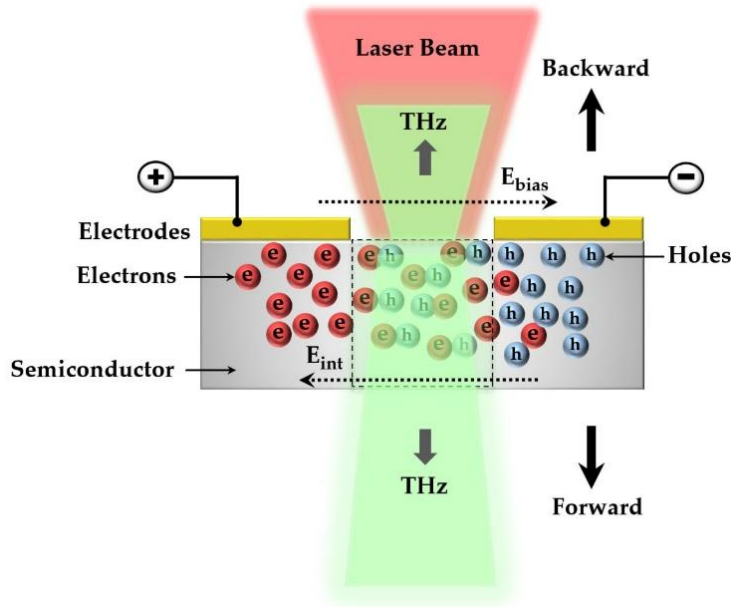
$$E_{THz}(t) \propto e \left( v_e \frac{dn}{dt} + v_h \frac{dp}{dt} \right) + e \left( n \frac{dv_e}{dt} + p \frac{dv_h}{dt} \right) \quad 1-4$$

The first term  $(v_e \frac{dn}{dt} + v_h \frac{dp}{dt})$  in the expression 1-4, suggests that generated THz pulse depends on the rates of generation of photo-charge carriers, which is determined by rise time of ultra-fast laser pulses, illuminating photoconductive gap.

However, the second term  $(n \frac{dv_e}{dt} + p \frac{dv_h}{dt})$  indicates that intensity of generated THz pulse depends on the rates of drift velocities of the charge carrier (i.e. acceleration of charge carriers under applied DC bias) which is further related to the mobilities of photo-charge carriers. The decay time of THz pulse (i.e. falling edge of THz pulse) depends on the lifetime or recombination rate  $\tau_c$  of photo-charge carriers [22].

The separation of photo-charge carriers under applied DC bias creates an internal field  $E_{int}$  which causes a screening of the applied bias field as shown in Figure 1.3. Screening due to photo-charge carriers can reduce the effective electric field seen by

photo-charge carriers generated subsequently. Therefore, a higher recombination rate of photo-charge carriers is of critical importance in order to minimise the screening effect. A method of achieving higher recombination rate (i.e. low carrier lifetime) in a direct band-gap semiconductor such as GaAs is discussed in the following section.



**Figure 1.3** An illustration of THz emission in both forward and backward direction from a photoconductive switch.

It is worth mentioning that the THz radiation generated using photoconductive switches radiates in both the forwards (i.e. radiating through semiconductor) and backward (i.e. radiating in the opposite direction of laser beam illumination) directions, as shown in Figure 1.3. Interestingly, THz field radiated in the backward direction yields a substantially higher bandwidth compared to that of radiating in the forward direction, which is attributed to attenuation and dispersion losses added while THz field is radiating through the semiconductor substrate in the forward direction [23].

### 1.3.1.1 Suitable photoconductive materials

A variety of photoconductive materials have been used for THz generation and detection. Generally, photoconductive materials are grown in a molecular-beam epitaxy (MBE) process by the precise control of deposition rate (one atomic layer at a time). An ultra-high vacuum of  $\sim 10^{-10}$  mbar is required in order to perform molecular-beam epitaxy. To achieve the desired epitaxial growth, elements in the form of

atomic/molecular beams from a heated crucible are directed at a single host substrate. Deposition of the epitaxial layer is controlled by dedicated shutters in front of each crucible.

Photoconductive material	Carrier lifetime (ps)	Mobility (cm <sup>2</sup> /(Vs))	Resistivity (ΩV/cm)	Band gap (eV at R.T.)
Cr:doped ST-GaAs	50 - 100	≈ 1000	10 <sup>7</sup>	1.43
LT-GaAs	0.3	150-200	10 <sup>6</sup>	1.43
SI-InP	50 - 100	≈ 1000	4 × 10 <sup>7</sup>	1.34
Ion-Implanted InP	2 - 4.0	200	> 10 <sup>6</sup>	1.34
RD-SoS	0.6	30	-	1.10
Amorphous Si	0.8 - 20.0	1	10 <sup>7</sup>	1.10
MOCVD CdTe	0.5	180	-	1.49
LT-In <sub>0.52</sub> Al <sub>0.48</sub> As	0.4	5	-	1.45
Ion-Implanted Ge	0.6	100	-	0.66
ErAs:GaAs [ BCL <sup>+</sup> 04, SBG <sup>+</sup> 03]	≈ 0.25	> 100	5 × 10 <sup>5</sup>	1.43

**Table 1-2 Characteristics of photoconductive materials suitable for THz generation and detection (taken from Ref. [24]).**

Photoconductive materials suitable for THz generation-detection are listed in Table 1-2. Low temperature grown GaAs has been most widely used among the listed materials to fabricate efficient photoconductive switches for THz generation and detection due to its property of having a low carrier lifetime. However, MBE-growth of GaAs at low temperature (~ 200 °C) creates a significant number of point defects in the GaAs lattice with a consequent increase in As atoms incorporated into the wafer. Due to these defects, a deep-level donor state is formed [25-27] which substantially decreases the carrier lifetime by increasing recombination rate of photo-charge carriers. For growth temperature of ~ 200 °C, a carrier lifetime of ~ 90 fs have since been observed

[28]. However, the growth of GaAs at a low temperatures introduces a large number of donor states, which yields a low resistivity with a consequent increase in dark (background) current.

To circumvent this issue, a post-growth annealing technique is used in which LT-GaAs is thermally annealed to reduce the number of point defects which allows the resistivity to be increased up to six orders of magnitude for an annealing temperature of  $\sim 600$  °C. However, carrier lifetime is also affected by post-growth annealing. Therefore, a trade-off between low carrier lifetime and high resistivity needs to be reached. In this project, an optimised annealing temperature of  $\sim 575$  °C has been used which meets the trade-off between low carrier lifetime and high resistivity for LT-GaAs used in device fabrication.

### 1.3.2 THz generation by optical rectification

Optical rectification is a non-linear process in which a laser pulse with broad-spectrum interacts with an electro-optic nonlinear crystal causing DC polarisation. Optical rectification is a second-order phenomenon (also known as difference frequency generation) in which two frequency components within the broad spectrum of laser pulse induce dielectric polarisation, which causes THz to be generated from the crystal at the beat frequency.

This can further be understood as when a laser beam consisting of ultra-short pulses passes through a non-linear electro-optic crystal; the driving electric field causes the atoms to develop an oscillating dipole moment which tends to radiate electromagnetic energy.

The change in optical polarisation due to the incident field can be expressed by Taylor's series expansion as:

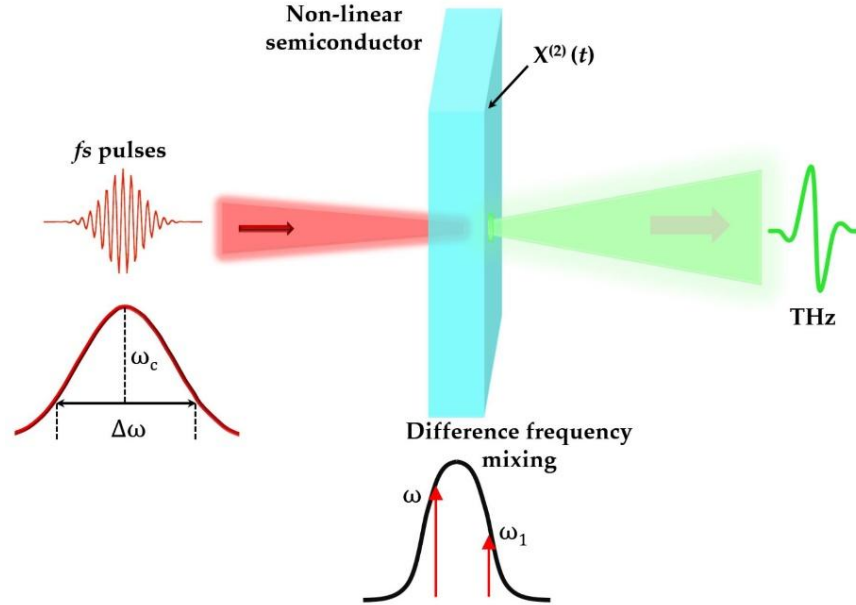
$$P(t) = \varepsilon_0(\chi^{(1)}E(t) + \chi^{(2)}E^2(t) + \chi^{(3)}E^3(t) + \chi^{(4)}E^4(t) + \dots) \quad 1-5$$

$$= P^{(1)}(t) + P^{(2)}(t) + P^{(3)}(t) + \dots \quad 1-6$$

where, non-linear term  $P^{(2)}(t)$  can be represented in frequency domain as [29]:

$$P_i^{(2)}(\omega)/\epsilon_0 = \int_{\omega_c - \Delta\omega/2}^{\omega_c + \Delta\omega/2} \chi^{(2)} E_i(\omega_1) E_K(\omega_1 - \omega) d\omega_1$$

Where,  $\omega_c$  is the centre frequency of incident laser beam and  $\Delta\omega$  represents the bandwidth of the broad spectrum of the laser beam. The bandwidth present in the laser pulses determines the frequency components contributing to second order polarization.

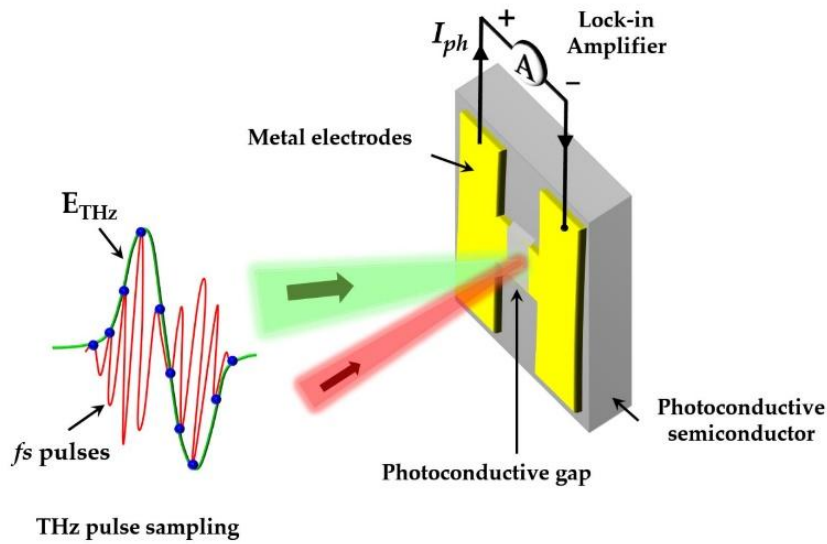


**Figure 1.4 THz generation from a non-linear electro-optic crystal due to difference frequency mixing.**

In Equation 1-5,  $E_i(\omega_1)E_K(\omega_1 - \omega)$ , the Fourier transforms of electric field's components of the laser beam in the frequency domain, indicate that induced polarisation is due to difference frequency generation (DFG).

### 1.3.3 THz detection by photoconductive switch

The working principle of THz detection using a photoconductive switch is similar to that of THz generation [30-32] in which photoconductive gap is illuminated by ultra-short laser pulses (referred as probe beam) with energy being greater than band-gap energy of the semiconductor in order to generate photo-charge carriers. THz field incident on the photoconductive gap acts as a bias to the photoconductive switch in order to accelerate photo-charge carriers. A photocurrent then flows through metal electrodes, which can be measured by a lock-in amplifier connected in series.



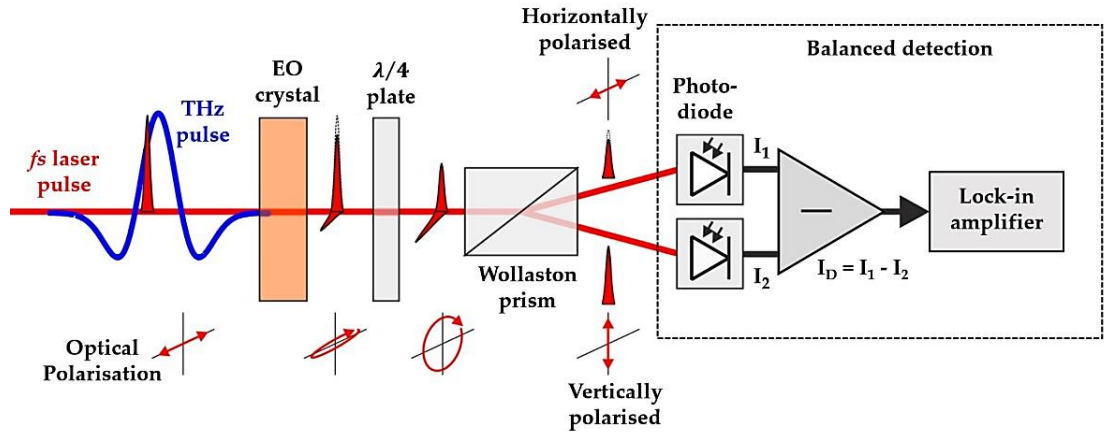
**Figure 1.5** Detection of the THz field using a photoconductive switch, where an average current mapped by time-delayed probe beam is measured by lock-in amplifier connected in series with a metal electrode.

Since the width of the laser pulse is much smaller ( $\sim 100$  fs) than that of the incident THz pulse, therefore, only a small portion of THz field can only be sampled by the photoconductive switch. However, a full THz pulse can be mapped by a time-delayed probe beam with respect to the incident THz pulse. Also, a short carrier lifetime of charge carriers is desirable.

### 1.3.4 THz detection by an Electro-optic crystal

THz detection by an electro-optic crystal exploits the optical property of a non-linear material such as ZnTe, GaP, and GaSe [33, 34], which becomes linearly birefringent under the influence of an external electric field. This electro-optic effect, producing birefringence is known as linear electro-optic effect or Pockel's effect [35]. In order to detect THz radiation using this effect, THz pulses are first passed co-linearly with ultra-short laser pulses (probe beam) through EO crystal as shown in Figure 1.6. The incident THz field acts as a bias field for EO crystal which then changes the refractive index of the EO crystal (change in the refractive index is proportional to the intensity of the incident THz field).





**Figure 1.6** Detection of THz field using EO crystal as a relative change in field components of NIR laser beam (Image reproduced from Ref. [17]).

This change in the refractive index reflects a change in incident probe beam polarisation (from circular to elliptically polarised [36]). The orthogonal field components of the probe beam are then separated by using a quarter wave plate and a Wollaston prism as shown in Figure 1.6. The orthogonal components separated by Wollaston prism are then detected by a pair of photo-diodes, by measuring relative intensities of field components. The relative difference between photocurrents (which is proportional to THz field intensity [37]) is then measured by a lock-in amplifier. In balanced detection, a zero relative difference between the generated photocurrents implies that no THz field was present (i.e. birefringence did not occur).

THz pulse detection using electro-optic sampling technique has been widely used for free-space terahertz time-domain spectroscopy (THz-TDS) [33]. However, this technique is limited by the thickness of EO crystal as optical dispersion and the mismatch between phase velocities of the incident laser pulse, and THz pulse may substantially be increased while passing through a thicker EO crystal.

## 1.4 Free-space THz time-domain spectroscopy

Over the last few decades, free-space THz-TDS has been widely used to obtain spectroscopic signatures of a variety of chemicals including explosive drugs and biological tissues [38-42].

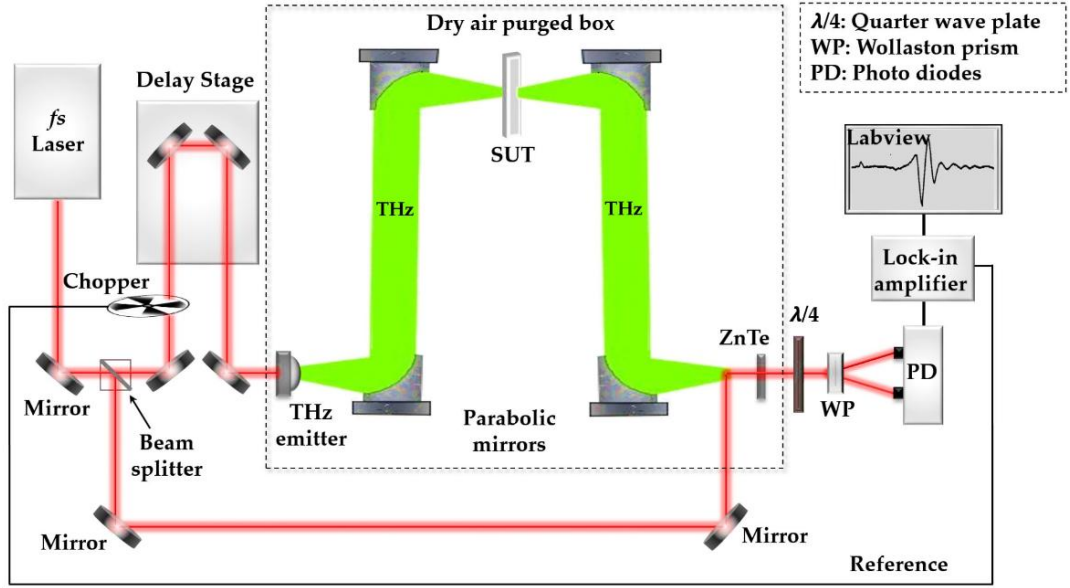
THz-TDS is based on a coherent detection technique; therefore, both the amplitude and phase information of detected pulse are readily available, which enable us to extract frequency-dependent parameters such as absorption coefficient and refractive index from SUT (sample under test such a lactose monohydrate, for example) by applying a Fourier transformation on detected time-domain pulses in order to obtain their fast Fourier transform (FFT) spectra. In this section, the components of a typical THz-TDS are described, and spectral features of lactose monohydrate obtained from THz-TDS measurement are discussed. A technique to measure differential THz pulse using free-space THz-TDS will also be discussed.

A typical THz-TDS system consists of the following components: A femtosecond laser source to excite photo-charge carriers in the photoconductive gap of a biased photoconductive switch (often called as emitter) in order to generate THz pulses; an electro-optic crystal for THz detection; a motorised optical delay stage used to time-delay probe beam to map out incident THz pulses; a mechanical chopper for optical modulation and a lock-in amplifier which measures amplitude and phase of detected THz pulse as shown in Figure 1.7.

In Figure 1.7, a laser beam (driven by Ti:Sapphire laser) having ultra-short pulses with duration of  $\sim 100$  fs, repetition rate of 80 MHz and centre wavelength of  $\sim 800$  nm is first split into a pump and a probe beam by using a 50:50 beam splitter placed at angle of  $45^\circ$ . The pump is focused onto a biased photoconductive emitter in order to generate the THz field which is then collected and collimated by using a pair of parabolic mirrors. The THz field then interacts with SUT and picks up spectral features associated with SUT. THz field is, then again, collected and re-collimated by another pair of parabolic mirrors in order to focus it onto the detector (an electro-optic crystal ZnTe, for example) in coincidence with probe beam.

A lock-in amplifier measures the THz field intensity as a relative change in orthogonal field components of the probe beam sensed by the balanced photodiodes. A motorised optical delay stage is then used to change the relative time delay between THz pulse and probe beam in order to map out a full THz pulse. A mechanical chopper is also employed with chopping frequency set as a reference to the lock-in amplifier in order to increase the sensitivity of THz pulse detection (i.e. improving signal-to-noise

ratio).



**Figure 1.7** Free-space THz-TDS system consisting of femtosecond laser source, motorised optical delay stage, a mechanical chopper, guiding mirrors, a 50:50 beam splitter, mechanical chopper, EO crystal and balanced photodiodes for THz detection.

THz-TDS measurements are performed in the purged environment in order to avoid any attenuation due to water absorption [43]. In doing so, nitrogen (N<sub>2</sub>) gas is filled into a sealed chamber of silica glass, which contains the optical components. As N<sub>2</sub> gas does not absorb the THz field, a much cleaner THz-TDS signal can be obtained without water lines. The purge box (covering optical path of THz radiation) is indicated by dotted lines in Figure 1.7. The measured THz signal at the detector end can be expressed by following expression [44]:

$$I(\Delta t) = \int_{t=0}^T E_{THz} n(t + \Delta t) dt \quad 1-8$$

Where,  $\Delta t$  is relative time delay between pump and probe beams,  $E_{THz}$  is the incident THz field,  $n$  is the induced photo-carrier density and  $T$  is the sampling time window for THz pulse.

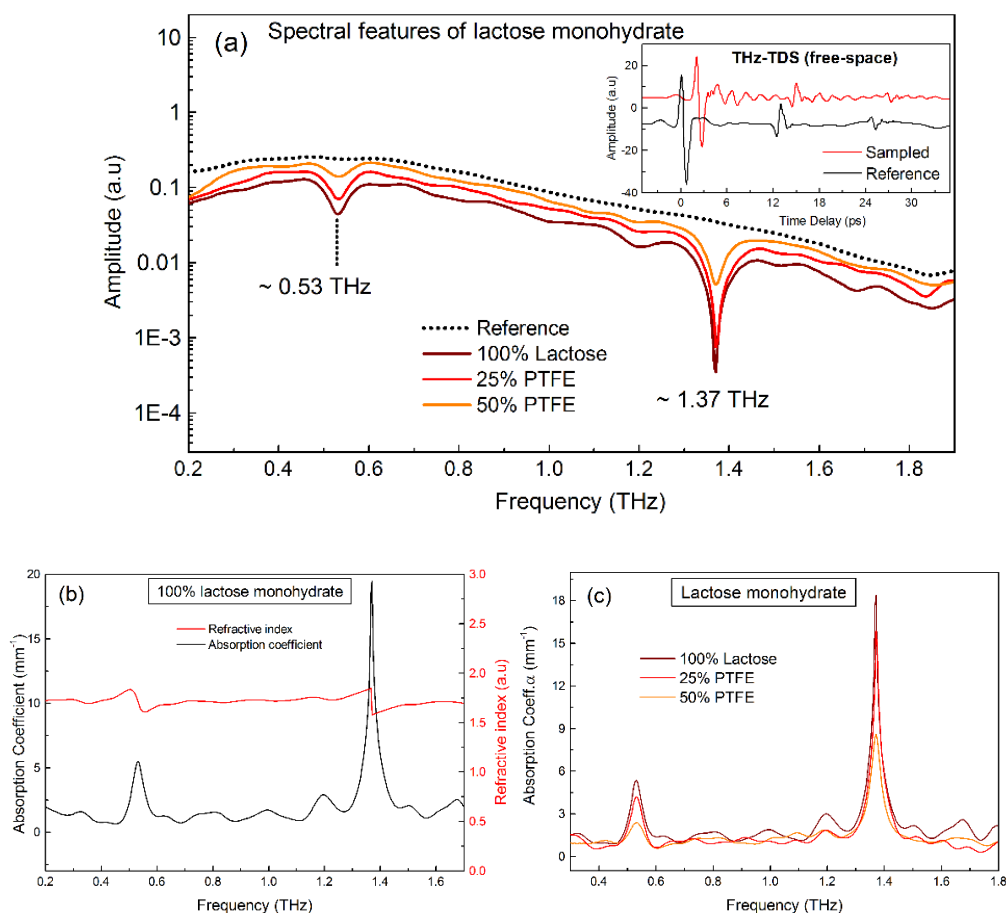
### 1.4.1 THz-TDS of polycrystalline lactose monohydrate

Free-space THz-TDS measurement was performed in order to obtain spectral features of lactose monohydrate followed by a comparison with spectroscopy results obtained from an on-chip THz-TDS. Components required to perform THz-TDS have already been explained. Therefore, a discussion on results obtained from THz-TDS will be covered in this section.

Firstly, lactose monohydrate in the powdered form with 100% purity (weighed 40 mg) was pressed into a circular pellet inside a copper-O ring using SPECAC Manual Hydraulic Press (A detailed description of sample preparation is given in Chapter 5). Lactose pellet pressed inside a copper ring can easily be mounted in the THz-TDS setup. Similarly, two more test samples of lactose monohydrate were prepared by diluting lactose monohydrate powder with polytetrafluoroethylene (PTFE) to 75:25 and 50:50 ratios by weight. PTFE was used as a matrix material due to its property of high transparency and featureless spectrum [40].

In THz-TDS, THz field generated from a photoconductive emitter is collected and collimated by the parabolic mirrors in order to focus onto the SUT (lactose monohydrate). A reference time-domain THz pulse was first measured without mounting lactose sample in THz-TDS system (shown in inset graph, Figure 1.8 a).

A lactose pellet was then placed into the sample holder in order to measure a sampled THz pulse. For each pellet, five scans were performed in order to reduce noise (due to fluctuation of laser intensity, optical, electronic and mechanical noise [45, 46]) in the averaged data. The reference and sampled THz pulse traces obtained were truncated at a  $\sim 12$  ps time window in order to remove etalons observed in time-domain pulses. Traces of measured pulses were then zero padded to a length of 250 ps time window in order to maintain a frequency resolution of  $\sim 4$  GHz in their respective FFT spectra while performing Fourier transformation on measured time-domain pulses.



**Figure 1.8 Free-space THz-TDS of lactose monohydrate a) A comparison of spectral features obtained from three different samples of lactose monohydrate. b) Calculated refractive index and absorption coefficient. c) A comparison of absorption coefficients calculated from three separate samples of lactose monohydrate.**

FFT spectra obtained from sampled THz pulses then revealed two well-known absorption features at  $\sim 0.53$  and  $\sim 1.73$  THz respectively, as previously observed [47-50]. More pronounced spectral features were observed from the FFT spectra of the 100% purity lactose sample, suggested a greater interaction of THz field with the lactose molecules. On the other hand, diluted lactose samples yielded spectral features of relatively lower magnitude compared to the 100% lactose sample as shown in Figure 1.8 a.

Frequency-domain data was then analysed in order to obtain the refractive index, the absorption coefficient of measured lactose samples of varying concentration (i.e. 25% and 50% diluted by mixing PTFE). Lactose pellets that were pressed into the

copper ring assumed to be of quasi-uniform surface and therefore, scattering of THz field from the pellet surface was not taken into consideration. Mathematical formulae to obtain frequency-dependent parameters are taken from Ref. [51].

The refractive index  $n_{sample}(v)$  of SUT, Fresnel reflection coefficient  $R(v)$ , absorption coefficient  $\alpha_{TDS}(v)$  and the maximum measureable absorption coefficient  $\alpha_{MAX}$  can be expressed as:

$$n_{sample}(v) = 1 + \frac{c}{2\pi dv} [\varphi_{sample}(v) - \varphi_{ref}(v)] \quad 1-9$$

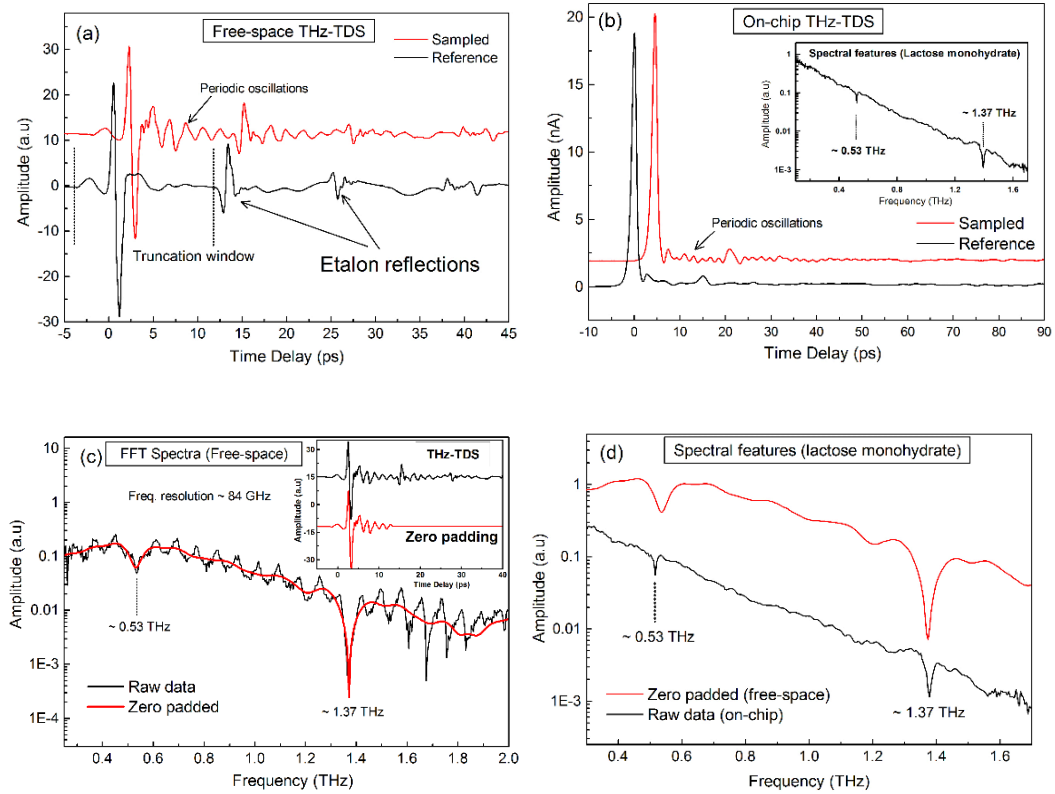
$$R(v) = \left| \frac{n_{sample}(v) - n_{air}}{n_{sample}(v) + n_{air}} \right|^2 \quad 1-10$$

$$\alpha_{TDS}(v) = -\frac{2}{d} \ln \left\{ \frac{A_{sample}(v)}{A_{ref}(v)(1 - R(v))} \right\} \quad 1-11$$

$$\alpha_{MAX}(v) = \frac{2}{d} \ln \left\{ DR \frac{4n_{sample}(v)}{(n_{sample}(v) + 1)^2} \right\} \quad 1-12$$

Where,  $c$  is the speed of light,  $v$  is the frequency,  $A_{sample}(v)$  and  $\varphi_{sample}(v)$  and are the amplitude and phase of sampled signal,  $A_{ref}(v)$  and  $\varphi_{ref}(v)$  are the amplitude and phase of reference signal,  $DR$  is the dynamic range and  $n_{air}$  is the refractive index of the air which is assumed to be 1 [52].

In Figure 1.8 b, refractive index and absorption coefficient of 100% lactose sample calculated using Equations 1-9, 1-10 and 1-11 are plotted as a function of frequency. In Figure 1.8 c, the absorption coefficient of all three lactose samples is plotted as a function of frequency. It is evident from the graph that the value of the absorption coefficient increases for higher concentration. Despite being a widely used system for spectroscopic measurements, one of the major drawbacks of free-space THz-TDS is that time-domain THz pulses suffer from etalon reflections.



**Figure 1.9** A comparison of spectral features obtained from free-space THz-TDS with on-chip THz-TDS. a) A comparison of sampled and reference pulses measured from free-space THz-TDS. b) A comparison of sampled and reference pulses measured from On-chip THz-TDS. c) A comparison of FFT spectra with and without zero padding (free-space THz-TDS). d) A comparison of spectral features of lactose monohydrate obtained from free space and On-chip THz-TDS.

These etalon reflections mainly occur in the form of repetitions of the main pulse but with a lower relative amplitude [53]. The origin of such etalon reflection is due to the THz pulses travelling back-and-forth between two surfaces [54]. Etalon reflections may emerge from the surface of the SUT or the photo-emitter used for THz generation or EO crystal while a pulse is being detected [53]. An example of etalon reflections occurred in the trace of a THz output pulse is shown in Figure 1.9 a, in which similar etalon reflections are observed in both the reference and sample THz pulses suggest that reflections mainly emerged from photo-emitter used for THz generation. In Figure 1.9 c, FFT spectra of the sampled pulse both with and without zero-padding are compared in order to emphasise that how sharp reflections in time-domain influence the frequency-domain [55] and cause poor spectral estimation of the sample under test.

Also, calculations of the refractive index and absorption coefficient can be erroneous.

On the other hand, in an on-chip spectroscopy system, unwanted reflections caused by waveguide discontinuities can be substantially delayed by modifying the device design after knowing the origins of reflections and a very high-frequency resolution ( $\sim 2$  GHz or higher) can thus be achieved. An example of on-chip spectroscopy measurement is shown in Figure 1.9 b, in which no secondary reflections with significant amplitude were observed in a time-window of 250 ps. Therefore, no zero-padding is required in order to perform a high-frequency resolution Fourier transformation. Finally, FFT spectra of the sampled pulses measured using a free space THz-TDS, and an on-chip system were compared as shown in Figure 1.9. These results provide confirmatory evidence that on-chip systems can better resolve spectral features of a sample under test without modifying time-domain data. Throughout this thesis, we will discuss the development of on-chip waveguide systems with the aim of achieving higher bandwidth and frequency resolution, subsequently performing on-chip spectroscopy of lactose monohydrate using these systems.

### 1.4.2 Differential THz-TDS system

Differential THz-TDS, a time-domain spectroscopy technique which is an alternative to conventional THz-TDS, was developed by a group of biophysicists at Rensselaer Institute, New York, and first demonstrated in the year 2000 in order to determine the refractive index of a  $1.8 \mu\text{m}$ -thin monolayer of the biological cell [56]. To characterise such thin films ( $\sim 1 \mu\text{m}$ ), refractive index is measured as a relative phase shift in THz signal caused by the biological cell given as:

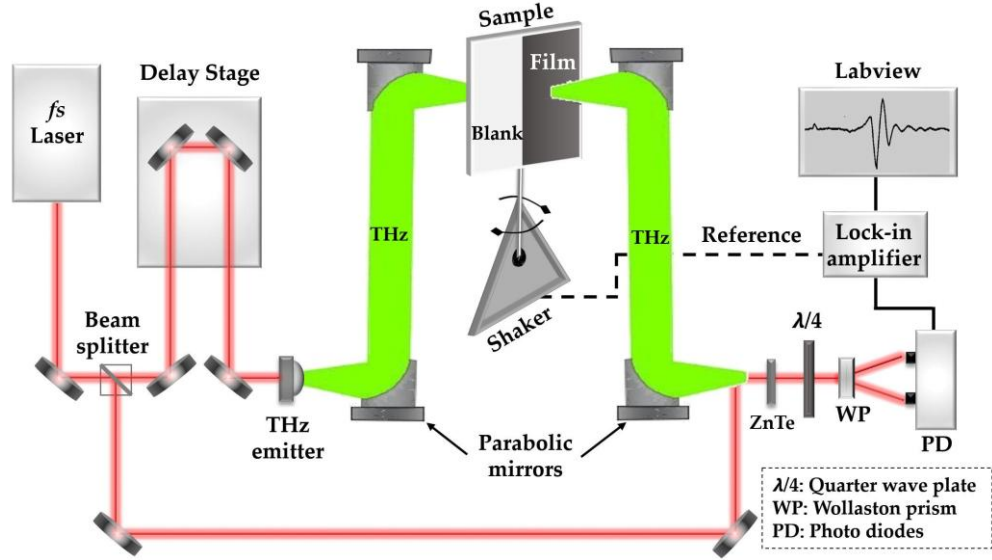
$$\Delta\phi \propto (\tilde{n} - 1)d / \lambda \quad 1-13$$

Where,  $\tilde{n}$  is the refractive index of the medium,  $d$  is the sample thickness and  $\lambda$  is the wavelength present in the THz radiation interacting with sample.

Conventional THz-TDS system yields a coherence length of about  $150 \mu\text{m}$  with a centre wavelength of  $800 \text{ nm}$  and bandwidth of  $2 \text{ THz}$ , for example. It would be difficult to see phase shifts less than the coherence length of THz radiation [57, 58]. This

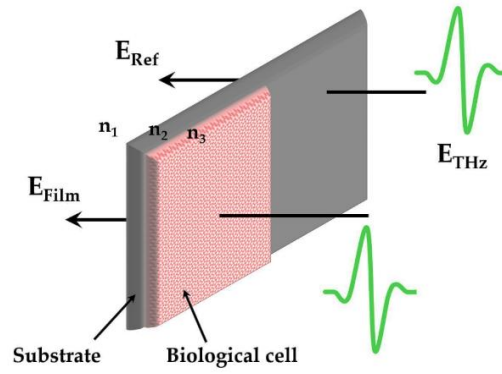


requires a very high sensitive measurement with the signal-to-noise ratio ( $>10^7$ ). To overcome this, differential THz-TDS improves the SNR by measuring a differential THz signal, which is the difference between THz radiation passing through the biological cell and blank substrate subsequently. An illustration of differential THz-TDS system is given in Figure 1.10.



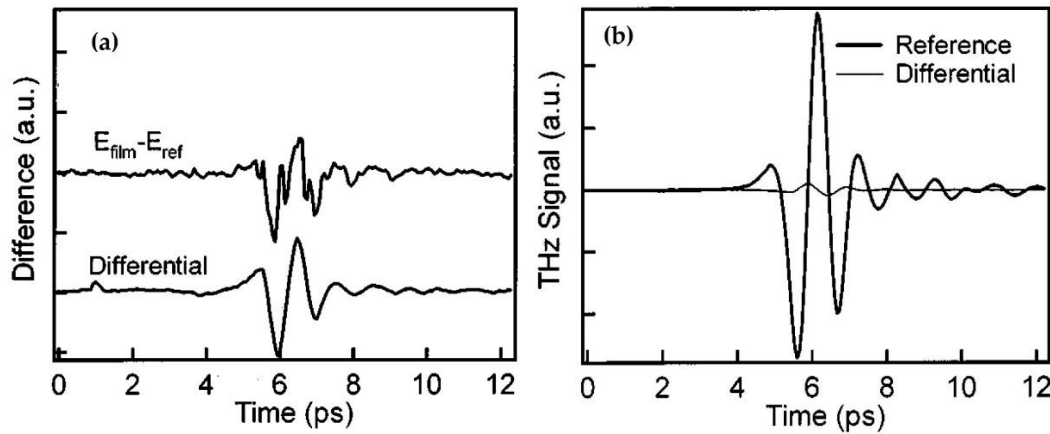
**Figure 1.10** A differential THz-TDS system (free-space) consisting of femtosecond laser source, motorised optical delay stage, a mechanical chopper, guiding mirror, a 50:50 beam splitter, mechanical chopper, EO crystal and a mechanical vibrator to move the sample in and out.

A differential THz-TDS system is similar to that of a conventional THz-TDS system, except that a mechanical shaker is attached to the sample under test. The mechanical shaker is used to vibrate the sample under test, which so acts as a modulator in differential THz-TDS, unlike conventional THz-TDS, where a mechanical chopper is used to modulate either the pump beam or the THz radiation. In doing so, a sample (substrate) partly covered with biological tissue is moved in and out of the focused THz radiation using a shaker as shown in Figure 1.10. The frequency of vibration is set as a reference for the lock-in amplifier. Therefore, a differential signal ( $E_{diff}(t) \equiv E_{film}(t) - E_{ref}(t)$ ) is then measured by the lock-in amplifier, yielding a much higher SNR ( $\sim 5$  times) [59].



**Figure 1.11** An illustrative representation of the THz field passing through the blank substrate ( $E_{\text{ref}}$ ) and biological cell ( $E_{\text{film}}$ ), where the difference of  $E_{\text{ref}}$  and  $E_{\text{film}}$  will generate a differential THz pulse.

However, the amplitude the differential signal is found to be much smaller than that of a conventional signal.



**Figure 1.12** a) A comparison of a conventional difference signal (measured without using mechanical vibrator) with a differential THz signal (measured when the sample was moving in and out). b) Amplitudes of reference (through the blank substrate) and the differential signal (with sample moving in and out) are compared (taken from Ref. [56]).

An example of a differential signal is shown in Figure 1.12 a, in which differential signal measured using differential THz-TDS technique is compared with a difference signal (difference of reference and sampled signals measured without modulating THz field which means shaker was not used). It is clear from the graph that the difference signal has more background noise than that of the differential signal. In Figure 1.12 b, a differential signal compared with reference signal indicates that amplitude of the differential signal is much smaller than that of the reference signal.

In this differential THz-TDS technique, relative change in phase of THz radiation is given by the ratio of amplitudes of differential and reference signals as [56, 59]:

$$\frac{E_{diff}(\omega)}{E_{ref}(\omega)} \approx i \frac{\omega}{c} d \left[ n_2 - 1 + \frac{(n_2 - n_1)(n_2 - n_3)}{(n_1 + n_3)} \right] - \alpha(\omega) d \left[ 1 + \frac{(n_2 - n_1)(n_2 - n_3)}{(n_1 + n_3)} \right] \quad 1-14$$

where,  $n_1, n_2$  and  $n_3$  are the refractive indices of air, substrate and biological cell respectively,  $c$  is the speed of light,  $d$  is the thickness of monolayer biological cell and  $\alpha$  is the absorption coefficient.

In this project, we have used a free-space differential THz-TDS analogy to develop an on-chip differential THz-TDS waveguide system in which the conductivity of a coupling switch (embedded in the middle of coplanar waveguide) is modulated by means of a mechanical chopper, and ultra-short laser pulses in order to generate a differential THz pulse ( $S_{on} - S_{off}$ ), and subsequently measured this signal by a lock-in amplifier (see Chapter 3).

## 1.5 On-chip THz generation and detection

On-chip THz generation and detection are similar to that of free space THz-TDS except that the THz field is confined and guided by a waveguide structure patterned on to a dielectric substrate. To gain a better understanding of on-chip waveguide systems, an example of a free-standing waveguide which can be employed with a free-space THz-TDS system in order to couple and guide THz radiation along waveguide surface such a metal wire [60, 61], is discussed in the following section.

### 1.5.1 Free-standing waveguide system

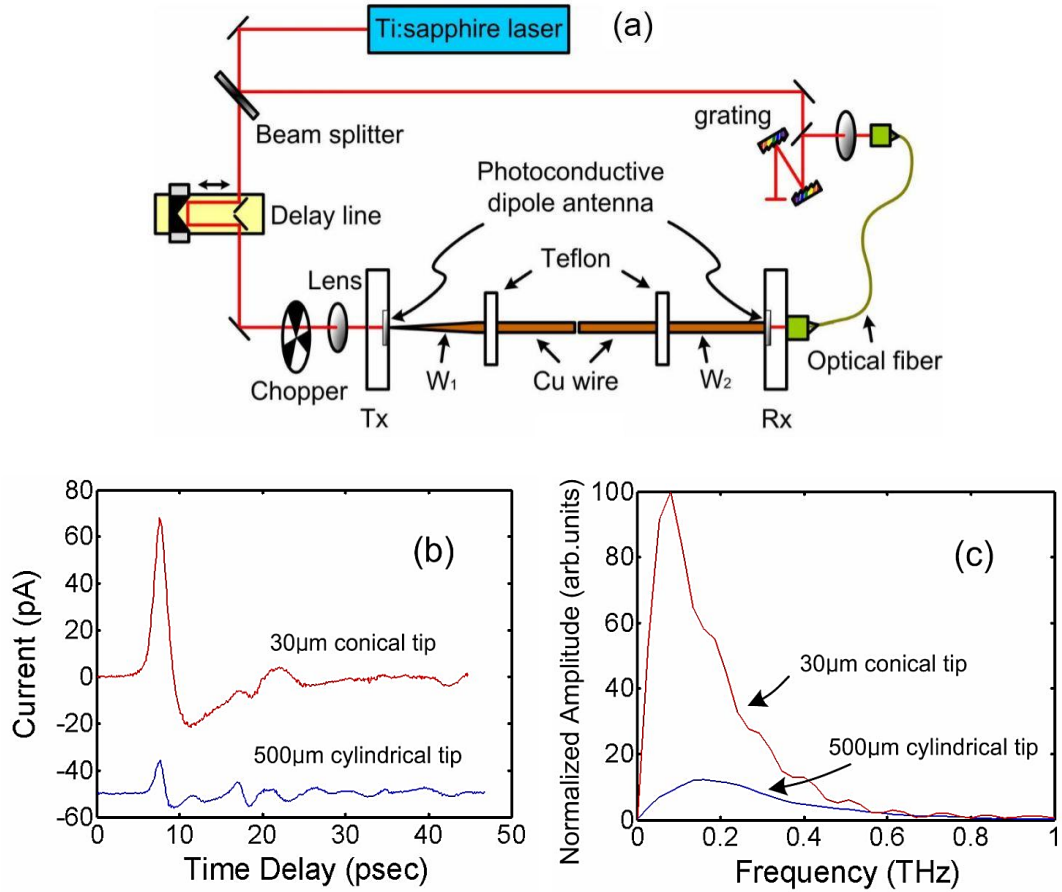
Freestanding waveguides were developed with the intention of coupling THz fields generated in free-space into a waveguide structure in order to achieve different modes of propagation (such as surface wave) of THz field compared to that of free-space propagation. Study of these fundamental modes of propagation in a guided medium allowed further development of spectroscopy techniques such as on-chip spectroscopy

of polycrystalline materials [47, 62-64]. The early efforts in the development of free-standing waveguides include dielectric ribbons [65], suspended metal wires [60], parallel plate waveguides [66].

Freestanding waveguides made of metal wire were found to be problematic because THz field launched in metal wire with transient current pulses varying on a picosecond scale causes high radiation and ohmic losses [67]. To overcome ohmic losses, waveguides made of plastic ribbon have also been used to couple free-space THz field [68].

An example of a metal wire waveguide is shown in Figure 1.13 a, in which a conical wire tip is used to couple THz field on a metal wire waveguide while the cylindrical end of the metal wire connected to the receiver (Rx) is used to detect the THz surface waves. Two photoconductive antennae (Tx and Rx) patterned on SOS (silicon-on-sapphire) with metal electrodes separated by 5  $\mu\text{m}$  gap are used as transmitter and receiver for THz generation and detection. The reason for using SOS is that it is an optically transparent material, and therefore, the photo-emitter (Tx) can be excited from the backside using a pump beam (driven by Ti: Sapphire laser). The receiver (Rx) part of waveguide system can freely be moved as it is excited by the probe beam coupled with an optical fibre. Metal waveguide consists of a metal wire cut into two pieces W1 and W2 and separated by 150  $\mu\text{m}$  air gap as shown in Figure 1.13 a.

The reason for choosing two metal wire segments over continuous metal wire is to keep the receiver end movable. Also, W2 can be replaced with any wire structure in order to further investigate THz pulse propagation in different metal wire waveguides. The conical wire tip (diameter  $\sim 30 \mu\text{m}$ ) was located close to photo-emitter (Tx) so that THz pulse can directly be coupled to the metal tip, without using any silicon lens, for example. The cylindrical tip (diameter  $\sim 500 \mu\text{m}$ ) of metal wire (W2) was placed close to the receiver photo-antenna (Rx). When THz pulse launched from Tx, propagates along the metal wire through 150  $\mu\text{m}$  air gap before being detected at Rx. Finally, field intensities of conical wire tip (diameter  $\sim 30 \mu\text{m}$ ) and cylindrical wire tip (diameter  $\sim 500 \mu\text{m}$ ) were compared in order to observe how the THz field couple with different geometry of metal wires.



**Figure 1.13 a) An illustration of free standing metal wire waveguide in which THz field is coupled to metal wire tip. b) Time-domain pulses measured with metal wire of different diameters. c) Normalised amplitudes.**

It is clear from Figure 1.13 b and c that metal wire tip with a smaller diameter  $\sim 30 \mu\text{m}$  showed much greater coupling of THz pulse compared to that of the metal tip with a diameter  $\sim 500 \mu\text{m}$ .

Another example of a free-standing waveguide similar to the metal wire is shown in Figure 1.14 in which a flat dielectric ribbon is attached to two silicon lenses. THz field emerging from transmitter chip is coupled to dielectric ribbon using silicon lenses. Coupled THz pulses propagate along the dielectric ribbon before being guided by another silicon lens in order to direct them to a receiver chip. Dielectric ribbons made from high-density polyethylene [68, 69] and single crystal sapphire [70, 71] have been used for pulsed THz transmission.

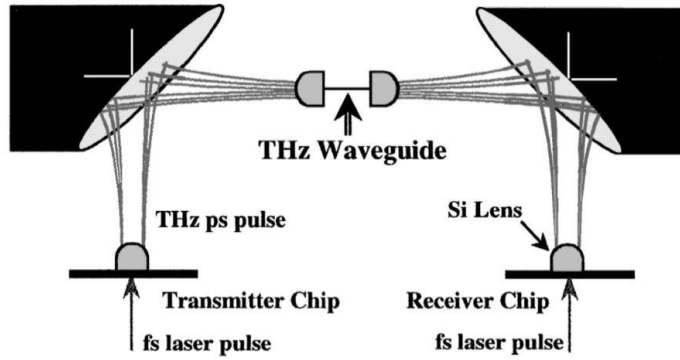


Figure 1.14 An illustration of a ribbon dielectric waveguide coupled with THz field in THz-TDS system using Si lenses.

### 1.5.2 On-chip waveguide system

In an on-chip waveguide system, photoconductive switches are embedded with a waveguide structure in order to generate a THz pulse at the generation switch with subsequent detection of the same pulse after a propagation time delay  $\Delta t$  at the detection switch.

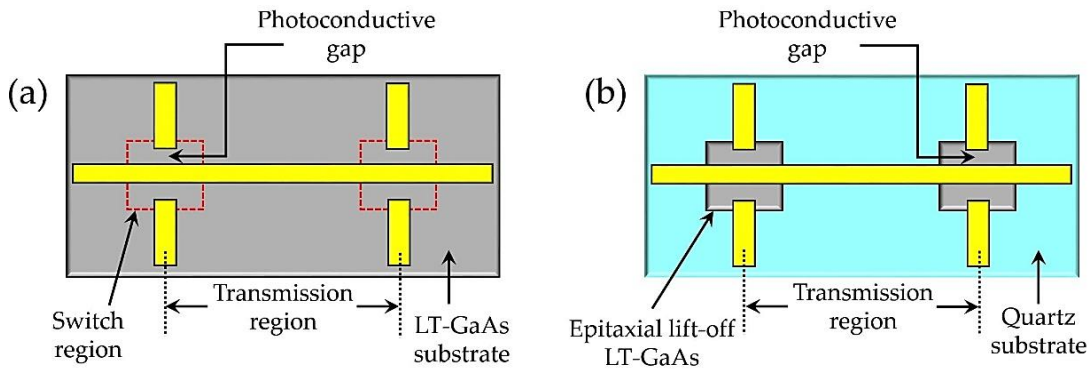
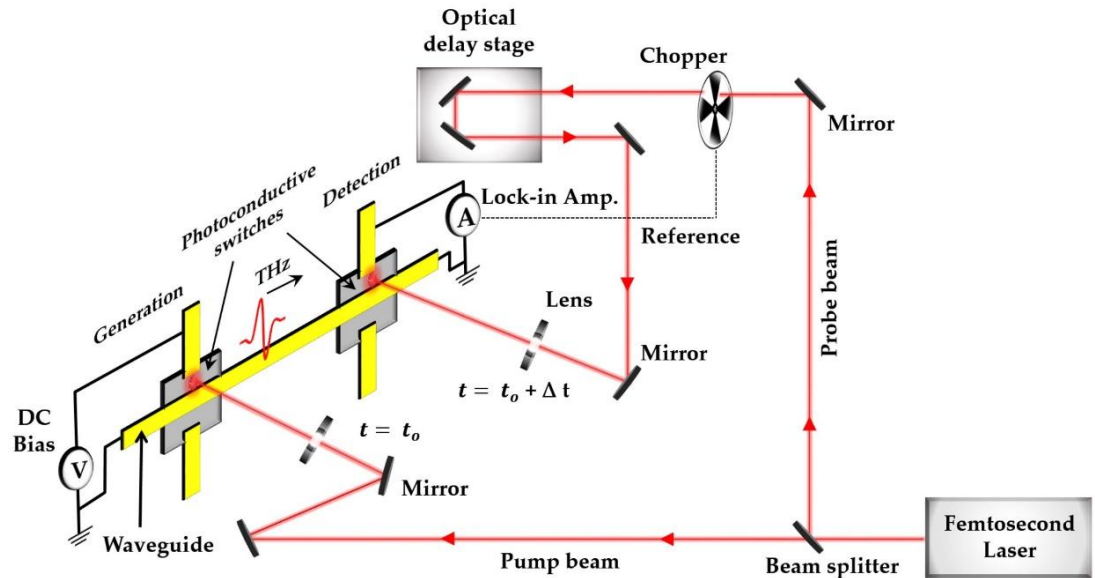


Figure 1.15 a) Photoconductive switches along with transmission region patterned on the LT-GaAs substrate. b) Photoconductive switches patterned on LT-GaAs overlaid onto quartz substrate (selectively etched by epitaxial lift-off technique).

Generation and detection switches are patterned (along with the transmission region) either directly onto a photoconductive material such as LT-GaAs (bulk substrate) or by selective epitaxial lift-off of a very thin LT-GaAs layer on a host substrate such as quartz or BCB (benzo-cyclobutene) [72, 73] as shown in Figure 1.15.

An example of on-chip waveguide system for THz generation and detection is shown in Figure 1.16, in which a DC biased generation switch is excited by focusing a pump laser beam (driven by Ti: Sapphire laser) onto the switch. Generated transient current pulses are then directly coupled to the metal waveguide and propagate along before being detected at the detector switch. A probe beam (split off from the main beam) illuminates the photoconductive gap ( $\sim 5 \mu\text{m}$ ) in the detector switch in order to excite photo-charge carriers in the photoconductive gap. THz pulses arriving at the detector switch act as a bias voltage to detector switch and therefore, a photocurrent is then measured by lock-in amplifier connected in series with detector switch probe arms. In order to sample a full THz pulse arriving at the switch, the probe beam is time-delayed about pump beam. A mechanical chopper is also employed in order to sample THz pulse.



**Figure 1.16** An illustration of on-chip waveguide system for THz generation and detection in which photoconductive switches are embedded with a metal waveguide in order to transmit THz pulse from the emitter to detector. Components: a femtosecond laser source, motorised optical delay stage, a mechanical chopper, guiding mirrors, beam splitter, and a lock-in amplifier.

On-chip waveguides have several advantages over free-space THz-TDS system as:

- On-chip waveguides can be designed to integrate the transmission region and generation, and the detection switch regions all into one planar geometry.

- THz fields can be confined to propagate along a small cross-section which makes on-chip waveguide systems much more compact compared to free-space THz-TDS.
- A much higher frequency resolution ( $\sim 2$  GHz or greater) can be obtained by carefully designing device geometry.
- By choosing a substrate of low dielectric constant, attenuation and dispersion can be minimised.

## 1.6 Thesis structure

This chapter has presented a general introduction to techniques of THz generation and detection. Also, THz-TDS results obtained from both free-space and on-chip waveguide systems were compared to point out their merits and demerits.

Chapter 2 presents basic building blocks of transmission line theory needed in order to develop on-chip CPW devices intended for operation at THz frequencies. Electromagnetic simulations are performed using HFSS to extract the characteristics of various on-chip CPWs on GaAs and quartz substrate. Further, different CPW discontinuities are discussed with particular emphasis on coupling gap discontinuity which will further be explored experimentally subsequently in this thesis.

Chapter 3 discusses on-chip measurements of the first generation of conventional and centre gap (CGAP) CPW devices fabricated on both GaAs and quartz substrate. On-chip measurements are performed using both two-beam and three-beam on-chip systems in order to measure both conventional and differential THz pulses. Results obtained from on-chip measurements are then compared to those obtained from HFSS simulations.

Chapter 4 discusses on-chip measurements of second generation CPW devices fabricated on a quartz substrate. Optimised device design that was used to increase the frequency resolution by delaying secondary reflections is discussed. Further, on-chip measurements of a THz Y-splitter and coupler are also discussed.



Chapter 5 discusses further optimisation of second generation device design required in order to minimising radiation losses with a subsequent increase in bandwidth. Further, on-chip spectroscopy measurements of lactose monohydrate using optimised second generation CPW devices at both room and low temperature are discussed.

## Chapter 2

# Transmission Line Theory and Modelling of On-Chip Waveguides using HFSS

### 2.1 Introduction

This Chapter discusses the fundamental concepts of transmission line theory for the design and simulation of on-chip waveguide systems operating at THz frequencies. In particular, the transmission properties of commonly used on-chip waveguides such as coplanar waveguide (CPW), conductor-backed CPW, stripline, slotline, Goubau-line and microstrip-line are discussed.

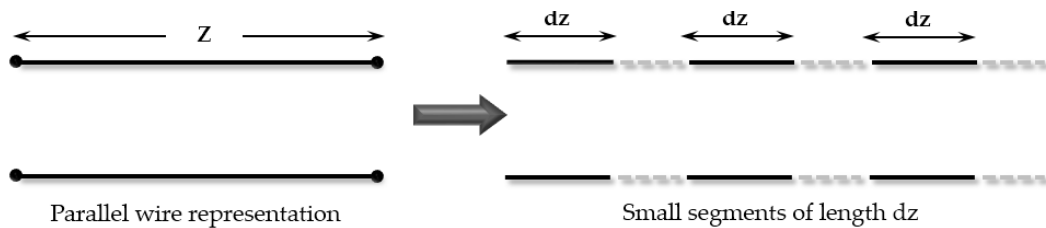
Electromagnetic simulations were performed to investigate the interaction and propagation of electromagnetic waves (EM) along coplanar waveguide structures at THz frequencies. Electromagnetic simulations discussed in this Chapter were performed using the Ansoft High-Frequency Structure Simulator (HFSS). Scattering parameters are obtained from HFSS simulations, giving an insight into the expected signal bandwidth, reflection, attenuation, and the characteristic impedance of on-chip CPW waveguides at THz frequencies.

Further, typical CPW discontinuities such as waveguide step, waveguide bend, waveguide T-junction and waveguide coupling gap, and their equivalent circuits are discussed. The capacitance and photo-conductive resistance of discontinuities in the CPW (referred to here as “coupling-gap” CPWs, or CGAP-CPWs) were calculated from an equivalent circuit model using S and Y parameters.

Over the last few decades, coupling gap discontinuities in coplanar microwave circuits have been investigated by researchers, for example, in order to perform high-speed switching [74, 75], the generation of photo-current [76], and the sampling of microwave signals up to 100 GHz. However, CPW discontinuities have not been investigated at frequencies  $\geq 1$  THz, yet. We, therefore, investigate coupling-gap discontinuities bridged by photoconductive switches in the coplanar on-chip waveguide by electromagnetic simulations and numerical modelling in THz regime. The processing of THz CGAP-CPWs (centre gap coplanar waveguides) and their measurement using ultra-fast laser beams are discussed in Chapter 3.

## 2.2 Transmission line theory

A transmission line consists of two or more conductors connecting a power source to a load. At microwave frequencies, typical transmission lines include a coaxial cable, a two-wire line and parallel plates. A two-wire transmission line can be represented by a distributed network when the length of the conductor is comparable to signal wavelength (shown in Figure 2.1). It can be divided into small segments of length  $dz$  in which both phase and magnitude of EM waves can vary. A transmission line is characterised by its characteristic impedance,  $Z_0$  and propagation constant  $\gamma$ . In this section, transmission line theory based on lumped element method for a two conductor system supporting a TEM mode is discussed.



**Figure 2.1 A two-wire transmission line and its distributed network model.**

An infinitesimal segment ( $dz$ ) of the transmission line can be modelled as a lumped element circuit as shown in Figure 2.2, where  $v(z, t)$  and  $i(z, t)$  are time-dependent incident voltage and current respectively,  $R$  is the series resistance per unit length, due to the finite conductivity of the conductor and  $L$  is the series inductance per

unit length due to self-inductance of the conductor.

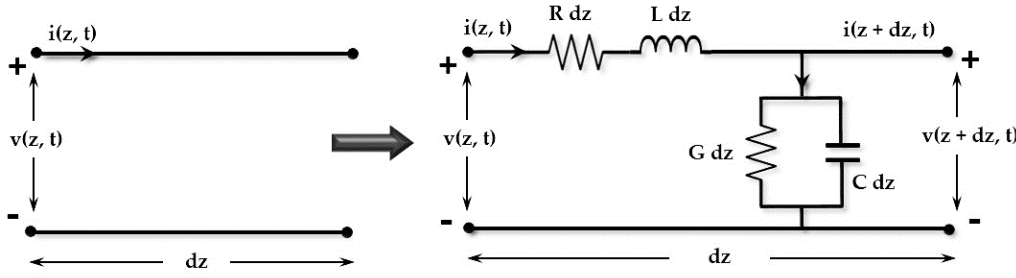


Figure 2.2 A two conductor transmission line represented as a lumped element model.

When a voltage  $v(z, t)$  is applied across the transmission line, some electrical energy is stored due to the capacitance,  $C$  from two conductors. The conductance  $G$  is responsible for the loss in the dielectric material (lossy by nature) present between two conductors [77].

Using KVL and KCL circuit theorems, the following equations can be derived from the lumped model shown in Figure 2.2:

$$v(z, t) = R dz i(z, t) + L dz \frac{\partial i(z, t)}{\partial t} + v(z + dz, t) \quad 2-1$$

$$i(z, t) = G dz v(z + dz, t) + C dz \frac{\partial v(z + dz, t)}{\partial t} + i(z + dz, t) \quad 2-2$$

By applying limit  $dz \rightarrow 0$ , the above equations lead to partial differential equations:

$$-\frac{\partial v(z, t)}{\partial z} = R i(z, t) + L \frac{\partial i(z, t)}{\partial t} \quad 2-3$$

$$-\frac{\partial i(z, t)}{\partial z} = G v(z, t) + C \frac{\partial v(z, t)}{\partial t} \quad 2-4$$

For time-varying voltage and current, we can use the phasor forms:

$$v(z, t) = \text{Re}\{V(z)e^{j\omega t}\} \quad 2-5$$

$$i(z, t) = \text{Re}\{I(z)e^{j\omega t}\} \quad 2-6$$

Where,  $V(z)$  and  $I(z)$  are phasor forms of  $v(z, t)$  and  $i(z, t)$  respectively, which lead to following equations:

$$-\frac{dV(z)}{dz} = (R + j\omega L)I(z) \quad 2-7$$

$$-\frac{dI(z)}{dz} = (G + j\omega C)V(z) \quad 2-8$$

Differentiating again with respect to  $z$ , we obtain:

$$\frac{d^2V(z)}{dz^2} = -(R + j\omega L)\frac{dI(z)}{dz} \quad 2-9$$

$$\frac{d^2I(z)}{dz^2} = -(G + j\omega C)\frac{dV(z)}{dz} \quad 2-10$$

After substituting the values of  $dI(z)/dz$  and  $dV(z)/dz$  from Equation 2-9 and 2-10, the following differential equations can be obtained:

$$\frac{d^2V(z)}{dz^2} = (R + j\omega L)(G + j\omega C)V(z) = \gamma^2 V(z) \quad 2-11$$

$$\frac{d^2I(z)}{dz^2} = (R + j\omega L)(G + j\omega C)I(z) = \gamma^2 I(z) \quad 2-12$$

$$\gamma = \alpha + j\beta = \sqrt{(R + j\omega L)(G + j\omega C)} \quad 2-13$$

Where,  $\gamma$  is the complex propagation constant with the real part  $\alpha$ , attenuation constant (in Neper/meter) and the imaginary part  $\beta$  is the phase constant (rad/m)). The attenuation and phase constants are a function of frequency,  $\omega$  ( $2\pi f$ ) [77]. The attenuation constant,  $\alpha$ , is a measure of the signal amplitude reduction arising from the transmission line. Attenuation arises from three factors, conductor loss  $\alpha_c$ , dielectric loss  $\alpha_d$  and radiation loss  $\alpha_R$ , which will be discussed in detail in the Section 2.4.3. Phase constant  $\beta$  is a measure of change in signal phase along a transmission line at certain time intervals.

Further, second order differential Equations 2-11 and 2-12 yield solution to  $V(z)$  and  $I(z)$ :

$$V(z) = V^+(z)e^{-\gamma z} + V^-(z)e^{+\gamma z} \quad 2-14$$

$$I(z) = I^+(z)e^{-\gamma z} + I^-(z)e^{+\gamma z} \quad 2-15$$

Where,  $e^{-\gamma z}$  and  $e^{+\gamma z}$  represent wave propagation in the forward (+z) and backward (-z) directions, respectively. By differentiating Equation 2-14 with respect to  $z$  and substituting the value of  $dV(z)/dz$  in Equation 2-7, the following relation can be obtained:

$$I(z) = \frac{\gamma}{R + j\omega L} (V^+ e^{-\gamma z} - V^- e^{+\gamma z}) = \frac{1}{Z_0} (V^+ e^{-\gamma z} - V^- e^{+\gamma z}) \quad 2-16$$

The characteristic impedance,  $Z_0$  is defined as:

$$Z_0 = \frac{R + j\omega L}{\gamma} = \frac{\gamma}{G + j\omega C} = \sqrt{\frac{(R + j\omega L)}{(G + j\omega C)}} \quad 2-17$$

From the above expression, it is clear that characteristic impedance,  $Z_0$  depends on the distributed parameters  $R$ ,  $L$ ,  $C$  and  $G$  of the transmission line, but not the length. A specific value of  $Z_0$  can be achieved by altering waveguide design parameters.

### 2.2.1 Lossless transmission line

A transmission line is considered lossless if the dielectric medium separating its conductors is lossless ( $\epsilon \approx 0$ ), and the conductor is perfect conductors ( $\sigma \approx \infty$ ). Therefore, for a lossless transmission line,  $R$  and  $G$  are considered as zero and the  $Z_0$  reduces to:

$$Z_0 = \sqrt{\frac{L}{C}} \quad 2-18$$

### 2.2.2 Distortionless transmission line

A signal propagating down the transmission line consists of a band of frequencies. Different frequency components propagate at different velocities producing signal distortion, known as dispersion. In other words, the information carried by the signal spreads across a band of frequencies, and this information gets distorted, as different frequency components travel at different velocities.

In most cases, phase velocity  $v_p$  depends on frequency causing dispersion in signal transmission and is expressed as:

$$v_p = \frac{\omega}{\beta} \quad 2-19$$

For a distortion-less transmission line, the phase velocity must be frequency independent. To achieve that, line parameters need to satisfy:

$$\frac{R}{L} = \frac{G}{C} \quad 2-20$$

Substituting values from Equation 2-20, the propagation constant  $\gamma$  can be represented as:

$$\gamma = R \sqrt{\frac{C}{L}} + j\omega\sqrt{LC} \quad 2-21$$

Attenuation coefficient and phase constant can be defined as:

$$\alpha = \text{Re}\{\gamma\} = R \sqrt{\frac{C}{L}}, \quad \beta = \text{Im}\{\gamma\} = \omega\sqrt{LC} \quad 2-22$$

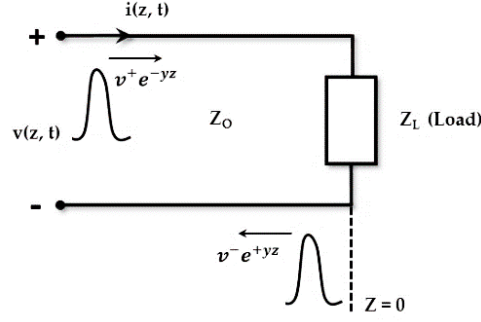
The phase velocity for a distortion-less line is thus defined as:

$$v_p = \frac{\omega}{\beta} = \frac{1}{\sqrt{LC}} \quad 2-23$$

From the above expression, it is clear that phase velocity is frequency independent for a distortion-less transmission line. The transmission line is thus non-dispersive.

### 2.2.3 Reflection Coefficient

In a terminated transmission line, the wave propagating down the line may or may not be reflected back, depending on the load conditions. In transmission line theory, the reflection coefficient  $\Gamma$  is the ratio of reflected and incident wave amplitudes. In waveguide design, the reflection coefficient gives an insight into any reflections originating from waveguide discontinuities by revealing their magnitude and phase (a large value may be caused by breaks and bends in the transmission line, for example).



**Figure 2.3 Transmission line terminated into a load  $Z_L$ .**

Figure 2.3 shows an incident wave  $V^+ e^{-\gamma z}$  propagating down the transmission line terminated in a load  $Z_L$  (where,  $Z_L \neq Z_0$ ), at  $z = 0$ . A reflected wave  $V^- e^{+\gamma z}$  will then be excited and propagates back towards the signal generator. A standing wave pattern is generated on the transmission line due to interference (constructive or destructive) of incident and reflected waves, provided the excitation source is a continuous-wave signal. This standing wave pattern yields a succession of maxima and minima with a period of  $\lambda/2$ .

To obtain the reflection coefficient as a ratio of incident and reflected waves, Equations 2-14 and 2-16 can be used to solve load impedance  $Z_L$  at  $z = 0$  as:

$$Z_L = \frac{V(0)}{I(0)} = \left( \frac{V^+ + V^-}{V^+ - V^-} \right) Z_0 \quad 2-24$$

Equation 2-24 can further be rearranged as:

$$\Gamma = \frac{V^-}{V^+} = \frac{Z_L - Z_0}{Z_L + Z_0} \quad 2-25$$

## 2.2.4 Different load conditions

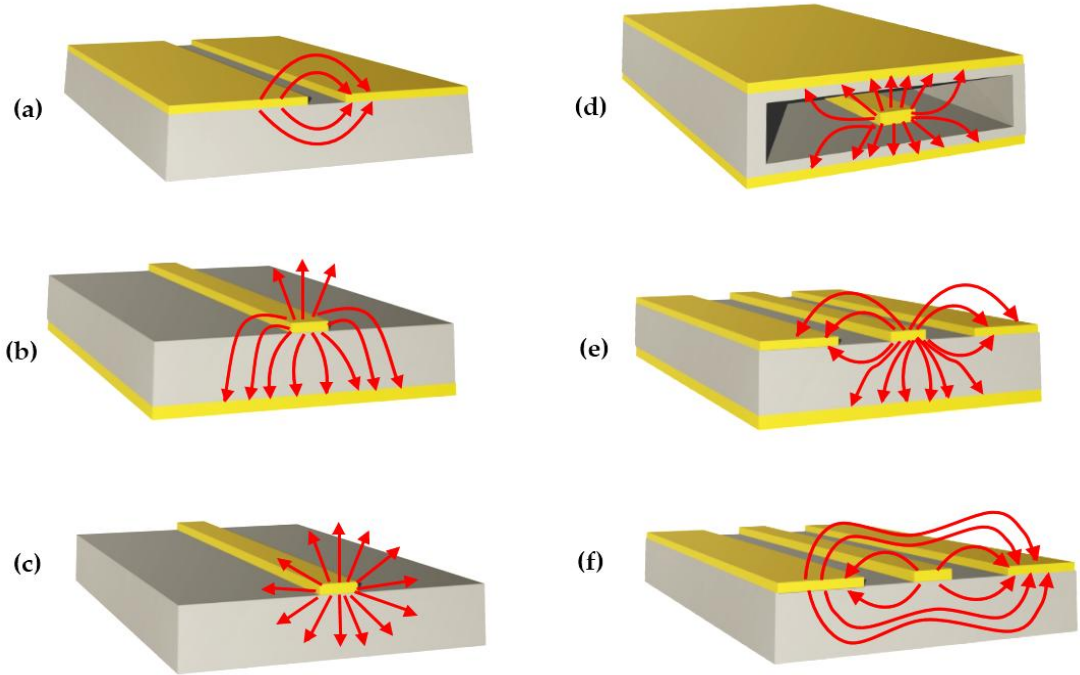
When a transmission line with characteristic impedance  $Z_0$  is terminated in a load impedance  $Z_L$  (provided  $Z_L = Z_0$ ), a matched load condition arises. The generated power is transmitted from source to load, and reflection coefficient returns the value  $\Gamma = 0$ . In case of an open circuit for which the load impedance is assumed to be infinity, the entire incident power is reflected back to the source and the reflection coefficient is



$\Gamma = 1$ . When a transmission line is short-circuited at one end (when the load is removed), the incident power is reflected back ( $\Gamma = -1$ ) with  $180^\circ$  phase change.

## 2.3 Planar transmission lines

In the last few decades, planar transmission lines have been widely used in modern electronics as essential components of microwave integrated circuits [78-80]. Besides signal transmission, planar transmission lines can also be used to realise many circuit elements such as filters, couplers, resonators, etc. Signals propagating down the transmission line are mainly affected by its physical geometry and choice of dielectric material.



**Figure 2.4** Planar transmission lines with electric field distribution shown in red a) Slot line. b) Microstrip. c) Goubau line. d) Strip line. e) Conductor-backed co-planar waveguide. f) Coplanar waveguide.

For designing high-frequency on-chip waveguides consisting of a planar transmission line, it is crucial to gain knowledge of their electrical characteristics such as characteristic impedance, effective dielectric constant, conductor and dielectric losses, etc. This section covers the design and characterisation of commonly used planar

transmission lines.

### 2.3.1 Slotline

A slotline waveguide consisting of a narrow gap in the conductive film on one side of the dielectric substrate was first discussed by Cohn [81]. They are relatively easy to fabricate due to its simple structure. Most of the electric field lines are concentrated in the central gap between two metal tracks (shown in Figure 2.4 a) contributing to the highly dispersive behaviour. Slotline does not support TEM modes, but rather its fundamental mode is a quasi-TEM mode. Since it lacks the ability to suppress higher-order modes, slotline is not very useful for broadband applications. Also, conductor losses are higher than the dielectric losses [82].

The characteristic impedance of a slotline increases with slot gap width, which makes it advantageous for achieving higher impedance, compared to microstrip for the same dielectric substrate [83]. Slotline possesses a low-quality factor due to its lossy and dispersive behaviour.

### 2.3.2 Microstrip

A single conductor waveguide on a dielectric substrate was invented by Grieg and Engelmann at ITT Laboratories [84]. It has been used extensively and is the most popular transmission line for high-frequency applications. In microstrip, a ground plane on the back of the substrate can be used both as a heat sink and as a device mount. Therefore, microstrip is easy to integrate with other solid-state devices. Most of the electric field lines are concentrated in the dielectric substrate placed between a single conductor and the ground plane. A fraction of the field lines passes through the air (shown in Figure 2.4 b), causing a pure TEM mode propagation impossible. Therefore, microstrip supports a hybrid TE and TM mode (quasi-TEM mode) of propagation. At low frequency, effective permittivity depends on the physical dimensions of conductor and a dielectric substrate. At high frequency, higher-order modes are lossy in nature can propagate. Its characteristic impedance is given by the expression [77]:

$$Z_0 = \begin{cases} \frac{60}{\sqrt{\epsilon_{eff}}} \ln\left(\frac{8h}{W} + \frac{W}{4h}\right) & \frac{W}{h} < 1 \\ \frac{120\pi}{\sqrt{\epsilon_{eff}}[W/h + 1.393 + 0.667\ln(W/h + 1.444)]} & \frac{W}{h} \geq 1 \end{cases} \quad 2-26$$

Where,  $w$  is the width of the conductor,  $h$  is the height of dielectric substrate and effective permittivity,  $\epsilon_{eff}$  can be expressed as:

$$\epsilon_{eff} = \frac{\epsilon_r + 1}{2} + \frac{\epsilon_r - 1}{2} \frac{1}{\sqrt{1 + 12h/w}} \quad 2-27$$

Signal attenuation in microstrip waveguide is mainly due to the conductor and dielectric losses. For quasi-TEM mode propagation, conductor and dielectric losses in microstrip can be expressed as [85]:

$$\alpha_c = \frac{R_s}{Z_0 W}, \quad \alpha_d = \frac{k_0 \epsilon_r (\epsilon_{eff} - 1) \tan \delta}{2 \sqrt{\epsilon_{eff}} (\epsilon_r - 1)} \quad 2-28$$

where,  $R_s$  is the surface resistivity given by [86]:

$$R_s = \sqrt{\pi \mu_r \mu_0 f \rho} \quad 2-29$$

where  $\rho$  is the bulk resistivity,  $f$  is the frequency of operation and  $\mu_r \mu_0$  are relative and free space permeability, respectively.

### 2.3.3 Goubau line

Goubau line is a single-conductor waveguide supported by a dielectric substrate with no ground plane. An ideal Goubau line is circular metallic wire suspended in free space in which surface waves can propagate along the wire. Surface wave on a single wire was first investigated by A. Sommerfeld [87]. In 1905, G. Goubau applied Sommerfeld's surface wave theory to the single conductor transmission line on a dielectric substrate which is now known as planar Goubau line [88]. It supports a low loss quasi-TEM mode of propagation, which is also known as Goubau mode. In Goubau line, the electromagnetic field extends radially from the conductor (shown in Figure 2.4 c), with most of the field lines concentrated in the substrate.

With the development of on-chip technology, Goubau-line has been modified to couple with a CPW in order to excite a specific modes of propagation. Goubau-line can

be excited by a CPW fed from a horn antenna [89]. In Goubau-line, a high characteristic impedance can be achieved by choosing a substrate with low dielectric constant and narrower conductor strip width  $W$ . To minimise the conductor losses; the thickness of the conductor strip needs to be small in order to reduce the surface resistivity. In order to reduce the signal attenuation and dispersion, the substrate thickness needs to be small. C. Russell *et al.* demonstrated that an increase in propagation velocity, and a reduction in signal attenuation can be achieved in Goubau-lines by substrate thinning [90]. In the same reference, Goubau-lines were used for dielectric sensing and spectroscopy of poly-crystalline materials in the THz range.

### 2.3.4 Stripline

The term “stripline” was first coined by R. Barrett in 1950 [91]. It is the earliest form of the planar transmission line which supports a pure TEM mode [78]. It consists of a central conductor surrounded by a homogeneous dielectric medium sandwiched between two parallel ground planes as shown in Figure 2.4 d. The dielectric medium used in stripline is a solid material. It provides good electromagnetic shielding and very low attenuation losses compared to CPW and microstrip line, which make it suitable for low-interference applications. Due to its non-dispersive behaviour, it has a high cut-off frequency.

One of the main disadvantages of stripline is its complex geometry (conductor is sandwiched between two equal slabs of a dielectric medium) which makes fabrication process difficult, unlike CPW and microstrip line. Stripline design also presents difficulties in realising various circuit elements, which require bias to operate.

The characteristic impedance of stripline is given by [92]:

$$Z_0 \approx \frac{60}{\sqrt{\epsilon_r}} \ln \left( \frac{4h}{0.67\pi(T + 0.8W)} \right) \quad 2-30$$

The phase velocity of TEM mode in stripline is given by:

$$v_p = \frac{c}{\sqrt{\epsilon_r}} \quad 2-31$$

### 2.3.5 Coplanar waveguide

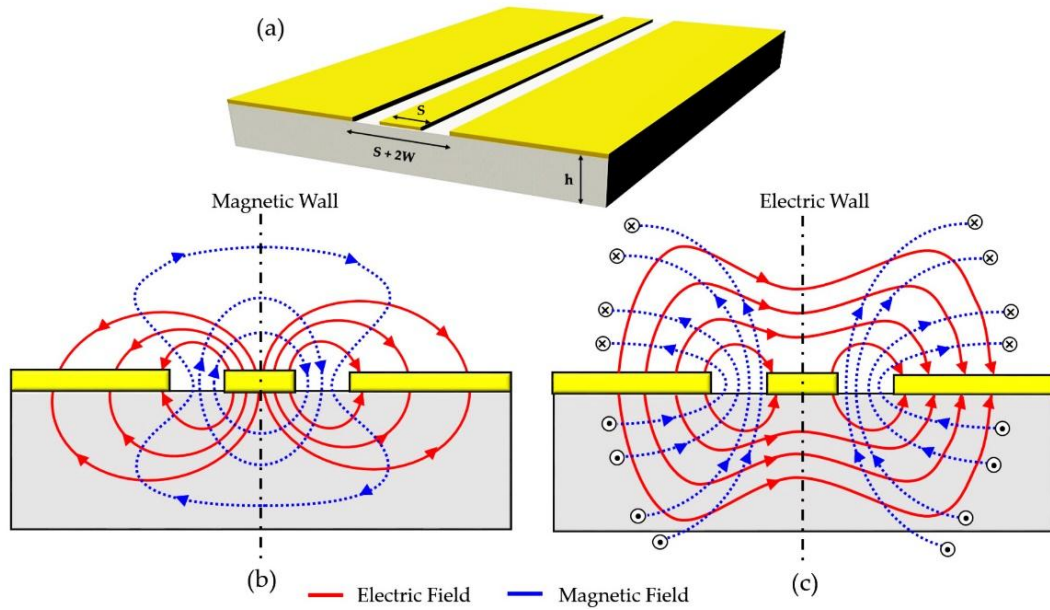
In the last few decades, CPW has been widely used in the microwave integrated circuits. In 1969, coplanar waveguide (CPW) was invented by Cheng P. Wen at RCA's Sarnoff Laboratories [93]. It consists of a centre conductor separated by a narrow gap from two ground planes located on either side on a dielectric substrate. Interestingly, at higher frequencies, the field is found to be concentrated into slot gaps so that the effective mode of propagation is changed from microstrip to a coplanar mode. CPW has to be carefully designed, to achieve a single mode of propagation for specific applications. In this project, coplanar waveguide working at THz frequencies is studied extensively with the help of both electromagnetic simulations and numerical modelling, and necessary modifications are made to optimise device design.

A schematic of a typical coplanar waveguide is shown in Figure 2.5 a. There are two different types of mode of propagation in a CPW. One is the slot line mode, often called as the even mode, where electric field lines are extending from one ground plane to other (shown in Figure 2.5 c). The other is a coplanar mode which is a quasi-TEM mode, often called as odd mode, where electric field lines extend from centre conductor to ground planes on both sides (shown in Figure 2.5 b) and are  $180^\circ$  out of phase.

For coplanar mode, an electric field is tightly confined to slot gaps, which makes it less dispersive and the most desirable mode for broadband applications [94, 95]. However, a mixed-mode signal (consisting of both odd and even field components) can propagate with zero cut-off frequency if the two ground planes are not held at the same potential. There is sometimes an additional ground plane placed on the bottom of the substrate (shown in Figure 2.4 e) which forms a conductor-backed coplanar (CBCPW) structure. For relatively large  $W/h$  ratios in a CBCPW, the field distribution is similar to that of a microstrip waveguide due to the presence of a bottom ground plane [96]. For smaller slot gap widths  $W$  (where the field is strongly coupled to ground planes on both sides), it acts as a typical coplanar waveguide.

Different air-bridge techniques have been used to suppress the unwanted slot-mode (even mode) [97, 98]. In this project, the unwanted even mode is suppressed by optical excitation of a pair of PC switches and by careful bias arrangements, which will

be discussed in detail in Chapter 3.



**Figure 2.5** Schematic of CPW and its field distribution: a) A CPW geometry with spacing ( $S+2W$ ) between two ground planes. b) The field distribution in coplanar mode (odd mode). c) The field distribution in slot line mode (even mode).

One of the main advantages of choosing CPW over other transmission lines such as slot line, microstrip, Goubau line and strip line is that it has more degrees of freedom for optimisation. The two design parameters (the centre conductor width  $S$  and the slot gap width  $W$ ) allowed optimisation of device design to meet the on-chip spectroscopy requirements in this project.

A few other advantages of CPW design are listed as follows:

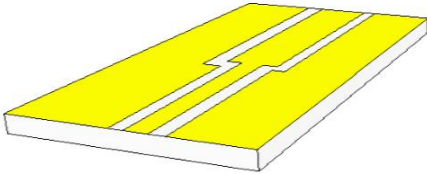
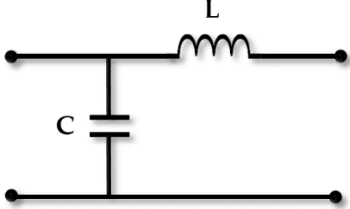
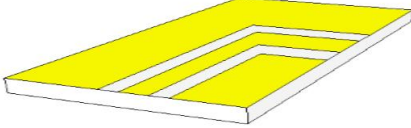
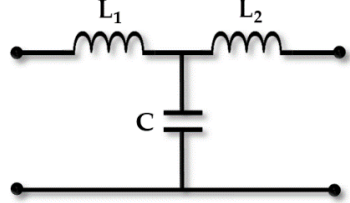
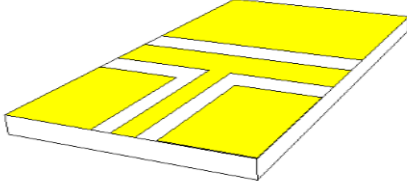
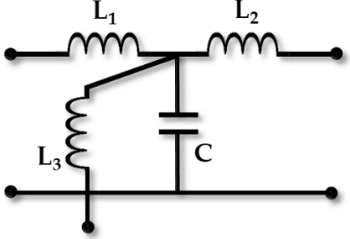
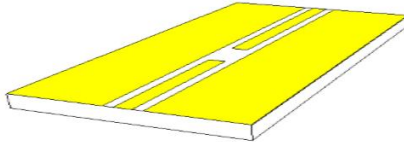
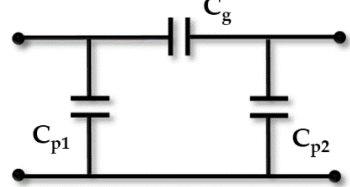
- Planar microwave circuits can be realised from CPWs because the centre conductor and ground planes are in the same plane.
- As the field is confined to the slot gaps, CPW can work with arbitrarily thick substrates. Therefore, substrate thinning is not needed in CPW [99] while Goubau line is highly affected by the substrate thickness and requires substrate thinning [90].

- Series and parallel connections of active and passive lumped elements can be realised in microwave circuits without using via-hole (through substrate) techniques.
- The fundamental coplanar mode of CPW is less dispersive than the fundamental mode of microstrip line which makes it more suitable for millimetre (in the range of THz frequency) wave circuits.
- It is possible to design highly condensed (i.e. high packaging density) microwave integrated circuits using CPW because the ground planes provide shielding between adjacent CPW lines.
- Fundamental lumped elements and filter elements (High-pass, stop-band, pass-band, and e.tc.) can be realised by introducing various discontinuities in the centre conductor of a CPW.

Signal attenuation in a CPW mainly occurs due to the conductor, dielectric and radiation losses. Frankel *et al.* [100], Cheng *et al.* [95] and Zhang *et al.* [101] investigated millimeter-wave attenuation in CPW using electro-optic sampling technique up to 1 THz. Dielectric losses  $\alpha_d$  can be minimised by choosing substrate material of low dielectric constant such as benzocyclobutane (BCB) and quartz. In this project, GaAs and quartz are both used for the waveguide substrate, and the results of electromagnetic simulations of CPW in THz range with both GaAs and Quartz substrates are presented in Section 2.5.3.2. Conductor losses  $\alpha_c$  in CPW arise due to finite conductivity  $\sigma$ , skin depth  $\delta$  (where  $\delta = \sqrt{\pi\sigma\mu f}$ ) and substrate roughness of the conductive material. At high frequencies, the field is tightly confined into the slot gaps, and the situation of current crowding occurs at the edges of the conductors, which causes a significant increase in ohmic losses (also called conductor losses) in CPW [102]. Conductor losses increase for narrower gaps. Radiation loss  $\alpha_R$  occurs due to two factors: One is the interference between the dominant mode and higher parasitic modes at higher frequencies. The other one is due to leakage (often called shock waves) into the substrate when phase velocity  $v_p$  of dominant mode is higher than substrate mode [103, 104]. Dispersion in CPW is also related to the interference between the fundamental mode and higher order

modes propagating at higher frequencies, which can be minimised by decreasing the slot gap width  $W$ .

### 2.3.6 Coplanar waveguide discontinuities

Type of Discontinuity	Waveguide Geometry	Equivalent Circuit Element
Waveguide step		
Waveguide bend		
Waveguide T-junction		
Waveguide coupling gap		


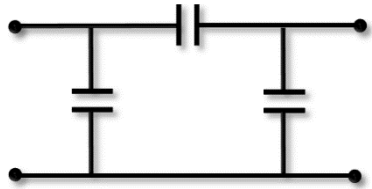
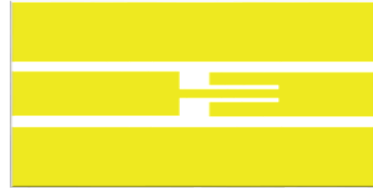
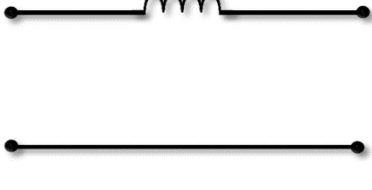


**Table 2-1 Essential coplanar waveguide discontinuities and their equivalent circuits (Images are reproduced from Ref. [99]).**

A discontinuity in a coplanar waveguide is usually caused by abrupt changes in the geometrical parameters. Such abrupt change may arise from lithographic defects introduced during the fabrication process, but a discontinuity may also be deliberately introduced in the geometry to realise specific circuit elements. In this section, only those discontinuities will be discussed that result from an intended change in the geometry of



the centre conductor of CPW.

Both reflections and losses (radiation loss) due to waveguide discontinuities increase with frequency of operation [105-107]. Radiation is mainly caused by the coupling of the fundamental coplanar mode to substrate modes. Therefore, characterisation of discontinuities becomes especially important when the operation frequency approaches the THz range. If the fundamental mode (quasi-TEM mode) is propagating along a CPW, then both the electric and magnetic field will be scattered at the discontinuity, and a mixture of the fundamental odd (coplanar mode) and even (slot-line mode) can be excited in the discontinuity region.

Type of Filter	Design	Equivalent Circuit Element
High-pass filter		
Stop-band filter		
Pass-band filter		

**Table 2-2 Fundamental filter elements realised in coplanar waveguide technology (Images are reproduced from Ref. [99].**

Table 2-1, the most common CPW discontinuities are shown, along with their equivalent circuit elements, the CPW step, bend, T-junction and a series coupling gap. By introducing discontinuities into the CPW, fundamental filter elements can also be realised, as shown in Table 2-2. The broad application range of coplanar waveguide discontinuities was first recognised by Houdart [108, 109].

In this project, the series coupling gap discontinuity was first investigated theoretically (using electromagnetic simulations); experimental results are presented in Chapter 3. Coupling gap discontinuities can be represented as a two-port pi network, where  $C_g$  represents series coupling capacitance and two shunt capacitances  $C_{p1}$  and  $C_{p2}$  represent fringing capacitances between centre conductor and ground planes [99]. The value of the coupling capacitance  $C_g$  decreases with increasing gap length. For very large gaps, coupling capacitance  $C_g$  tends to zero and discontinuity becomes an open-end circuit.

A three-dimensional full-wave analysis of coplanar discontinuities using the finite difference time domain (FDTD) technique has been given in the literature [106, 110-112]. However, full wave analysis techniques such as FDTD are computationally intensive, and particularly so at THz frequencies. Therefore, an alternative technique called quasi-static analysis [96, 113-115] draws the attention of many researchers to investigate waveguide discontinuities. In quasi-static analysis technique, a pure TEM mode of propagation is considered inside the discontinuity. Quasi-static analyses of conventional and discontinuous (with a coupling gap) CPWs are discussed in detail in Section 2.4.2.

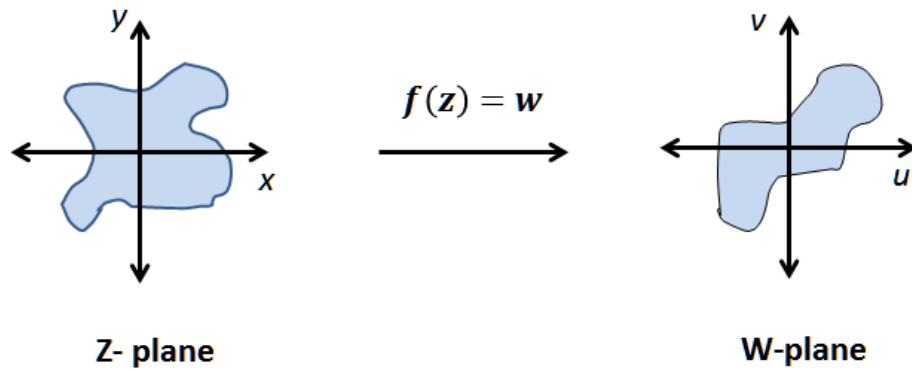
## 2.4 Quasi-static analysis of coplanar waveguide

As discussed in the previous section, the fundamental mode of propagation in CPW is a quasi-TEM mode. Quasi-TEM parameters such as characteristic impedance ( $Z_0$ ) and effective permittivity ( $\epsilon_{eff}$ ) can be derived from quasi-static analysis. In quasi-static analysis, conformal mapping techniques have been widely used to determine closed-form expressions for  $\epsilon_{eff}$  and  $Z_0$  for CPW variants with: infinite ground planes and substrate [93], finite substrate thickness and shielding walls [96], finite ground planes [116], and multilayer substrates [117]. One of the main advantages of using conformal mapping is that open planar structures (CPW, Slot-line, Microstrip, etc.) can be transformed into a closed geometry which can further lead to analytical closed-form expression for the transmission line characteristics. However, the limitation of conformal transformation technique is that it provides analytical solution for static

fields only. An introduction to the conformal mapping technique is presented in the following section.

### 2.4.1 Conformal mapping

The conformal mapping technique is a powerful mathematical tool for solving two-dimensional boundary problems in planar structures. It is a geometric technique which performs a transformation or mapping between two complex planes  $z(x, y)$  and  $w(u, v)$  using a mapping function  $f$ . With this concept, the function  $f(z) = w$  transforms a curve or a region containing points  $(x, y)$  in the  $z$ -plane into another curve or region consisting of points  $(u, v)$  in the  $w$ -plane as shown in Figure 2.6. This geometrical transformation or mapping is conformal if the function  $f$  is analytical at the point  $z$  and its derivative  $f'(z) = df/dz \neq 0$  [78]. A function is analytic at a point  $z$  if its derivative is always non-zero and unique at  $z$ . By exploiting conformal mapping technique, complex transmission line geometries can be mapped to much simpler structures whose solutions can be easily obtained.



**Figure 2.6** Function  $f(z) = w$  transforms a region in  $z$ -plane into  $w$ -plane.

For example, the mapping function,  $f(z) = w = \ln z$  transforms a circle in  $z$ -plane to a line segment in  $w$ -plane as shown in Figure 2.7. Using mapping function  $f(z) = w = \ln z$ , points on the circle with  $r = a$  and  $0 \leq v \leq 2\pi$  in  $z$ -plane are mapped to points  $u = \ln a$  and  $0 \leq v \leq 2\pi$  in  $w$ -plane.

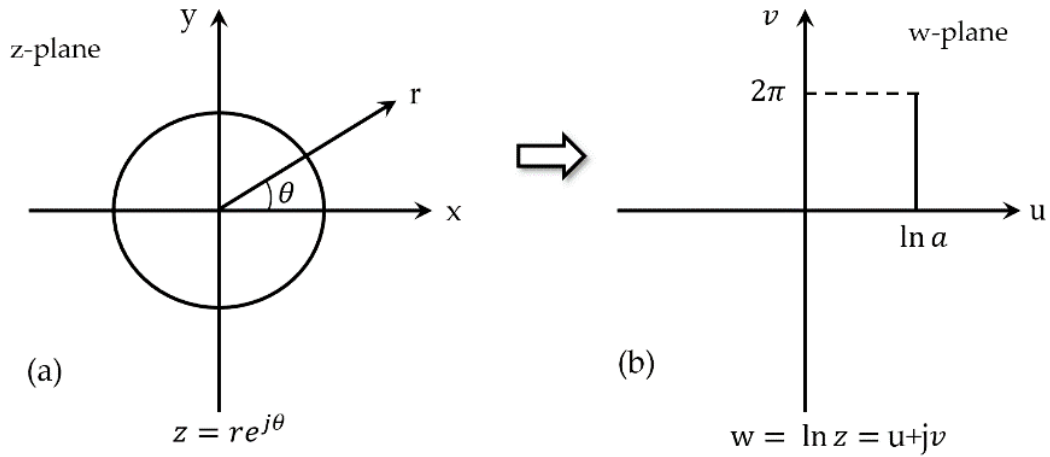


Figure 2.7 Mapping between a circle in z-plane and a line segment in w-plane [78].

The “Schwarz-Christoffel” transformation is the most commonly used conformal mapping technique for planar waveguide structures such as the strip line, a microstrip line and CPW. This transformation solves electromagnetic boundary problems involving structures with polygonal boundaries. This transformation maps the  $x$ -axis of the  $z$ -plane onto a closed polygon in  $\zeta$ -plane and the upper half of  $z$ -plane ( $y > 0$ ) onto the interior of the closed polygon as shown in Figure 2.8.

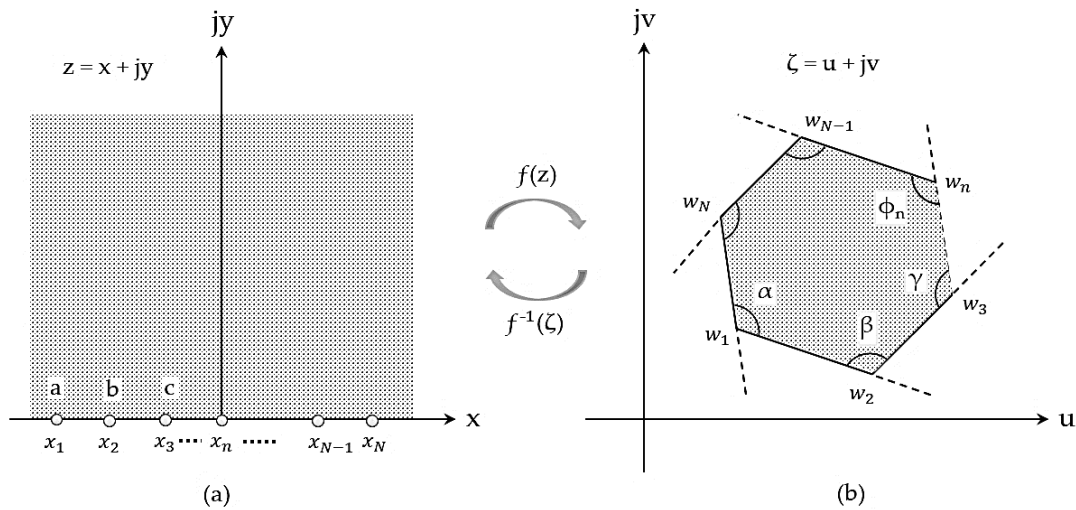


Figure 2.8 The Schwarz-Christoffel transformation: a)  $z$ -plane. b)  $\zeta$ -plane.

The Schwarz-Christoffel transformation can be written in differential form as:

$$\frac{dz}{d\zeta} = A(\zeta - a)^{\frac{\alpha}{\pi}-1}(\zeta - b)^{\frac{\beta}{\pi}-1}(\zeta - c)^{\frac{\gamma}{\pi}-1} \dots (\zeta - x_n)^{\frac{\varphi_n}{\pi}-1} \quad 2-32$$

And integral form as:

$$f(\zeta) = \int_{\zeta_0}^{\zeta} \frac{A}{(\zeta' - a)^{1-\frac{\alpha}{\pi}}(\zeta' - b)^{1-\frac{\beta}{\pi}}(\zeta' - c)^{1-\frac{\gamma}{\pi}} \dots (\zeta' - x_n)^{1-\frac{\varphi_n}{\pi}}} d\zeta' + B \quad 2-33$$

Where  $a, b, c \dots x_n$  are points on the real axis of  $z$ -plane and  $\alpha, \beta, \gamma \dots \varphi_n$  are the interior angles of closed polygons such that:

$$\alpha + \beta + \gamma + \dots = (n - 2)\pi \quad 2-34$$

$A$  is a complex number which controls the size and orientation of the polygon in  $\zeta$ -plane and  $B$  is an arbitrary constant.

This type of conformal transformation of planar transmission lines is valid for those geometries in which the electric field lies along the air-dielectric interface, and magnetic field is normal to the interface so that half-planes above, and below the metallization plane can be analysed separately [80].

#### 2.4.2 Quasi-TEM parameters of coplanar waveguide

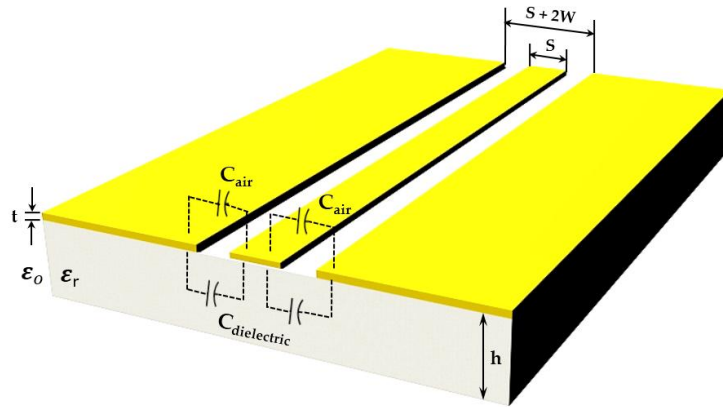
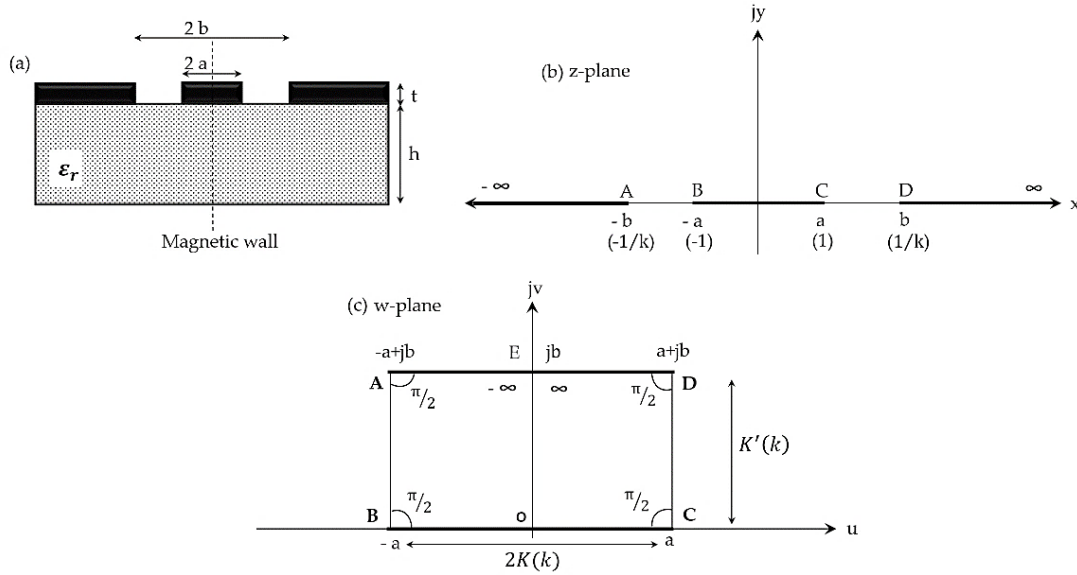


Figure 2.9 Schematics of CPW showing line capacitances above and below of metallization plane.

Quasi-TEM parameters such as the effective dielectric constant ( $\epsilon_{eff}$ ) and characteristic impedance ( $Z_0$ ) can be derived from the line capacitances above (air filled) and below (dielectric filled) the metallisation plane of CPW as shown in Figure 2.9. The total line capacitance of CPW is the algebraic sum of these two capacitances. In order to determine these capacitances using conformal mapping (Schwarz-Christoffel transformation), a few assumptions are made:

- Metal thickness ( $t$ ) is assumed to be zero ( $t \ll h$ ).
- Substrate thickness is assumed as infinite ( $h \gg S+2W$ ).
- The centre strip width is taken to be  $2a$  and the separation between the two ground planes is  $2b$  (see Figure 2.10 a). The ratio  $a/b$  (defined as the modulus) is represented by a parameter  $k$ .

Under these assumptions, the CPW geometry can be represented by a metallization plane with zero thickness (shown in Figure 2.10 b) in the  $z$ -plane. In Figure 2.10 b, CPW dimensions are normalised by ' $a$ ' which makes centre conductor width ' $2$ ' and the separation between ground planes  $2/k$ .



**Figure 2.10 Geometric transformation of CPW a) Schematic of a CPW showing dimensions. b) Cross section of CPW with metallisation plane of zero thickness. c) Schwarz-Christoffel mapping of a CPW with zero thickness into a parallel plate capacitor.**

The upper half of  $z$ -plane (air filled) is then mapped onto the rectangle 'BCDA' (to form a parallel plate capacitor) in the  $w$ -plane with each interior angle of  $\pi/2$  and vertices at  $w = \pm a, \pm a + jb$ , where  $2a$  and  $b$  are the width and the height of the rectangle (shown in Figure 2.10 c). The dimensions  $a$  and  $b$  are determined from one-to-one mapping between the points in the  $z$ -plane and  $w$ -plane. Since the rectangle is symmetric about the  $v$ -axis, the right half rectangle 'OCDE' maps points  $w = 0, a, jb$  and  $a + jb$  in  $w$ -plane to points  $z = 0, 1, \infty$  and  $1/k$  in  $z$ -plane. Similar mapping can be applied to the left-half rectangle 'OEAB'.

Using S-C transformation, Equation 1-33, points in  $z$ -plane are mapped into  $w$ -plane as:

$$w = \int_{z_0}^z \frac{A}{(z' - 1)^{1-\frac{1}{2}} \cdot (z' + 1)^{1-\frac{1}{2}} \cdot \left(z' - \frac{1}{k}\right)^{1-\frac{1}{2}} \cdot \left(z' + \frac{1}{k}\right)^{1-\frac{1}{2}}} dz' + B \quad 2-35$$

Further simplifying expression, we obtain:

$$w = \int_{z_0}^z \frac{A}{\sqrt{(z' - 1)(z' + 1) \left(z' - \frac{1}{k}\right) \left(z' + \frac{1}{k}\right)}} dz' + B \quad 2-36$$

Mapping point  $z = 0$  onto  $w = 0$ , the constant  $B$  becomes zero, Therefore,

$$w = \int_0^z \frac{A}{\sqrt{(z' - 1)(z' + 1) \left(z' - \frac{1}{k}\right) \left(z' + \frac{1}{k}\right)}} dz' + 0 \quad 2-37$$

Applying boundary value ( $z = 1$  at  $w = a$ ), we obtain:

$$a = \int_0^1 \frac{A'}{\sqrt{(1 - z'^2)(1 - k^2 z'^2)}} dz' \quad 2-38$$

Where,  $kA' = A$

Applying boundary value ( $z = 1/k$  at  $w = a + jb$ ), we obtain:

$$a + jb = \int_0^{1/k} \frac{A'}{\sqrt{(1 - z'^2)(1 - k^2 z'^2)}} dz' \quad 2-39$$

$$= A' \left[ \int_0^1 \frac{dz'}{\sqrt{(1 - z'^2)(1 - k^2 z'^2)}} + \int_1^{1/k} \frac{dz'}{\sqrt{(1 - z'^2)(1 - k^2 z'^2)}} \right] \quad 2-40$$

Using expression 2-38, we obtain:

$$= a + jA' \int_1^{1/k} \frac{dz'}{\sqrt{(z'^2 - 1)(1 - k^2 z'^2)}} \quad 2-41$$

With  $A' = 1$ , we obtain:

$$b = \int_1^{1/k} \frac{dz'}{\sqrt{(z'^2 - 1)(1 - k^2 z'^2)}} \quad 2-42$$

The values of  $a$  and  $b$  given by expressions 2-38 and 2-42 are form of a special function  $K(k)$  called the complete elliptic integral (also called elliptic sine function) of first kind [118]:

$$a = K = K(k) = \int_0^1 \frac{dz'}{\sqrt{(1 - z'^2)(1 - k^2 z'^2)}} \quad 2-43$$

$$b = K' = K(k') = \int_1^{1/k} \frac{dz'}{\sqrt{(z'^2 - 1)(1 - k^2 z'^2)}} \quad 2-44$$

Where,  $k' = \sqrt{1 - k^2}$ .

The ratio of these complete elliptic integrals  $K(k)/K(k')$  is widely used in quasi-static analysis of various planar transmission lines and can be determined as:

$$\frac{K(k)}{K(k')} = \frac{K(k)}{K'(k)} = \begin{cases} \frac{1}{\pi} \ln \left( 2 \frac{1 + \sqrt{k}}{1 - \sqrt{k}} \right), & \frac{1}{\sqrt{2}} \leq k \leq 1 \\ \frac{\pi}{\ln \left( 2 \frac{1 + \sqrt{k'}}{1 - \sqrt{k'}} \right)}, & 0 \leq k \leq \frac{1}{\sqrt{2}} \end{cases} \quad 2-45$$

The capacitance  $C_{air}$  between the centre conductor and ground planes in the upper half  $z$ - plane (air filled) can be obtained from the parallel plate capacitance formed by dimensions ' $2a$ ' (plate width) and ' $b$ ' (separation between plates) in the  $w$ -plane:

$$C_{air} = \epsilon_0 \frac{2K(k)}{K(k')} \quad 2-46$$

The lower half (below the metallisation plane) filled with the substrate with a dielectric constant  $\epsilon_r$ , will also contribute a capacitance  $C_{dielectric}$ . Due to symmetric structure, similar conformal transformation can be used to obtain  $C_{dielectric}$ . Therefore, the total capacitance of CPW line is algebraic sum of  $C_{air}$  and  $C_{dielectric}$ .

$$C_{CPW} = \epsilon_0 \frac{2K(k)}{K(k')} + \epsilon_0 \epsilon_r \frac{2K(k)}{K(k')} = \frac{1 + \epsilon_r}{2} \epsilon_0 \frac{4K(k)}{K(k')} \quad 2-47$$



Where, the factor  $1 + \epsilon_r/2$  is defined as:

$$\frac{1 + \epsilon_r}{2} = \epsilon_{eff} = \frac{C_{CPW}}{C_{air}} \quad 2-48$$

Similarly, the total inductance ( $L_{air} + L_{dielectric}$ ) can be determined as:

$$L_{CPW} = \mu_0 \frac{K(k')}{4K(k)} \quad 2-49$$

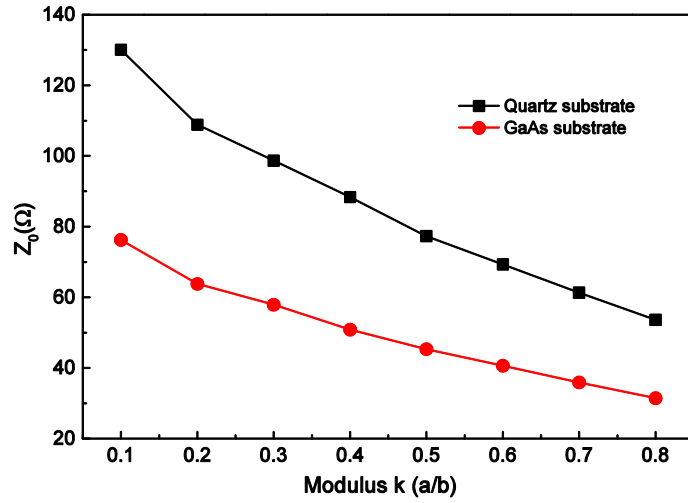
It is worth mentioning that both air and dielectric substrate have  $\mu = 1$ . Therefore, the dielectric substrate does not affect the inductance. Further, phase velocity  $v_p$  and characteristic impedance  $Z_0$  are defined as:

$$v_p = \frac{c}{\sqrt{\epsilon_{eff}}} \quad , \quad Z_0 = \frac{1}{C_{CPW} \cdot v_p} \quad 2-50$$

where,  $c$  is the velocity of light. Equations 2-47, 2-48 and 2-50 give:

$$Z_0 = \frac{1}{c C_{air} \sqrt{\epsilon_{eff}}} = \frac{30\pi}{\sqrt{\epsilon_{eff}}} \cdot \frac{K(k')}{K(k)} \quad 2-51$$

The above expression for  $\epsilon_{eff}$  and  $Z_0$  are similar to those given by [93, 119, 120].



**Figure 2.11** Plot of calculated characteristic impedance of CPW as a function of modulus  $k$  on a) GaAs substrate (plotted in red). b) Quartz substrate (plotted in black).

In Figure 2.11, characteristic impedance is plotted as function of modulus  $k$  which is a ratio of CPW dimensions (shown in Figure 2.9 and Figure 2.10) such that:

$$k = \frac{a}{b} = \frac{s/2}{s/2 + W} \quad 2-52$$

Using analytical expression 2-51,  $Z_0$  is calculated for different  $k$  values. It is clear from the Figure 2.11 that characteristic impedance  $Z_0$  of CPW is much higher for larger slot gap widths  $W$  (smaller  $k$  value).  $Z_0$  decreases dramatically for narrow slot gaps or smaller separation between ground to ground planes. Also,  $Z_0$  of CPW on the quartz substrate found to be much higher than those of GaAs based. Modulus  $k$  is one of the key design parameters, which needs to be taken into account to achieve desired characteristic impedance.

### 2.4.3 Losses in coplanar waveguide

It is vital to study transmission losses in CPW for the development of low loss on-chip CPW for millimeter-wave applications. As mentioned earlier, there are three types of transmission losses that cause signal attenuation in coplanar circuits: conductor loss  $\alpha_c$ , dielectric loss  $\alpha_d$  and radiation loss  $\alpha_R$ . In this section, these losses are studied using analytical expressions and numerical modelling. 3D-electromagnetic simulations are used to evaluate signal attenuation in CPW in Section 2.5.3.2.

#### 2.4.3.1 Conductor loss

Conductor loss in CPW is mainly due to the skin depth of material used in metallisation plane. The skin depth is defined as the depth of penetration into the conductive material at which the current density drops to  $1/e$  of its initial value. Skin depth is related to the surface resistivity and operation frequency, given by:

$$\delta = \sqrt{\frac{2\rho}{2\pi f \mu_0 \mu_r}} \quad 2-53$$

Where,  $\rho$  is the bulk resistivity,  $\mu_0 = 4\pi \times 10^{-7}$  Henry/meter,  $\mu_r$  is relative permittivity,  $f$  is the frequency of operation.

It is evident from the Figure 2.12 that skin depth drops drastically above 200 GHz and can reach to a few nanometers above 1 THz. In the above graph, skin depth found to be  $\sim 80$  nm at 1 THz. Therefore, the metal (Au) thickness of on-chip CPW devices should be more than 80 nm to minimise loss. In this project, the material (Au) thickness of 150 nm is used in cleanroom fabrication.

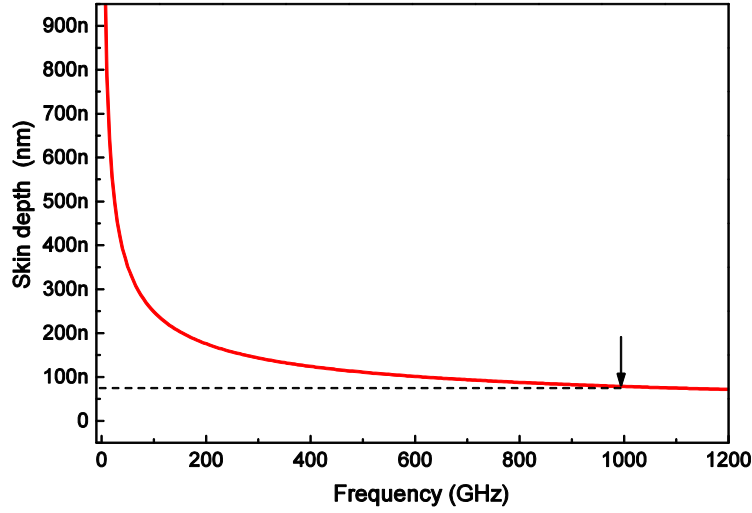


Figure 2.12 Skin depth of gold (Au) plotted against frequency of operation.

The conductor loss  $\alpha_c$  in terms of conductor resistance is given by [121]:

$$\alpha_c = 8.867 \frac{R_c + R_g}{2Z_0} \text{ dB/meter} \quad 2-54$$

Where,  $R_c$  and  $R_g$  are series resistance of the centre conductor and ground planes respectively defined as:

$$R_c = \frac{R_s}{4(2a)(1 - k^2)K^2(k)} \left[ \pi + \ln \left( \frac{4\pi(2a)}{t} \right) - k \ln \left( \frac{1+k}{1-k} \right) \right] \quad 2-55$$

$$R_g = \frac{kR_s}{4(2a)(1 - k^2)K^2(k)} \left[ \pi + \ln \left( \frac{4\pi(2b)}{t} \right) - \frac{1}{k} \ln \left( \frac{1+k}{1-k} \right) \right] \quad 2-56$$

Where,  $k$  is modulus,  $K(k)$  is elliptical integral of first kind and  $R_s$  is the surface resistance  $R_s = 1/\delta\sigma$  ohms.

In Figure 2.13, the conductor loss for CPW on both GaAs and quartz substrate is calculated with skin depth of  $\sim 80$  nm at the frequency of 1 THz and gold's bulk conductivity of  $4.1 \times 10^7$  S/m using expressions 1-52, 1-53 and 1-54. It can be seen from the graph in Figure 2.13 that conductor loss increases with increasing modulus  $k$  (decreasing the slot gap  $W$  or increasing centre conductor width  $s$ ).

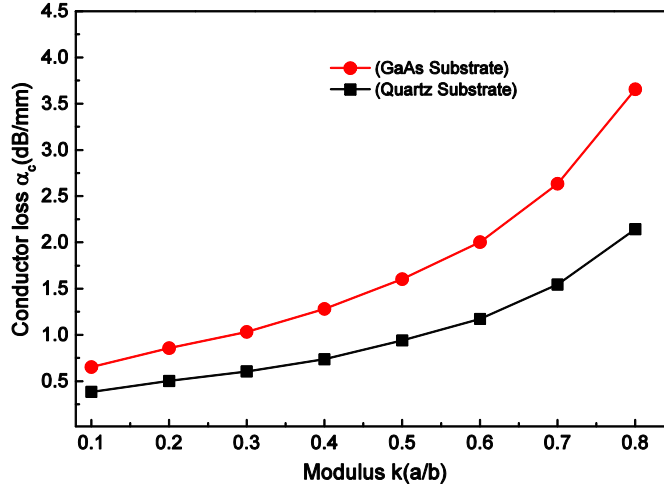


Figure 2.13 Calculated conductor loss for gold (Au), CPW on both GaAs and quartz substrates plotted against modulus k (ratio of CPW dimensions).

It implies that narrow slot gaps result in an increased conductor loss compared to wider slot gaps. This can further be explained by increased current density at the edges of conductors when slot gaps are much narrower. It can also be seen from the graph that CPW on GaAs substrate (possess low impedance, see Figure 2.13) is more susceptible to conductor losses than CPW on a quartz substrate.

#### 2.4.3.2 Dielectric loss

Dielectric loss is related to the substrate conductive properties and is proportional to loss tangent of the dielectric material. Therefore, high-quality substrate material with low conductivity and loss tangent should carefully be chosen to minimise the dielectric loss.

Dielectric loss  $\alpha_d$  for a CPW is given by:

$$\alpha_d = 8.867 \frac{\tan \delta_c}{\lambda_0} \frac{\epsilon_r}{\sqrt{\epsilon_r}} \frac{\epsilon_{eff} - 1}{\epsilon_r - 1} \text{ dB/meter} \quad 2-57$$

where,  $\lambda_0$  is the wavelength in free space,  $\tan \delta_c$  is the loss tangent,  $\epsilon_r$  and  $\epsilon_{eff}$  are the relative and effective permittivity and  $q$  is the filling factor given by:

$$q = \frac{1}{2} \frac{K(k_1)}{K(k'_1)} \frac{K(k')}{K(k)} \quad 2-58$$

Where,  $K(k)$  and  $K(k_1)$  are the complete elliptic integrals of the first kind with moduli  $k$  and  $k_1$  given by:

$$k_1 = \frac{\sinh(\pi s/4h_1)}{\sinh[\pi(s+2W)/4h_1]}, \quad k = \frac{a}{b} = \frac{s/2}{s/2+W} \quad 2-59$$

#### 2.4.3.3 Radiation loss

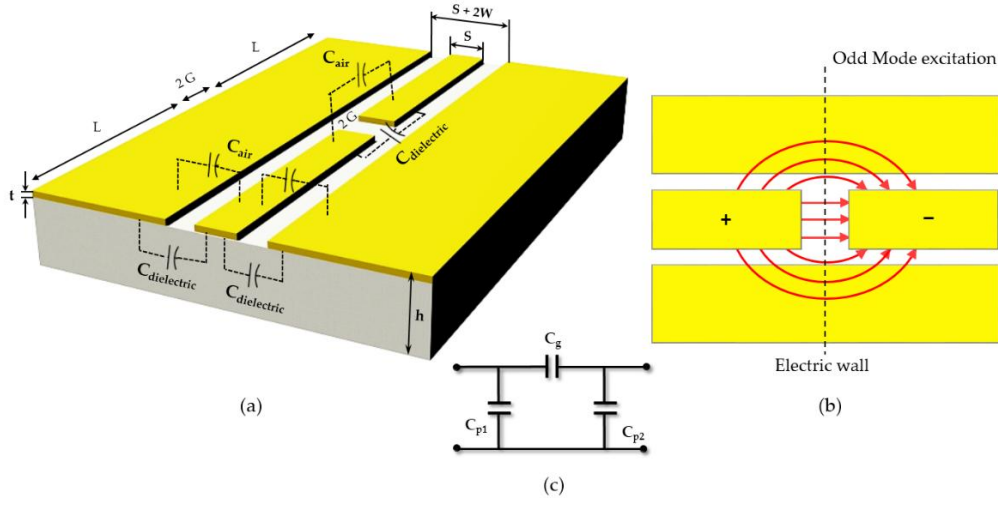
In CPW geometries, where substrate thickness is comparable to the wavelength of a signal propagating down the transmission line, a coupling between CPW mode and substrate mode may occur [122]. In this situation, the phase velocity of CPW mode exceeds the phase velocity of the substrate mode forcing the electromagnetic fields to radiate from the transmission line into substrate region. This radiation starts at a certain frequency when the phase velocities of CPW and substrate mode found to be equal and above this frequency, more power radiates (radiation loss increases) from transmission line with increasing operation frequency [123].

#### 2.4.4 Discontinuous (series coupling gap) coplanar waveguide

The coupling gap discontinuity has been used as a capacitive coupling switch in coplanar microwave circuits for high-frequency sampling and switching operations. It is a small (order of few microns) gap in the centre conductor (shown in Figure 2.14 a) acting as a resonator and can be used as a high-pass filter to suppress low-frequency components in transmitted signal [124, 125].

In few literatures [99, 126-128], the coupling discontinuity has also been reported as Metal-Insulator-Metal (MIM) discontinuity due to the presence of a dielectric thin film underneath the coupling gap. Therefore, the coupling discontinuity provides a method of dielectric characterisation using on-chip coplanar structures. K. Nadaud *et. al.* [128] extracted permittivity of a thin film with the help of mathematical model describing the capacitance of coupling discontinuity in the coplanar waveguide. H. S. Skulason *et. al.* [129] extracted graphene sheet impedance parameter in MIM configuration using discontinuous coplanar waveguide system while performing measurements from 0.01 to 110 GHz. Despite many advantages of this type of CPW discontinuity, only a limited literature is available describing its equivalent capacitive

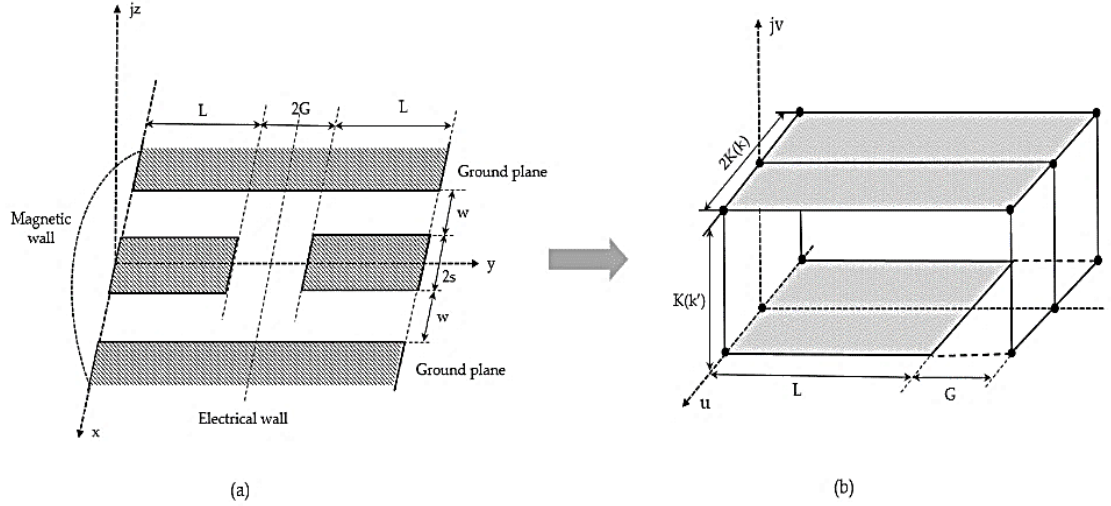
model [99, 105, 106].



**Figure 2.14 Schematic of CGAP-CPW a) Showing line capacitances above and below of metallisation plane. b) Electric field distribution in discontinuity region. c) Equivalent capacitive  $\pi$ -model of coupling discontinuity.**

The equivalent capacitive  $\pi$ -network consists of capacitances  $C_g$ ,  $C_{p1}$ , and  $C_{p2}$  as shown in Figure 2.14 c.  $C_g$  represents coupling capacitance of centre conductor discontinuity. Two shunt Capacitances,  $C_{p1}$  and  $C_{p2}$  represent fringing capacitances between center conductor and ground planes [99]. Due to symmetry, the value of shunt capacitances must be equal ( $C_{p1} = C_{p2}$ ). The value of coupling capacitance  $C_g$  decreases with increasing gap length ( $C_g$  is proportional to  $1/2G$ , where  $2G$  is coupling gap length shown in Figure 2.14 a). For very large gap, coupling capacitance  $C_g$  tends to zero and discontinuity becomes an open-end circuit.

The coupling discontinuity has been analysed using quasi-TEM three-dimensional finite difference method (FDM) in the literature [106, 130]. However, S. Gevorgian *et. al.* [131, 132] used conformal mapping technique (see Section 2.4.2) to derive closed-form expressions for the equivalent capacitive  $\pi$ -network of coupling discontinuity.



**Figure 2.15** Schwarz-Christoffel transformation of a planar CGAP-CPW into parallel plate capacitor [132].

Expression for series and shunt capacitances are defined as [132]:

$$C_g = 2\epsilon_0\epsilon_{eff} \left[ \frac{K(k_2)}{K(k'_2)} - \frac{K(k_3)}{K(k'_3)} \right] L K(k)s \quad 2-60$$

$$C_p = C_{p1} = C_{p2} = 4\epsilon_0\epsilon_{eff} \left[ \frac{K(k_3)}{K(k'_3)} k(k)s - \frac{K(k)}{K(k')} L \right] \quad 2-61$$

Where,  $\epsilon_{eff}$  is effective permittivity,  $L$  is the distance (transmission length) from the edge of coupling gap both side (see Figure 2.15 a),  $s$  is the centre conductor width and  $k, k', k_2, k'_2, k_3$  and  $k'_3$  are moduli of the elliptic integrals defined as:

$$k = \frac{a}{b} = \frac{s/2}{s/2 + W}; \quad k_2 = sn \left[ \frac{L}{L+G} K(k_1), k_1 \right]; \quad k_3 = k_1 k_2 \quad 2-62$$

Where,  $G$  is the half-length of coupling gap (see Figure 2.15 a).

$$k' = \sqrt{1 - k^2}; \quad k'_2 = \sqrt{1 - k_2^2}; \quad k'_3 = \sqrt{1 - k_3^2} \quad 2-63$$

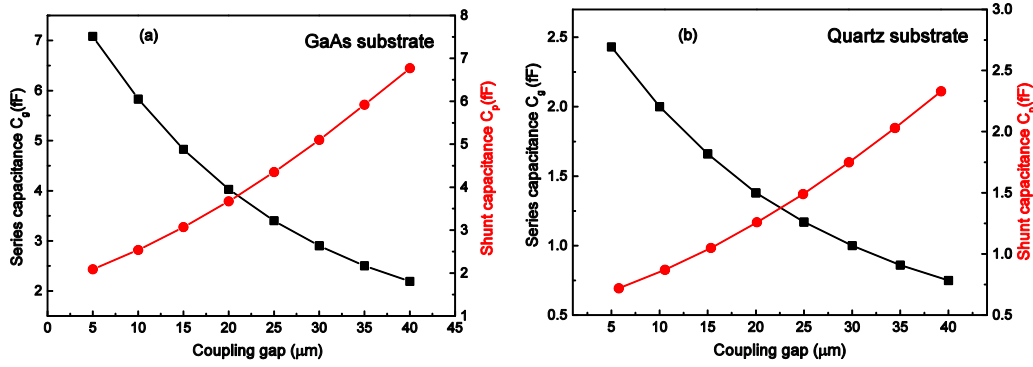
$k_1$  is obtained using inverse Hilbert transform from the relation given as[133]:

$$\frac{K(k_1)}{K(k'_1)} = \frac{L+G}{sK(k)} \quad 2-64$$

For larger values of  $L$  (tending to infinity), closed-form expressions are approximated by S. Gevorgian *et. al.* as:

$$C_p = \frac{4}{\pi} \epsilon_o \epsilon_{eff} \left( \frac{s}{2} \right) K(k) \left[ \frac{8}{1 + 8 \exp \left( \frac{-\pi G}{s K(k')} \right)} \right] \quad 2-65$$

$$C_g = \frac{2}{\pi} \epsilon_o \epsilon_{eff} \left( \frac{s}{2} \right) K(k) \left[ 1 + 8 \exp \left( \frac{-\pi G}{\frac{s}{2} K(k')} \right) \right] \quad 2-66$$



**Figure 2.16** The series and shunt capacitances of a CPW as function of coupling gap length  
a) GaAs substrate with dielectric constant  $\epsilon_r = 12.9$ . b) Quartz substrate with dielectric constant  $\epsilon_r = 3.78$ .

In this work, approximated expressions are used to calculate shunt and series capacitances of CGAP-CPW with design parameters: centre conductor width  $s = 30 \mu m$ , spacing between centre conductor and ground plane  $W = 20 \mu m$ , modulus  $k = \frac{s}{s/2 + W}$ , relative dielectric constant of substrate  $\epsilon_r = 12.9$  (GaAs) and 3.78 (Quartz).

In Figure 2.16, series and shunt capacitances are plotted as a function of coupling gap length for both GaAs and quartz substrates. It is clear from graphs that series coupling capacitance  $C_g$  decreases with increasing gap width  $W$  whereas shunt capacitance  $C_p$  (fringing capacitance between centre conductor and ground planes) gradually increases with coupling gap length. It is worth mentioning that series and shunt capacitances has the same value for the coupling gap length  $\sim 22 \mu m$ . It is also noted that capacitances values for CPW on GaAs substrate are higher than those of quartz substrate.

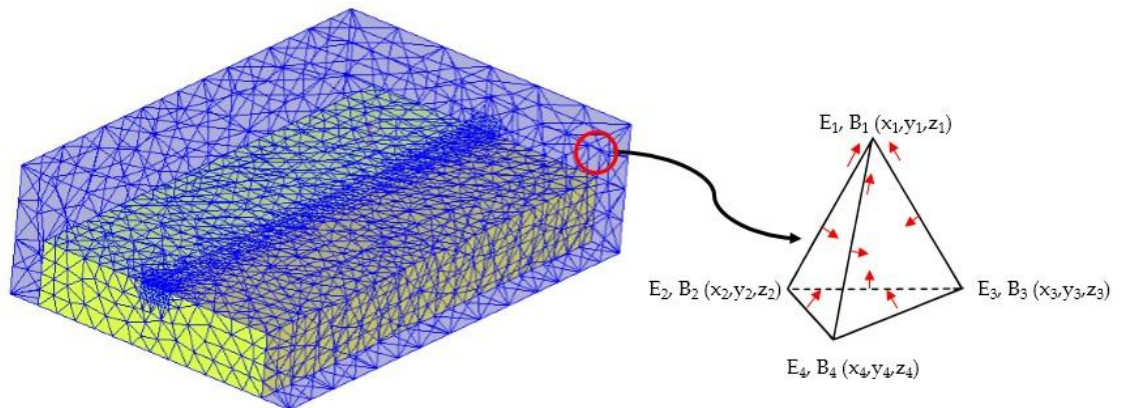


## 2.5 Electromagnetic simulations using High-Frequency Structure Simulator (HFSS)

In this project, a 3D EM simulator called Ansoft HFSS was also used for design optimisation and theoretical modelling of CPW structures. HFSS allows the user to draw a 3D structure of a waveguide of interest and simulate its EM behaviour over a broad frequency range. In this project, most of the EM simulations were performed in the THz regime (up to 1.2 THz). The following section gives an insight into working principle and underlying physics of HFSS.

### 2.5.1 Finite Elements Method and adaptive meshing

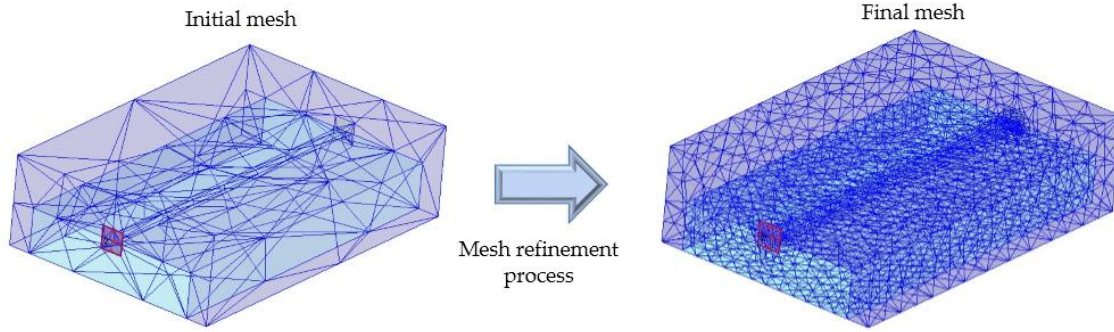
HFSS uses the Finite-Element Method (FEM) to break down the volume of the 3D simulation model into smaller elements in order to analyse them. The small elements used are tetrahedral mesh elements [134].



**Figure 2.17** A large volume of a 3D structure of a CPW decomposed into small elements (tetrahedrons). E-field values are calculated at vertices and edges of a single tetrahedron.

An example of a single tetrahedron is shown in Figure 2.17, where each vertex represents a nodal value (electric field component). These individual nodal values are used to generate the vector field quantities (solving field inside tetrahedron using nodal values). HFSS uses interpolation technique to derive vector field quantities (such as the H-field and E-field) from nodal values.

After decomposing 3D structure, HFSS identifies material defined in waveguide design and boundary conditions (such as radiation boundary, which acts as absorbent for E-H field radiation emanating from waveguide). HFSS also identifies wave/lump port drawn in 3D structure to assess power in/out to the waveguide structure. HFSS then sub-divides the 3D structure with an initial mesh based on solution frequency (represents the wavelength to determine the initial tetrahedron dimension) provided by the user.



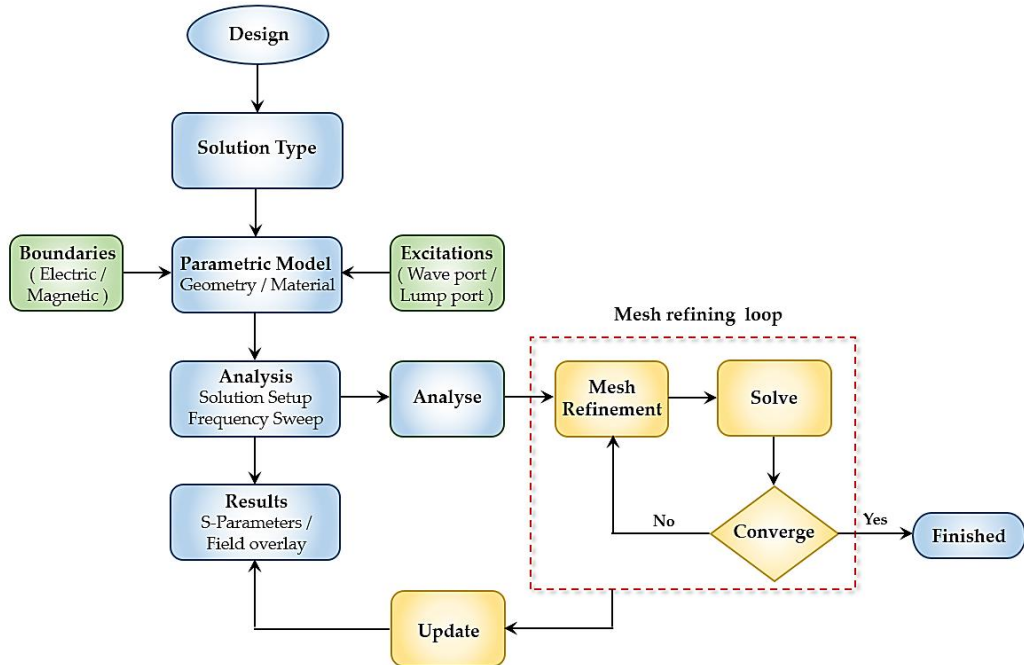
**Figure 2.18 Adaptive mesh refinement process based on solution frequency value.**

Using an adapting meshing process (see mesh refining loop in Figure 2.18), HFSS generates a solution that is biased on an initial mesh first and then sub-divide the area where the finer mesh (denser meshing, shown in Figure 2.18) is required. The adaptive meshing process refines the tetrahedral dimensions in areas where the electric field gradient is largest. After several iterative mesh refining processes (adapting meshing loops), E-field values calculated from the current mesh are compared to those of the previous mesh. If the difference is less than or equal to an assigned threshold value (often called as delta  $S$ ), the process is considered, converged and adapting meshing loop terminates. Delta  $S$  can be defined as:

$$\Delta S \geq S_{ij}^N - S_{ij}^{(N-1)} \quad 2-67$$

Where,  $N$  is an adaptive pass number,  $\Delta S$  is threshold value (or delta  $S$ ) assigned by the user,  $S_{ij}^N$  is the value from current adaptive pass and  $S_{ij}^{(N-1)}$  is the value from previous the adaptive pass. It is clear from the expression 2-67 that for smaller values of delta  $S$ , denser meshes will be formed to minimise the difference between current and previous adaptive pass. However, choosing small values of delta  $S$  will increase the simulation

time. The default value of  $\Delta S = 0.02$  (can also be modified) provided by HFSS which can be found in driven solution setup. In this work, the default value of  $\Delta S = 0.02$  is used in the mesh refinement process. In Figure 2.19, HFSS solution process is represented with the help of flow-chart, including all the crucial steps:



**Figure 2.19** Flow chart showing HFSS's 3D-field solving steps.

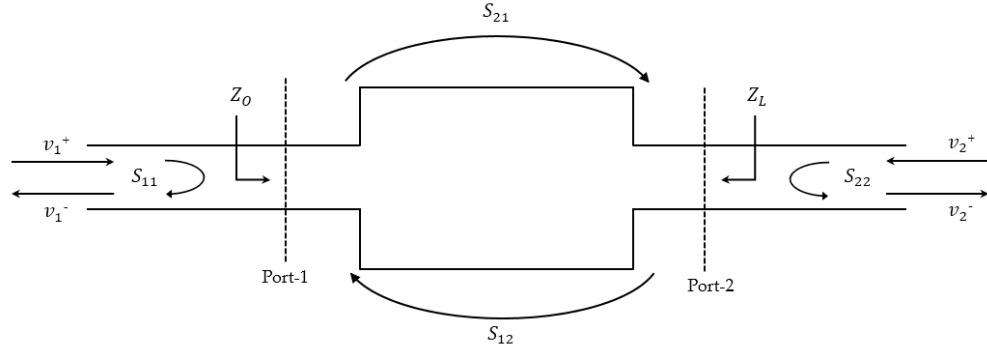
- After drawing a 3D model of the waveguide structure, the material assignment is one of the crucial steps. An extensive material library is available in the HFSS modeller. The predefined materials in the library are frequency independent but can be customised to make them frequency dependent to meet the user's requirement. Also, new materials can be defined and added to the library by assigning parameters such as permittivity, conductivity and loss tangent.
- There are mainly two types of excitation ports used in electromagnetic simulations defined as Waveport and lumped port. Excitation ports are usually placed at the ends of a transmission line to feed the electromagnetic power from one end and to measure output power at the other end. Lumped ports are commonly used in antenna design simulation in which ports are placed internally to the structure (usually between conductors). Waveport excitation is

commonly used with planar waveguide structures such as CPW, microstrip, slotline, Goubau line, etc. Waveports are defined at the outer boundary of 3D (perpendicular to the transmission line) structure and coincide with the radiation boundary plane. A 2D eigenmode *port solver* is initiated before the adaptive meshing when the port is excited. Port solver computes the port impedance and identifies propagating modes that can exist in the transmission line. Integration lines (electric field vectors) can be drawn on the ports to specify a mode of propagation (such as an odd or even mode). Default incident power on the port is set to 1 Watt.

- A *radiation boundary* is assigned to all the faces of air box surrounding the waveguide structure. It can act as an absorbing wall to the emanating electromagnetic radiation and prevents reflections.
- Once material, excitation ports and radiation boundary are defined, HFSS needs solution frequency information (provided by the user) to create an initial mesh of the 3D structure. Another crucial parameter which is known as a *frequency sweep* defines the range of frequency over which 3D model is simulated. Solution frequency can be chosen 80% of (or equal to) maximum frequency selected in the frequency sweep. In frequency sweep, step size will determine the frequency resolution of generated  $S$ ,  $Y$  and  $Z$  parameters.
- HFSS reflects simulation results of a waveguide structure in terms of  $S$ ,  $Y$ ,  $Z$ ,  $\gamma$ ,  $\lambda$  and  $\epsilon$  parameters in a modal solution data report. With the help of these parameters, transmission properties such as the mode of propagation, bandwidth, permittivity, attenuation, the extent of the field and characteristic impedance can be estimated.  $S$ -parameters are discussed in the next section.

### 2.5.2 S-parameters

$S$ -parameters, also often called as “scattering parameters” are convenient mathematical tools to describe the electromagnetic behaviour of a transmission line (forming a two-port network) in terms of reflection ( $S_{11}$ ) and transmission ( $S_{21}$ ) coefficients.



**Figure 2.20** A schematic of the two-port network with reflection and transmission coefficients. Incident and reflected waves at port-1 and port-2 are  $v_1^+$ ,  $v_2^+$  and  $v_1^-$ ,  $v_2^-$ .

A schematic of two-port network is shown in Figure 2.20, where incident and reflected waves at port-1 and port-2 are  $v_1^+$ ,  $v_2^+$  and  $v_1^-$ ,  $v_2^-$ . Scattering parameters can be defined using a matrix equation as:

$$\begin{pmatrix} v_1^- \\ v_2^- \end{pmatrix} = \begin{pmatrix} S_{11} & S_{12} \\ S_{21} & S_{22} \end{pmatrix} \begin{pmatrix} v_1^+ \\ v_2^+ \end{pmatrix} \quad 2-68$$

Further simplifying matrix equation, we obtain:

$$v_1^- = S_{11}v_1^+ + S_{12}v_2^+ \quad \text{and} \quad v_2^- = S_{21}v_1^+ + S_{22}v_2^+ \quad 2-69$$

Now,  $S_{11}$  can be determined as a ratio of magnitudes of reflected wave to incident wave,  $S_{11} = (v_1^-/v_1^+)$  at port-1 (assuming output is terminated in a perfect load  $Z_0$  and therefore,  $v_2^+ = 0$ ). Likewise,  $S_{21}$  can be determined as  $S_{21} = (v_2^-/v_1^+)$ . For a symmetric two-port network, S-parameters are related as  $S_{11} = S_{22}$  and  $S_{21} = S_{12}$ . Although, these reflection and transmission coefficients are unitless, they can be converted to their decibel (dB) format as  $20 \log$  of the voltage ratios as:

$$S_{11}(\text{dB}) = -20 \log_{10}(v_1^-/v_1^+) = \text{input reflection loss} \quad 2-70$$

$$S_{21}(\text{dB}) = -20 \log_{10}(v_2^-/v_1^+) = \text{forward transmission loss} \quad 2-71$$

Where negative and positive dB value suggests attenuation and gain in the transmission line. To determine power loss in a transmission line (for  $Z_L = Z_0$ ), power ratios can also be used instead voltage ratios as mentioned in ref [101]:

$$\frac{P_r}{P_i} = |S_{11}^2|, \quad \frac{P_L}{P_i} = |S_{21}^2| \quad 2-72$$

Where,  $P_i$  is the incident power,  $P_r$  is the reflected power and  $P_L$  is the power delivered to the load.  $|S_{11}^2|$  and  $|S_{21}^2|$  are reflected and transmitted power respectively.

Further, signal attenuation  $\alpha$  can be related to power ratios as:

$$\frac{P_r}{P_i} + \frac{P_L}{P_i} = |S_{11}^2| + |S_{21}^2| = e^{-2\alpha l} \quad 2-73$$

By taking log of both sides, we get attenuation constant  $\alpha$  as:

$$\alpha = -\frac{1}{2l} \ln(|S_{11}^2| + |S_{21}^2|) \quad 2-74$$

Power loss in dB can be given by:

$$\text{Power loss} = -10 \log_{10}(P_{out}/P_{in}) \quad 2-75$$

In Table 2-3, Voltage and power ratios are calculated using expression 2-70 and 2-71 for different roll-off values in dB where zero dB corresponds to a unity voltage/power ratio. In ideal situation (no loss condition), 0 dB implies that there is no attenuation in the transmission line and  $v_{out} = v_{in}$  or  $p_{out} = p_{in}$ . At -20 dB roll off, signal amplitude falls to 10% ( $v_{out}/v_{in} = 0.10$ ) of its initial value. In terms of power ratio, only 1% power is delivered to the load at -20 dB roll off.

Roll off	Voltage ratio	Power ratio
0 dB	1.00	1.00
-3 dB	0.707	0.501
-6 dB	0.501	0.251
-9 dB	0.354	0.125
-12 dB	0.251	0.063
-15 dB	0.177	0.031
-18 dB	0.125	0.015
-20 dB	0.100	0.010

**Table 2-3 Values of voltage and power ratios against roll off values of signal amplitude in dB.**

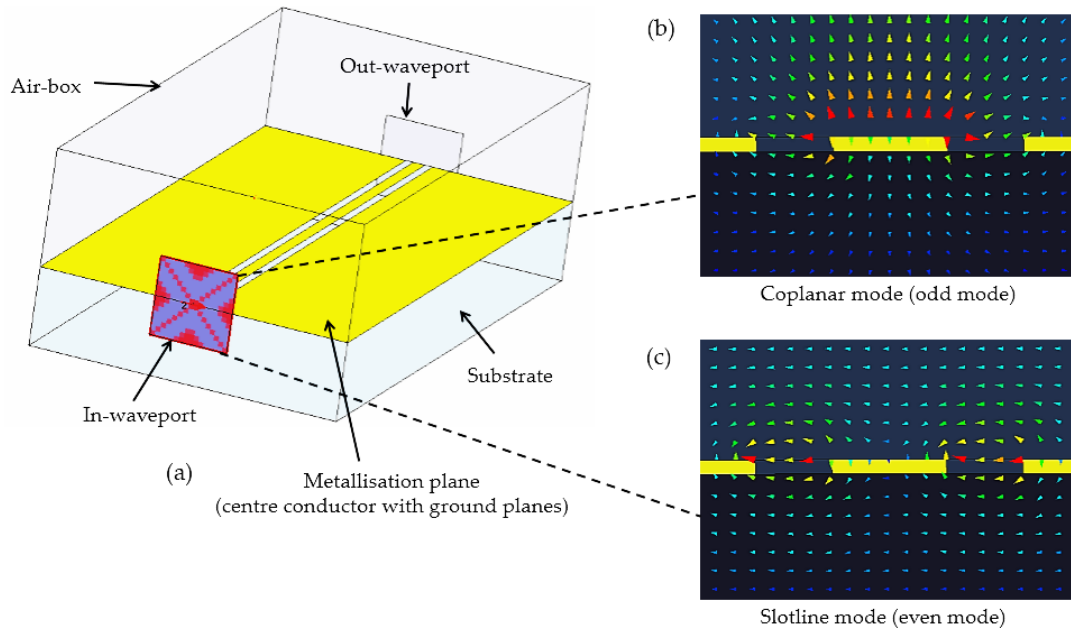
To estimate CPW device's bandwidth from HFSS simulations, -14 dB was used as a reference at which signal amplitude falls to 20% ( $v_{out}/v_{in} = 0.199$ ) of its initial value. The estimated bandwidth was in good agreement with the bandwidth obtained from FFT spectra (when signal amplitude gradually falls to the level of noise floor- see Chapter 3) of on-chip CPW measurements in the THz lab.

### 2.5.3 CPW simulation setup and results

In this section, the THz transmission properties of a conventional CPW simulated using HFSS is discussed. The dependence of substrate materials (GaAs and quartz) on the transmission line characteristics (such as bandwidth, characteristic impedance, attenuation and loss factor) from sub-THz to the THz frequency range is studied. Simulation results obtained for both GaAs and quartz substrate are compared for better understanding. Further, CGAP-CPWs are simulated to investigate coupling gap characteristics that gives insight into high-pass filtering function (rejecting low-frequency components) and resonating behaviour of CPW discontinuity.

#### 2.5.3.1 Simulation setup (Continuous CPW)

A 3D structure of CPW comprising a centre conductor and ground planes drawn in HFSS is shown in Figure 2.21. Au (gold) material with bulk conductivity of  $4.1 \times 10^7$  siemens/m selected from HFSS' material library was assigned to CPW's metallisation plane. CPW dimensions include centre conductor width of 0.03 mm, the slot gap between the centre conductor and the ground plane of 0.02 mm wide, and substrate thickness of 350  $\mu\text{m}$ . The transmission length of CPW was 1.5 mm (same as CPW device fabricated in the cleanroom). The relative permittivity values of GaAs and quartz used for simulation are 12.9 and 3.78 (values from the material library), respectively. The waveport dimension was chosen carefully to avoid excitation of lossy substrate modes. The waveport dimension is determined by using "solve port only" utility in HFSS for a given port impedance. The rule of thumb for designing a waveport is that its size should not exceed  $\lambda/2$  in any dimension. Integration lines (electric field vectors) for waveports were drawn to specify the mode of propagation in the transmission line. Odd and even modes of excitation are shown in Figure 2.21 b and c.



**Figure 2.21 3D model of CPW with excitation modes: a) An air box surrounding a CPW on a dielectric substrate. b) Electric field vectors are showing odd mode excitation in waveport. c) Electric field vectors are showing even-mode excitation in waveport.**

After defining the design parameters of the CPW, simulations were performed in the frequency range (often called as the frequency sweep) of 0.01 to 1.2 THz, with the solution frequency set to 1.1 THz. Simulation results were then exported from HFSS to Origin (data analysis and graphics software).

### 2.5.3.2 Simulation results (continuous CPW)

The transmission loss parameter  $S_{21}$  obtained from HFSS simulation is plotted as function of frequency in Figure 2.22. It is clear from the graph that CPW on GaAs substrate shows higher attenuation (higher roll off) compared to CPW on quartz with increasing frequency. The -14 dB point was taken as (discussed in Section 2.5.2) reference to estimate bandwidths of CPW<sub>GaAs</sub> and CPW<sub>quartz</sub>. The points at which -14 dB reference line intersects plots in Figure 2.22, bandwidths of CPW<sub>GaAs</sub> and CPW<sub>quartz</sub> are obtained at 0.45 and 1.01 THz, respectively. The features appeared at 0.45 THz in  $S_{21}$  parameter obtained for CPW<sub>GaAs</sub> is due to dispersion (excitation of higher-order hybrid modes and coupling between dominant CPW mode and surface waves on the substrate) at higher frequencies.



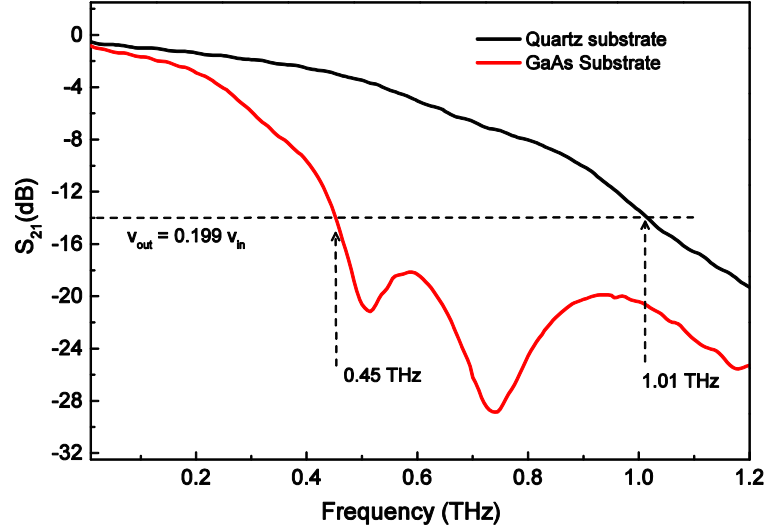
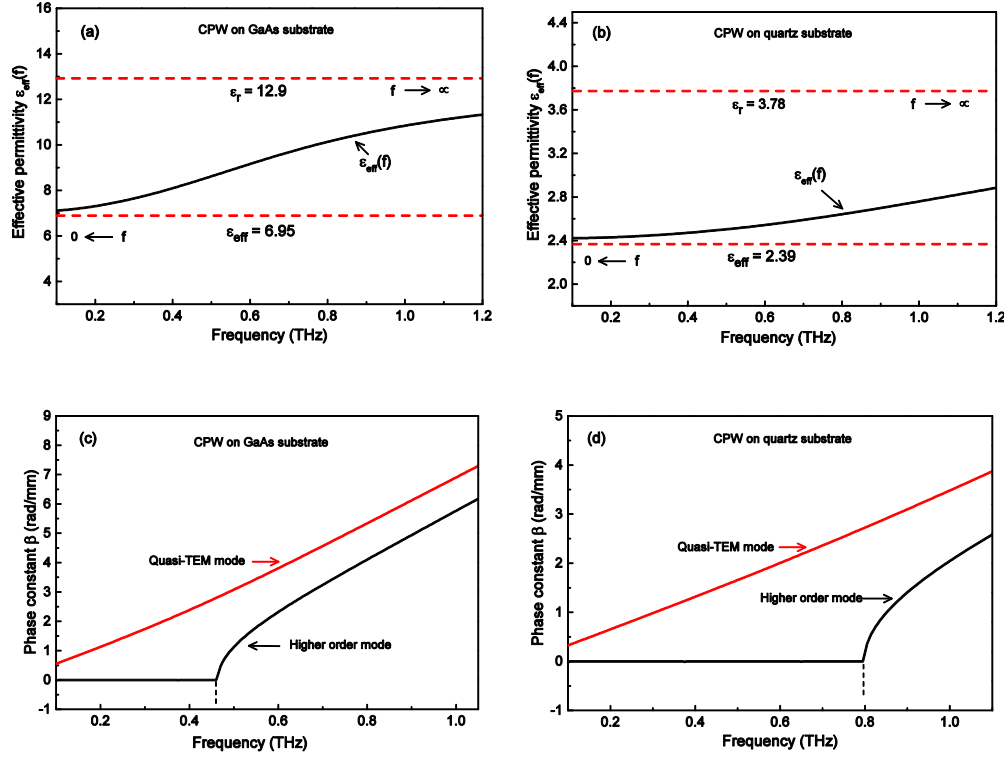


Figure 2.22  $S_{21}$  parameter for both CPW<sub>GaAs</sub> and CPW<sub>quartz</sub> plotted as a function of frequency.

Plotting phase constant  $\beta$  (imaginary part of propagation constant  $\gamma$ ) and frequency-dependent effective permittivity  $\epsilon_{eff}(f)$  can give an insight into propagation of higher-order modes above certain frequency. At low frequencies, EM field's distribution is uniform above and below the metallisation plane and therefore, effective permittivity is nearly an average of relative permittivity of substrate and air ( $\epsilon_{eff} = (\epsilon_{air} + \epsilon_{substrate}) / 2$ ). However, at higher frequencies EM fields tend to couple into the substrate in greater proportion (see Figure 2.24) therefore, frequency-dependent effective permittivity needs to be taken into account. Frequency-dependent effective permittivity  $\epsilon_{eff}(f)$  based on dispersion phenomenon in CPW is defined as [135, 136]:

$$\sqrt{\epsilon_{eff}(f)} = \sqrt{\epsilon_{eff}} + \frac{(\sqrt{\epsilon_r} - \sqrt{\epsilon_{eff}})}{(1 + aF^{-b})} \quad 2-76$$

Where,  $f$  is the frequency of operation,  $F = f/f_{TE}$  is the normalised frequency,  $f_{TE} = c/4h\sqrt{\epsilon_r - 1}$  is the cut off frequency for the first lowest order surface wave TE mode,  $\epsilon_{eff}$  is effective permittivity at low frequency ( $f \rightarrow 0$ ) and  $b \approx 1.8$  is a constant.

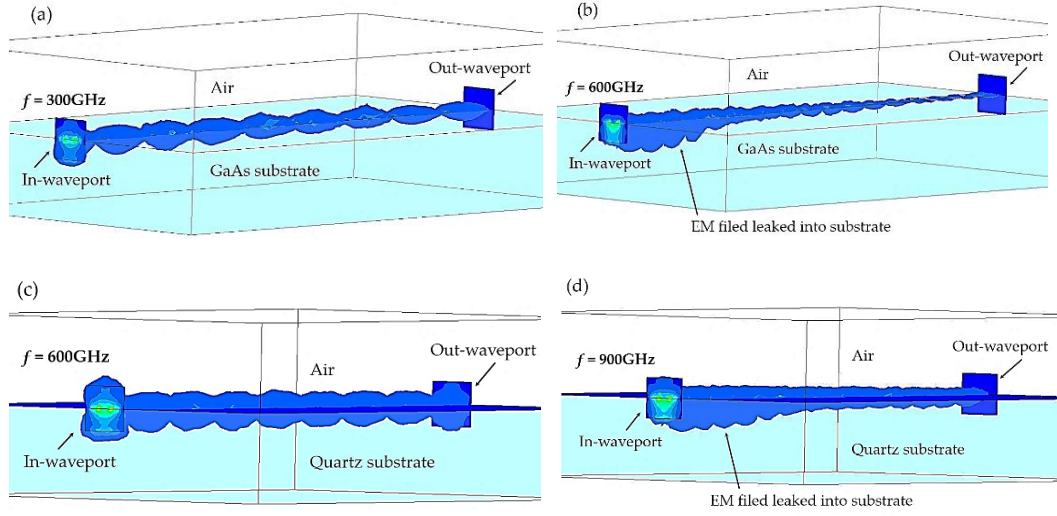


**Figure 2.23** Frequency dependent effective permittivity plotted as a function of frequency  
a) CPW<sub>GaAs</sub>. b) CPW<sub>quartz</sub> Phase constant for quasi-TEM mode and the first higher mode is plotted. c) CPW<sub>GaAs</sub>. d) CPW<sub>quartz</sub>.

It is evident from Figure 2.23 a and b that the value of  $\epsilon_{eff}(f)$  lies between effective permittivity  $\epsilon_{eff}$  (where  $f \rightarrow 0$ ) and relative permittivity of dielectric (GaAs and quartz) substrates (where  $f \rightarrow \infty$ ). We note that  $\epsilon_{eff}(f)$  of CPW<sub>GaAs</sub> changes dramatically above 400 GHz while  $\epsilon_{eff}(f)$  of CPW<sub>quartz</sub> reasonably linear up to 600 GHz and then gradually increases with frequency.

Propagation is related to the wavelength of transmitted signal as  $= 2\pi/\lambda$ , where wavelength  $\lambda$  can be related to effective permittivity as  $\lambda = v_p/f = c/f\sqrt{\epsilon_{eff}}$  which suggests that phase constant  $\beta$  is closely related to effective permittivity as  $\beta = \omega\sqrt{\epsilon_{eff}}/c$ . Therefore, at higher frequencies, change in the effective permittivity can be attributed to the change in phase constant  $\beta$ . In Figure 2.23 c and d, phase constant  $\beta$  for both CPW<sub>GaAs</sub> and CPW<sub>quartz</sub> is plotted as a function of frequency, where linear phase change for quasi-TEM mode is shown in red. It is clear from Figure 2.23 c that first higher-order mode starts to propagate at 460 GHz in CPW<sub>GaAs</sub>. For CPW on quartz substrate, first higher-order mode starts to propagate at 800 GHz as shown in Figure

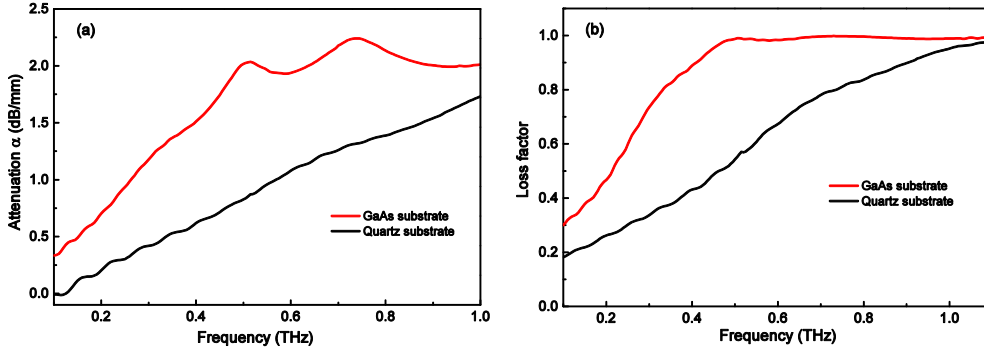
2.23 d.



**Figure 2.24** EM field's distribution above and below the metallisation plane a) EM field at 300 GHz in CPW<sub>GaAs</sub>. b) EM field at 600 GHz in CPW<sub>GaAs</sub>. c) EM field at 600 GHz in CPW<sub>quartz</sub>. d) EM field at 900 GHz in CPW<sub>quartz</sub>.

This dispersive behaviour of CPW can further be investigated by plotting EM field's distribution in both CPW<sub>GaAs</sub> and CPW<sub>quartz</sub> as a function of frequency as shown in Figure 2.24. EM field distribution above and below the metallisation plane in both CPW<sub>GaAs</sub> and CPW<sub>quartz</sub> is uniform (shown in Figure 2.24 a and c) at lower frequencies (at which quasi-TEM mode propagates). However, at higher frequencies ( $> 460$  GHz for GaAs and  $> 800$  GHz for quartz) EM fields leak into the substrate (shown in Figure 2.24 b and d) due to propagation of higher-order lossy modes.

Further, attenuation and loss factor in CPW as a function of frequency was investigated. As discussed earlier, attenuation in CPW occurs due to the  $\alpha_c$ , dielectric  $\alpha_d$  and radiation  $\alpha_r$  losses that can be defined as  $\alpha_{total} = \alpha_c + \alpha_d + \alpha_r$ . In Figure 2.25 a, attenuation constant is plotted as a function of frequency using expression 2-74 ( $\alpha = -\frac{1}{2l} \ln(|S_{11}^2| + |S_{21}^2|)$ ). Attenuation for CPW<sub>quartz</sub> increases linearly with frequency and attains a value of 1.5 dB/mm at 1 THz. CPW<sub>GaAs</sub> exhibits higher attenuation compared to CPW<sub>quartz</sub> and above 0.45 THz attenuation changes dramatically (possibly due to dispersion at higher frequencies).



**Figure 2.25 a) Attenuation in both CPW<sub>GaAs</sub> and CPW<sub>quartz</sub> b) Loss factor in both CPW<sub>GaAs</sub> and CPW<sub>quartz</sub> calculated from S-parameters.**

Another figure of merit is loss factor ( $L.F$ ) which is given by:

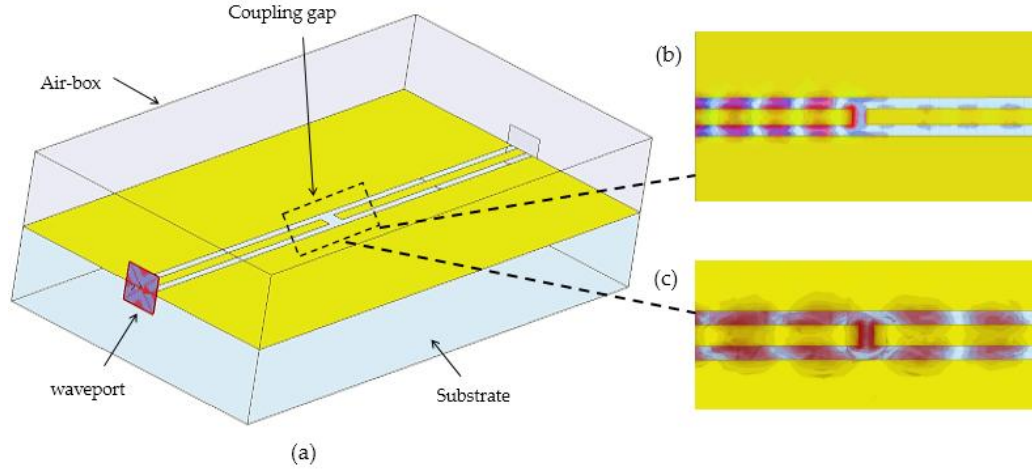
$$L.F = 1 - |S_{11}|^2 - |S_{21}|^2$$

2-77

where,  $|S_{11}|^2$  is reflected power,  $|S_{21}|^2$  is transmitted power and total input power is normalised to "1". In Figure 2.25 b, loss factor for both CPW<sub>GaAs</sub> and CPW<sub>quartz</sub> is plotted as a function of frequency. For CPW<sub>GaAs</sub>, loss factor rises to a value of 0.9 at a frequency above 0.45 THz. For CPW<sub>quartz</sub> loss factor is reasonably low compared to CPW<sub>GaAs</sub> but increases rapidly above 0.60 THz. For low loss CPW, loss factor should be as low as possible.

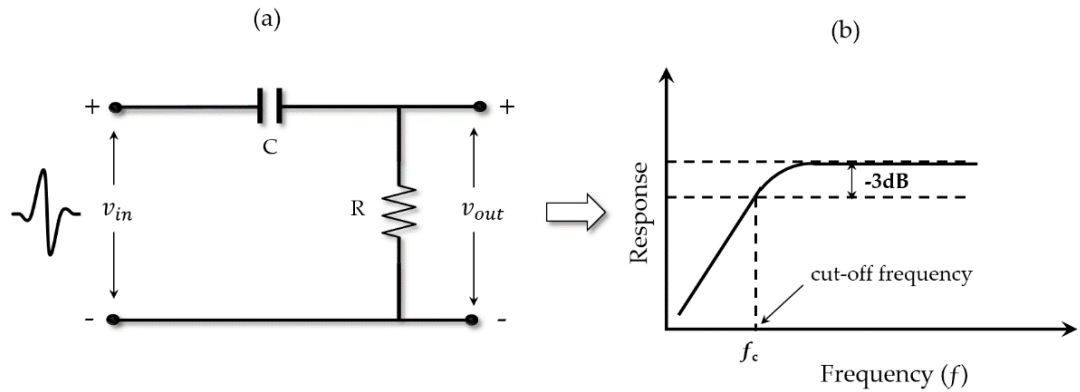
#### 2.5.4 Simulation results (discontinuous CPW)

The steps defining a 3D simulation model for CPW in HFSS were discussed in the Section 2.5.3.1. The only structural difference between conventional CPW and CGAP-CPW is that a coupling gap discontinuity is engineered in the centre conductor trace of CPW. In this work, CGAP-CPW with varying gap length (from 10 to 60  $\mu\text{m}$ ) was simulated. S-parameters are then analysed to observe how the coupling gap with varying length attenuates or couples electromagnetic waves propagating down the transmission line. Due to capacitive nature of coupling gap discontinuity, low-frequency components of EM fields are filtered (or rejected) while high-frequency components are coupled to the other half of the transmission line as shown in Figure 2.26 b and c.



**Figure 2.26 Schematic of 3D simulation model a) CGAP-CPW. b) EM fields at low-frequency c) EM fields at a higher frequency.**

The attenuation at low frequencies in CGAP-CPW can be explained by high-pass filter response of the coupling gap. CGAP-CPW makes a high-pass filter circuit (see Table 2-2) in the transmission line due to line impedance and capacitance (due to the potential difference across the gap, a capacitor formed by the gap – shown in Figure 2.14 b). Response of a high-pass filter is shown in Figure 2.27, where cut-off frequency  $f_c$  represents -3 dB roll off in signal amplitude.



**Figure 2.27 High pass filter a) Circuit diagram. b) The frequency response of high pass filter.**

In Figure 2.27, transfer function of high pass filter can be calculated as:

$$\frac{v_{out}}{v_{in}} = \frac{j\omega C}{1 + j\omega\tau} \quad 2-78$$

Where,  $\tau = RC$  and  $1/\tau = \omega_o$  is cut off frequency in radian/sec. Magnitude and phase of transfer function are given by:

$$|H(\omega)| = \frac{\tau\omega}{\sqrt{1 + \tau^2\omega^2}} = \frac{2\pi fRC}{\sqrt{1 + 4\pi^2 f^2 R^2 C^2}} \quad 2-79$$

$$\angle H(\omega) = \tan^{-1} \left( \frac{\omega_o}{\omega} \right) \quad 2-80$$

In Figure 2.28, transmission loss  $S_{21}$  parameter (often called as insertion loss) is plotted as function of frequency for coupling gap CPWs on both GaAs and quartz substrates.  $S_{21}$  parameter obtained from continuous CPW (on GaAs and quartz) is used as a reference in Figure 2.28. Ripples seen in  $S_{21}$  parameter obtained from CGAP-CPWs can be explained by self-resonating frequency of the coupling gap capacitor. When time-varying EM fields appear across the coupling capacitor, it starts to resonate at a certain frequency. At higher frequency, oscillations (ripples) die out because the coupling gap becomes more resistive and less capacitive (as  $X_c \propto 1/f$ ).

We note that for CPW on GaAs, low-frequency components (below 335 GHz) are suppressed with a maximum coupling loss of -36, -40, -43, -45, -47 and -50 dB for 10, 20, 30, 40, 50 and 60  $\mu\text{m}$  gap lengths respectively. Above 335 GHz, EM fields are coupled through the gap and CGAP-CPW acts as a continuous CPW reasonably. For CPW on quartz substrate, signal attenuation in CGAP-CPWs is observed up to 700 GHz with maximum coupling loss of -42, -45, -48, -51, -54, -56 and -57 dB for 10, 20, 30, 40, 50 and 60  $\mu\text{m}$  gap lengths respectively. Above 700 GHz, a good coupling is observed. However, resonance features were also present with a frequency shift of  $\sim 5$  GHz (from 920 to 945 GHz) with increasing gap length (from 10 to 60  $\mu\text{m}$ ). Features above 1 THz are due to dispersion (excitation of higher-order modes) in the CPW.

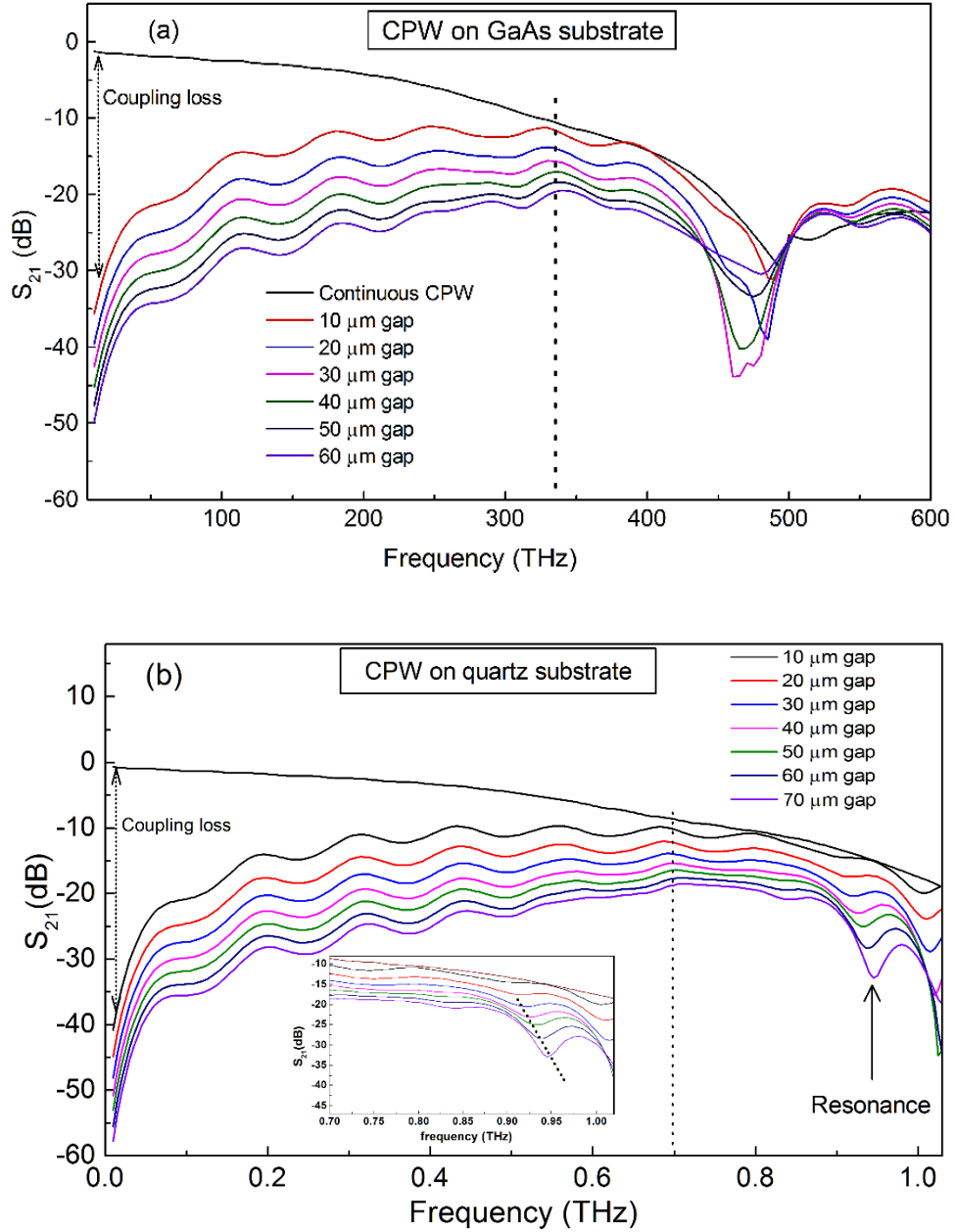
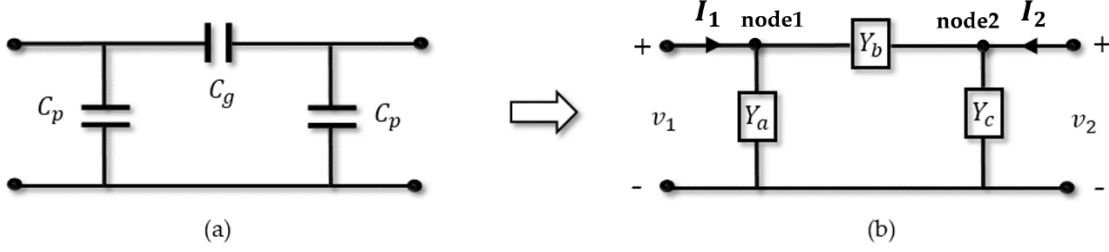


Figure 2.28  $S_{21}$  parameter obtained from HFSS simulation for a) CPW<sub>GaAs</sub> and CGAP-CPW<sub>GaAs</sub> with varying gap length. b) CPW<sub>quartz</sub> and CGAP-CPW<sub>quartz</sub> with varying gap length and a frequency shift in resonance feature at 920 GHz is shown in inset graph.

## 2.6 Series and Shunt Capacitances

Simulation results obtained from HFSS can further be exploited in order to extract lumped elements of an equivalent circuit model representing a coupling gap

discontinuity. A capacitive pi-circuit model can be represented by Y-parameters as shown in Figure 2.29. By solving Y-parameter matrix, values of series and shunt capacitances can be calculated in terms of Y-parameters.



**Figure 2.29 a) A capacitive pi-circuit model of coupling gap discontinuity. b) An equivalent pi-model represented in terms of Y-parameters.**

Applying KCL at node1 current  $I_1$  can be obtained as:

$$I_1 = V_1 Y_a + (V_1 - V_2) Y_b = (Y_a + Y_b) V_1 - Y_b V_2 \quad 2-81$$

Applying KCL at node2 current  $I_2$  can be obtained as:

$$I_2 = V_2 Y_c + (V_2 - V_1) Y_b = -Y_b V_1 + (Y_b + Y_c) V_2 \quad 2-82$$

Using Equations 2-81 and 2-82, a matrix of admittance parameter (Y) is obtained as:

$$[Y] = \begin{bmatrix} Y_{11} & Y_{12} \\ Y_{21} & Y_{22} \end{bmatrix} = \begin{bmatrix} Y_a + Y_b & -Y_b \\ -Y_b & Y_b + Y_c \end{bmatrix} \quad 2-83$$

Values of series ( $C_g$ ) and shunt capacitances ( $C_p$ ) can be derived from Equation 2-83 as:

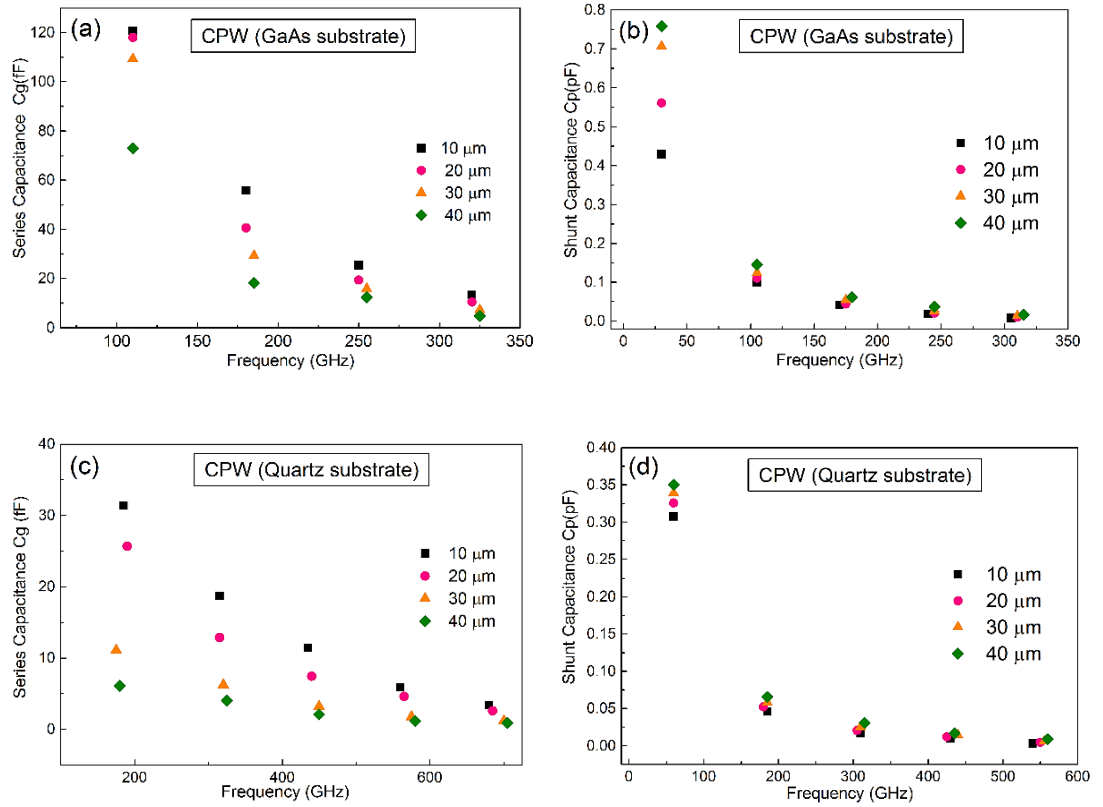
$$C_g = -\frac{\text{Im}g(Y_{21})}{2\pi f} \quad 2-84$$

$$C_p = \frac{\text{Im}g(Y_{11} + Y_{21})}{2\pi f} \quad 2-85$$

Where,  $Y_{21} = -Y_b$  and  $Y_{11} + Y_{21} = Y_a = Y_c$

In Figure 2.30, calculated series and shunt capacitances are plotted as a function of frequency.





**Figure 2.30** Capacitance of CGAP-CPW plotted a function of frequency a) Series capacitance (GaAs substrate). b) Shunt capacitance (GaAs substrate). c) Series capacitance (quartz substrate). d) Shunt capacitance (quartz substrate).

## 2.7 Conclusion

Quasi-TEM parameters ( $Z_0$ ,  $\epsilon_0$ ) for CPW<sub>LT-GaAs</sub> and CPW<sub>quartz</sub> were derived from theoretical modelling. Modelling results showed a higher characteristic impedance for a CPW on the quartz substrate. However, conductor losses in CPW<sub>quartz</sub> were found to be relatively smaller than that of CPW<sub>LT-GaAs</sub> which suggests that THz field will suffer less attenuation on the quartz substrate.

Coupling and shunt capacitances of the CGAP-CPW device were calculated using analytical modelling. Results suggest that coupling capacitance decreases with increasing gap length. Also, series and shunt capacitances reach the almost same value for a coupling gap length of  $\sim 22 \mu\text{m}$ . It was also noted that capacitance's values for CPW on GaAs substrate were relatively higher than that of CPW on quartz substrate.

From the simulations results obtained from HFSS. The bandwidth of CPW<sub>LT-GaAs</sub> and CPW<sub>quartz</sub> were estimated as 0.45 and 1.01 THz respectively.

## Chapter 3

# Conventional and Differential On-Chip THz Systems: Device Design, Fabrication and Measurements

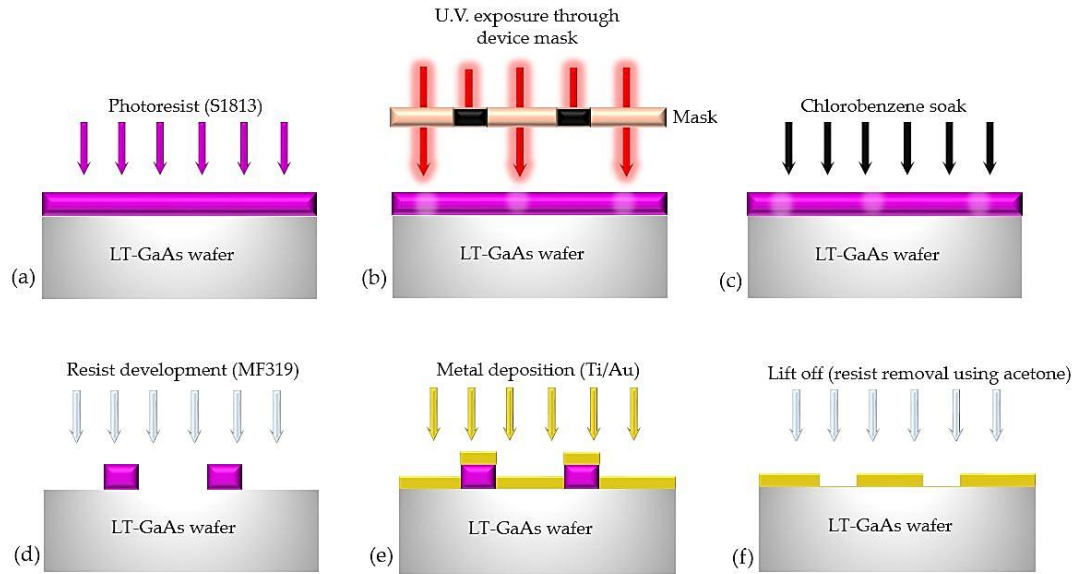
### 3.1 Introduction

In Chapter 2, it was discussed that how two different dielectric substrates (GaAs and quartz) affect the transmission characteristics such as characteristic impedance, signal attenuation and usable bandwidth of a coplanar waveguide. This chapter presents the design, fabrication and testing of on-chip CPWs (continuous and centre gap (CGAP)) on both GaAs and quartz substrates. The fabrication steps, device design and on-chip measurement setup are first discussed. A full characterisation of a first-generation CPW devices overlaid onto GaAs and quartz substrates will then be carried out using an on-chip measurement system.

The high-pass filter characteristics (i.e. rejection of low-frequency components) of CGAP-CPWs with different coupling gap lengths (10, 20, 30 and 40  $\mu\text{m}$ ) are measured using an on-chip three-beam measurement system. Further, a coupling switch modulation or differential measurement technique (a similar technique has been used for thin film characterisation in free space, see Chapter 1) for CGAP-CPW devices which exploits a three-beam on-chip measurement system to measure differential picosecond pulses will also be discussed.

### 3.2 Fabrication of the first generation CPW device on LT-GaAs substrate

After analysing electromagnetic simulation results of CPW obtained from HFSS tool, a photo-mask for a first generation of THz CPW devices was first designed in AutoCAD tool, and CPW devices were then fabricated in a cleanroom.



**Figure 3.1 Fabrication steps for first generation CPW on a LT-GaAs substrate a) Deposition of photoresist. b) UV exposure through photo-mask. c) A chlorobenzene soak process. d) Resist development process e) Metal (Ti/Au) deposition process f) A lift-off process.**

For CPW device fabrication, an LT-GaAs wafer (Leeds MBE wafer no. L849) consisting of a 2- $\mu\text{m}$ -thick LT-GaAs layer on the top of a 400 nm AlAs layer (itself grown by MBE on a 500- $\mu\text{m}$  thick SI-GaAs at  $\sim 200^\circ\text{C}$ ) was used. The LT-GaAs wafer was first cleaved into 6 mm  $\times$  6 mm pieces followed by an annealing ex-situ at  $575^\circ\text{C}$  ( $575^\circ\text{C}$  was chosen being an optimised annealing recipe to achieve short carrier lifetime and high resistivity- see Section 3.4.1) for 15 minutes. The wafer was then cleaned in an acetone bath using ultra sonication for 5 minutes, and IPA for 3 minutes, and DI- $\text{H}_2\text{O}$  for 2 minutes before being blow-dried under a flow of  $\text{N}_2$ . After the cleaning process was complete, a photoresist (Shipley S1813) was spun-on at 5000 rpm for 30 seconds, followed by a hot plate bake at  $115^\circ\text{C}$  for 3 minutes in order to obtain a 1.2- $\mu\text{m}$ -thick

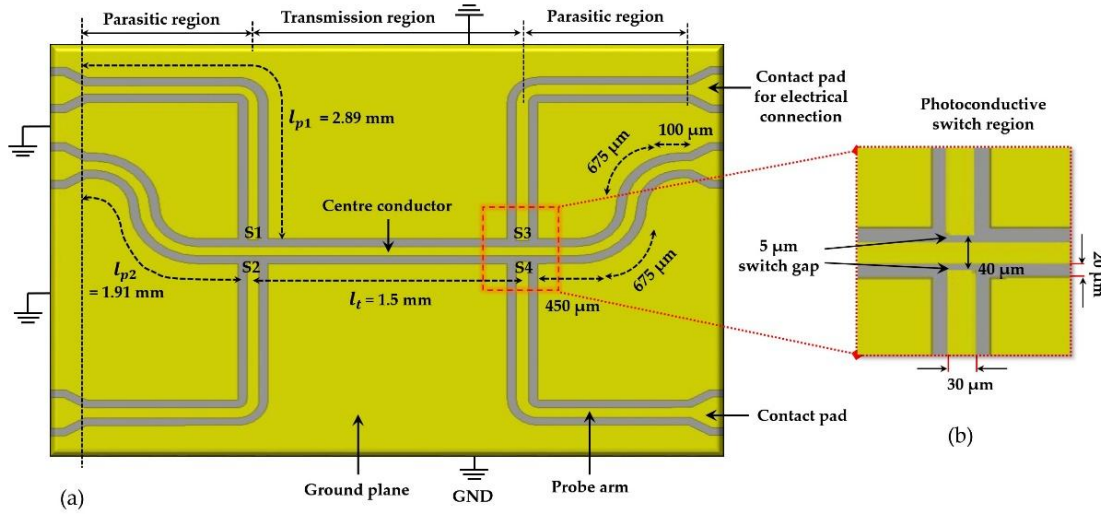
resist layer (shown in Figure 3.1 a). The sample covered with baked photoresist was then exposed to UV light through the CPW photo-mask (shown in Figure 3.1 b) for 7 seconds at a UV-intensity of  $3.7 \text{ mW/cm}^2$ , then soaked in chlorobenzene soak in order to define lithographic pattern. Soaking the sample in chlorobenzene for 2 minutes made the resist harder inducing an undercut to improve subsequent lift-off. After the chlorobenzene soak, the photoresist was developed by immersion in a solution of a MF-319 developer for  $\sim 70$  seconds (with mild agitation), followed by a rinse in DI- $\text{H}_2\text{O}$  in a separate beaker to stop further development and blow dried under an  $\text{N}_2$  flow. Once the lithographic pattern was defined on the sample, oxygen plasma ashing (50 watts, 70 sec) was used to remove any organic impurities left behind. After CPW lithography, the sample underwent a metallisation process in which  $\sim 150 \text{ nm}$  of gold (Au) was deposited on the top of a 20-nm-thick titanium (Ti) layer (titanium layer provides good adhesion to the gold layer [137]). The sample was then left overnight in acetone to achieve a good lift-off (removing metal from unwanted regions). The fabricated CPW devices were then mounted on a PCB (designed in AutoCAD and processed in the cleanroom, see Section 3.3.1) followed by wire-bonding between device's contacts and PCB's copper tracks for electrical connection allowing on-chip THz measurements as discussed later.

### 3.3 First generation CPW device design

In the first-generation device design, a 1.5 mm long coplanar waveguide was engineered along with the parasitic region consists of probing/biasing arms as shown in Figure 3.2 a. The probing/biasing arms can be used to provide DC bias and make a connection to the PC switch in order to probe the THz pulse. The CPW transmission region,  $l_t = 1.5 \text{ mm}$  consists of a centre conductor ( $30 \mu\text{m}$  wide) and two ground plane separated by  $20 \mu\text{m}$  slot gap from the centre conductor (CPW with the same dimensions was simulated using HFSS in Chapter 2) as shown in Figure 3.2 a. Parasitic regions (extended regions of CPW with lengths  $l_{p1} = 2.89 \text{ mm}$  and  $l_{p2} = 1.91 \text{ mm}$  at both ends of CPW) consisting of bias/probe arms around the centre conductor make a four photoconductive-switch layout (S1, S2, S3 and S4 as shown in Figure 3.2 a) for the on-chip CPW. A magnified view of the switch region is shown in Figure 3.2 b, where the

probe arms are separated by switch gaps (S2 and S4) each of 5  $\mu\text{m}$  from the centre conductor.

A four-switch layout allows a range of device characteristics to be obtained such as: detection of an “input” pulse (using a pair of switches S1 and S2), detection of an “output” pulse (using a pair of switches S1 and S3, or S2 and S4), detection of odd modes (quasi-TEM) signal by simultaneous excitation of a pair of switches S1- S2 by defocused pump beam and subsequent detection of the odd-mode signal either at S3 or S4. In a first-generation of CPW device design, the THz pulse generated either from the switch, S1 or S2 travels a length of  $l_t = 1.5 \text{ mm}$  in a time  $\Delta t$ , before being detected at the switch S3 or S4 (depending on the biasing and probing circuitry). The velocity of the pulse arriving at the detection switch (S3 or S4) can then be calculated as,  $V_p = l_t / \Delta t$ . Once the velocity of the pulse is known, the origins of reflections appearing in the input and output pulses can also be determined. Such reflections may be produced from any discontinuities located in the parasitic regions, for example.



**Figure 3.2 Photoconductive switch layout with dimensions. b) A magnified view of the photoconductive switch region.**

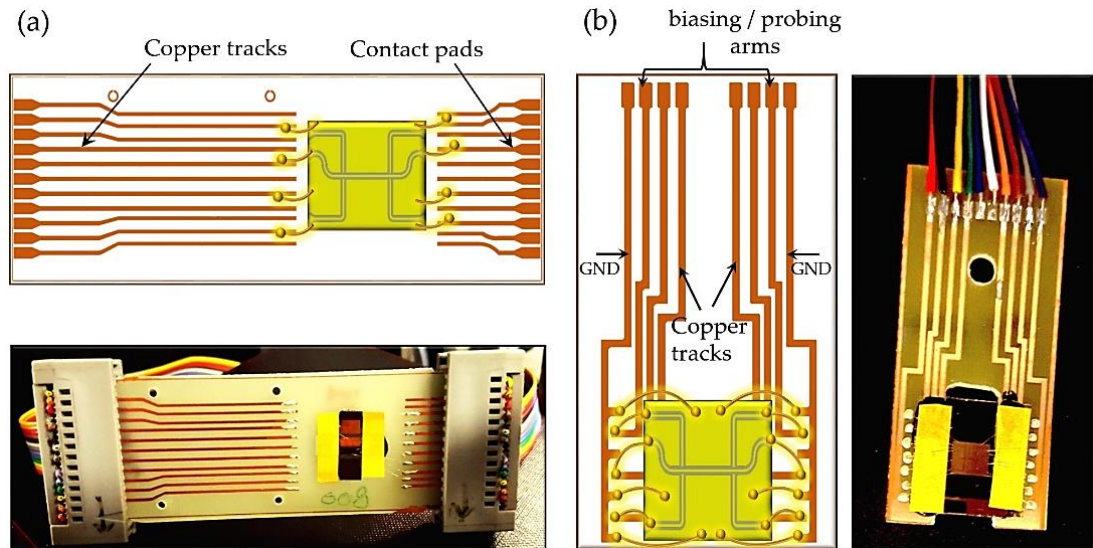
In order to obtain spectral features of a THz pulse over a wide range of frequencies ( $> 1 \text{ THz}$ ), secondary reflection originating from parasitic regions need to be removed from measured THz pulse trace. Therefore, parasitic regions can play a vital role in improving on-chip system performance. By employing extended parasitic regions at both ends of the transmission line in an on-chip system and carefully choosing

design parameters such as the radius of curvature of bends and length of biasing/probing arms, secondary reflections can significantly be delayed or suppressed yielding much higher frequency resolution.

### 3.3.1 PCB layout

After the fabrication of on-chip CPW devices, each device was mounted onto a PCB for electrical connections and in order to bias the photoconductive switches. In doing so, the contact pads (shown in Figure 3.3) of the CPW device were wire-bonded to the copper tracks of the PCB as shown in Figure 3.3. Initially, a simple PCB layout as shown in Figure 3.3 a, was designed (AutoCAD) and processed in the cleanroom. PCB design was then modified to a more compact PCB design compatible with an Oxford Instruments Microstat's cold finger in order to perform low-temperature on-chip spectroscopy measurements down to 4K (as discussed in Chapter 5).

In a modified PCB design, the outer-most copper tracks were used to ground the ground planes in the CPW while the remaining copper tracks were used to provide electrical connection to biasing/probing arms (shown in Figure 3.3 b).



**Figure 3.3** a) PCB layout compatible for room temperature measurements. b) A portable PCB layout compatible with both room and low-temperature measurements.

### 3.4 On-chip measurements of the first generation CPW device (LT-GaAs substrate)

In this section, we present a characterisation of CPW devices patterned on an LT-GaAs substrate using the on-chip THz measurement system. Generation and detection of the THz field in an on-chip system are quite similar to that of free space THz-TDS system (see Chapter 1) except that THz field is coupled to the guided medium (such as metallic transmission line) engineered in an on-chip system whereas in free space THz-TDS systems the THz field is guided by the parabolic mirrors under a purged environment (to remove water vapour). The working principle of an on-chip THz measurement system is described in the Section 3.4.1.

#### 3.4.1 Experimental setup: Two beams (pump-probe) on-chip system

In Figure 3.4 a, a laser beam driven by a pulsed infrared Ti:Sapphire laser (Tsunami, Spectra-Physics), with a 110 fs pulse width, a centre wavelength of 800 nm and repetition rate of 80 MHz was split into a pump and a probe beam using a 50:50 beam splitter (placed at an angle of 45°).

The average power of the main laser beam was  $\sim 700$  mW, where the total power available to the on-chip THz measurement system was  $\sim 54$  mW (i.e. remaining laser power was used to drive two other measurement systems). In on-chip THz system, laser intensities of pump and probe beams were controlled by placing neutral density filters in the optical path of pump and probe beams as shown in Figure 3.4 a. Neutral density filters were then tuned to give an average output power of 10 mW each in pump and probe beam.

In order to optically align pump and probe beams with respect to the generation and detection photoconductive switches (with dimensions  $5\text{ }\mu\text{m} \times 30\text{ }\mu\text{m}$ , see Figure 3.2 b) respectively, guiding mirrors placed (i.e. mounted on an optical bench) in the optical path were used. By adjusting the orientation of guiding mirror, pump/probe beam was steered and made to propagate along the desired axis.



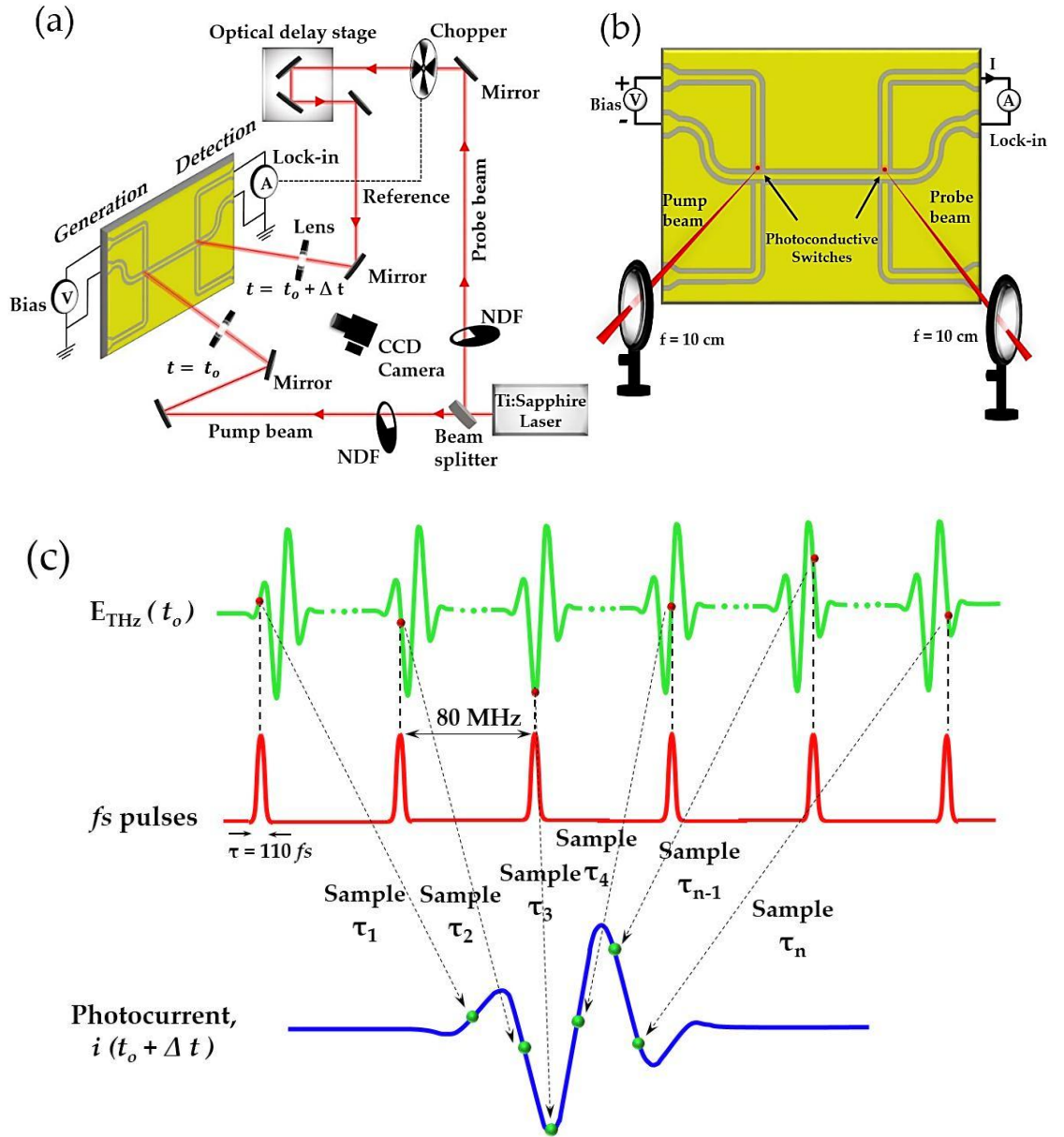


Figure 3.4 a) A schematic of an on-chip THz measurement system consisting of femtosecond laser source, motorised optical delay stage, a 50:50 beam splitter, guiding mirrors for beam alignment, neutral density filters (NDFs) to control laser beam intensity, a pair of lenses ( $f = 10\text{cm}$ ), CCD camera, Keithely source meter for DC bias, a mechanical chopper and lock-in amplifier to measure amplitude and phase of THz pulse. b) A magnified view of pump/probe beam alignment using a pair of lenses. c) An illustration of the THz pulse sampled by the probe beam, where an average THz current pulse is mapped out by collecting sampled data points at discrete time intervals.

The movement of pump and probe beams with respect to switches was monitored using a CCD camera placed in front of the device under test as shown in Figure 3.4 a. In doing so, pump/probe beam was first roughly aligned about

photoconductive switch regions, and Keithley source meter was connected across generation/detection switch to measure photocurrent from the corresponding switch.

Each beam was then tightly focused onto generation/detection switch region using a 10 cm focal length lens as shown in Figure 3.4 b. In doing so, each beam was carefully steered around generation/detection switch using guiding mirrors until a maximum photocurrent was measured by Keithley source meter. Typically, it takes 20 to 30 minutes to get both pump and probe beams well aligned with respect to the device under test in order to perform on-chip measurement.

A motorised optical delay stage (consists of a retro reflector on a linear translation stage) was used to introduce an optical time delay ' $\Delta t$ ' in the probe beam while the pump beam was directly focused onto a DC biased generation switch. The probe beam was optically chopped by a mechanical chopper for lock-in detection (where the chopper frequency was set as a reference to a lock-in amplifier as shown in Figure 3.4 a).

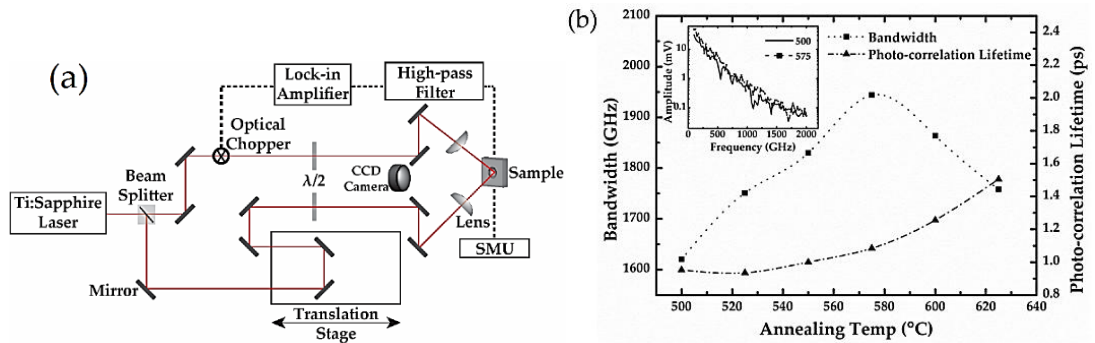
By employing a pump-probe scheme, the generated THz pulse propagating towards the detection switch has an arrival time,  $t = t_0 + \Delta t$ , and it is sampled (at discrete time intervals  $\tau_1 \dots \tau_n$  as shown in Figure 3.4 c) by a time-delayed probe beam at the detection switch. Finally, an averaged THz pulse is mapped out in the time domain (measured by a lock-in amplifier). For higher resolution, more data points can be sampled (or collected) at discrete time intervals by increasing the scan length (after the arrival time,  $t_0 + \Delta t$ ) of optical delay stage. In each set of on-chip measurements, a Keithley source meter, a lock-in amplifier and a motorised delay stage were controlled by a LabVIEW (National Instruments) program through a GBIP interface.

### **3.4.2 Annealing temperature and carrier lifetime of LT-GaAs material**

In photoconductive switching for THz generation-detection, a short carrier lifetime is of critical importance in ensuring that THz pulses are fast enough to accommodate THz-frequency components. Also, for an on-chip THz spectroscopy system, photoconductive switches with high resistivity are desirable in order to suppress any background dark

current, and so that a higher signal-to-noise ratio can be achieved subsequently revealing better spectral signatures of the sample under test. MBE-growth of LT-GaAs at low temperature ( $\sim 200$  °C) substantially decreases the carrier lifetime by creating point defects in the GaAs lattice (see Chapter 1).

A trade-off was then observed between the shortest carrier lifetime and higher resistivity as the number of point defects can substantially be reduced by a post-growth annealing process. Researchers in this research group at the University of Leeds performed post-growth annealing of LT-GaAs at different temperatures followed by autocorrelation measurements in order to see a trend in the carrier lifetime with increasing annealing temperatures [138]. In Figure 3.5 b, bandwidth and carrier lifetime obtained from LT-GaAs photo-mixers are plotted as a function of increasing annealing temperature. A trade-off between higher bandwidth and shortest carrier lifetime was then achieved at an optimum annealing temperature of 575 °C.

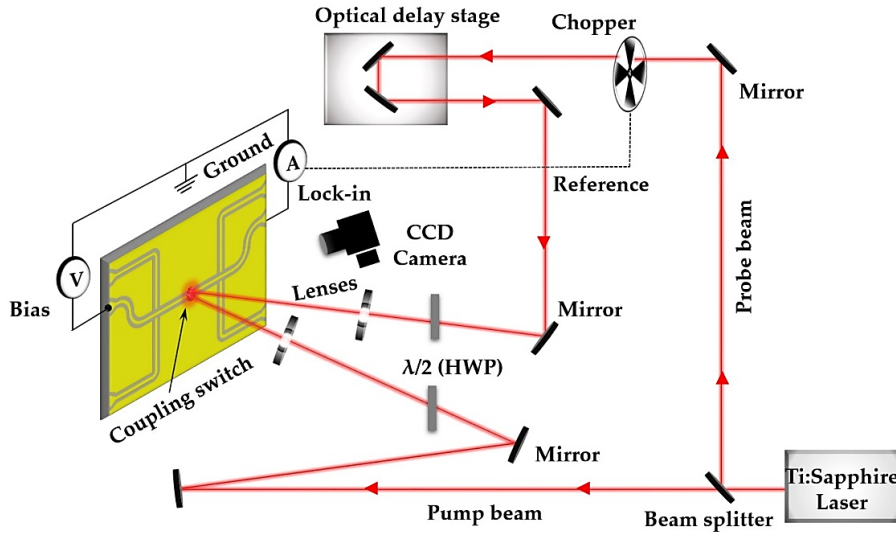


**Figure 3.5 a) An autocorrelation measurement setup. b) Bandwidth and carrier lifetime are plotted as a function of increasing annealing temperature (taken from Ref. [138, 139]).**

In this work, we performed autocorrelation measurements on the LT-GaAs material used in this project, annealed at the optimised temperature of 575 °C in order to measure the carrier lifetime. Calculated value of the carrier lifetime was then used in theoretical modelling of photoconductance of various photoconductive gaps (see Section 3.7).

### 3.4.2.1 Autocorrelation measurement to determine carrier lifetime

Carrier lifetime of LT-GaAs material used in this project was measured by performing an autocorrelation measurement. For these measurements, CGAP-CPW devices with 20  $\mu\text{m}$  coupling switches, simultaneously illuminated by the focused pump and probe beam using an on-chip system were used (shown in Figure 3.6). A lock-in amplifier was connected in series with an applied bias across the coupling switch in order to measure correlated photocurrent. Measurements were then performed by varying the applied bias across the coupling switch. Four consecutive scans were carried out in order to improve the signal-to-noise ratio. The shape of measured correlated photocurrent was found to be dependent on the beam polarisation. Therefore, half-wave plates were used to control any substantial polarisation (parallel and orthogonal).

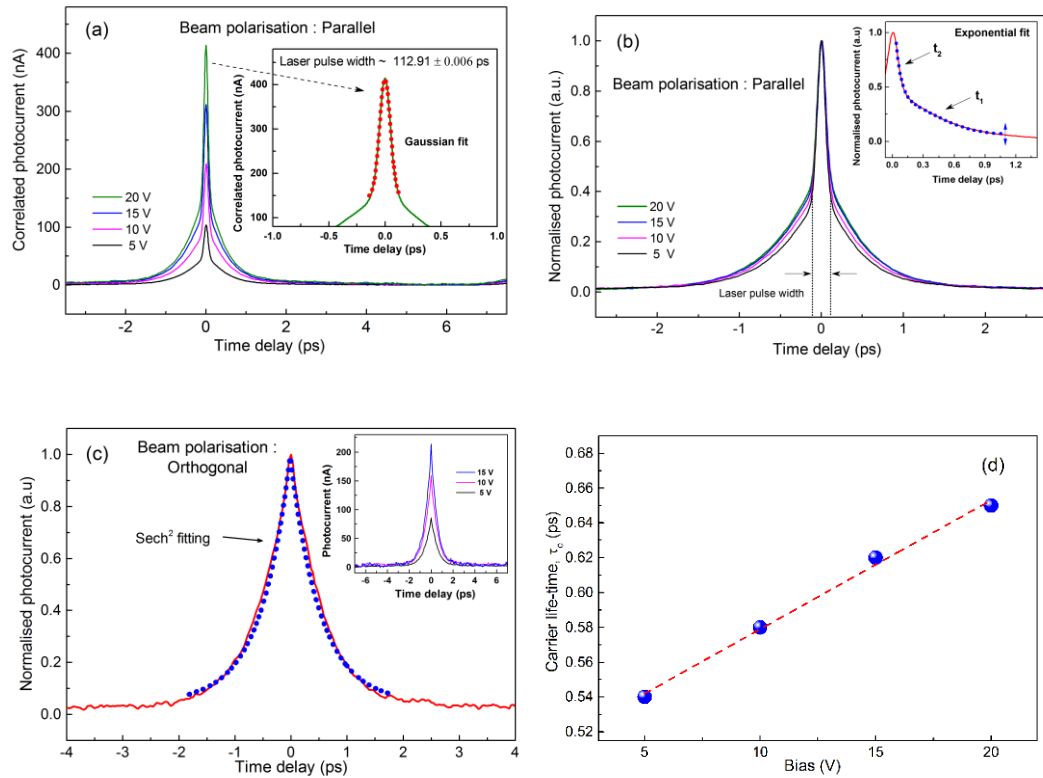


**Figure 3.6 A schematic representation of an on-chip system for autocorrelation measurement.**

For these measurements, CGAP-CPW devices with 20  $\mu\text{m}$  coupling switches, simultaneously illuminated by the focused pump and probe beam using an on-chip system were used (shown in Figure 3.6). A lock-in amplifier was connected in series with an applied bias across the coupling switch in order to measure correlated photocurrent. Measurements were then performed by varying the applied bias across the coupling switch. Four consecutive scans were carried out in order to improve the signal-to-noise ratio. The shape of measured correlated photocurrent was found to be

dependent on the beam polarisation. Therefore, half-wave plates were used to control any substantial change in polarisation (parallel and orthogonal). In autocorrelation measurement, photo-charge carriers generated in the photoconductive gap by illumination of the pump beam create a local charge field which then screens the carriers generated by the probe beam, resulting in an impulse photocurrent [26, 140].

In autocorrelation measurement, photo-charge carriers generated in the photoconductive gap by illumination of the pump beam create a local charge field which then screens the carriers generated by the probe beam, resulting in an impulse photocurrent [26, 140].



**Figure 3.7** a) Correlated photocurrent measured while pump and probe beam were of same polarisation. b) Normalised photocurrent with exponential fit to the falling edge of the pulse shown in inset graph. c) Correlated photocurrent measured while pump and probe beam were of different polarisation (orthogonal). d) Carrier lifetime plotted as function of increasing bias voltage.

In Figure 3.7 a and b, the correlated photocurrent was measured while beam

polarisations were made parallel, revealing a narrow spike on the top of a hump, which was attributed to the coherent interaction of pump and probe beams [141]. This coherence interaction was not seen (Figure 3.7 c) when beam polarisations were made orthogonal to each other using half wave plate. A Gaussian fit to the narrow spike (Figure 3.7 a) revealed a FWHM of  $\sim 113$  fs which agree well with the FWHM of the fs laser pulses used. The correlated photocurrent pulse can be fitted by an exponential decay function such as  $I(t) = A_1 e^{-(t/t_1)} + A_2 e^{-(t/t_2)}$ , however, Deng et al [142] proposed a modified exponential decay function for best fit as :

$$j(t) = \delta e^{-(t/\tau_c)} + (1 - \delta) e^{(t^2 \ln 2 / T_G^2)} \quad 3-1$$

Where,  $\delta$  is a ratio coefficient,  $T_G$  represents FWHM of laser pulse and  $t$  is time.

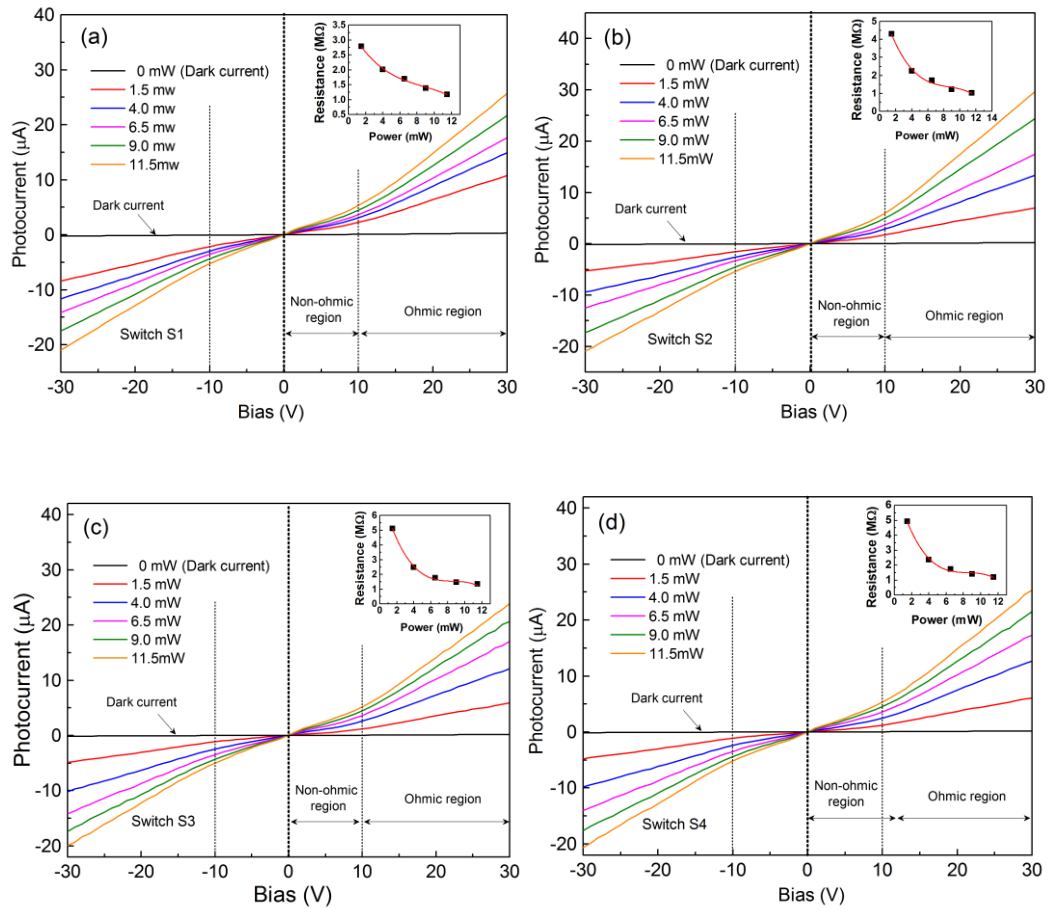
In Figure 3.7 b, the falling edge of the pulse was fitted by using a fitting Equation 3-1. As an alternative to exponential decay fitting, a  $\text{sech}^2$  fitting can be used to fit the correlated photocurrent when the two beam polarisations are orthogonal (i.e. when the narrow spike is absent). A carrier lifetime of 0.65 ps at 20 V bias applied across the photoconductive switch was obtained using  $\tau_c = 2 \ln(2) \tau_{1/2}$ , where  $\tau_{1/2}$  is FWHM obtained from  $\text{sech}^2$  fitting [143]. The measured carrier lifetime was found to be bias dependent as shown in Figure 3.7 d.

### 3.4.3 Characterisation of the first generation CPW device (LT-GaAs substrate)

Full characterisation of CPW devices involved DC measurement of photoconductive switches, and then the generation and detection of picosecond pulses (input and output pulses), extraction of the useful bandwidth present in the picosecond pulse, the bias voltage and power dependence of the picosecond pulses, and excitation of specific modes of propagation such as the quasi-TEM mode (odd mode), as well as calculation of the pulse velocity from on-chip measurements. Firstly, characterisation of photoconductive switches was performed in order to determine the photo-resistance characteristic with varying bias and laser power.

### 3.4.4 Switch Characterisation

IV sweeps for all four photoconductive switches were performed with varying bias and laser power. The bias voltage applied across switches was ramped from -30 V to 30 V in steps of 0.5 V using a Keithley source-meter controlled by a LabVIEW program while recording current. Laser power was then manually changed (using neutral density filters) in each set of measurements. In doing so, a laser beam (with pulse energy larger than GaAs band gap) was aligned (using mirrors) and focused (using a lens) onto the biased photoconductive switch. Laser power was then varied from 1.5 mW to 11.5 mW for each set of measurements.



**Figure 3.8 IV sweep characteristic with varying laser power and bias of all four switches a) S1 b) S2 c) S3 and d) S4.**

In Figure 3.8, IV sweeps showed a relatively ohmic behaviour above 10 V (up to 30 V) bias applied across the switch, with slight non-ohmic behaviour below 10 V. The non-ohmic behaviour is attributed to screening of electrons from the positive anode while the laser spot was close to the anode [23, 144]. Also, the net electric field is

modified by generated photo-charge carriers in the photoconductive gap. The non-linear response can also be attributed to the MIM (metal-insulator-metal) diode-like characteristic of the photoconductive switch at low bias.

The non-ohmic behaviour is attributed to screening of electrons from the positive anode while laser beam spot is close to the anode [23, 144]. Also, the net electric field is modified by generated photo-charge carriers in the photoconductive gap. The non-linear response can also be attributed to the MIM (metal-insulator-metal) diode-like characteristic of the photoconductive switch at low bias. A dark resistance of  $\sim 480 \text{ M}\Omega$  was measured with no illumination. Photoconductive switches S2, S3 and S4, showed a photo resistance of  $\sim 5 \text{ M}\Omega$  at 30 V with 1.5 mW of laser power. S1 showed relatively lower photo-resistance of  $\sim 3 \text{ M}\Omega$ , which may be due to slight variation in one of the processes involved during fabrication (contamination or defect).

### 3.4.5 Input pulse detection

Input pulse detection was carried out by focusing the pump and probe beams onto photoconductive switches S1 and S2 respectively. The photoconductive switches S1 and S2 are separated by the centre conductor only  $30 \text{ }\mu\text{m}$  wide as shown in Figure 3.9. When the switch S1 biased at 30 V was illuminated by the pump laser beam with 10 mW power, the THz pulse so generated was detected at the switch S2, with its probe arms connected to a lock-in amplifier, and by delaying the probe beam with respect to the pump beam using an optical delay stage.

Input pulses detected at the switch S2 are shown in Figure 3.10, for which FWHM (full-width at half maximum) was calculated as  $4.25 \pm 0.03 \text{ ps}$  using a Lorentz fit to the main pulse. Although pulse was detected at the switch, S2 but generated THz pulse keeps travelling further in all possible directions before being reflected back from a discontinuity formed in parasitic regions. In a time-window of 60 ps, three reflections (occurred at 26.13, 33.86 and 40.8 ps) after the main pulse were observed.



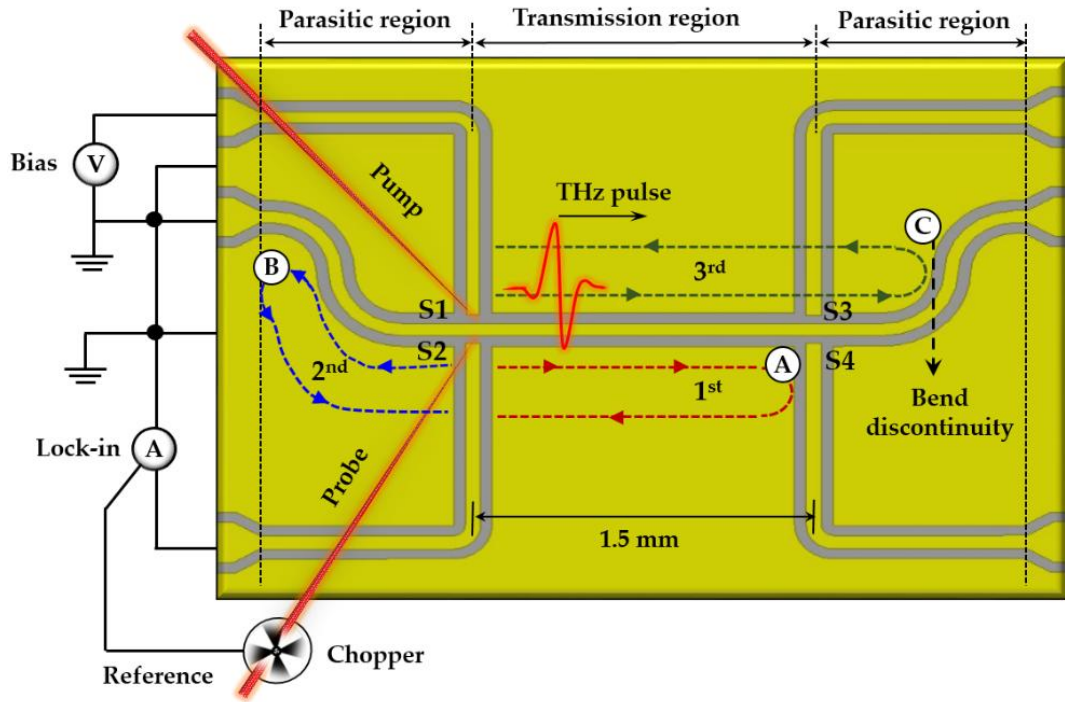
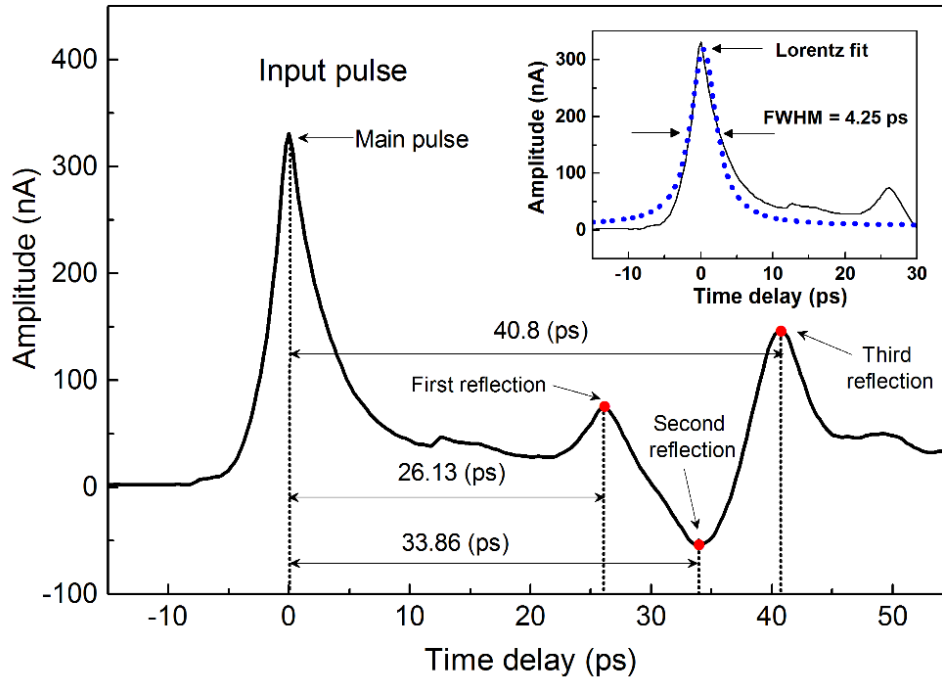


Figure 3.9 Schematic of the input pulses generation/detection in an on-chip CPW device, where the origins of reflections are indicated as A, B and C.

The origins of reflections (as shown in Figure 3.10) was then calculated by multiplying the pulse velocity (see Section 3.4.7) with the time differences relative to the main pulse. In Figure 3.9, the origins of reflections are pointed out as A, B and C, suggesting that first reflection occurred after the main pulse comes from the switch region formed by the gaps at S3 and S4. The first reflection in the input pulse trace is attributed to the higher impedance offered by switches S3 and S4 under dark conditions (as S3 and S4 are not illuminated by the laser beam).

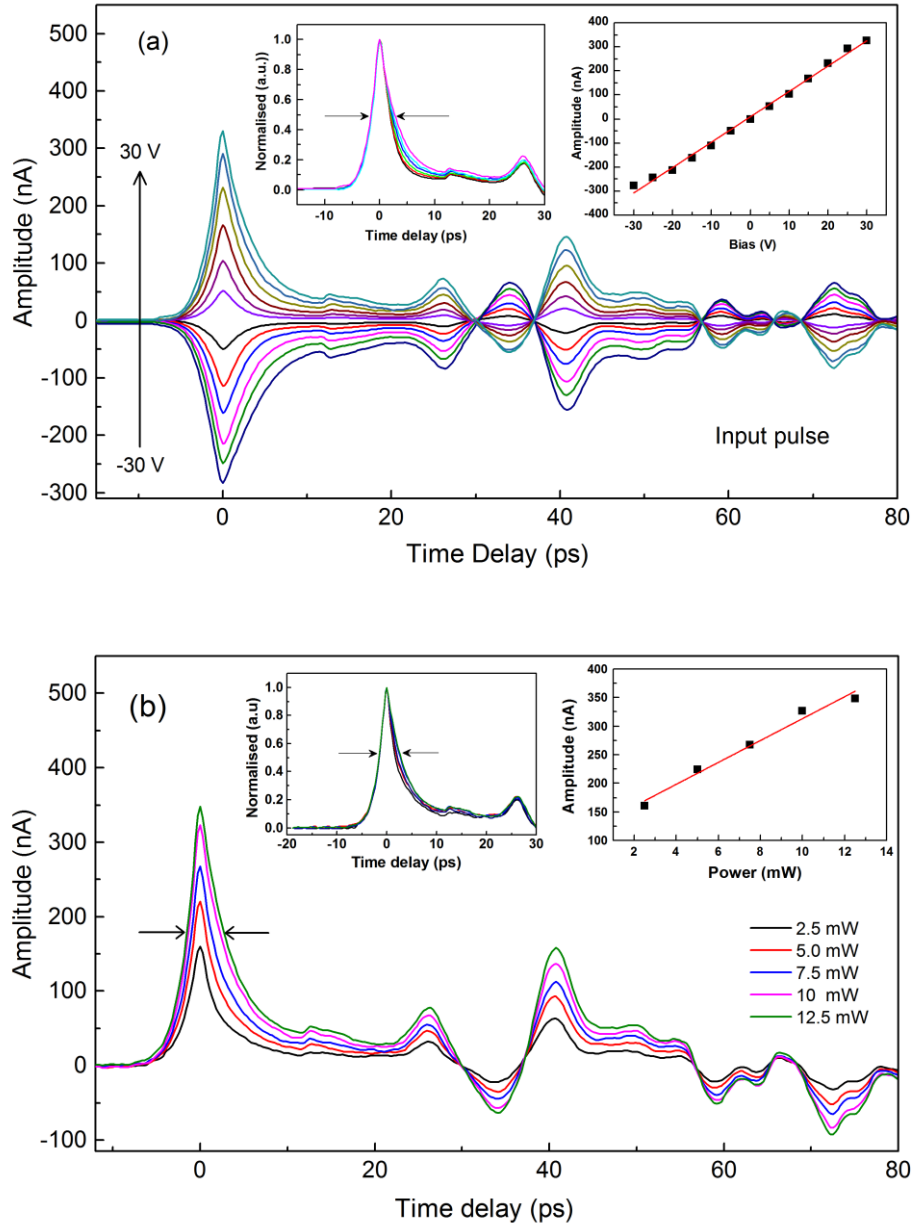
The second reflection occurring in a 60 ps time-window is due to impedance mismatch from the device's contact pad discontinuity (an abrupt change in dimensions) indicated by point B in Figure 3.9. The occurrence of the third reflection is due to a bend discontinuity (at bends, a fraction of THz pulse is reflected back depending on the radius of curvature) pointed out by C in the parasitic region.



**Figure 3.10** Trace of an input THz pulse in a time-window of 60 ps, where reflections are pointed out by red dots and calculated FWHM is shown in the inset graph.

It is also worth mentioning that pulse propagating through a bend discontinuity can experience a slight difference between physical and its actual electrical length of propagation due to the change in pulse velocity (as the THz pulse slows down at bend discontinuities) [145].

To characterise the input THz pulse, the bias across the switch S1 was varied from -30 V to 30 V in 5 V increments while the laser power was fixed at 10mW in each set of measurements. The bias-dependence characteristic of the input pulse is shown in Figure 3.11 a, for which we note a linear dependence on the applied bias (plotting the maximum pulse amplitude at different bias). Interestingly, A slight change in the FWHM, i.e., a broadening of the input pulses with increasing applied bias across the switch. S1 was observed (see inset graph in Figure 3.11 a).



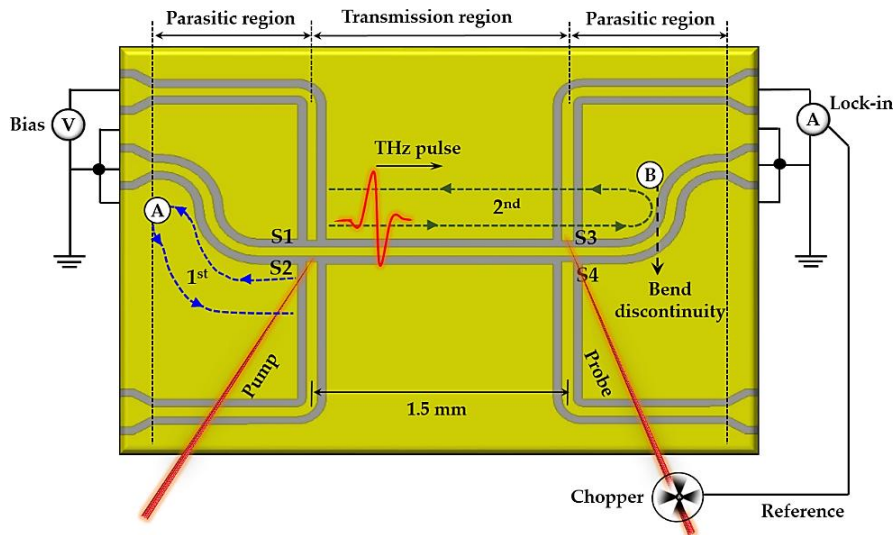
**Figure 3.11** An input THz pulse trace a) As a function of varying bias. b) As a function of varying laser power. Peak amplitude is linear fitted, and FWHM is non-linear curve fitted in the inset graphs.

Only the falling edge of input pulse (which is defined by carrier lifetime or recombination rate of charge carriers - see Chapter 1) was affected by increasing applied bias, and therefore, the change in FWHM (from 3.93 at 5 V to 4.25 at 30 V) is attributed to a change in charge carrier dynamics at higher bias (see Section 3.4.2.1) as the carrier lifetime increases with increasing bias. In Figure 3.11 b, input pulse shows a linear dependence on laser power varying from 2.5 mW to 12.5 mW while the bias voltage was

fixed at 30 V. We also note a slight change in the FWHM (relatively lower than that with increasing bias) of the input pulse (see inset graph in Figure 3.11 b) with varying laser power, which can be attributed to heating of LT-GaAs due to illumination at higher laser power [146]. It is clear from Figure 3.11 that input pulse has a linear dependence on both the laser power and the applied bias across the switch.

### 3.4.6 Output pulse detection

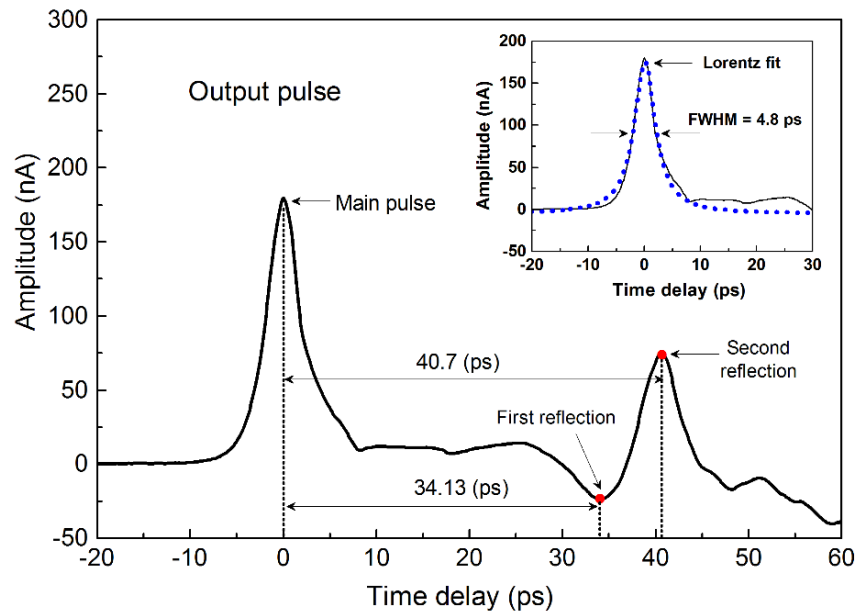
Output pulses were detected by focusing a time-delayed probe beam (synchronised to pump beam) onto the switch S3 while bias was applied across the switch S1 as shown in Figure 3.12. As discussed earlier in the Section 3.4.4, this generated a THz pulse at the switch S1 which travels in both possible directions, and therefore, the output pulse is a result of detection of time-delayed input pulse (travelling from the switch S1 to S3).



**Figure 3.12 Schematic of an output pulse detection in an on-chip CPW device, where origins of reflections are indicated as A and B.**

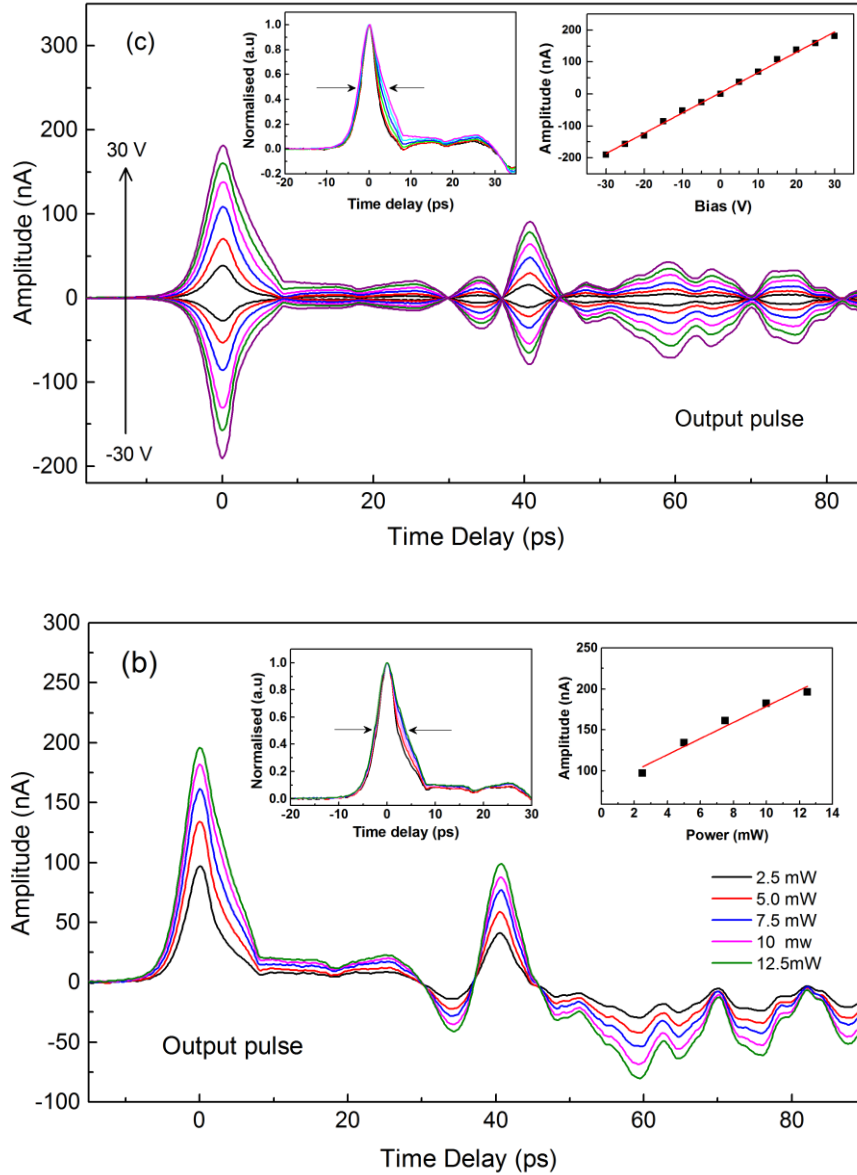
A lock-in amplifier was connected to the probe arms of the switch S3 to measure the amplitude and phase of output pulse arrived at the switch S3. In Figure 3.13, a trace of an output pulse followed by reflections in the time-window of 60 ps is shown. A substantial decrease in pulse amplitude (compared to the input pulse) is attributed to attenuation while the pulse is propagating from the switch S1 to S3 over the length of 1.5 mm. Interestingly, the first reflection that occurred (at 26.13 ps) in the input pulse trace (as shown in Figure 3.10) was substantially reduced (almost disappearing) in the

output pulse trace (Figure 3.13) measured at the switch h S2. Suppression of the first reflection is attributed to simultaneous illumination of photoconductive switches (S1 and S3) situated at both ends of the transmission line (minimise the impedance mismatch) by pump-probe beams. In the 60 ps time-window, only two reflections (pointed out as A and B in Figure 3.12) occurred, at time differences of 34.13 and 40.7 ps relative to the main pulse. However, the origin of these reflections remains the same as those calculated for the input pulse trace, due to the symmetric device design.



**Figure 3.13** Trace of a THz output pulse in a time-window of 60 ps, where reflections are pointed out by red dots and calculated FWHM is shown in inset graph.

A FWHM of  $4.8 \pm 0.02$  ps was calculated by a Lorentz fit to the main pulse detected in the output pulse trace. The increased FWHM (compared to FWHM of input pulse) is attributed to two main reasons: i) the generated THz pulse has a hybrid mode of propagation (combination of quasi-TEM and slot line mode) in which slot-line mode is found to be more dispersive (see Chapter 2), and therefore, the FWHM increases due to dispersion at higher frequencies. ii) Change in the FWHM is also attributed to attenuation losses such as dielectric, conductor and radiation losses added to the THz pulse over the length of propagation.



**Figure 3.14** An output THz pulse trace a) As a function of varying bias. b) As a function of varying laser power. Peak amplitude is fitted by a straight line as a guide to the eye, and the

To investigate the bias dependence characteristics of the output THz pulses, the bias applied across the switch S1 was varied from -30 to 30 V while the pump beam power was fixed at 10 mW and similarly, for power dependence characteristic, bias was fixed at 30 V while pump beam power was varied from 2.5 to 12.5 mW. Similar to the input pulse, the output pulse shows a linear dependence on both the applied bias and power. A slight change in pulse width was also observed at higher biases applied across the switch due to similar reasons as mentioned before.

To investigate the frequency response of the CPW on LT-GaAs substrate, an FFT (Fast-Fourier Transform) was performed on the time-domain output pulses detected at the switch S2. In doing so, the time-domain pulses were first truncated at 30 ps (just before the first reflection) to remove reflections (if not removed, artefacts occurred in the FFT spectra) in the trace of the output pulse and then zero padded to improve the frequency resolution (the actual frequency resolution is limited up to 33 GHz). In Figure 3.15, the FFT spectra showed a useful bandwidth of  $\sim 420$  GHz, in good agreement with the estimated bandwidth of  $\sim 450$  GHz obtained from HFSS simulation results (see Chapter 2).

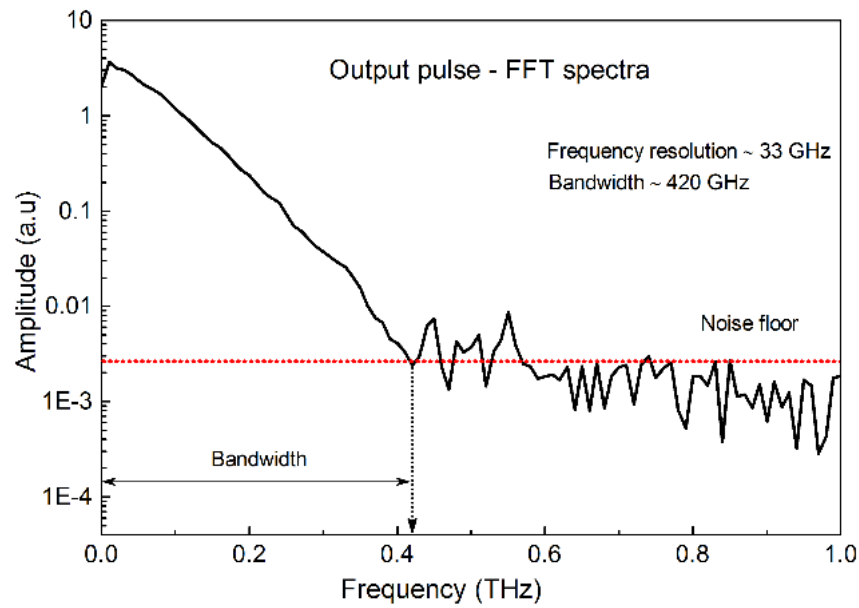
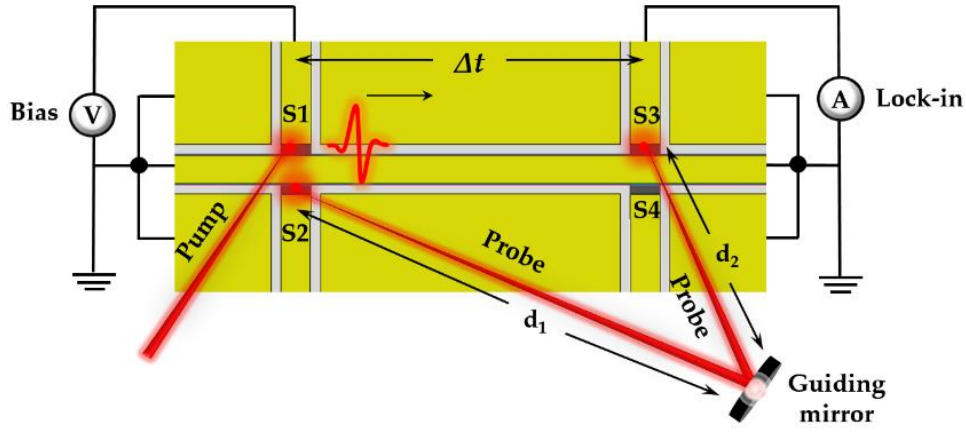


Figure 3.15 FFT spectra of an output pulse detected at switch S2, where the noise floor is indicated by red dotted line to distinguish useful bandwidth present in the signal.

### 3.4.7 THz Pulse velocity (GaAs substrate)

The velocity of generated THz pulse can be determined by knowing the propagation delay of the input pulse (time elapsed in propagation from S1 to S3) when it arrives at the detector switch S3 and the transmission length travelled by pulse, since  $V_p = l_t / \Delta t$ , where  $V_p$  is propagation velocity,  $l_t$  is transmission length and  $\Delta t$  is the propagation delay. However, this method requires the detection of input and output pulses in the same time-window in order to find the propagation delay.





**Figure 3.16 Schematic of input-output pulse detection in the same time-window by moving probe beam between switches S2 and S3.**

An illustration of this method is shown in Figure 3.16, where the probe beam was first focused onto the switch S2 in order to detect an input pulse. The probe beam was then focused onto the switch S3 by moving it from S2 to S3 (using a guiding mirror) in order to detect an output pulse.

In doing so, the probe beam path length is changed from  $d_1$  to  $d_2$ , due to which the total propagation delay  $\Delta t$  becomes  $\Delta t = l_t/V_p + (d_1 - d_2/c)$ , where  $d_1 - d_2$  is path difference, and  $c$  is speed of light in free space [64]. Therefore, calculation of the pulse velocity using this method requires an accurate measurement of beam path lengths and their respective angles in order to determine path differences. Nevertheless, an alternative method which compares two output pulses detected (in two consecutive scans) in the same time-window at the switch S1 and S3 respectively by swapping their electrical bias and probing connections was used as shown in Figure 3.7 a and b. The velocity of pulse was then calculated as:

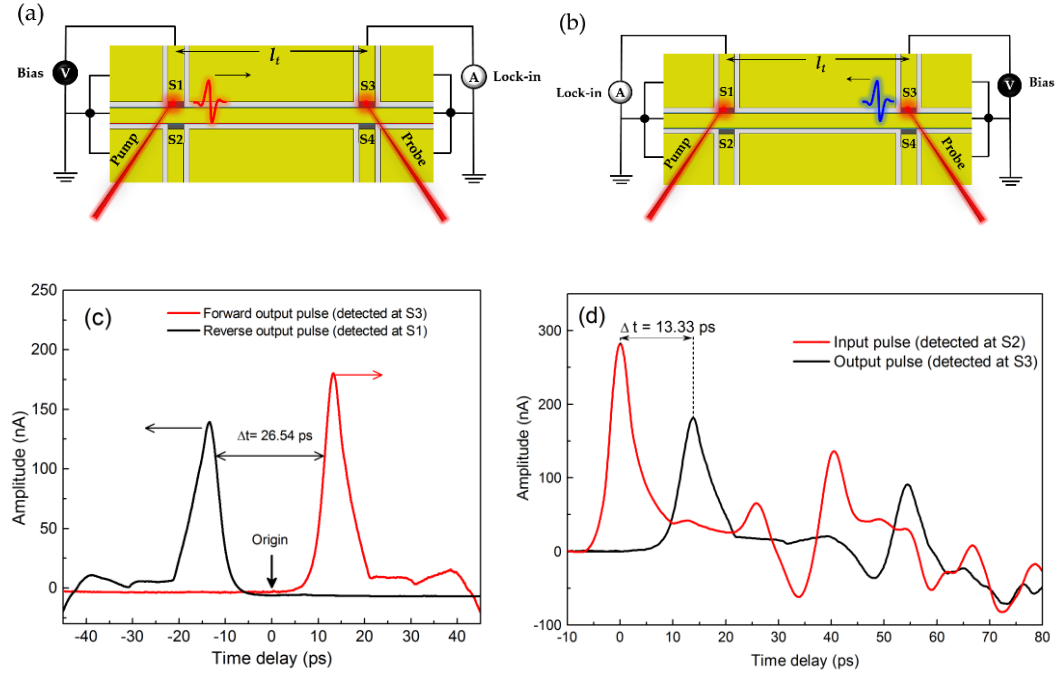
$$V_p = 2l_t/\Delta t_r \quad 3-2$$

Where,  $l_t$  is the transmission length between switches and  $\Delta t_r$  is the relative time difference between detected pulses.

Traces of two output pulses (moving away from zero time delay point, where zero time delay represents the origin of input pulse generation) with a relative time



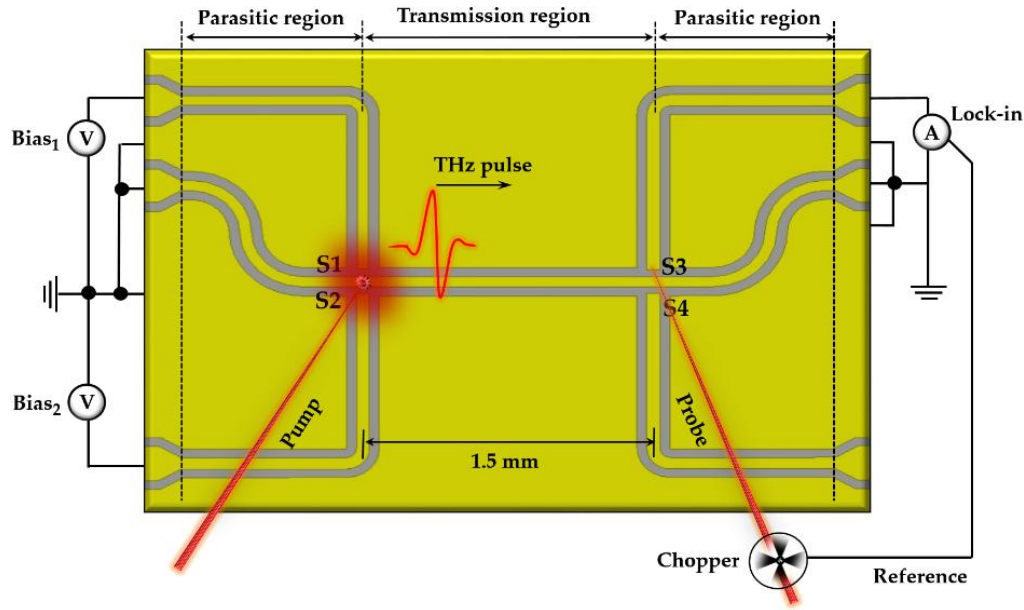
difference of 26.54 ps detected at the switch S1 and S3 respectively are shown in Figure 3.17 c. The velocity of the pulse is then calculated as,  $V_p = 2 \times 1.5/26.54 = 1.13 \times 10^8$  m/s. In Figure 3.17 d, traces showing the input and output pulses with a relative time delay of 13.33 ps were detected in the same time-window.



**Figure 3.17** Forward and reverse detection of output pulses a) Pulse generation-detection at S1 and S3 respectively. b) Pulse generation-detection at S3 and S1 respectively by swapping biasing and probing connections. c) Traces of two output pulses detected in the same time-window. d) Traces of input and out pulses detected in the same time-window.

### 3.4.8 Mode excitations

As discussed earlier, the THz pulse generated propagates with a hybrid mode consisting of odd mode (symmetric field pattern, see Chapter 2) and even mode (anti-symmetric field pattern) modes of propagation in which anti-symmetric even mode (dispersive in nature) causes broadening in the pulse travelling down the transmission line. However, the unwanted even mode can be suppressed by the optical excitation of a pair of generation switches (e.g. switch S1 and S2) by defocusing pump beam (covering both switch regions) and careful bias arrangement (similar technique has previously been demonstrated [94, 147, 148]) as shown in Figure 3.18.



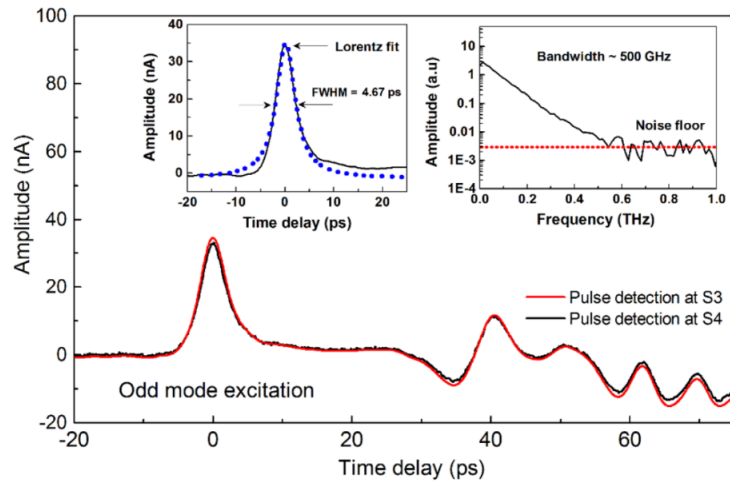
**Figure 3.18** Excitation of the symmetric odd mode by optical excitation of a pair of switches S1 and S2 in which the pump beam is defocused to cover both switch regions.

A symmetric mode (odd mode) can be launched from a pair of generation switches (S1 and S2) by applying an equal bias (with similar polarity, shown in Figure 3.18) across the switch S1 and S2 and simultaneously illuminating both switches by defocused pump beam. In doing so, the even mode is suppressed as both ground planes of CPW are at the same potential while the symmetric mode starts propagating down the transmission line (with field lines extending from the centre conductor to ground planes, see Chapter 2). The symmetric mode is less dispersive in nature as the field is tightly confined in slot gaps of CPW.

Similarly, the “anti-symmetric (even) mode” can be deliberately launched by applying an equal bias with opposite polarity across switches S1 and S2 and the simultaneous illumination of switches by a defocused pump beam. With opposite polarity applied to the switches, the ground planes in CPW are set at different potentials and therefore, an anti-symmetric mode is launched with field lines extending from ground to ground (with few field lines touching the centre conductor, see Chapter 2). The anti-symmetric even mode radiates more power due to its larger field distribution (similar to a slot line) and therefore, suffers greater losses (especially at higher frequencies).

### 3.4.8.1 Coplanar mode (Odd mode)

An example of “symmetric odd mode” excitation (with an equal bias of +30 V applied across the switch S1 and S2 and simultaneous illumination by the pump beam) is shown in Figure 3.18, where an output pulse was first detected at the switch S3 by focusing probe beam onto the switch S3 and then was detected at the switch S4 by focusing probe beam onto the switch S4 (this requires two consecutive scans). The detected output pulses were of similar shape and polarity, which suggest propagation of a symmetric mode (a symmetrical field around the centre conductor) in the CPW. Lorentz fit to “odd mode-output pulse” revealed a FWHM of  $4.67 \pm 0.2$  ps (see inset graph, Figure 3.19) which suggests that pulse broadening was reduced (compared to FWHM of 4.8 ps output pulse with the hybrid mode of propagation, discussed in the Section 1.4.4.2) due to suppression of dispersive “even mode”. An increased bandwidth of  $\sim 500$  GHz was revealed by FFT spectra of the “odd mode-output pulse” suggesting that odd mode is less dispersive.



**Figure 3.19** Detection of an output pulse at switch S3 and S4 (in two consecutive scans) in odd mode excitation. Lorentz fit to main pulse and FFT spectra of output pulse are shown in inset graphs.

### 3.4.8.2 Slot line mode (Even mode)

An even mode pulse was launched by applying an equal bias of -30 V across switches S1 and S2 with simultaneous illumination by defocused pump beam. Two consecutive scans were then performed to detect the “even-mode” output pulse first at the switch

S3 by focusing probe beam onto S3 and then at S4 by focusing probe beam onto the switch S4. Traces of the output pulses were of the same shape, but opposite polarity is showing the propagation of the anti-symmetric mode in CPW.

A Lorentz fit to the main pulse revealed an increased FWHM of  $\sim 5.52 \pm 0.4$  ps indicating pulse broadening relative to that of measured from the odd mode. Also, a substantial reduction in useful bandwidth (from  $\sim 500$  to  $\sim 390$  GHz) was observed from FFT spectra of the even mode-output pulse.

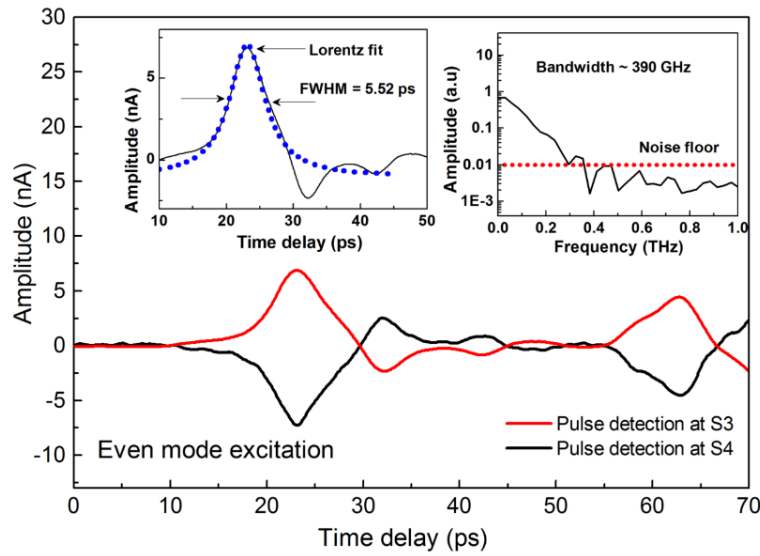


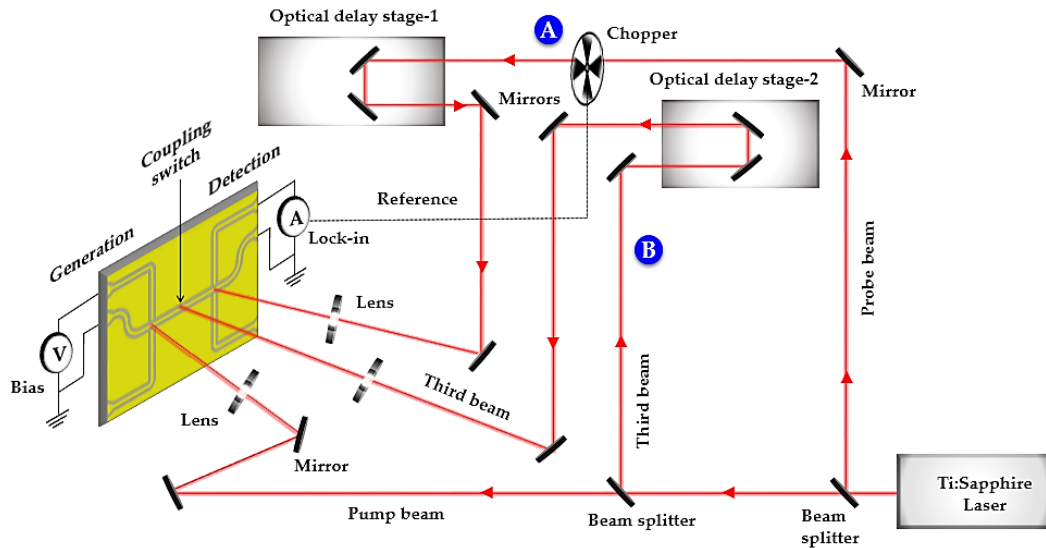
Figure 3.20 Detection of an output pulse at switch S3 and S4 (in two consecutive scans) in even-mode excitation. Lorentz fit to main pulse and FFT spectra of output pulse are shown in inset graphs.

### 3.5 On-chip measurements of the first generation CGAP-CPW device (LT-GaAs substrate)

After characterising a conventional CPW (with no discontinuity present in a centre conductor) device using the two-beam (pump-probe) on-chip system, a CGAP-CPW (with a gap discontinuity introduced in the centre conductor) device was measured using a three-beam (pump-pump-probe) on-chip system. The working principle of the three beam system is similar to that of the two-beam system except a third beam is added (split off from the pump beam), where the third beam is used to modulate the

conductivity of a coupling switch (a lithographically defined switch in the centre conductor of a conventional CPW) by changing the carrier concentration while a THz pulse passes through the discontinuity region before being detected at the detector switch. The addition of the third beam to an existing system allows us to manipulate THz pulse (such as Gaussian to mono cycle pulse and vice-versa) by controlling the third beam optical power using an ND filter. Also, this will allow us to perform ultra-fast switching in which coupling switch goes through a series of on/off transition states by modulating the conductivity of LT-GaAs (underneath coupling switch region).

### 3.5.1 Experimental setup: Three-beam on-chip system



**Figure 3.21 Schematic of the three-beams on-chip system, where the third beam split from pump beam is used to illuminate coupling switch. A and B indicates the position of the mechanical chopper while performing conventional and differential pulse measurements respectively.**

A three-beam system was realised by splitting the existing pump (using a beam splitter) beam into two independent beams each able to illuminate a photoconductive switch. The path length of the third beam was controlled by the addition of a motorised optical delay stage (referred to as delay stage 2, shown in Figure 3.21) in order to synchronise the third beam with the existing pump-probe system. The third beam guided by a mirror was then focused onto the coupling switch in order to perform three-beam on-chip measurements.

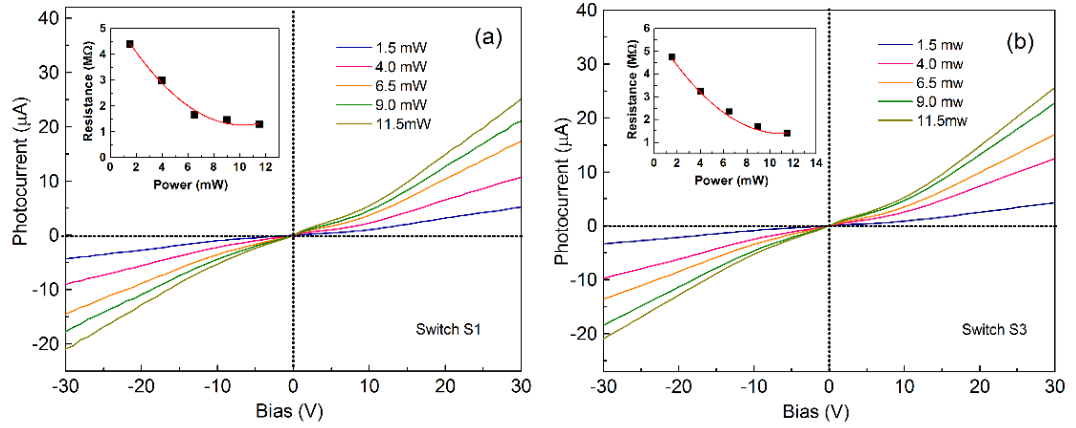
Throughout the three-beam measurements, the mechanical chopper was moved from position A to B (as indicated by blue circles) depending on the experiment being performed. Chopper position A is referred to as conventional two/three beam measurements, where the probe beam is chopped at a frequency used as a reference to the lock-in amplifier, in order to map-out THz pulse arriving at the detector switch. Chopper position B is referred to as a differential pulse (or modulated pulse) measurement, where the third beam, illuminating coupling switch is chopped in order to generate a differential signal  $S_{\text{on}} - S_{\text{off}}$ , directly measured by a lock-in amplifier. Therefore, chopper positions (A and B) play a vital role in distinguishing conventional two/three beam measurements from differential (modulated) pulse measurement.

### **3.5.2 Characterisation of the first generation CGAP-CPW (LT-GaAs substrate)**

Initially, a CGAP-CPW device (with  $20\mu\text{m}$  gap discontinuity) was measured using the three-beam on-chip system in order to test any substantial change in THz pulse characteristics while propagating along a discontinuous CPW. In doing so, input and output THz pulses were measured with and without third beam in operation. Further, odd and even mode excitations were tested in order to investigate mode propagation in the discontinuous system.

### **3.5.3 Switch Characterisation**

Firstly, IV sweep measurements of photoconductive switches S1 and S3 (used as generation and detection switch) were performed by varying applied bias across switches and by then varying laser power intensities (controlled by an ND filter) in each set of measurements. IV sweeps of the switch S1 revealed a photo-resistance of  $4.5\text{ M}\Omega$  at 30 V bias applied across the switch with the laser power fixed at 1.5 mW. IV sweeps of the switch S2 was similar to S1, with a slight increase in photo-resistance (from 4.5 to  $4.8\text{ M}\Omega$ ) at 30 V and 1.5 mW laser power. The value of the photo-resistance was reduced to  $1.5\text{ M}\Omega$  as the laser power was increased from 1.5 to 11.5 mW as shown in inset graphs, Figure 3.22. A similar non-ohmic behaviour up to 10 V bias (as discussed in Section 3.4.4) was observed from IV sweep curves.

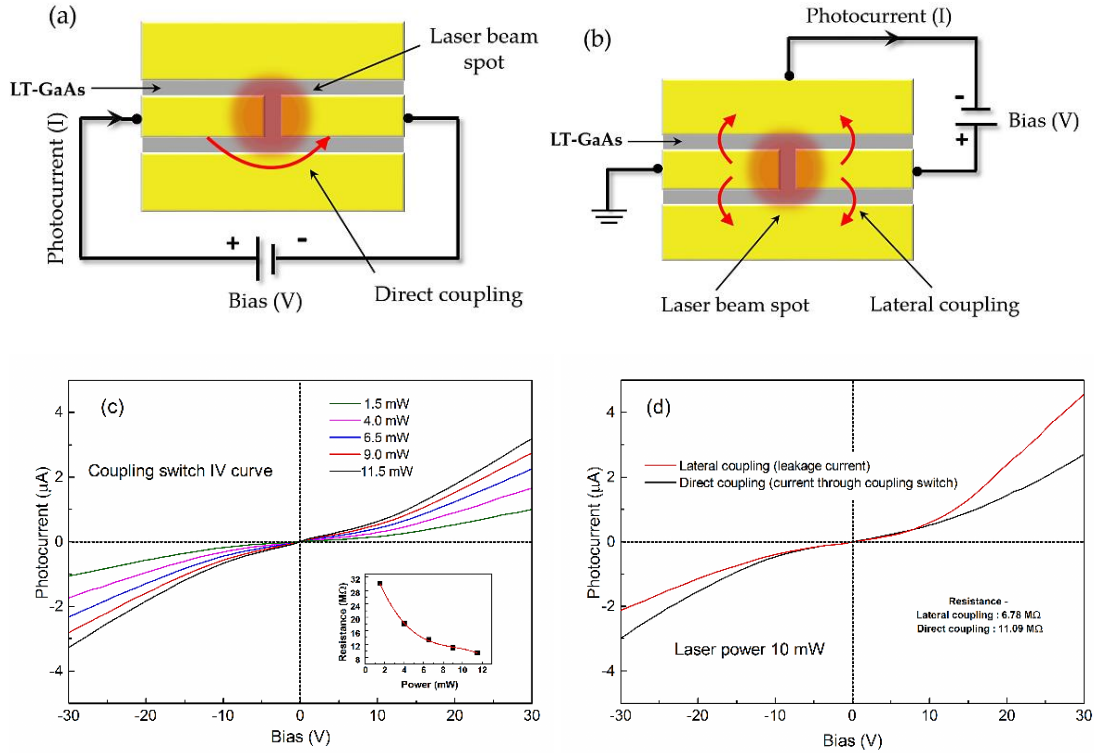


**Figure 3.22** IV characteristics of photoconductive switches a) S1. b) S3.

After characterising photoconductive switches S1 and S3, IV sweep measurements of the coupling switch were performed using a similar method (varying bias and laser power). IV sweep of the coupling switch showed a relatively higher photo-resistance of  $\sim 11 \text{ M}\Omega$  at 30 V bias applied across the centre conductor of the CPW (see Figure 3.23 a and c) at 1.5 mW laser power. The high photo-resistance is attributed to the large aperture ( $20 \times 30 \text{ }\mu\text{m}$ ) of the photoconductive switch formed by  $20 \text{ }\mu\text{m}$  gap discontinuity.

It is clear from Figure 3.23 that IV characteristic of the coupling switch is similar to that of obtained from the switch S1 and S3 except a higher value of photo-resistance obtained for same laser beam power, and bias applied. To further study the characteristics of the coupling switch, bias arrangements were made as shown in Figure 3.23 a and b, in which bias was applied across a centre conductor (with  $20 \text{ }\mu\text{m}$  gap) while illuminating the coupling switch with the third beam in operation, (referred as direct coupling). Bias was then applied across the centre conductor and ground plane as shown in Figure 3.23 b while the third beam was in operation; this is referred to as lateral coupling.

Interestingly, IV sweeps showed a higher photo-current in lateral coupling (indicating a greater coupling) compared to photo-current measured from direct coupling (indicating a weaker direct coupling) as shown in Figure 3.23 d.



**Figure 3.23 Coupling switch IV and slot gap leakage current. a) Schematic representation of photocurrent measurement while the coupling gap is illuminated by the laser beam. b) Measurement of leakage photocurrent due to later coupling between the centre conductor and ground planes. c) Coupling switch IV curves. d) A comparison of photocurrents due to direct and lateral coupling.**

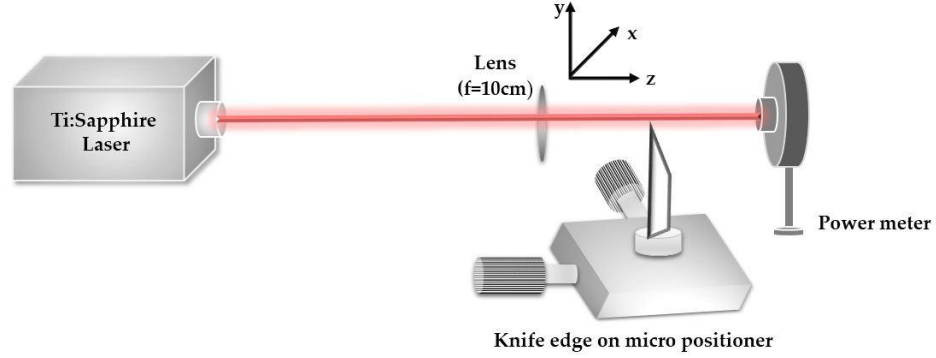
A greater coupling between the centre conductor and the ground plane is attributed to the formation of a photoconductive gap (due to overlaid CPW pattern onto 2  $\mu m$  thick LT-GaAs layer ) between the centre conductor and the ground plane (separated by 20  $\mu m$  –shown in Figure 3.23) along the length of CPW. A higher lateral coupling also indicates that spot size ‘W’ of the third beam in operation is larger than the aperture of the coupling switch and therefore, can excite photo-charge carriers in the photoconductive gap between the centre conductor and the ground plane. To further investigate this, a knife-edge experiment was performed to measure the spot size of the laser beam (W). Knife edge experiment is discussed in the following section.

### 3.5.4 Knife edge experiment to determine the spot size

The focused spot size ‘W’ of the laser beam was measured using a surgical scalpel blade mounted on an XYZ manual translation stage. In doing so, a power metre was placed



behind the knife-edge (as shown in Figure 3.24) in order to measure any substantial change in beam power and lens (focal length of 10 cm) was used to focus the beam over a distance of 10 cm. The beam profile was then measured by moving the scalpel knife (in steps of 0.1 mm), and the beam power was measured as a function of the knife. Edge position.

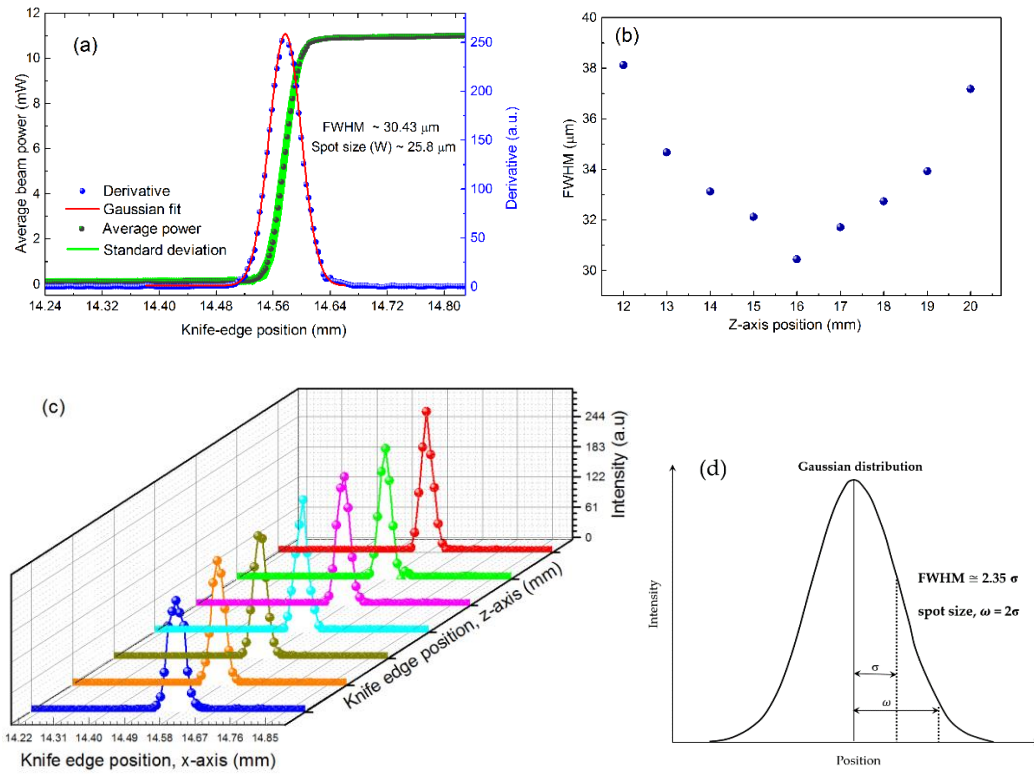


**Figure 3.24 Knife-edge experiment: a surgical scalpel blade mounted on an XYZ manual translation stage.**

The measurement was repeated for several distances, and the measured beam power was plotted as a function of knife edge position as shown in Figure 3.25 a. A Gaussian beam profile (defined by Gauss error function [149]) was then obtained from the first derivative of the measured average beam power. Finally, a Gaussian fit to first derivative yields the beam radius by extracting the half width at  $1/e^2$  of the peak value (shown in Figure 3.25 a).

A Gaussian error function  $P(x) = \frac{P_0}{2} \left\{ 1 \pm \operatorname{erf} \left[ \frac{\sqrt{2}(x-x_0)}{w_x} \right] \right\}$  can be used to fit the first derivative obtained from average beam power, where  $\operatorname{erf}$  is the error function,  $P_0$  is measured power,  $w_x$  is  $1/e^2$  radius of the Gaussian beam, and  $x_0$  is the offset in the centre coordinate [149]. In Figure 3.25 c, the first derivatives (indicating beam intensities at different positions in the Z-axis) of the average power measured as a function of knife edge position in X-axis while incrementing the position of the XYZ stage in z-axis in each set of measurements. It is clear from the graph that the Gaussian beam profile and intensity changes (increases) as the knife edge reaches to the point where beam spot size is smallest (or beam waist is narrowest). Gaussian fit to the first derivative revealed a FWHM of  $\sim 30.43 \mu\text{m}$  and spot size was then calculated as  $W = 2\sigma = \sim 25.8 \mu\text{m}$  (as shown

in Figure 3.25 a and d).

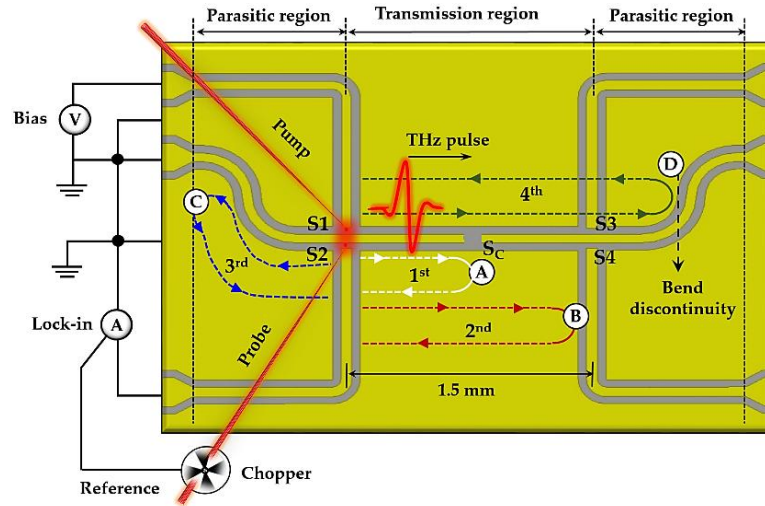


**Figure 3.25** Laser beam spot size measurement. a) Average beam power measured and its first derivative plotted as a function of knife edge position in X-axis b) FWHM of Gaussian beam profile plotted as a function of knife edge position in z-axis c) Intensity of Gaussian beam by taking the first derivative of average power plotted as function of knife edge in x and z-axes d) An example of beam spot size calculation for the FWHM of the Gaussian profile.

The beam-spot size calculated from knife-edge experiment suggests that photo-charge carriers can be excited in the photoconductive gap formed between the centre conductor and ground plane while the coupling switch is illuminated by the third beam. The lateral coupling can be avoided by placing an LT-GaAs layer underneath the photoconductive regions and then removing (by selective etching using a chemical etch process) the unwanted regions (where the photoconductive switch pattern is not overlaid).

### 3.5.5 Input pulse detection

Input pulse detection in the CGAP-CPW devices was performed by focusing the pump and probe beams (without the third beam) on to switches S1 and S2 respectively. A bias of 30 V was then applied across the switch. S1, and probing circuitry was connected to the lock-in amplifier in order to measure the probed THz pulse as shown in Figure 3.26.

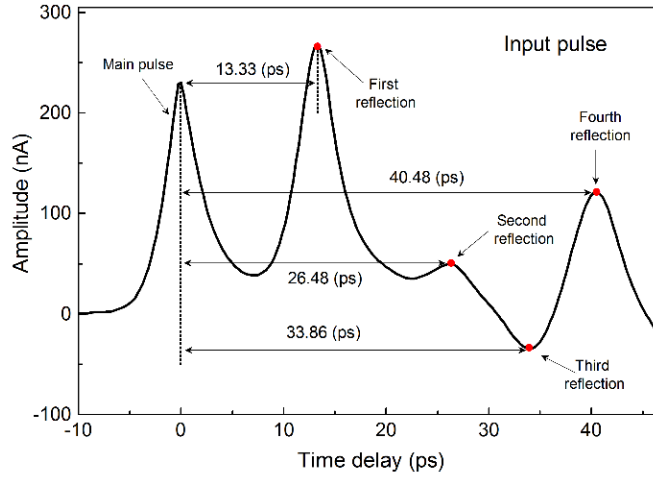


**Figure 3.26** A schematic showing generation-detection of an input pulse in a CGAP-CPW device.

An input THz pulse was then mapped out by the delaying probe beam using an optical delay stage. Traces of the input pulse showed a reflection with much larger amplitude (compared to secondary reflections- shown in Figure 3.27) which can be attributed to the coupling gap discontinuity introduced in the centre conductor of CPW.

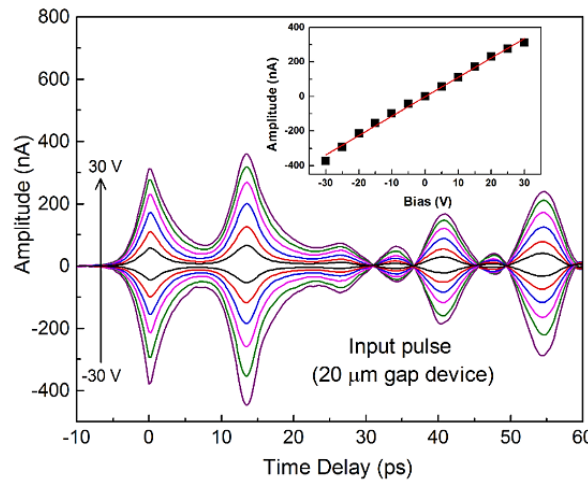
It is worth mentioning that main pulse and first reflection in the input pulse are in the same phase which is due to reflection of the input pulse from an open-ended discontinuity (this situation is similar to the 'no load' condition of the transmission line, where the signal reflects back with the same phase and a reflection coefficient of  $\Gamma=1$ , see Chapter 2). Also, the baseline of the input pulse trace was somewhat increased, which is attributed to constructive interference between generated THz pulse at the switch S1 and the reflected pulse travelling back in the opposite direction. Reflections occurring at 26.48, 33.86 and 40.48 ps delay after the main pulse (pointed out as B, C and D in Figure 3.26) come from the same discontinuities which were discussed in Section

3.4.5. The FWHM of input pulse was not calculated as fitting to the main pulse was not feasible.



**Figure 3.27** A trace of an input pulse, where the main pulse followed by three reflections is shown in a 50 ps time-window.

Traces of the input pulse taken by varying bias applied across switch S1 showed a linear dependence on the bias as shown in Figure 3.28.



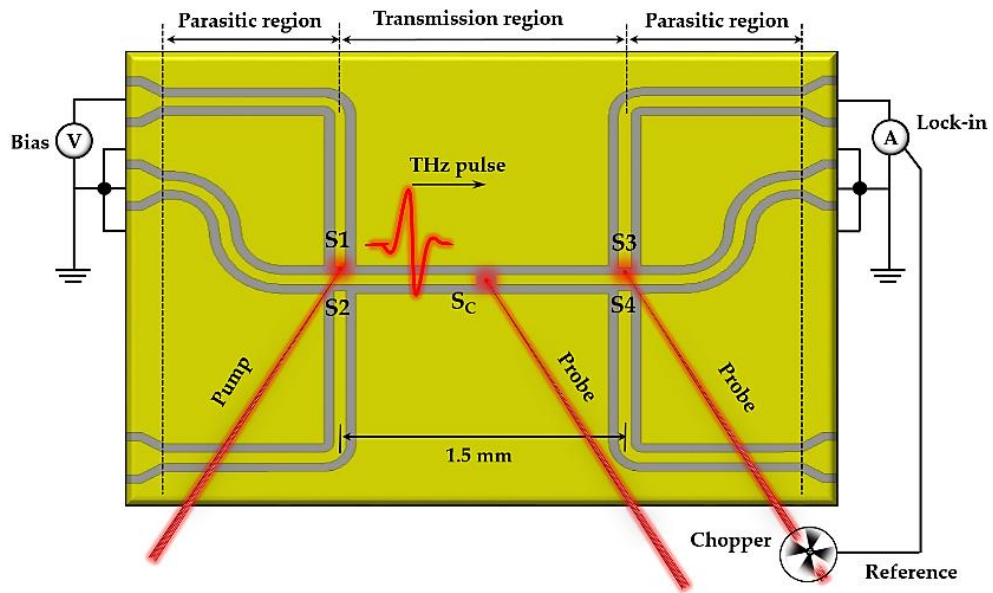
**Figure 3.28** Multiple traces of an input pulse taken by varying bias applied across switch S1, where a linear dependence is obtained by fit to the pulse amplitudes.

### 3.5.6 Output pulse detection

Output pulse detection CGAP-CPW was carried out by focusing the pump and probe beams onto switches S1 and S3 respectively, with a bias applied across the switch S1 as shown in Figure 3.29. The probe arms of the switch S3 were connected to a lock-in

amplifier. Traces of output pulses were taken with and without third beam in operation (to illuminate the coupling switch). There was no substantial change in amplitude observed when multiple traces of output pulse were taken as shown in inset graph, Figure 3.30. This can be attributed to a lateral coupling between the centre conductor and ground planes of CPW.

Therefore, removal of LT-GaAs from unwanted regions is found to be necessary in order to see any significant change due to third beam illumination onto the coupling switch. A Lorentz fit to the main output pulse trace revealed a FWHM of  $\sim 5.36 \pm 0.01$  ps indicating a pulse broadening. Interestingly, the FWHM of the output pulse is very close to the FWHM of  $\sim 5.52$  calculated for the output pulse in even-mode excitation in conventional CPW, which further suggests propagation of an anti-symmetric field (avoiding the centre conductor) along the CPW.



**Figure 3.29** Output pulse detection in a CGAP-CPW device, where third beam (not chopped) is focused onto coupling switch.

The output pulse could only consist of even mode field components because odd mode excitation (symmetric field) is mainly supported by the centre conductor while odd mode fields can propagate along ground-to-ground.

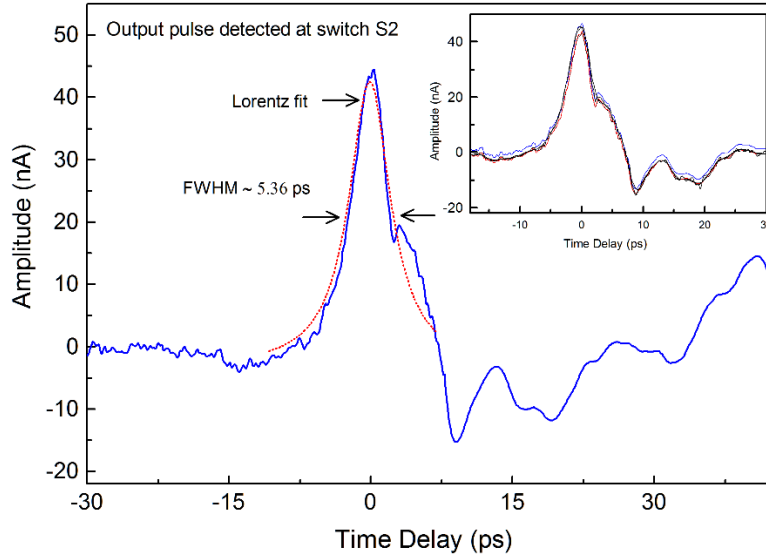


Figure 3.30 A trace of an output pulse detected at photoconductive switch S2 and multiple traces shown in inset graph, taken while coupling switch is illuminated by the third beam.

### 3.5.7 Mode excitation

Odd and even modes were excited in CGAP-CPW in order to investigate any substantial change in pulse amplitude while the coupling switch was illuminated by a third beam (synchronised with the other two beams).

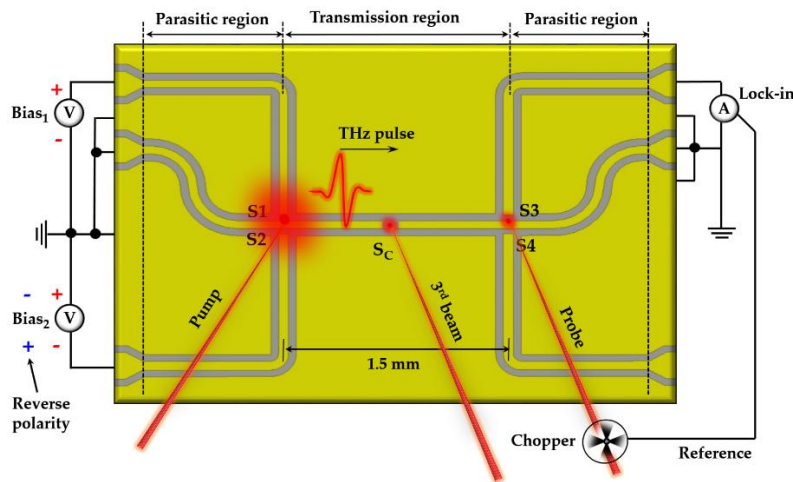
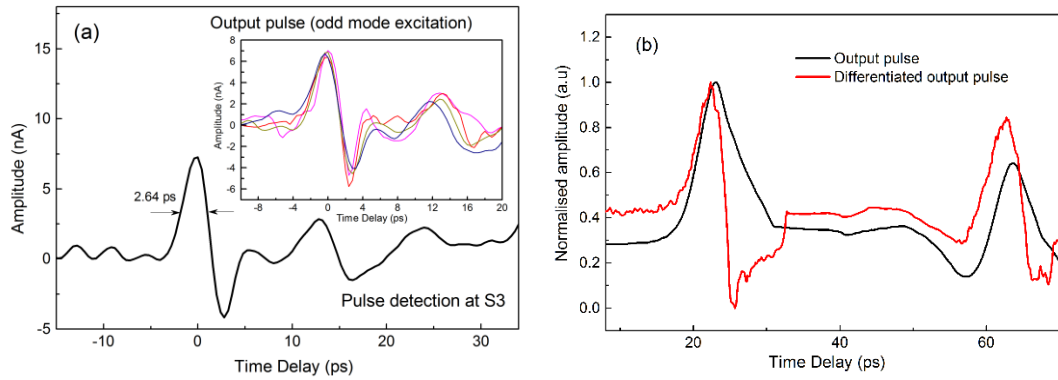


Figure 3.31 A schematic representation of odd/even mode excitation in a CGAP-CPW device by a defocusing pump in order to excite a pair of switches (S1 and S2) while the coupling switch is illuminated by the third beam.

### 3.5.7.1 Co-planar mode (Odd mode)

An “odd mode” was excited in a CGAP-CPW device by illuminating photoconductive regions S1 and S2 by a defocused pump beam while an equal bias voltage of the same polarity was applied across the switch S1 and S2 (shown in Figure 3.31). Odd mode signals launched from S1-S2 were detected by illuminating the focused probe beam on to switch S3. A substantial change in the shape of the detected output pulses was observed. A change in the shape of the output pulse is attributed to the high-pass filter characteristic of the coupling switch (see Chapter 2). One of the characteristics of HPF (high-pass filter pass filter) is to suppress low-frequency components and allowing high-frequency components above its cut-off frequency (often called as “-3 dB” frequency) in the frequency domain.

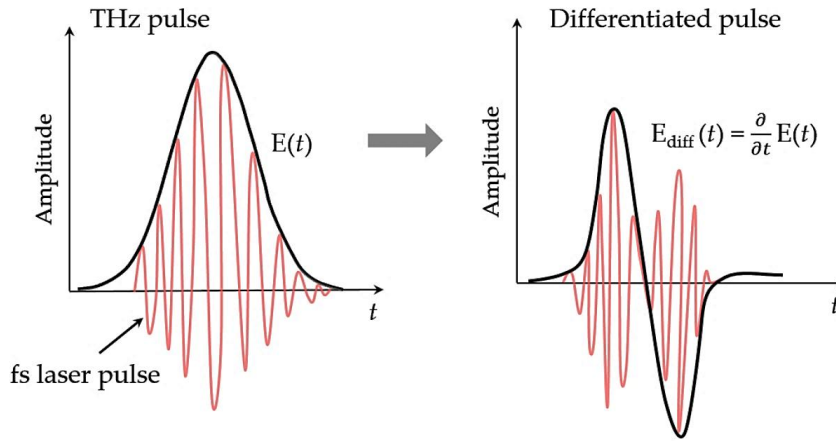


**Figure 3.32 a) An odd mode excited output pulse detected at switch S3 and multiple scans of odd mode pulse taken while coupling switch was illuminated by the third beam are shown in inset graph. b) An output THz pulse and its first derivative plotted as a function of time delay.**

However, in the time-domain, a HPF effectively performs the first-order derivative on a signal passing through it. Therefore, in a CGAP-CPW device, a first-order derivative of the odd mode pulse propagating along CPW is obtained. First-order derivatives performed on THz pulse by HPF (Gaussian in nature) changes its shape to a monocycle pulse [150-152]. To further investigate it, an output pulse is plotted with its first derivative (performed numerically), indicating a monocycle pulse kind of shape formation as shown in Figure 3.32 b. An illustration of conversion of a Gaussian pulse



into a monocycle pulse (by performing differentiation) is shown in Figure 3.33.



**Figure 3.33 An illustration of conversion of a Gaussian THz pulse into monocycle pulse by performing differentiation operation.**

In “odd mode” excitation, symmetric field propagates along CPW with fields extending from the centre conductor to ground planes ensuring most of the THz field is passing through the centre conductor. Therefore, odd mode-output pulse is substantially affected by HPF characteristic of coupling discontinuity.

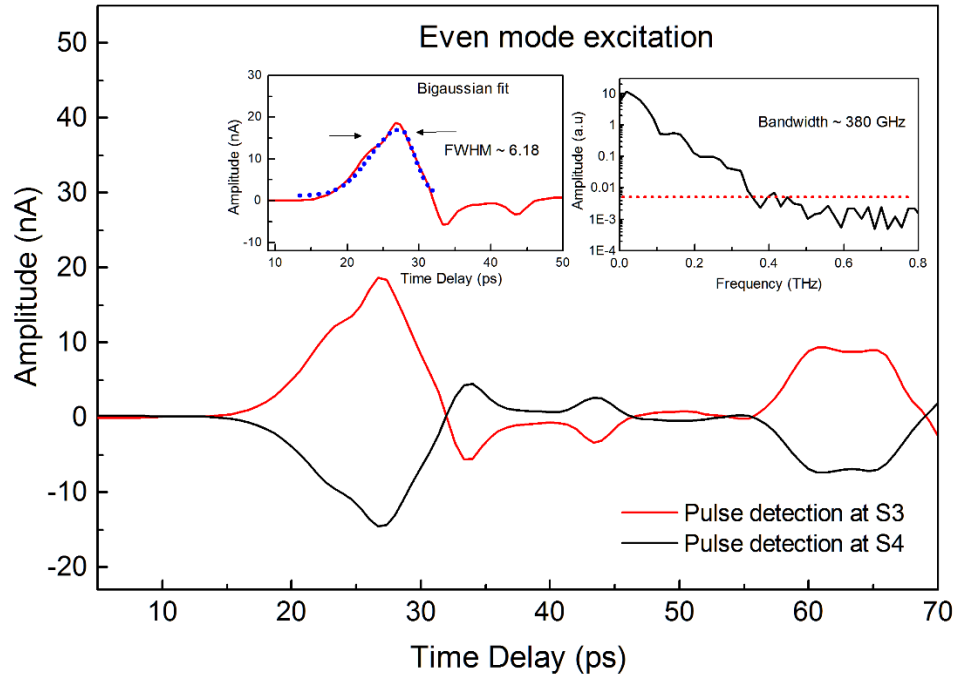
By illuminating a coupling switch using a focused third beam should allow us to effectively tune the R and C value of HPF by changing the carrier concentration of the LT-GaAs underneath (and hence changing switch impedance and capacitance). However, CGAP-CPW devices on LT-GaAs substrate suffer from lateral coupling, and therefore, no substantial change was observed in the odd mode pulse.

### 3.5.7.2 Slot-line mode (Even mode)

The “even mode” was launched in a CGAP-CPW by reversing the polarity of the bias of 20 V applied across the switch S2 so that the ground planes remain at a different potential. Switches S1 and S2 were illuminated by a defocused pump beam in order to excite both photoconductive switch regions (S1 and S2) as shown in Figure 3.31. Switch S3 was then illuminated by the probe beam in order to detect THz pulse launched by even-mode excitation. Probe beams were then focused on to switch S4 to detect an “even mode-output pulse” in the following scan. Traces of output pulse detected at the switch S3 and S4 were of opposite polarity suggesting an anti-symmetric



mode of propagation along the CPW.



**Figure 3.34** Traces of an output pulse measured at S3 and S4 respectively by exciting an even mode at switch S1 and S2, FFT spectra and Bigaussian fit to main are shown in inset graph.

Also, a trace of the output pulse is similar to that of the conventional CPW in Section 1.4.4.4.2. A Bi-Gaussian fit (Gaussian fit was not feasible) to the main pulse revealed a FWHM of  $\sim 6.18 \pm 0.2$  ps (shown in Figure 3.34) suggesting further broadening in pulse width, owing to higher radiation losses produced by gap discontinuity at higher frequencies [67]. FFT spectra revealed a reduced bandwidth of  $\sim 380$  GHz (see inset graph, Figure 3.34) indicating that dispersion had increased in CGAP-CPW device.

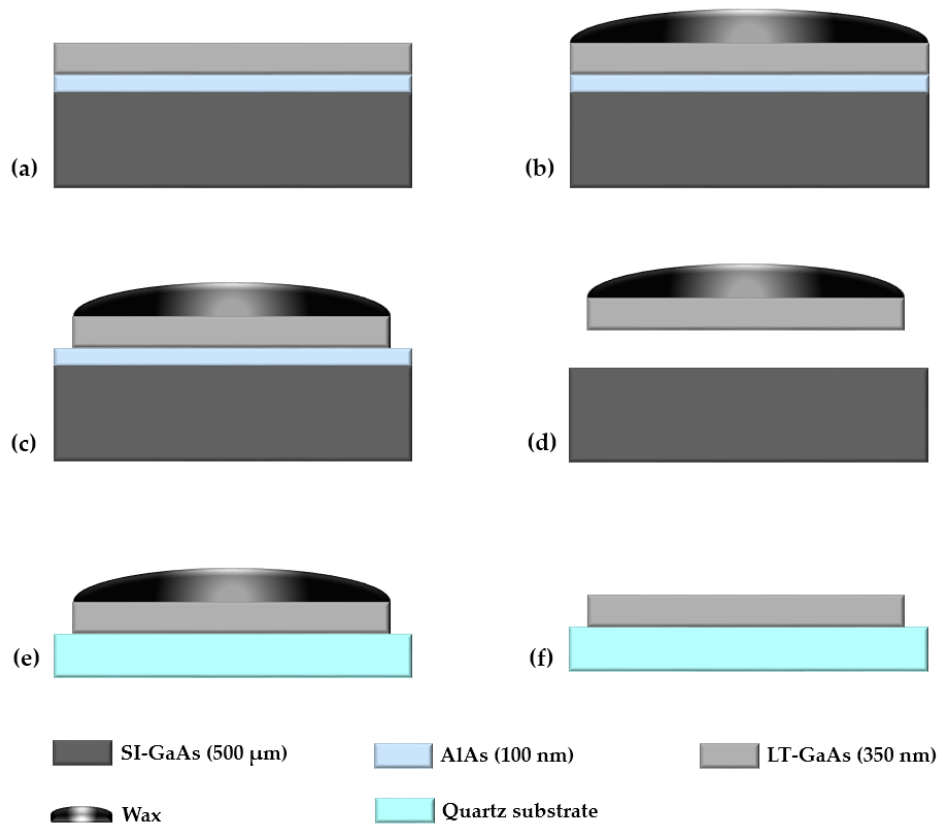
### 3.6 First generation CPW devices on quartz substrate

In Section 3.5, it was discussed that the coupling efficiency of a coupling switch in CGAP-CPW on LT-GaAs substrate is affected by lateral ground-to-ground coupling. The lateral coupling can be minimised (or removed completely) by selective etching and transferring the LT-GaAs material on to a low permittivity dielectric substrate material

such as quartz. Also, electromagnetic simulations using HFSS discussed in Chapter 2 showed a much higher bandwidth ( $\sim 1.01$  THz) for CPW formed on the quartz substrate compared to CPW on GaAs substrate ( $\sim 0.45$  THz). In this section, the fabrication steps and on-chip measurements of CPW on quartz substrates are therefore discussed, and bandwidth extracted from FFT spectra of time-domain picosecond pulse detected from on-chip measurements is compared with simulation results obtained from HFSS.

### 3.6.1 Fabrication of the first generation CPW on quartz substrate

Fabrication steps for CPW on the quartz substrate were first based on the recipe used for Goubau line device fabrication [90, 153, 154] by the Leeds research group, but were then improved by several iterative improvements to the existing process.



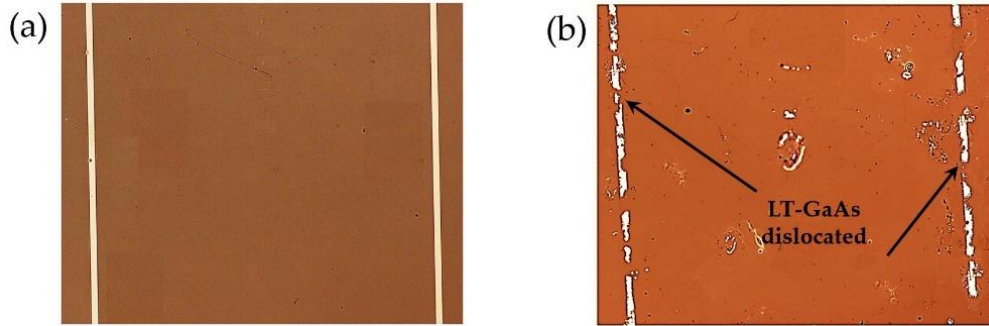
**Figure 3.35** Transfer process for thin LT-GaAs layers on to quartz substrates in CPW device fabrication: a) LT-GaAs layer on SI-GaAs separated by AlAs layer. b) LT-GaAs covered with black wax. c) Removal of wax from outer edges. d) AlAs layer etched away by HF. e) Sample placed onto quartz chip f) Black wax removed from LT-GaAs.

In the fabrication process, 350 nm thick LT-GaAs material (was grown on a 500  $\mu\text{m}$  thick SI-GaAs wafer separated by 100 nm AlAs sacrificial layer at  $\sim 180^\circ\text{C}$  using molecular beam epitaxy) was chemically etched and then transferred to quartz material before CPW lithography. In doing so, the LT-GaAs material was first cleaved into 3 mm  $\times$  3 mm size chips large enough to cover both photoconductive switch regions, followed by sonication (5 minutes each) in acetone, IPA and DI- $\text{H}_2\text{O}$  to clean the wafer. LT-GaAs wafer samples were then annealed at  $575^\circ\text{C}$  for 15 minutes to achieve high resistivity. The next step was to etch away the 100 nm AlAs sacrificial layer in order to separate the 350 nm top LT-GaAs layer from the 500  $\mu\text{m}$  thick SI-GaAs. In the etching process, the top LT-GaAs layer was first covered with black wax (by melting it on a hot plate at  $\sim 120^\circ\text{C}$ ) in order to protect it from the chemical etch (shown in Figure 3.35 b). Black wax was then removed from the outer edges (about  $\sim 0.5$  mm) of samples, and LT-GaAs layer (not covered by wax) was etched down (using  $\text{H}_2\text{SO}_4:\text{H}_2\text{O}_2:\text{H}_2\text{O}$  solution in the volumetric ratio of 1:40:80) to the AlAs layer as shown in Figure 3.35 c in order to expose 100 nm AlAs layer in HF etching process. The next step was to etch away the 100 nm AlAs layer by chemical etching. In doing so, HF solution was diluted in DI-  $\text{H}_2\text{O}$  in the volumetric ratio of 40(DI-  $\text{H}_2\text{O}$ ):10 (HF), and samples were then submerged in solution at  $\sim 4^\circ\text{C}$  in order to achieve a slow etch rate to avoid micro-cracking in the separated thin LT-GaAs layer.

Samples were then transferred onto 15 mm  $\times$  15 mm quartz chips (already cleaved and cleaned) and left to dry for 3 to 4 days to produce Van der Waals bonding between the thin LT-GaAs layer and the quartz substrate. Once the LT-GaAs samples were bonded with quartz, the wax was removed from the top of the LT-GaAs layer using trichloroethylene in order to perform lithography for photoconductive switches. As a final step towards the LT-GaAs transfer, the sample was heated in a vacuum oven for 15 hours in order to enhance bonding (desorb any moisture trapped at the quartz/GaAs interface) between the LT-GaAs and the quartz substrate.

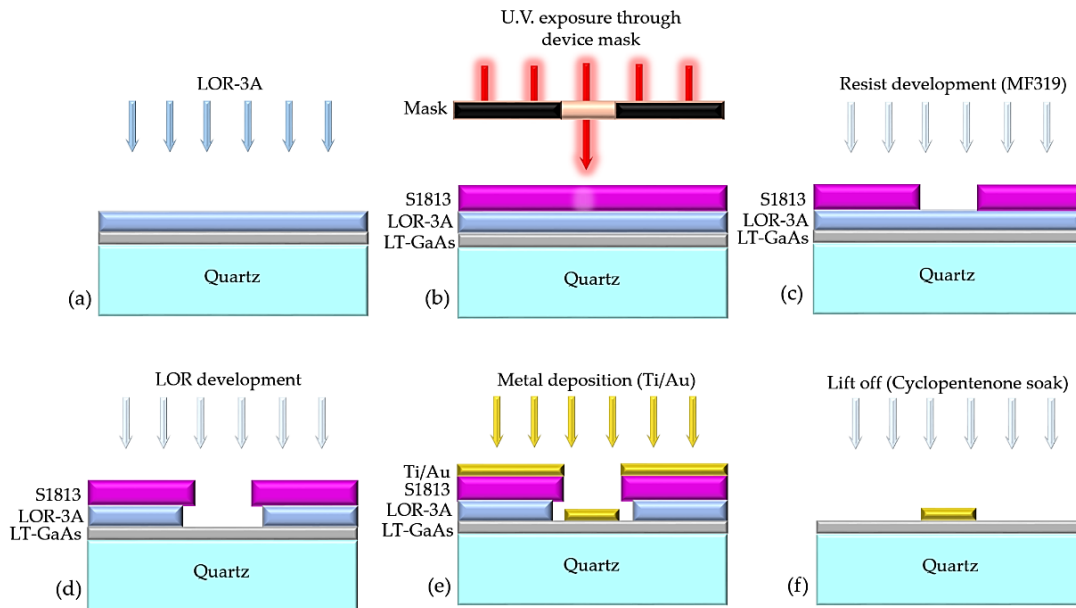
A separate photo mask was used to pattern (lithographically) photoconductive switches on to the transferred LT-GaAs. Lithography for photoconductive switches was performed using the same CPW lithography recipe discussed in Section 3.2. Once the switch pattern was defined, excess LT-GaAs was etched away by the chemical etching

(for ~ 4 minutes in  $\text{H}_2\text{SO}_4$ :  $\text{H}_2\text{O}_2$ :  $\text{H}_2\text{O}$  in a volumetric ratio of 1:8:950) process. It is worth mentioning that transferred LT-GaAs is very fragile and can be knocked off by etching and cleaning process involved in the whole fabrication process. Therefore, an extra precaution in sample handling and precise time-control in a chemical etch is needed.



**Figure 3.36** a) A good quality LT-GaAs transfer b) LT-GaAs lifted-off after an etching and sample cleaning process.

An example of good and poor-quality LT-GaAs transfer (after etching and cleaning process) is shown in Figure 3.36 a and b.

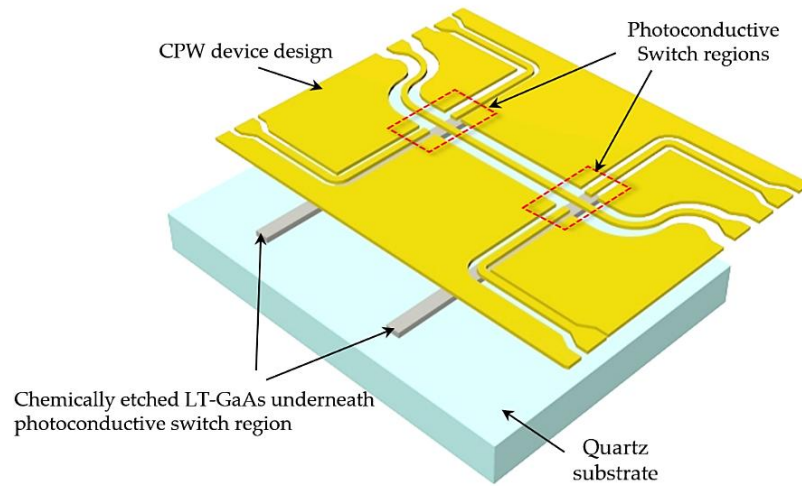


**Figure 3.37** CPW lithography on a quartz substrate a) Deposition of bilayer resist on quartz. b) UV exposure through device mask. c) Development of resist in developer MF319 d) LOR development. e) Deposition of Ti/Au in metallisation process. f) Lift-off process.

In the final phase of processing CPW on quartz, the CPW pattern was defined lithographically onto the prepared sample. In doing so, a bi-layer photo-resist (shown

in Figure 3.37 b) technique was used to achieve well-defined undercuts to the sidewalls, which makes metal come off more easily during the lift-off process compared to a single layer resist technique. In the bi-layer resist technique, Microchem LOR 3A was first spun onto the sample at 2000 rpm for 30 seconds and baked for 5 minutes using a hot plate at 200 °C. Spinning at 2000 rpm for 30 seconds gives a ~ 420 nm thick layer of LOR 3A. After deposition of the first layer of resist, the S1813 photoresist was spun at 4000 rpm for 30 seconds followed by baking at 115 °C for 3 minutes. UV light was then exposed for 17.5 seconds using a mask aligner in order to pattern CPW device design onto the sample.

The sample was then baked again (post exposure bake technique) at 110 °C for 30 seconds in order to reduce rippling effects (caused by the high reflectivity of the quartz substrate) of resist and crosslinks formed between positive and negative resist. The sample was then developed in MF319 photoresist developer for 30 seconds followed by a rinse in DI-H<sub>2</sub>O to stop further development. The sample was baked again (this time, to reflow S1813 resist to get a well-defined undercut) at 150 °C for 1 minute followed by second development in MF319 for 30 seconds.



**Figure 3.38 A schematic representation of LT-GaAs transfer on quartz substrate followed by CPW metallisation process.**

After defining the lithographic pattern of the CPW on the quartz, 20 nm Ti (titanium) followed by 150 nm Au (gold) was deposited in a metallisation process. The sample was then immersed into cyclopentenone and left overnight for metal to lift off

from unwanted regions (slot gaps) of CPW. Next day, the sample was taken out and cleaned with acetone and IPA.

In Figure 3.38, a schematic of CPW overlaid onto a quartz substrate, showing how LT-GaAs is selectively etched and transferred onto a quartz substrate (to go underneath photoconductive regions) followed by the CPW metallisation process.

### 3.6.2 Characterisation of the first generation CPW (quartz substrate)

Characterisation of CPW devices on a quartz substrate was again carried out by detecting the input and output THz pulses, testing bias and power dependence of THz pulses, and extraction of the useful bandwidth of the THz pulses by performing FFT on time-domain signal and excitation of even and odd modes.

### 3.6.3 Switch Characterisation

IV sweep measurement was performed on the photoconductive switches S1 and S4 by varying applied bias (-30 to +30 V) across switches with laser power varied (0 to 10 mW) in each set of measurements. IV sweep curves showed a relatively ohmic behaviour (for a whole range of bias applied) compared to photoconductive switches patterned onto 2  $\mu\text{m}$  thick LT-GaAs layer on an SI-GaAs substrate (see Section 3.4.4).

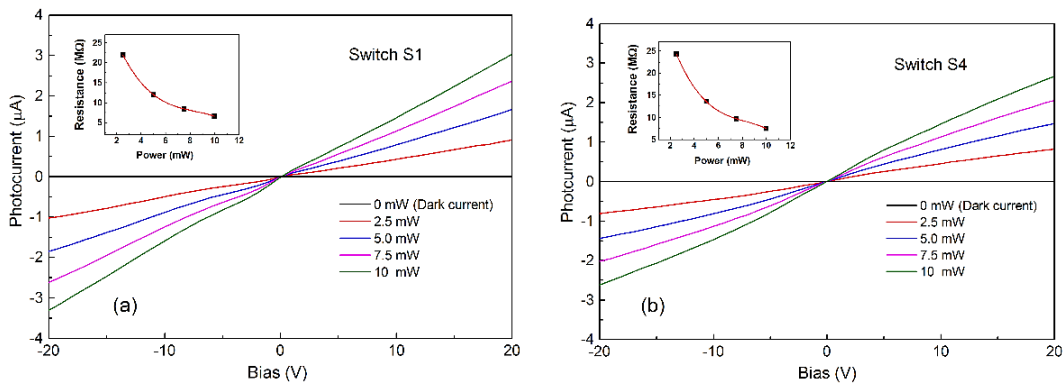
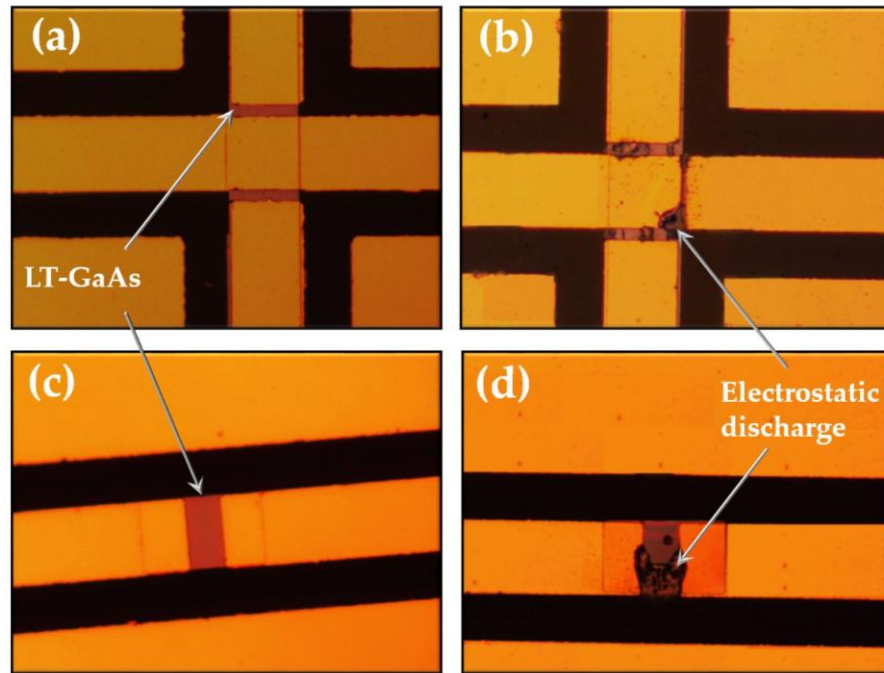


Figure 3.39 IV characteristics of switch S1 and S4 with varying bias and laser power.

The dark resistance of photoconductive switches was measured as being of the order of few G $\Omega$ , much higher than those formed on a LT-GaAs substrate ( $\sim 500 \text{ M}\Omega$ ). Due to the high dark resistance, the background DC photo-current was completely

suppressed in quartz devices. Interestingly, a much higher photo-resistance (in order of 22 - 25 M $\Omega$ ) of photoconductive switches was measured on a quartz substrate, owing to a thin layer (350 nm) of LT-GaAs transferred onto a quartz substrate by epitaxial lift-off (often referred as free standing LT-GaAs switches [155]).

The photo-charge carriers generated in photoconductive switches on a bulk GaAs substrate have a higher carrier lifetime compared to switches on the quartz substrate [156] (transferred by an epitaxial lift-off). Due to higher dark resistance and low carrier lifetime, free standing LT-GaAs switches can provide a higher bandwidth [157] and larger signal-to-noise ratio in order to perform on-chip spectroscopy of overlaid polycrystalline material onto CPW device (see Chapter 5).



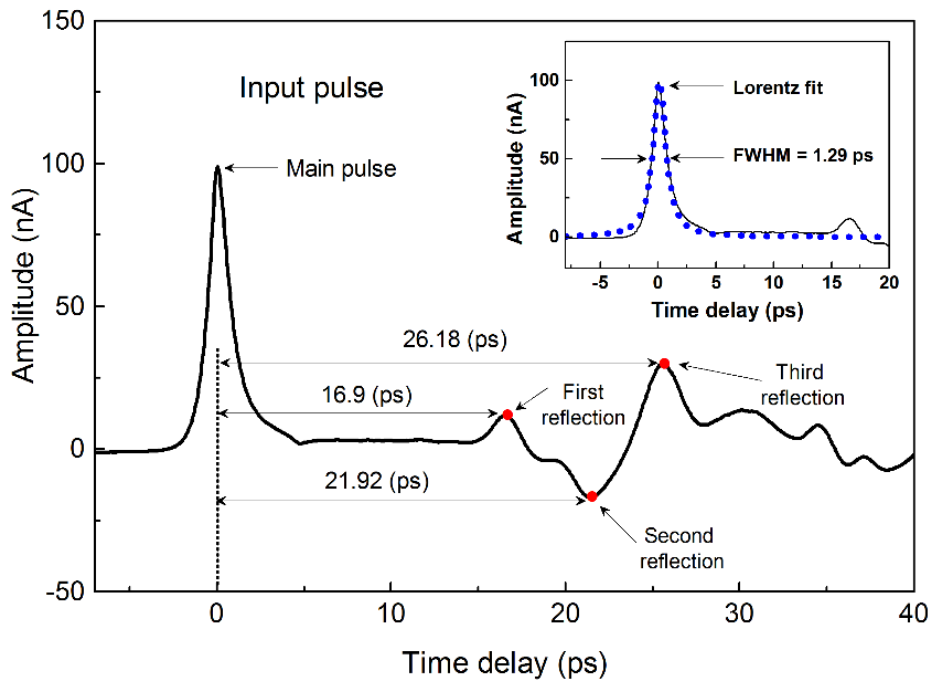
**Figure 3.40** a) A pair of photoconductive switches fabricated by epitaxial lift-off of LT-GaAs. b) Switches damaged by electrostatic discharge. c) A small patch of LT-GaAs is forming a coupling switch. d) A damaged coupling switch.

Initial testing of CPW on the quartz substrate revealed that free-standing photoconductive switches were sensitive to electrostatic discharge, unlike conventional photoconductive switches. Free standing LT-GaAs switches were damaged by electrostatic discharge while performing wire-bonding using a ball bonder (which uses an electric spark in a bonding process) are shown in Figure 3.40. Therefore, a wedge

bonder (which uses mechanical pressure to form wire-bonds) was used in order to avoid any further damage by electrostatic discharge.

### 3.6.4 Input pulse detection

The measurement setup for input pulse detection has already been discussed in previous sections. Therefore, only analysis of input pulses generated at the switch S1 (by applying a bias of 20 V) and detected at the photoconductive switch S2 by focusing a probe beam onto the switch S2, are discussed throughout this section.

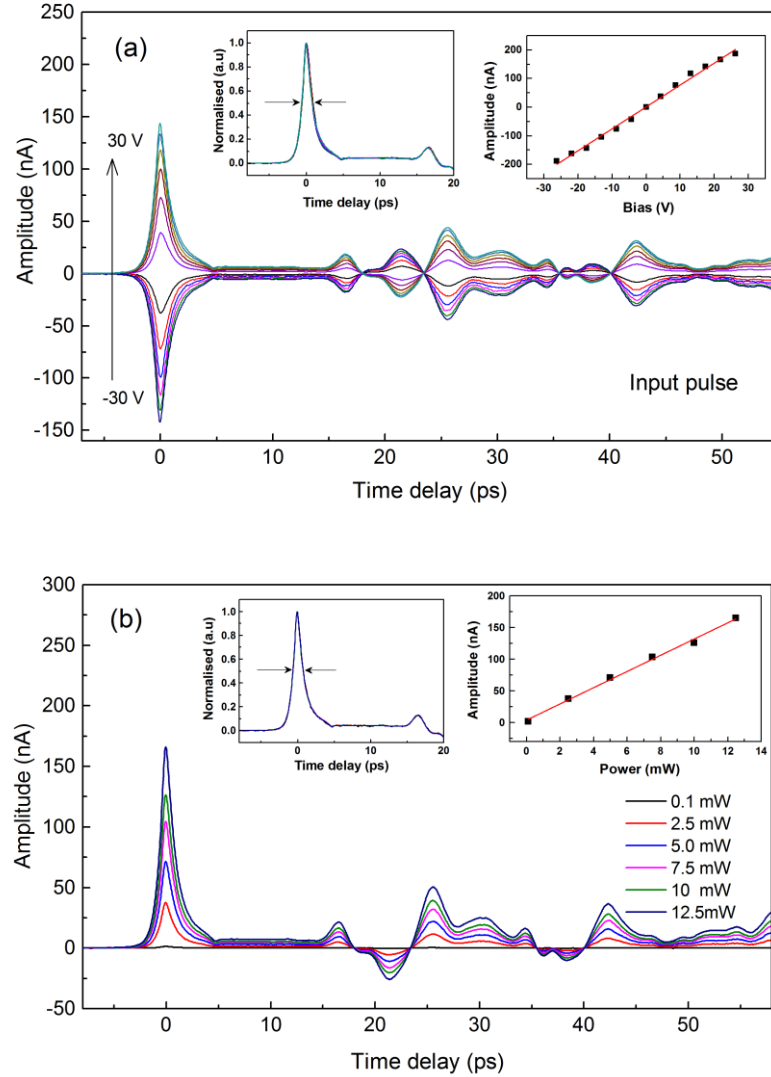


**Figure 3.41** A trace of input THz pulse consisting of the main pulse at zero ps followed by secondary reflections. FWHM calculated by Lorentz fit to the main pulse is shown in inset graph.

In a time window of 40 ps, the input pulse traces showed the main pulse with a much narrower FWHM of 1.29 ps followed by secondary reflections as shown in Figure 3.41. The reduced FWHM is attributed to a lower carrier lifetime of the generated photo-charge carrier in free standing LT-GaAs switches and suppression of background dark current. Interestingly, secondary reflections occurred (at 16.9, 21.92 and 26.18 ps) in input pulse trace appear a little earlier compared to that of measured from CPW on LT-GaAs substrate, suggesting THz pulse travels at a higher velocity in CPW on a quartz



substrate. Higher velocity of THz pulse is attributed to low effective permittivity  $\epsilon_{eff} = 2.39$  for quartz substrate as phase velocity is related to effective permittivity as  $v_p = c/\sqrt{\epsilon_{eff}}$ , where  $c$  is speed of light. The velocity of generated THz pulse will be calculated in the following sections. The origins of reflections remain same as that of measured for CPW on LT-GaAs substrate due to similar device design.



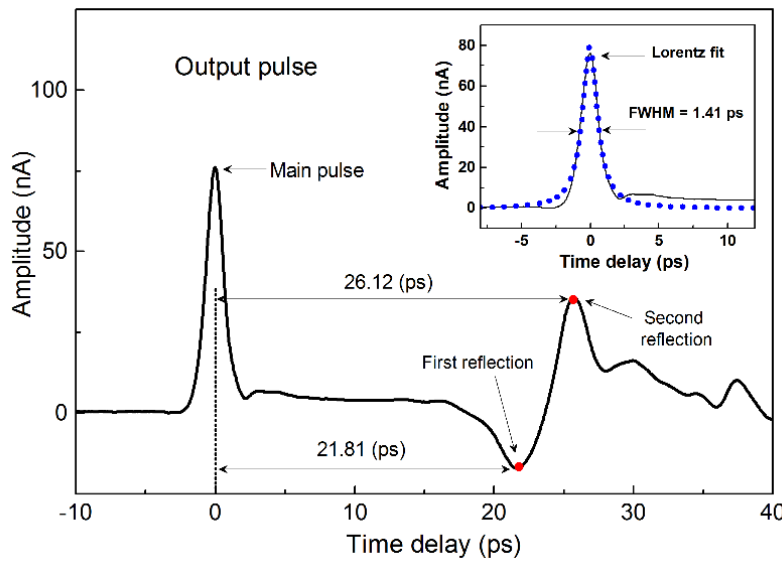
**Figure 3.42 Input THz pulse a) A linear bias dependence shown by linear fit in inset graph.  
b) A linear power dependence shown by linear fit in inset graph.**

Bias and laser power dependence characteristic of the input pulse is shown in Figure 3.42 a and b respectively. A linear dependence on both bias and power was observed with a very small change in FWHM (a spreading in falling edge of THz pulse was noticed -see inset graph, Figure 3.42 a, was observed with increasing applied bias,

suggesting a bias dependence on carrier lifetime.

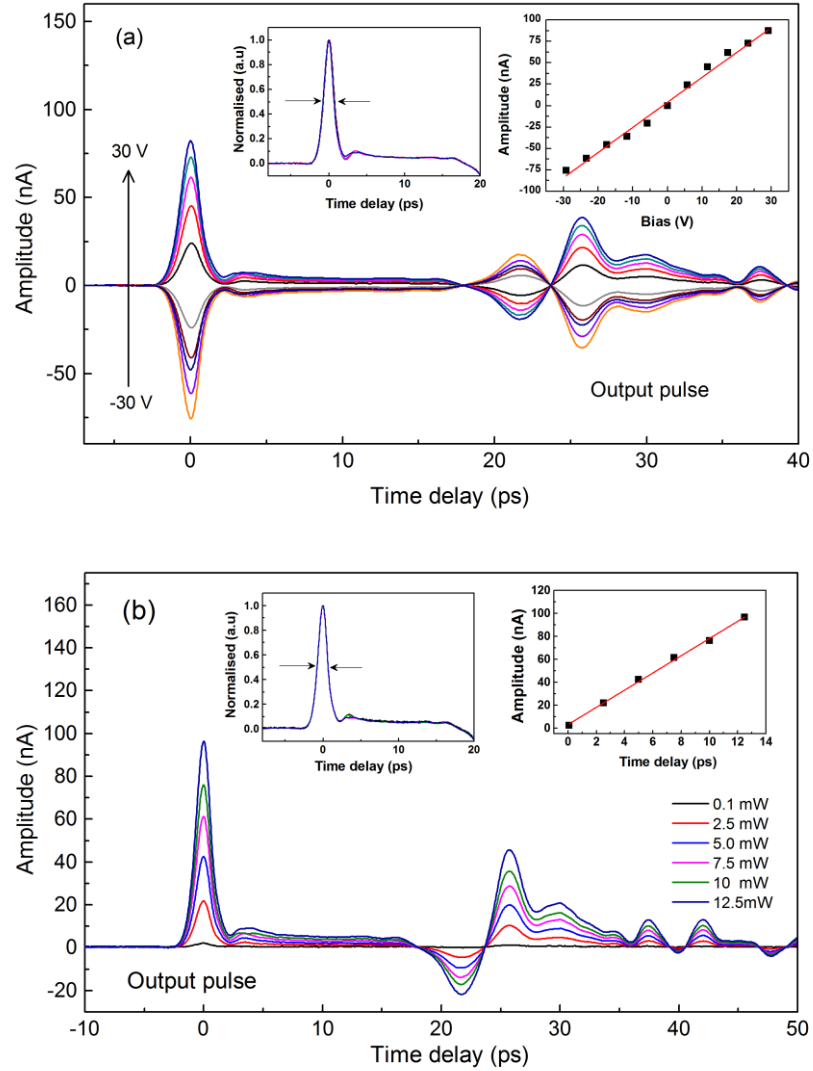
### 3.6.5 Output pulse detection

In a time-window of 40 ps, a typical output pulse trace showed the main pulse followed by two secondary reflections, occurred at 21.81 and 26.12 ps delay after the main pulse. Origins of reflections can be calculated by multiplying respective time delay relative to the main pulse to the velocity of the pulse.



**Figure 3.43** A trace of an output pulse, where the main pulse occurred at zero time delay is followed by two secondary reflections occurred at 21.81 ps and 26.12 ps respectively and Lorentz fit to the main pulse is shown in inset graph.

Lorentz fit to the main pulse revealed a FWHM of  $1.41 \pm 0.01$  ps, which is relatively less broadened pulse width compared to that of measured for CPW on LT-GaAs substrate. Less broadened pulse width attributes to low effective permittivity of the waveguide on the quartz substrate due to which THz pulse experiences less dispersion. Traces of output pulse taken by varying applied bias (-30 to + 30V) and varying laser power (0.1 to 12.5 mW) showed a linear dependence on both applied bias and laser beam power as shown in inset graphs, Figure 3.44.

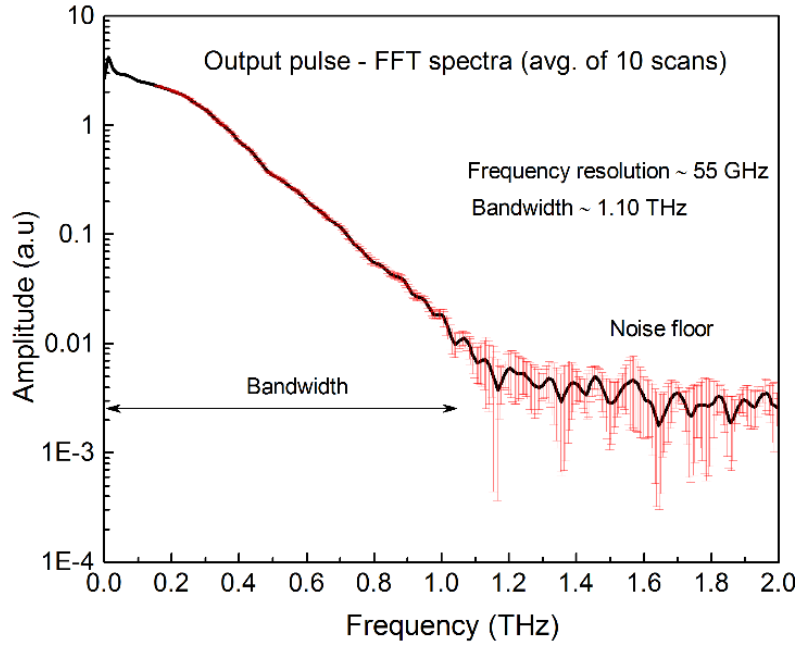


**Figure 3.44** Traces of output pulse taken at different bias and laser powers showing a linear dependence by a linear fit to pulse amplitude shown in inset graph.

Also, dielectric losses are minimised by using quartz substrate instead of a LT-GaAs substrate as quartz has a lower relative permittivity of  $\epsilon_r = 3.78$ . Less broadened pulse width also ensures a higher bandwidth present in the THz pulse.

To ensure a higher bandwidth, 10 consecutive scans of output pulse were performed, and FFT was then performed on each time-domain pulse (by applying a truncation window just before the first reflection followed by zero padding). An average of FFT results was then plotted against standard-deviation. This method revealed the noise level present in FFT spectra as shown in Figure 3.45. A much higher bandwidth of  $\sim 1.10$  THz was observed compared to that of measured from CPW on LT-GaAs

substrate ( $\sim 0.42$  THz). A higher bandwidth measured from CPW on the quartz substrate indicates that quartz devices can be used to perform on-chip spectroscopy of polycrystalline material overlaid onto the transmission line.



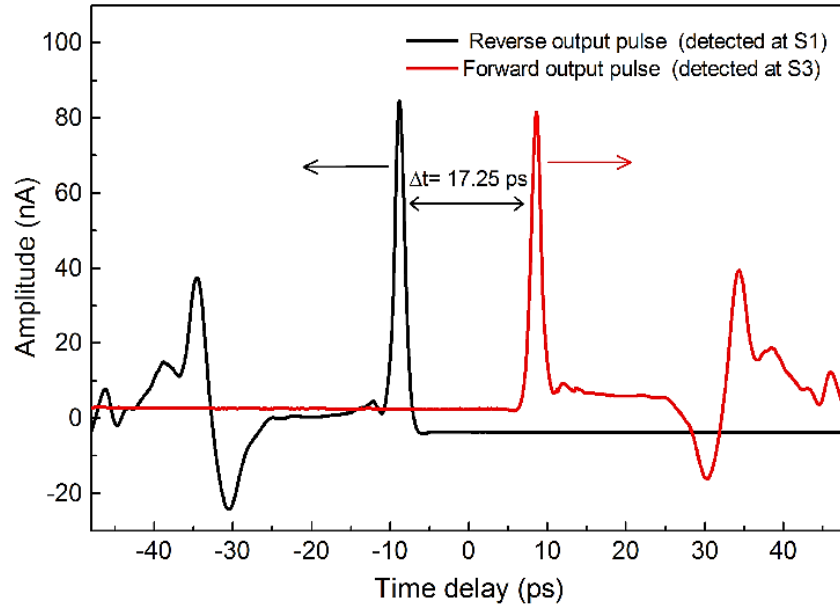
**Figure 3.45** An average of ten FFT spectra plotted against standard deviation to reveal noise level present in the signal.

However, quartz device suffers from the low-frequency resolution of 55 GHz whereas LT-GaAs device showed a frequency resolution of 33 GHz. Low-frequency resolution in a quartz device is attributed to secondary reflections occurred in output pulse trace arriving earlier than that of observed in CPW on LT-GaAs substrate, indicating THz pulse propagates at a higher velocity in a quartz device. To circumvent this situation in the quartz device, a modified geometry with long parasitic regions in order to further delay any secondary reflections coming from discontinuities, is required. A second generation CPW device with long parasitic regions will be discussed in detail in Chapter 4.

### 3.6.6 Pulse velocity (quartz substrate)

Pulse velocity of THz pulse propagating along CPW<sub>quartz</sub> was determined by using a similar method as discussed in Section 3.4.7. Traces of two output pulses detected at S1 and S3 by swapping their biasing and probing connection are shown in Figure 3.46. The

relative time delay between two output pulses was found to be 17.25 ps. The velocity of the pulse was then calculated as  $2 \times 1.5/17.25 = 1.74 \times 10^8 \text{ m/s}$ . It is clear from pulse velocity calculation that THz pulse propagating at higher velocity of  $1.74 \times 10^8 \text{ m/s}$  in a quartz device whereas velocity of THz pulse in the LT-GaAs device was calculated as  $1.13 \times 10^8 \text{ m/s}$ .



**Figure 3.46** Traces of two output pulse detected at switch S1 and S3 respectively, where zero time delay represents the origin of input pulse generation.

### 3.6.7 Excitation of odd (co-planar) mode

“Odd mode” was excited by simultaneously illuminating S1 and S2 using a defocused pump beam while the probe beam was focused onto S3 and S4 in two consecutive scans. A Lorentz fit to “odd mode-output pulse” revealed a FWHM of  $\sim 1.37 \text{ ps}$  which is slightly shorter than that of measured from the hybrid mode-output pulse, indicating suppression of anti-symmetric fields propagating along CPW. Pulse shape and polarity of detected output pulses were found to be similar, indicating propagation of a symmetric mode with field extending from the centre conductor to ground planes. An average FFT spectra of ten consecutive output pulses (odd mode excitation) plotted against standard deviation, revealed a bandwidth of  $\sim 1.15 \text{ THz}$ .

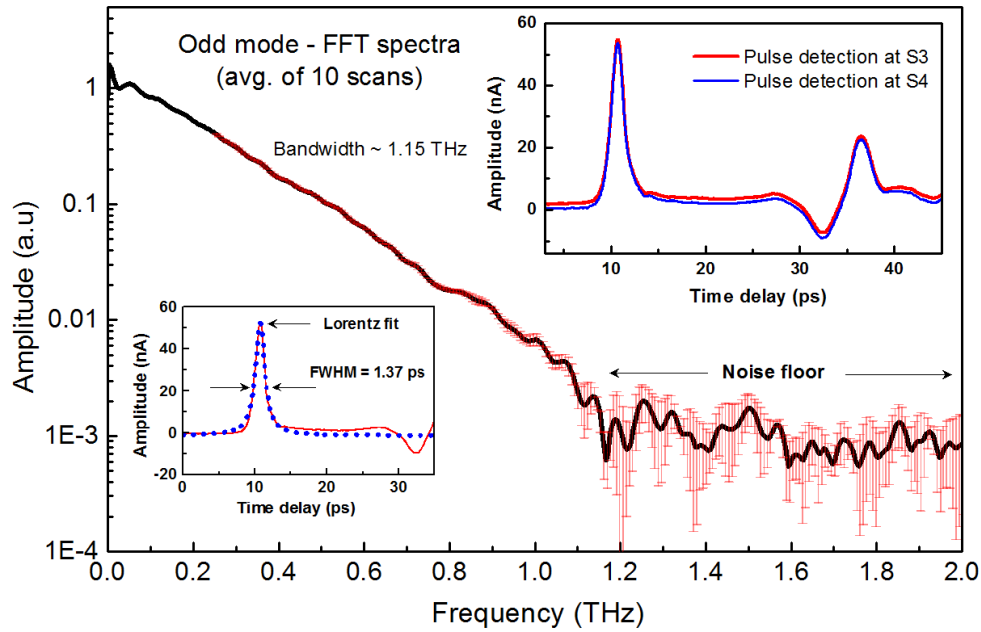


Figure 3.47 An average of ten FFT spectra of an “odd mode-output pulse” plotted against standard deviation to reveal noise level present in the signal.

### 3.6.8 Excitation of even (slot-line) mode

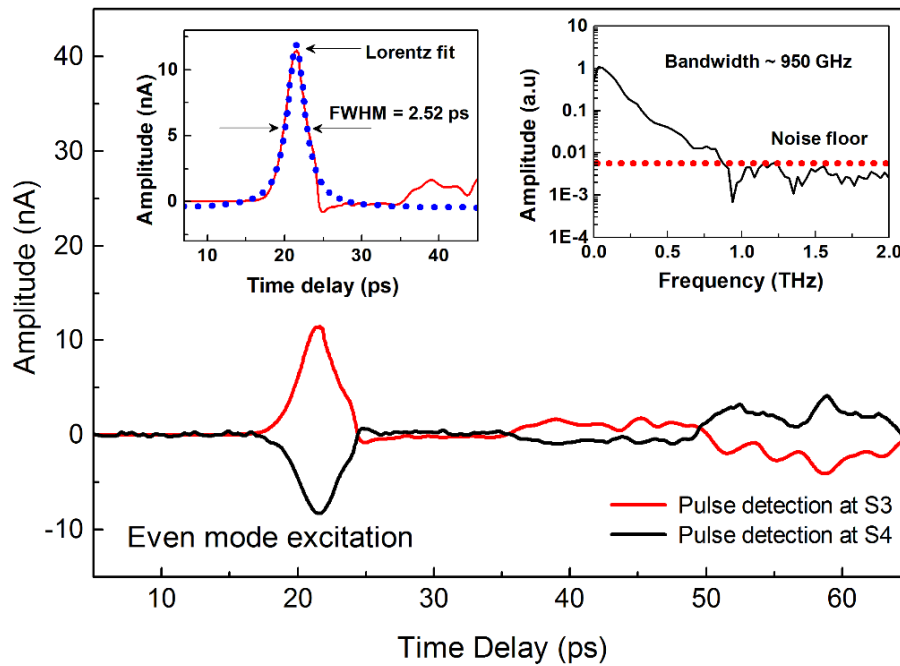


Figure 3.48 Trace of an “even mode-output pulse” detected at switch S3 and S4 in two consecutive scans.

“Even mode” was excited by reversing the polarity of bias applied across the switch S2 and switches S3-S4 were then illuminated by the focused probe beam in two consecutive scans in order to detect an even mode signal. Detected “even mode-output pulses” were of different polarity, ensuring propagation of anti-symmetric field along CPW. Lorentz fit to the main pulse revealed a FWHM of 2.52 ps, suggesting pulse broadening. FFT spectra of “even mode-output pulse” revealed bandwidth of  $\sim 950$  GHz. Therefore, even mode pulse was found to be more dispersive than that of measured from odd mode excitation.

### 3.7 Theoretical modelling of coupling gap

Before performing on-chip measurements of CGAP-CPW devices on a quartz substrate, a theoretical modelling of the coupling switch embedded (lithographically) into the centre conductor of CGAP-CPW was carried out in order to have a better insight into coupling switch characteristics.

#### 3.7.1 Photo-conductance

As discussed in Chapter 2 that a coupling gap discontinuity can be represented by a pi-capacitive model, where  $C_g$  was represented as coupling capacitance of the coupling switch. However, an illuminated coupling switch behaves differently as the conductivity of LT-GaAs can substantially be increased by laser beam illumination. With increased conductivity, coupling switch should essentially be modelled as time-varying photoconductor with conductance  $G(t)$ , connected in parallel with the coupling capacitor  $C_g$ . In this work, we will assume that coupling switch is purely resistive (capacitance is ignored) when illuminated with a focused laser beam. Now, if a bias  $V_0$  is applied across coupling switch, photocurrent  $i_c$  flowing through the switch will then be given as:

$$i_c = \frac{V_0}{Z_0 + G(t)^{-1}} \quad 3-3$$

Where  $Z_0$  is the characteristic impedance of CPW and  $G(t)^{-1}$  is photo-resistance of the coupling switch under illumination. Time-varying photoconductance depends on

several factors such as: effective illumination area  $A$ , the optical power of the laser beam  $P_{out}$ , carrier lifetime  $\tau_c$ , the reflectivity of LT-GaAs material  $R$ , optical the absorption coefficient of LT-GaAs, the wavelength of the optical beam etc. W. plattle *et al.* [158] derived a mathematical expression for calculating photoconductance (by taking above-mentioned parameters into account) of a photoconductive switch using conformal mapping techniques (see Chapter 2 for conformal mapping technique).

However, derived mathematical expression was further simplified by C. T. Canseliet *et al.* [159] given as:

$$G(t) = \frac{W\Delta\sigma_{ph}}{L_g} \left( \frac{1}{\alpha} - L \frac{\alpha L^2 + v_s \tau}{L + v_s \tau} \right) (1 - \alpha^2 L^2)^{-1} \quad 3-4$$

where, photoconductivity  $\Delta\sigma_{ph}$  is given as :

$$\Delta\sigma_{ph} = \left( \frac{e\lambda}{hc} \right) \left( \frac{P_{opt}}{A} \right) (\mu_n + \mu_p) \eta \alpha \tau (1 - R) \quad 3-5$$

where,  $\alpha$  is an optical absorption coefficient of LT-GaAs,  $\lambda$  is the wavelength of the optical beam,  $\tau$  is carrier lifetime,  $L$  is diffusion length,  $v_s$  is Surface recombination velocity,  $P_{opt}$  is optical power,  $A$  is effective illumination area,  $\eta$  is quantum yield,  $R$  is the surface reflection coefficient,  $L_g$  is gap length,  $W$  is gap width,  $\mu_n, \mu_p$  are electron and hole mobilities respectively.

Using expressions 3-4 and 3-5, photoconductance was calculated with following parameters: a carrier lifetime of  $\sim 0.65$  ps (measured by autocorrelation technique-see Section 3.4.2.1), optical power of 10 mW, centre wavelength of the optical beam  $\sim 800$  nm, effective illumination area was calculated from FWHM of optical beam waist measured by knife-edge experiment, reflectivity of LT-GaAs was assumed 30% (of total illumination), coupling switch length  $L_g$  and width  $W$  were taken from device geometry (see Figure 3.49 b), quantum yield of the photoconductive switch was assumed  $\eta = 1$  and the values of absorption coefficient  $\alpha$ , carrier diffusion length  $L$ , surface recombination velocity, mobility of the charge carrier ( $\mu_n + \mu_p$ ) were taken from ref. [159].

The values of photoconductance calculated using expression 3-4 and 3-5, are plotted as a function of varying gap size of the photoconductive gap in Figure 3.49 b. It



is clear from Figure 3.49 that for a smaller gap of 5  $\mu\text{m}$ , photoconductance is much higher and decreases drastically with increasing gap length. We note that photoconductance does not change much for a gap larger than 30  $\mu\text{m}$  as beam spot size (spot size of  $\sim 25.8 \mu\text{m}$  was estimated by knife-edge experiment, see Chapter 2) is not able to cover the whole photoconductive region of the photoconductive gap.

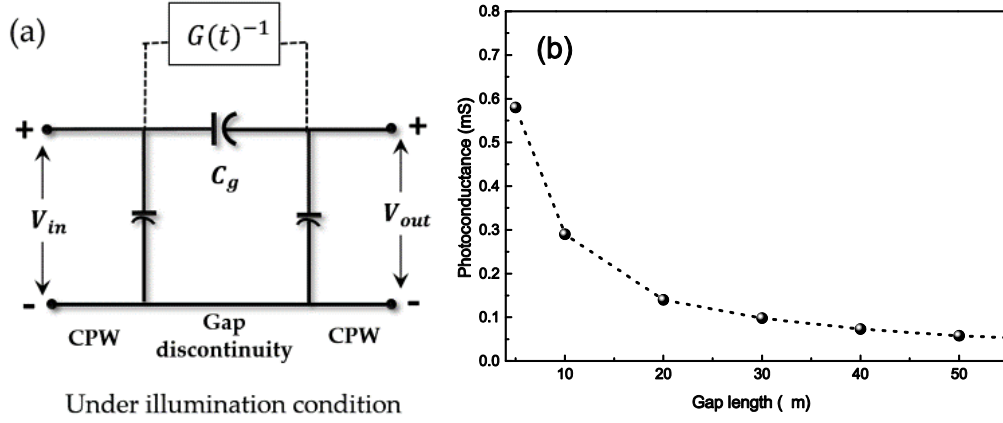


Figure 3.49 a) A capacitive pi-equivalent circuit model of coupling gap discontinuity, where a photoconductance  $G(t)$  is added in parallel to coupling capacitor under illumination condition b) Photoconductance plotted as function of gap length.

It is worth mentioning that IV characteristics obtained for photoconductive switches from IV sweep measurement yield an average photo-current (an average of peak photocurrent generated by  $f_s$  pulses at discrete time intervals) at fixed DC bias applied across the switch. Therefore, an estimation of time-varying photo-current (and photo-resistance) is desirable.

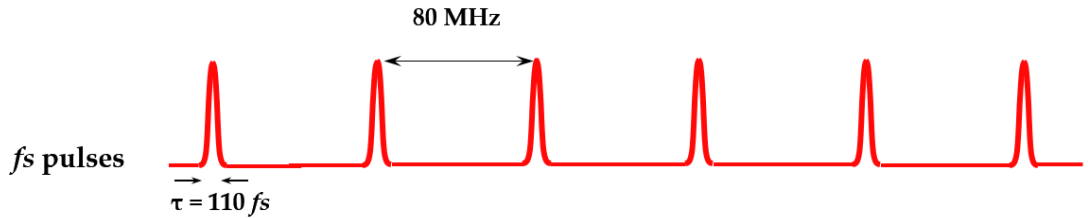


Figure 3.50 An illustration of ultra-fast  $f_s$  pulses with a repetition rate of 80 MHz and pulse width of 110 fs.

We estimate the time-varying photo-current by taking peak photocurrent generated per  $f_s$  pulse, into account. An illustration of  $f_s$  pulses emitting from ultra-fast

femtosecond laser is shown in Figure 3.50, where  $f_s$  pulses emitted with a repetition rate (frequency) of 80 MHz and pulse width of 110 fs. With given frequency, the period was calculated as  $\Delta t = 1/\text{repetition rate}$ , revealing a value of 12.5 ns. On-duty cycle  $\Delta t_{on}$  was then calculated by dividing duration (pulse width) of single  $f_s$  pulse by total time period as  $\Delta t_{on} = \text{pulse duration}/\text{total time period} = 8.80 \mu\text{s}$ . A typical value of an average photocurrent measured by applying DC bias of 30 V across photoconductive switch using kiethley source-meter is  $\sim 2.5$  to  $3 \mu\text{A}$  (depending on switch resistance). A peak current (photo-current per pulse) was then calculated as  $i_{peak} = \text{avg. photocurrent}/\text{on duty cycle} = 0.34 \text{ A}$ , where the on-duty cycle the is the period in which photoconductive switch is illuminated by  $f_s$  pulses. The value of peak photo-current was found to be much higher than the average photo-current measured from keithley source-meter. The resistance of the photoconductive gap was then calculated as  $R_p = \text{DC Bias}/\text{peak photocurrent} = \sim 88.23 \Omega$ .

### 3.8 On-chip measurements of the first generation CGAP-CPW device on quartz substrate

CGAP-CPW devices with different coupling gap lengths on a quartz substrate were characterised using the on-chip measurement system. Lateral coupling (showed by CPW on LT-GaAs devices) was circumvented completely by using an epitaxial transfer of thin LT-GaAs layer underneath the coupling switch gap.

#### 3.8.1 Switch characterisation

IV sweep measurement performed on photoconductive switches S1 and S3 of a CGAP-CPW device, revealed IV characteristics of S1 and S3 as shown in Figure 3.51. IV curves showed relatively ohmic behaviour with varying bias from -20 to +20 V. Switch S3 showed relatively higher resistance, which may be due to a difference in the quality of LT-GaAs transferred onto quartz in an epitaxial lift-off process. It was not feasible to maintain the same quality of thin (320 nm) LT-GaAs layer for all the photoconductive switches throughout the fabrication process.

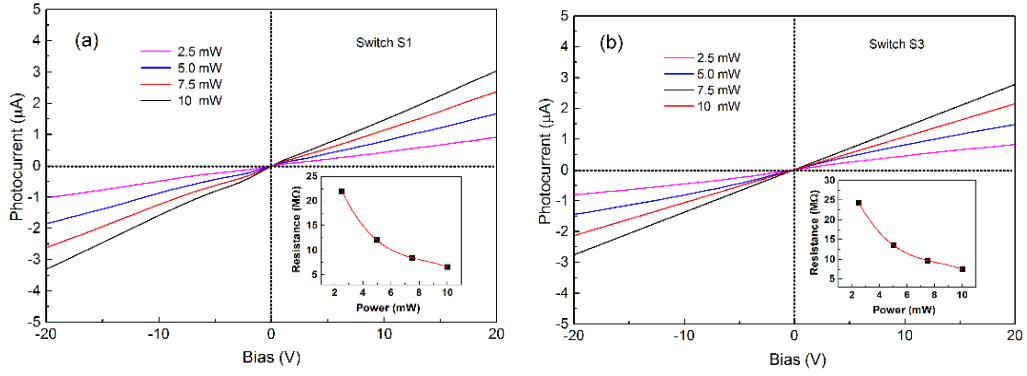


Figure 3.51 IV sweep characteristics of a) Photoconductive switch S1. b) Photoconductive switch S3.

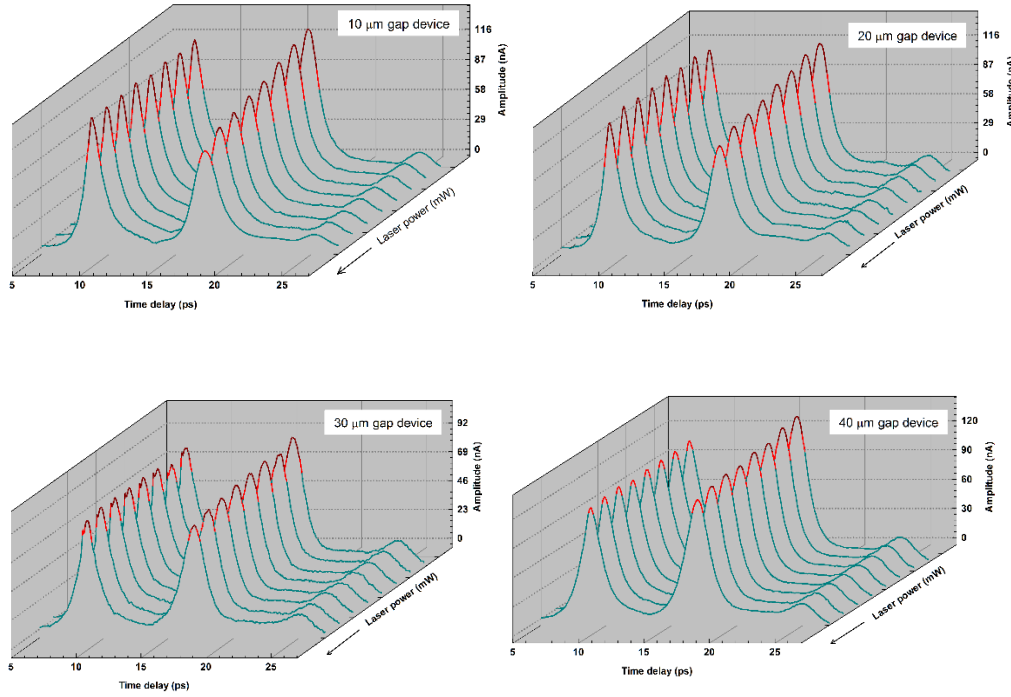
### 3.8.2 Detection of input and output pulse

Input and output pulses were measured in order to characterise CGAP-CPW devices with different coupling gap lengths. Measurements were performed with and without third beam in operation in order to observe any substantial change in pulse shape and amplitude by modulating the conductivity of the coupling switch.

#### 3.8.2.1 Input pulse detection

Input pulse measurement was performed for all four CGAP-CPW devices (10, 20, 30 and 40  $\mu\text{m}$  gap length). In doing so, the power of the third beam focused onto coupling, which was varied from 0 to 13 mW. The mechanical chopper was fixed at position A while performing the three-beam measurement. The relative position of the third beam was controlled by optical delay stage 2 in order to synchronise it with pump beam focused onto the generation switch S1. Generated THz pulse was detected at the switch S2 by focusing time-delayed probe beam (using optical delay stage 1) onto the switch S2.

Traces of input pulse showed the main pulse followed by a secondary reflection (CPW on the LT-GaAs device) originated from coupling gap discontinuity, in a time-window of 30 ps as shown in Figure 3.52. The base line of input pulse was somewhat uplifted due to constructive interference between main pulse and reflection coming from gap discontinuity.



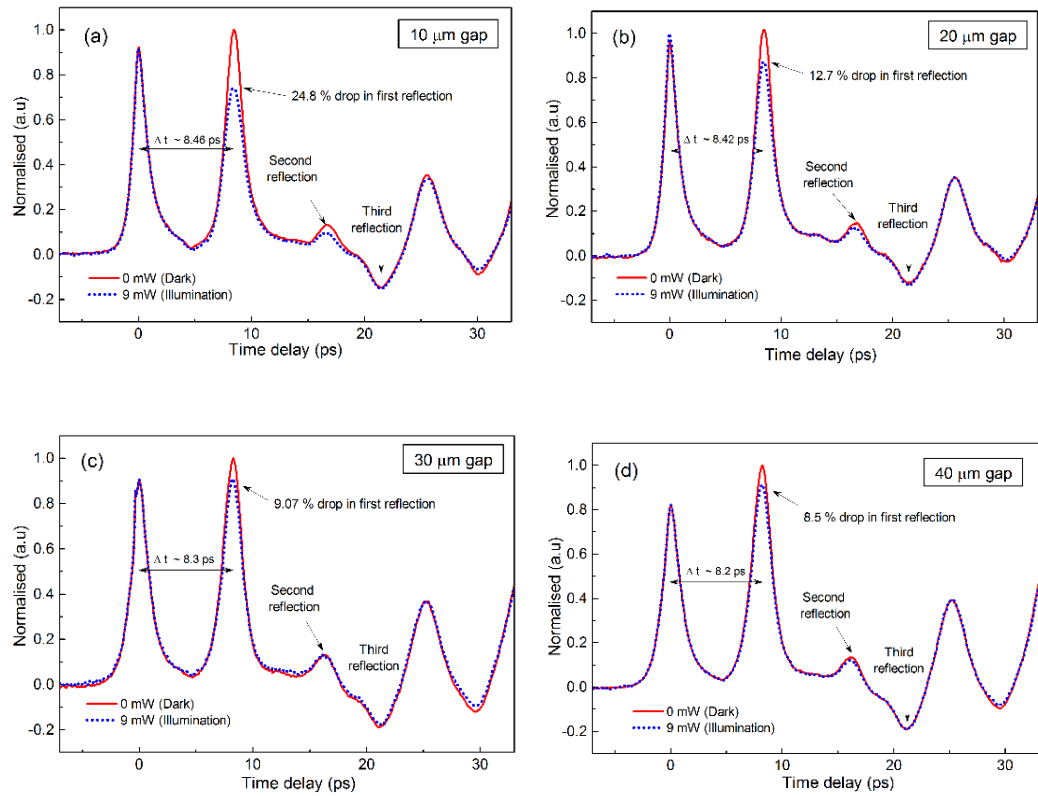
**Figure 3.52** A waterfall model of input pulse trace measured from four CGAP-CPW devices (10, 20, 30 and 40  $\mu\text{m}$  coupling gap), where a relative change in peak amplitude of secondary reflection is demonstrated by increasing third beam power from 0 to 13 mW.

Interestingly, reflection in input pulse trace gradually decreases with increasing third beam power (0 to 13 mW), suggesting a drop in coupling switch impedance (as the reflection was caused by an impedance mismatch), allowing a fraction of generated THz to pass through the coupling gap. This can further be understood by considering a formation of a local plasma of charge across the coupling gap by illumination LT-GaAs embedded with coupling switch. At sufficiently high laser beam power, the local plasma created by photo-charge carriers starts to bridge the coupling gap, allowing THz pulse to propagate along discontinuous CPW. It is clear from Figure 3.52 that relative change in amplitude of secondary reflection decreases with increasing coupling gap size, suggesting a greater impedance mismatch offered by larger coupling gap. 10  $\mu\text{m}$  gap device showed a substantial relative change in amplitude of the first reflection as shown in Figure 3.52.

In order to have a good observation of change in relative amplitude of the first reflection, a normalised trace of input pulse (illuminated by the third beam at 0 and 13

mW power) for all gap devices plotted as a function of time delay as shown in Figure 3.53. We note a maximum relative change of 24.8 % in the amplitude of the first reflection for a 10  $\mu\text{m}$  gap device, suggesting a stronger coupling through the gap. However, 30 and 40  $\mu\text{m}$  gap devices showed a relatively a smaller change in amplitude of the first reflection, suggesting a weaker coupling through the gap.

Further, it was noted that first reflection coming from coupling gap discontinuities of different gap lengths occurred at relative time-differences, indicating that first reflection is coming from metal-semiconductor interface and arrival time of first reflection changes with increasing gap lengths as pointed out by  $\Delta t$  in graphs, Figure 3.53.

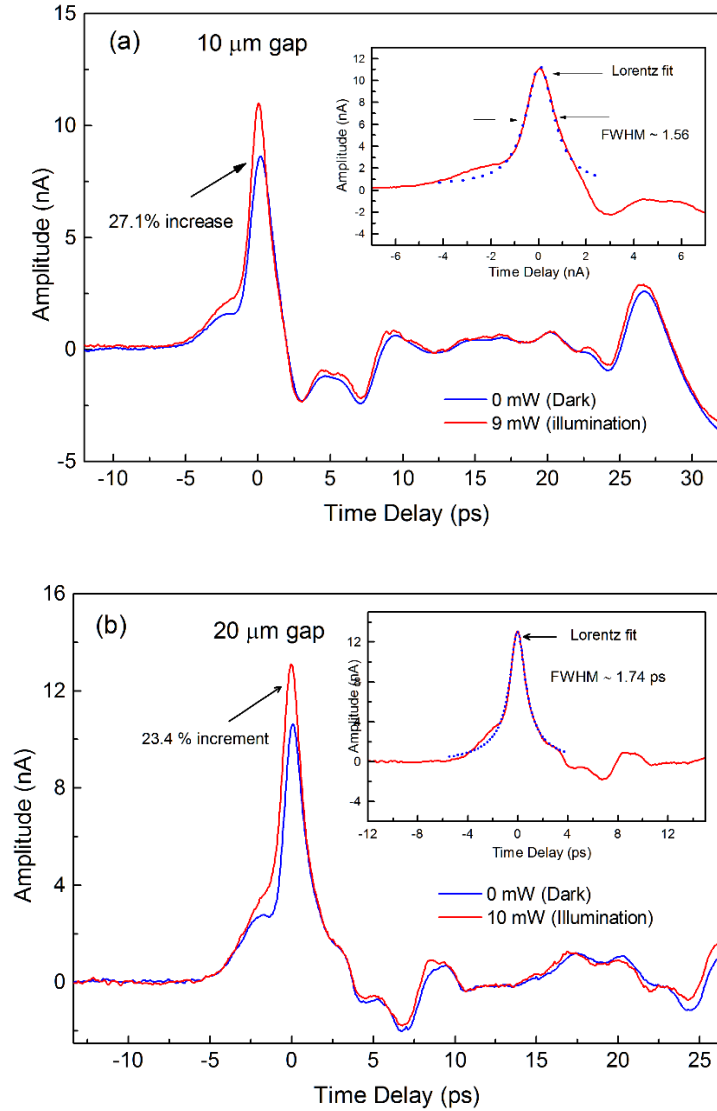


**Figure 3.53** Normalised input pulse traces for 10, 20, 30 and 40  $\mu\text{m}$  gap devices, where the relative amplitude of the first reflection compared at 0 and 13 mW power of the third beam.

### 3.8.2.2 Output pulse

Output pulse detection in the CGAP-CPW device was performed by focusing probe beam onto S3 while THz pulse generated at S1 (a hybrid mode pulse consists of odd-

even field components) at S1 propagating along discontinuous CPW. A third beam (synchronised with pump beam) was then focused onto the coupling switch in order to observe any substantial change in pulse amplitude.



**Figure 3.54** Traces of output pulse detected at switch S3 in a CGAP-CPW device with coupling gap length of 10 and 20  $\mu\text{m}$ .

As discussed in previous sections that THz output pulse generated in hybrid mode was not affected significantly by coupling discontinuity as broadened FWHM indicates that major field component present in the pulse was an even mode (anti-symmetric field). Therefore, output pulse in CGAP-CPW devices is of dispersive nature, propagates along ground-to-ground coupling ignoring centre conductor.

However, a small fraction of the field can pass through the coupling gap. Traces of output pulse detected (for 10 and 20  $\mu\text{m}$  gap devices) at the switch S3 are shown in Figure 3.54. A small change in pulse amplitude can be attributed that a small fraction of THz is passing through the coupling gap when illuminated by the third beam. However, it did not reveal much information about coupling efficiency of switch and therefore, output pulse measurement was not performed for all the gap devices.

### 3.8.3 Co-planar mode (Odd mode)

“Odd mode” pulse was launched by illuminating a pair of switches S1-S2 followed by detection of THz pulse at S3 by focusing probe beam onto S3 while third beam (chopper position A) was focused onto the coupling switch.

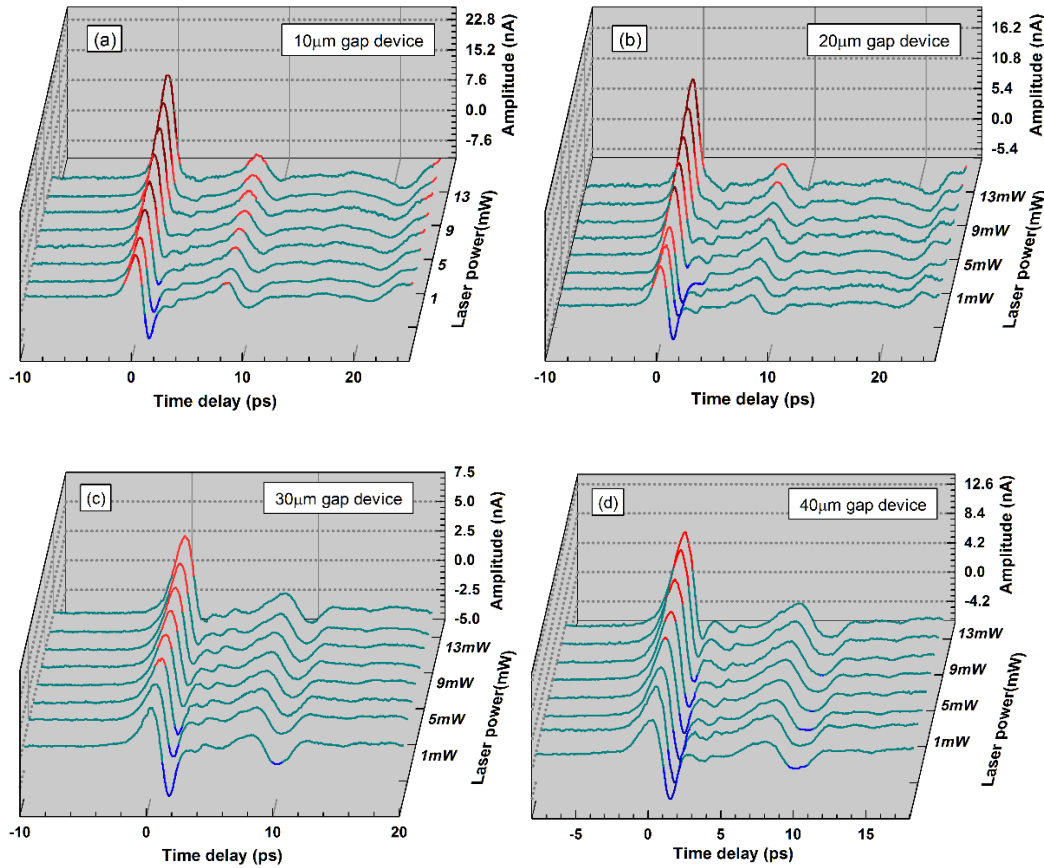
As discussed in last few sections that symmetric field of an odd mode pulse propagates along the centre conductor (extending fields from the centre conductor to ground planes) in a CPW device. Therefore, a major portion of THz pulse generated in odd mode excitation affected by conductivity modulation of the coupling switch.

It was also discussed that shape of a Gaussian THz pulse passing through a HPF can substantially be changed into a monocycle pulse. This change in the pulse shape occurred due to derivative properties of HPF consists of the coupling capacitor and line impedance. Capacitance and impedance parameters of HPF can substantially be changed or tuned by modulating the conductivity of the coupling switch by third beam illumination with varying laser power.

For 10  $\mu\text{m}$  gap device, shape of the monocycle pulse detected at 0 mW ( the third beam was blocked) is gradually changing into a Gaussian THz pulse when illuminated by 13 mW power (i.e. coupling switch illuminated by the third beam and chopper was set at position A), suggesting that capacitive nature of the coupling switch is dominated by switch impedance due to formation of local plasma of photo-charge carriers, bridging the coupling gap. Therefore, discontinuity in the centre conductor behaves as a continuous conductive film.

Since the monocycle pulse has shorter duration compared to a Gaussian pulse, monocycle pulses gained much interest over the past few years and have been used for

UWB (ultra-wideband) wireless technology (radio frequency range) for transmission of data at a higher rate [160, 161]. However, to date, manipulation of THz pulses (Gaussian to monocycle or vice-versa) at ultra-fast switching rate, using a femtosecond laser has not yet been reported in any literature to the best of our knowledge. Therefore, studying monocycle THz pulses, opens up a new field of research, in which manipulation of THz pulses can further be studied.



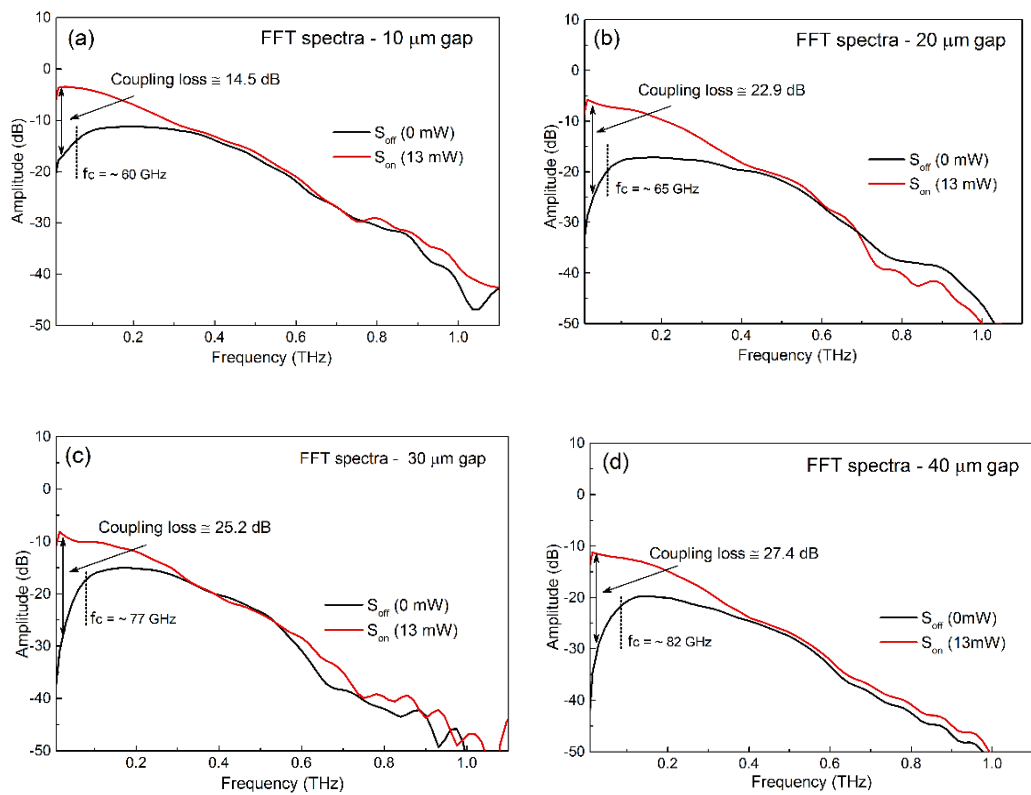
**Figure 3.55** Traces of output pulse in odd mode excitation in a CGAP-CPW device a) 10  $\mu\text{m}$  gap device. b) 20  $\mu\text{m}$  gap device. c) 30  $\mu\text{m}$  gap device. d) 40  $\mu\text{m}$  gap device.

Profile of the THz pulse changing from monocycle to Gaussian is shown in Figure 3.55 for all four 10, 20, 30 and 40  $\mu\text{m}$  gap devices. It is evident from the graphs c and d, Figure 3.55 that a complete Gaussian profile of THz pulse was not fully recovered from the monocycle shape with increasing laser beam power for a coupling gap larger than 20  $\mu\text{m}$ . Furthermore, the coupling loss occurred in the switching (on to off state) of the coupling switch (with different gap lengths) is estimated in the following section.



### 3.8.4 Coupling loss

When the state of the coupling switch was changed from 'on' to 'off', the coupling loss (in dB) occurring during the pulse transmission can be estimated by plotting dB values against frequency as shown in Figure 3.56. We note that the coupling loss occurred at lower frequencies (below 400 GHz) increases with increasing gap length, suggesting that larger gap lengths are more susceptible to coupling losses. Coupling losses at low frequencies were estimated as 14.5, 22.9, 25.2 and 27.4 dB for 10, 20, 30 and 40  $\mu\text{m}$  gap devices respectively.



**Figure 3.56** dB values obtained from FFT performed on  $S_{\text{on}}$  and  $S_{\text{off}}$  output pulses obtained under dark and illumination condition, plotted as a function of the frequency of operation.

However, coupling loss decreases with increasing frequency as capacitive reactance  $X_c$  (decreases with frequency as  $X_c = 1/j2\pi fc$ ) of the coupling discontinuity is dominated by impedance during the switching of states from  $S_{\text{off}}$  to  $S_{\text{on}}$  with increasing laser power.

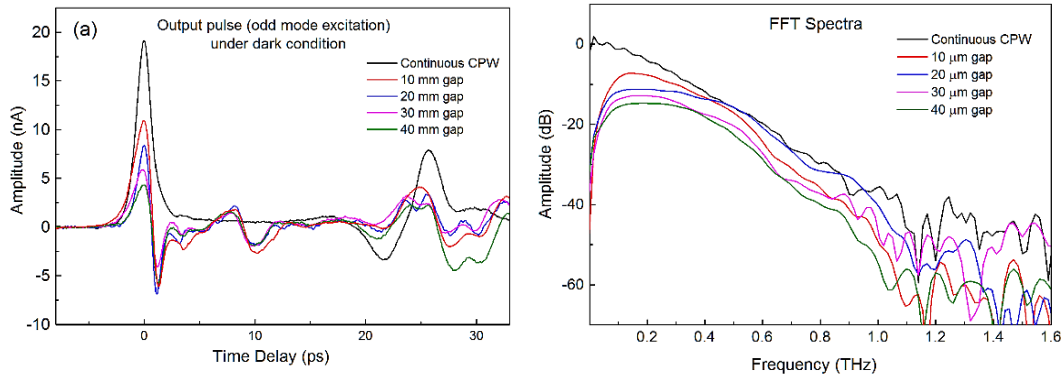


Figure 3.57 An average of ten FFT spectra plotted against standard deviation to reveal noise level present in the signal.

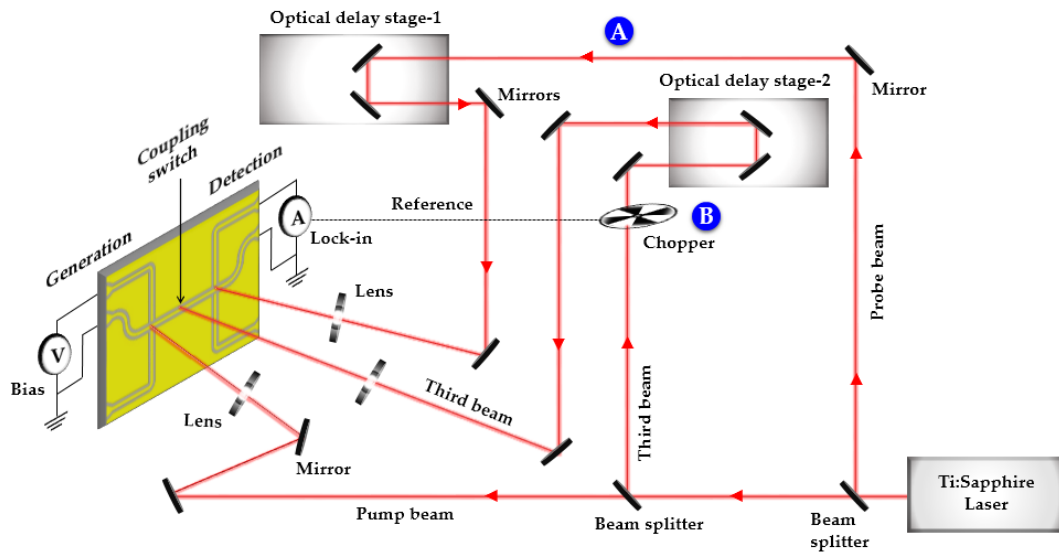
### 3.9 On-chip differential THz pulse measurement using CGAP-CPW (quartz substrate)

As discussed in Chapter 1 that a free-space differential THz-TDS was developed from conventional THz-TDS system, in which a test sample partly covered with thin film was moved in and out of THz beam (using a shaker as a modulator), resulted in a differential signal  $E_{\text{differential}}$  (i.e. a portion of the THz field transmitted when the sample is blank ( $E_{\text{ref}}$ ), subtracted by the THz field transmitted when the sample is covered with thin film ( $E_{\text{film}}$ )).

This section discusses a potential use of the coupling switch embedded in CGAP-CPW device as a modulator by employing a mechanical chopper and the three-beam on-chip measurement system in order to generate differential THz pulses.

#### 3.9.1 Experimental setup

The experimental setup for the differential measurement was similar to that of the three-beam on-chip measurement system except that the chopper was moved to position B, allowing third beam (i.e. used to illuminate coupling switch) to be chopped while a differential THz pulse was detected at the switch S3 by a lock-in amplifier. Before performing the differential (modulated) THz pulse measurement, the third beam was synchronised to pump beam using optical delay stage-2.



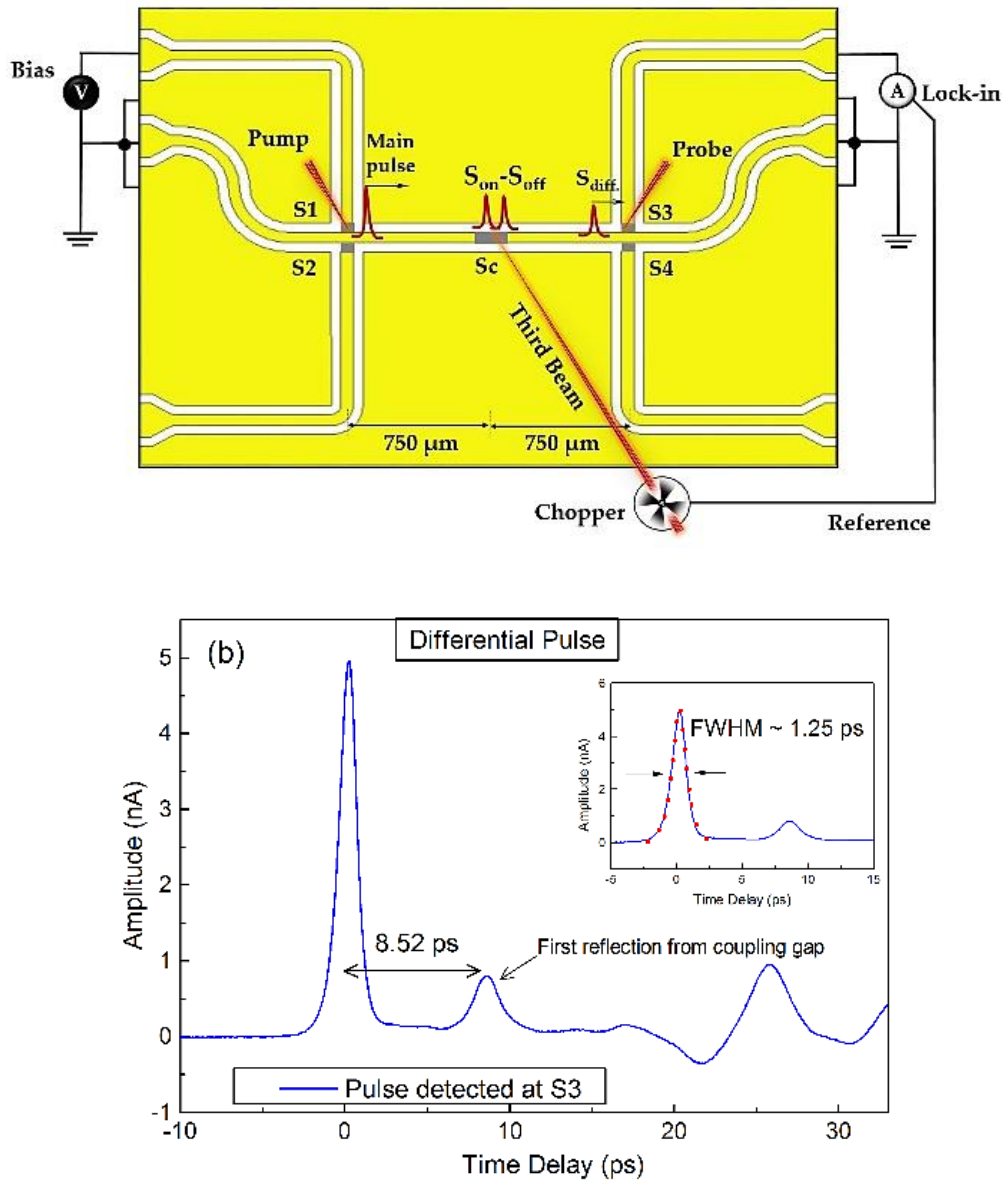
**Figure 3.58** An illustration of three-beam measurement setup in which the mechanical chopper is moved to position B in order to perform the differential pulse measurement.

Throughout this work, THz pulse measured by the three-beam system, in which third beam illuminating coupling switch is chopped (i.e. chopper position B), is referred as a modulated or differential THz pulse. However, chopper position A would indicate the detection of a conventional THz pulse (i.e. THz pulse mapped by the chopped probe beam at the detector switch S3 or S4).

### 3.9.2 Generation and detection of differential THz pulse

An example of the differential pulse measurement is shown in Figure 3.59 in which a differential THz pulse was detected by focusing a time-delayed probe beam onto the switch S3 while a DC bias of 20 V was applied across the switch S1.

In doing so, the pump beam was focused onto the biased switch S1 in order to generate a THz pulse. The generated THz pulse passes through the coupling switch while propagating along the transmission region. The third beam (split from the main pump beam) chopped by mechanical chopper was then focused onto the coupling switch in order to generate a modulated THz pulse (Son - Soff). Since the chopping frequency of the chopper was set as a reference to the lock-in amplifier connected in series with probe arms of the detector switch S3, a modulated THz signal was measured.

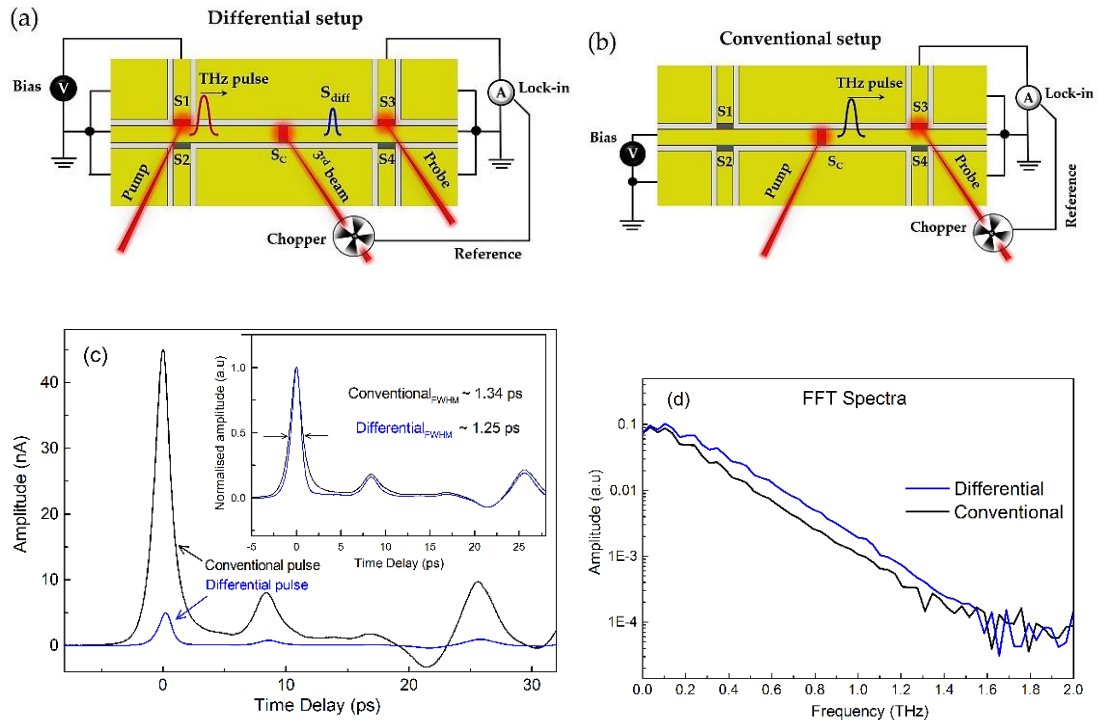


**Figure 3.59** a) A schematic showing differential pulse measurement using three-beam measurement system. b) A trace of detected differential pulse in the time-window of 40 ps.

The detected modulated signal essentially being the difference of signals  $S_{on}$  and  $S_{off}$  corresponding to “on” and “off” states of the modulated coupling switch  $S_c$ , is referred as a differential signal ( $S_{on} - S_{off}$ ). In Figure 3.59 b, a trace of differential THz pulse showed first reflection occurring at 8.52 ps delay after the main pulse. A Lorentz fit to the main pulse revealed a FWHM of  $\sim 1.25 \pm 0.2$  ps. The origin of the first reflection was found to be the coupling gap discontinuity, and indicates that differential pulse

travels one-half of the transmission region ( $\sim 740 \mu\text{m}$ ) before being detected at the switch S3. Other reflections seen in the differential pulse trace were found to be originated from bend discontinuities located in parasitic regions (as discusses in Section 3.4.6).

To further investigate the origin of the differential pulse, two different on-chip measurements (differential and conventional) were performed as shown in Figure 3.60 a and b. Firstly, a differential pulse was detected at the switch S3 using a differential measurement setup as shown in Figure 3.60 a. The one-half of the centre conductor was then used to DC bias the coupling switch in order to generate a THz pulse at S<sub>c</sub> using the conventional two-beam setup as shown in Figure 3.60 b.

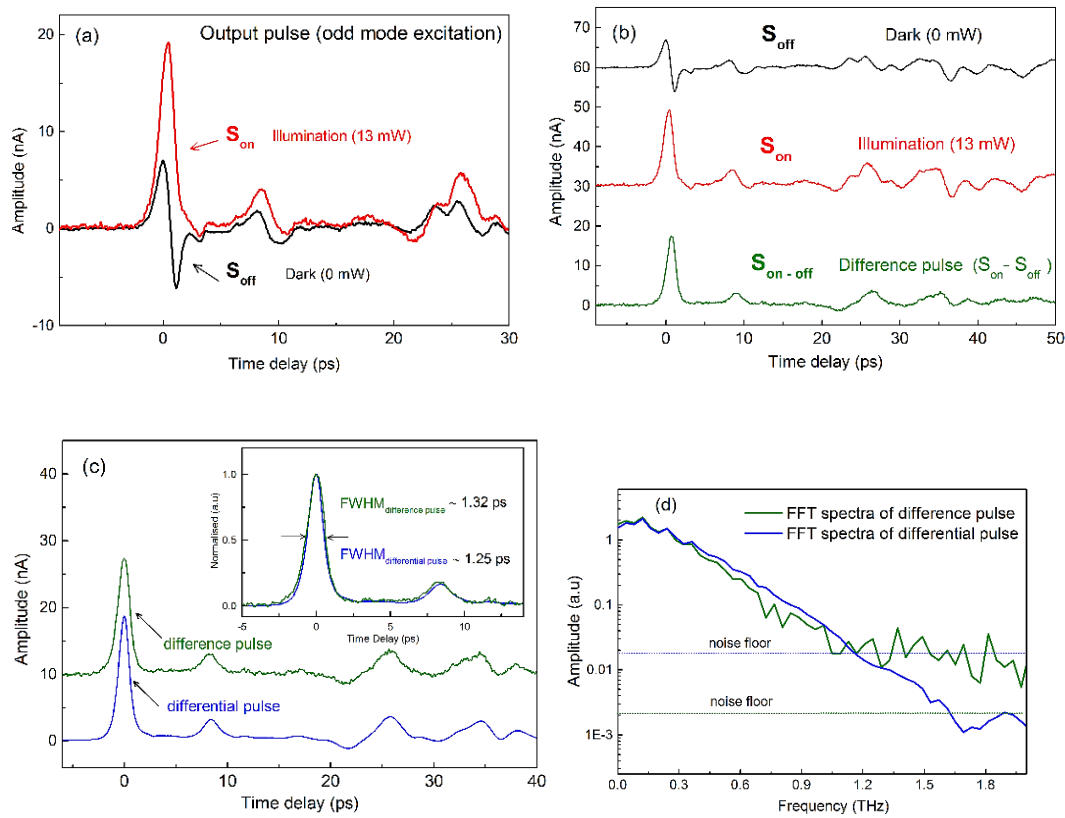


**Figure 3.60 a, b) Differential (modulated) and conventional pulse measurement setup. c) A comparison of conventional and differential pulse. d) A comparison of FFT spectra obtained from differential and conventional pulses.**

The generated THz pulse was detected by focusing probe beam onto the switch S3. THz pulses detected from the differential and conventional setup were found to be of similar shape and same polarity (shown in Figure 3.60 c), suggested that origin of both differential (modulated) and conventional pulse is same (i.e coupling switch region). However, the amplitude of differential pulse was found to be comparatively

smaller than that of the conventional pulse which is attributed to the relative difference between amplitudes of  $S_{on}$  and  $S_{off}$  THz pulses passing through the coupling switch.

Although, both differential (modulated) and conventional pulses traveled an equal distance propagating from  $S_c$  to  $S_3$ , calculated FWHM of the differential pulse ( $\sim 1.25$  ps) was found to be smaller than that of the conventional pulse ( $\sim 1.34$  ps). Also, a comparatively higher bandwidth of  $\sim 1.6$  THz compared to  $\sim 1.35$  THz for the conventional pulse, was observed from the FFT spectra of the differential pulse. The reduced broadening in the differential pulse width is likely to be caused by two possible reasons: i) The differential pulse propagating along one-half of the transmission region only carries a fundamental quasi-TEM mode of propagation (i.e., dispersive even mode with anti-symmetric field lines is not present) ii) the differential pulse has a relatively higher signal-to-noise ratio compared to conventional pulse.



**Figure 3.61** a) A comparison of “Odd mode” output pulses under dark and with laser illumination. b) A difference signal  $S_{on}-S_{off}$  was obtained by subtracting  $S_{off}$  from  $S_{on}$  c) A comparison of difference and differential pulses d) A comparison of FFT spectra obtained from difference and differential pulses.

In order to gain an insight into the characteristics of the differential pulse, THz pulses  $S_{on}$  (i.e. transmitted when switch  $S_c$  is illuminated) and  $S_{off}$  (i.e. transmitted when switch  $S_c$  is under dark condition) were separately measured with an “odd mode” excitation which ensures a symmetric field is propagating along the centre conductor.

In doing so, the chopper was moved to position A and switch  $S_3$  was illuminated by a focused probe beam. Switches  $S_1$  and  $S_2$  were then DC biased with the same polarity and simultaneously illuminated by a defocused pump beam. This allowed an “odd mode” pulse to be launched. Two consecutive scans of “odd mode” output pulse taken with and without third beam illumination (i.e. 13 mW and 0 mW beam power) resulted in output pulses  $S_{on}$  and  $S_{off}$  respectively as shown in Figure 3.61 a. A difference pulse was obtained by subtracting “odd mode” pulse  $S_{off}$  from  $S_{on}$ . Obtained difference pulse was then compared with differential pulse directly measured from a differential on-chip measurement setup. A closer look at the data indicates that both difference and differential pulses are of similar shape and polarity. However, FWHM of differential pulse  $\sim 1.25$  ps is shorter than that of the difference pulse ( $\sim 1.32$  ps). Also, the signal-to-noise ratio of difference pulse was found to be lower than that of the differential pulse. This was investigated by plotting FFT spectra in order to compare their noise levels.

The results mentioned above provide confirmatory evidence that differential THz pulse generated at  $S_c$  is due to a difference of THz pulses  $S_{on}$  and  $S_{off}$ , taking place at coupling switch  $S_c$ , owing to the switch modulation. The reduced noise level in the differential pulse can be attributed to the reduction in common mode noises associated with  $S_{on}$  and  $S_{off}$  while the coupling switch is modulated.

### 3.9.3 Mode testing

To investigate the mode of propagation of a differential THz pulse, two different sets of measurements were performed. In the first scheme, “odd” and “even” modes were excited by illuminating a pair of photoconductive switches  $S_1$ - $S_2$  by a defocused pump beam while DC bias applied across  $S_1$  and  $S_2$  as shown in Figure 3.62. The coupling switch was modulated using third beam illumination and chopper.

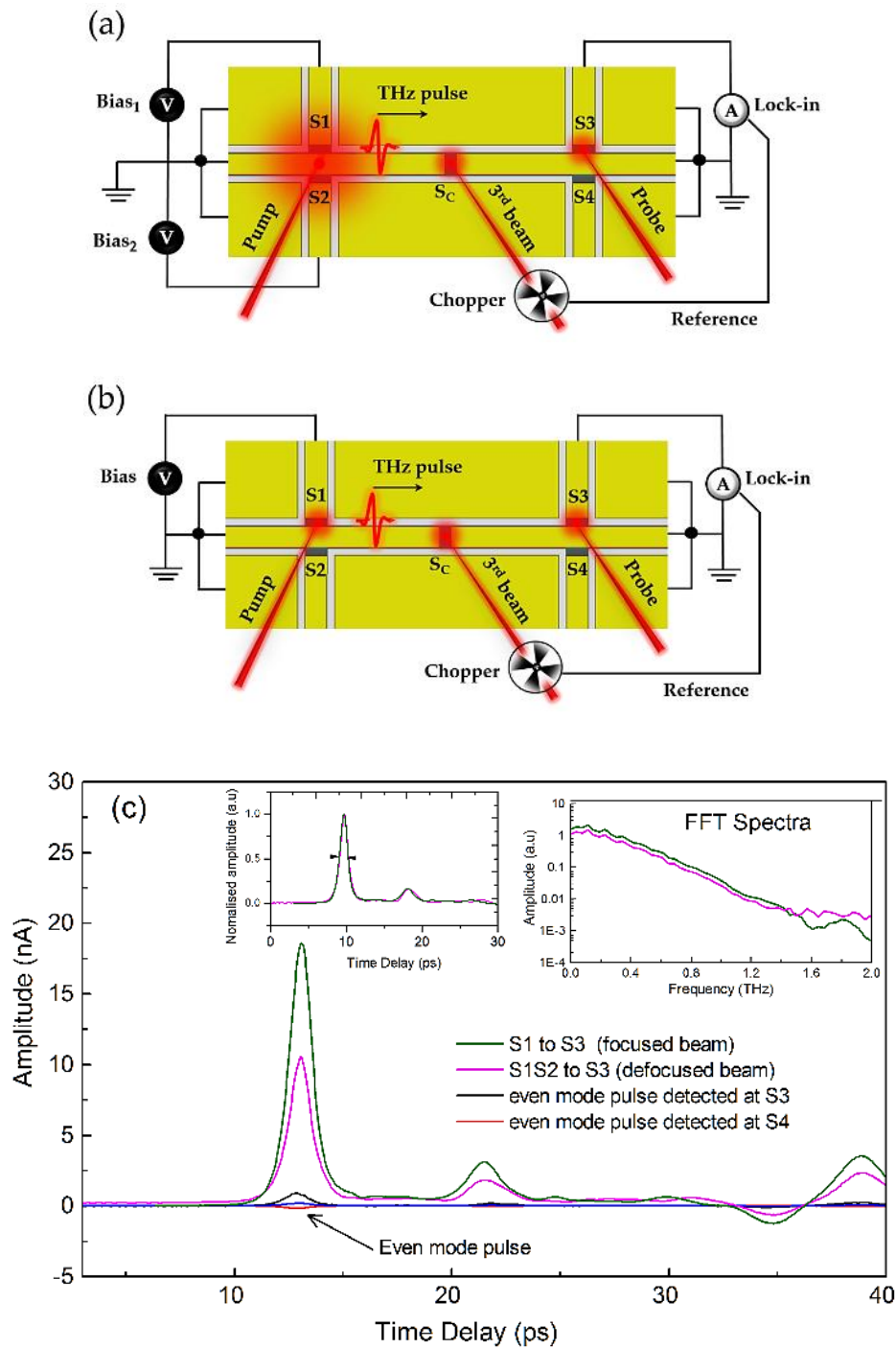
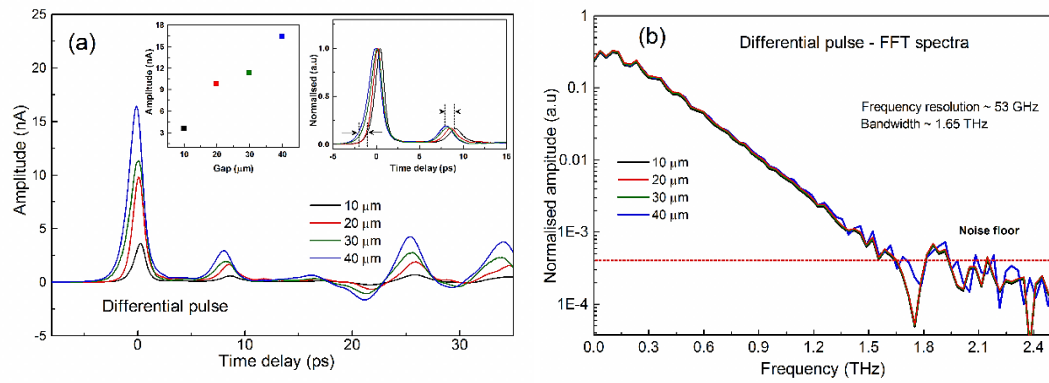


Figure 3.62 a) A schematic in which odd/even modes are launched by biasing a pair of switches and illumination with defocused pump beam b) A coupling switch filters out even mode component of field from the hybrid mode launched from switch S1 c) Output pulses measured from both measurement configurations are compared and FFT spectra of output pulses are compared in inset graph.



The generated differential pulse was then detected at the switch S3. In the second scheme, a hybrid mode pulse was launched by focusing pump beam onto DC biased switch S1, and coupling switch was then modulated in order to generate a differential pulse with subsequent detection of a pulse at S3.

Interestingly, normalised output pulses measured from both measurement schemes were found to be of the same shape, yielding equal FWHM, suggested propagation of symmetric field (odd mode) in both measurement schemes. Also, even mode output pulse much smaller in amplitude (about ~ 5% of odd mode) compared to the odd mode pulse was detected at the switch S3 in the first measurement scheme, suggested that excitation of the coupling switch only allows symmetric fields to propagate along one-half of the transmission region and anti-symmetric fields (ground to ground coupled) are not supported by the centre conductor.



**Figure 3.63** a) A comparison of differential pulses measured from CGAP-CPWs of different gap lengths (10, 20, 30 and 40  $\mu\text{m}$ ) b) A comparison of FFT spectra.

In Figure 3.62 a, differential pulses measured from 10, 20, 30 and 40  $\mu\text{m}$  gap CGAP-CPWs are compared. A comparison of time-domain differential pulses showed a relative time difference in the occurrence of pulses, which can be attributed to varying coupling switch length. In most cases, a THz pulse is launched from the metal-semiconductor interface, but it would not be feasible to pinpoint the exact location of the origin of the generated pulse within the photoconductive gap. FFT transformation performed on differential pulse yielded a useful bandwidth of ~1.65 THz.

### 3.10 Conclusion

Device design and fabrication techniques for both CPW<sub>LT-GaAs</sub> and CPW<sub>quartz</sub> were discussed. An on-chip measurement (two-beam/three-beam) was explained in detail. On-chip measurements performed on first-generation CPW<sub>LT-GaAs</sub> and CPW<sub>quartz</sub> demonstrated a full characterisation of these on-chip waveguide systems. From I-V characteristics of photoconductive switches patterned onto GaAs bulk substrate, an average value of  $\sim 5 \text{ M}\Omega$  of photoresistance was observed. However, a much higher photo resistance of  $\sim 25 \text{ M}\Omega$  was seen in epitaxially lifted-off free standing LT-GaAs switches patterned on a quartz substrate. Measurement of input and output THz pulses allowed us to measure the propagation velocity of a THz pulse in an on-chip waveguide. The propagation velocity of THz pulse in CPW<sub>LT-GaAs</sub> was calculated as  $\sim 1.13 \times 10^8 \text{ m/s}$ . A relatively higher pulse velocity of  $\sim 1.74 \times 10^8 \text{ m/s}$  was calculated for CPW<sub>quartz</sub>. Higher pulse velocity in CPW<sub>quartz</sub> is attributed to lower relative permittivity of quartz substrate as phase velocity is related to effective permittivity as  $v_p \propto 1/\sqrt{\epsilon_{eff}}$ .

Initial three-beam on-chip measurements performed on CGAP- CPW<sub>LT-GaAs</sub> showed a stronger lateral coupling of THz field between centre conductor and ground planes. Lateral coupling issue was then circumvented by employing free standing LT-GaAs switches and patterning CPW device on the quartz substrate. A useful bandwidth of 0.42 and 1.10 THz were observed from FFT spectra of output pulse measured from CPW<sub>LT-GaAs</sub> and CPW<sub>quartz</sub> using an on-chip measurement system. CGAP-CPW<sub>quartz</sub> devices demonstrated a potential use of the coupling switch as a high-pass filter (differentiator) by manipulating THz pulses. Also coupling efficiency of coupling switch with varying gap length (10, 20, 30 and 40  $\mu\text{m}$ ) was tested using a three-beam on-chip system. A differential THz-TDS on-chip system was realised using the analogy of free space differential THz-TDS. The differential THz pulse showed a useful bandwidth of 1.65 THz.

# Chapter 4

## On-Chip Measurements of Second Generation CPW Devices

### 4.1 Introduction

In Chapter 3, it was demonstrated that coplanar waveguide (CPW) devices transferred onto a quartz substrate ( $\text{CPW}_{\text{quartz}}$ ) yield a substantially higher bandwidth of  $\sim 1.10$  THz compared to that of measured from those formed on LT-GaAs ( $\text{CPW}_{\text{LT-GaAs}} \sim 0.42$  THz). However, the frequency resolution of THz pulse in  $\text{CPW}_{\text{quartz}}$  was found to be lower ( $\sim 55$  GHz) than that of observed in  $\text{CPW}_{\text{LT-GaAs}}$  ( $\sim 33$  GHz) as secondary reflections observed in the output pulse traces occurred little earlier compared to that of observed in  $\text{CPW}_{\text{LT-GaAs}}$ , owing to a higher propagation velocity of THz pulse in  $\text{CPW}_{\text{quartz}}$ . Therefore, a second generation CPW with long parasitic regions, designed in AutoCAD tool followed by the processing in the cleanroom was used in order to delay any substantial secondary reflections coming from discontinuities in the parasitic region. A THz pulse with high-frequency resolution will allow us to perform on-chip spectroscopy and to resolve THz spectral signatures in polycrystalline material overlaid onto the transmission line. Device design and characterisation of this second generation CPW device using an on-chip system will be discussed in following sections.

Further, we will discuss a low loss ( $\sim 5$  dB) THz Y-splitter (a branching waveguide system) and a Y-coupler which can both provide the spectral signatures of SUT (sample under test) and a reference signal measured from the same waveguide (using a second probe arm) in order to distinguish between spectral features, owing to sample under test and artefacts appearing due to reflections in the reference THz pulse. The differential (modulated) THz pulse measurements in a Y-coupler using a three beams excitation will also be discussed.

## 4.2 Second generation CPW device design

In the second generation device design, a transmission region of 1 mm was designed along with parasitic regions consisting of biasing/probing arms. As discussed in Chapter 3, attenuation losses are added to THz pulse over the length of propagation, and therefore, a shorter transmission length of 1 mm compared to that (1.5 mm) of the first-generation CPW<sub>quartz</sub> device was chosen in order to minimise attenuation loss, and to obtain higher bandwidth. Results obtained using the Ansys High-Frequency Structure Simulator (HFSS) on CPWs with different transmission lengths are discussed in Chapter 5.

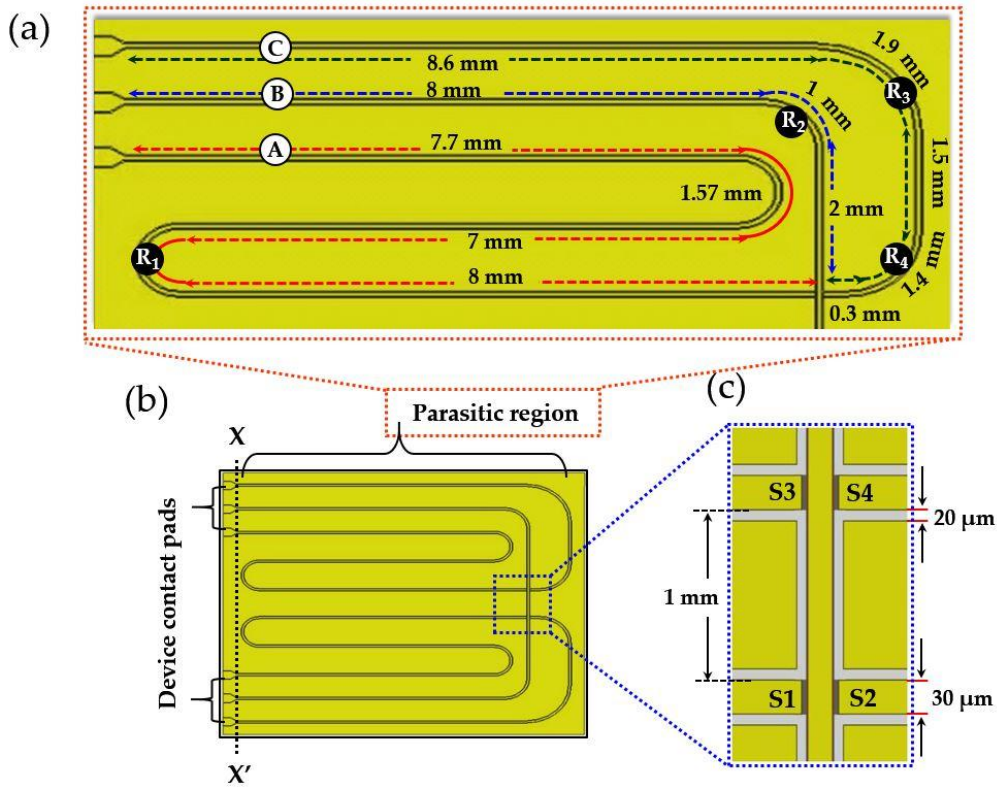


Figure 4.1 The second generation CPW device a) A magnified view of the parasitic region. b) A four photoconductive switch layout with parasitic regions. c) A magnified view of photoconductive switch regions.

### 4.3 PCB layout

The second generation CPW device, after cleanroom processing, was then mounted on to a modified portable PCB chip (compatible with both room and low-temperature measurements) for electrical connections. In this modified PCB design, the outermost copper tracks were used to ground the ground planes in the CPW, while the remaining copper tracks were used to provide electrical connection to biasing and probing arms as shown in Figure 4.2.

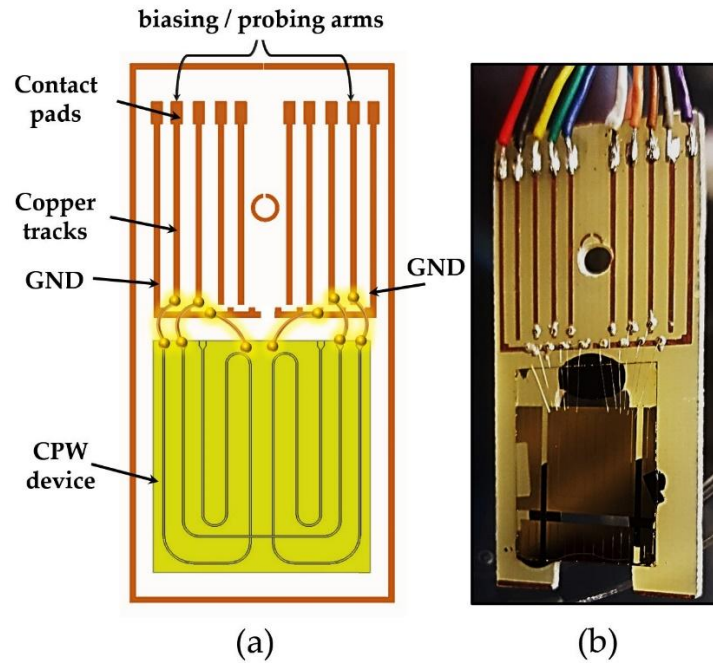


Figure 4.2 A PCB layout for the second generation CPW device and mounting PCB compatible with both room and low-temperature operation.

### 4.4 Characterisation of the second generation CPW device (quartz substrate)

This section will give an overview of the on-chip measurements performed on the second generation CPW<sub>quartz</sub> device in order to obtain the device characteristics. A full

characterisation involves DC measurements of the photoconductive switches, generation, and detection of THz pulses, the bias voltage and power dependence of the THz pulses and excitation of odd/even modes. Firstly, switch characterisation was performed as discussed in the following section.

#### 4.4.1 Switch characterisation

IV sweep measurements were performed on the photoconductive switch S2 and S4, used as generation and detection switch respectively, by varying the applied bias (-20 V to +20 V) across the switches. Laser power was then varied from 0 to 10 mW for each set of measurements. The dark resistance of photoconductive switches S2 and S4 was measured as being of the order of few G $\Omega$ . This high dark resistance ensures suppression of background DC photocurrent as seen in CPW<sub>LT-GaAs</sub>. IV curves showed relatively ohmic behaviour for a whole range of bias applied across the switch. Photoconductive switch S4 showed a relatively high photo-resistance ( $\sim 28\text{ M}\Omega$ ) compared to switch S2 ( $\sim 24\text{ M}\Omega$ ).

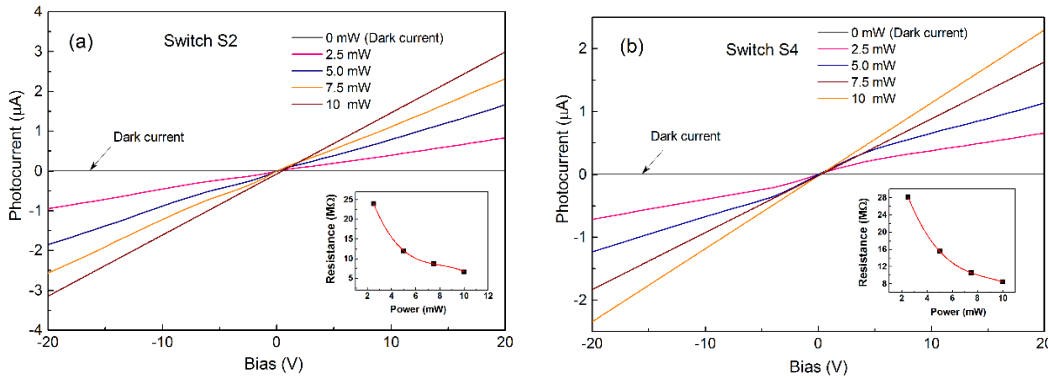
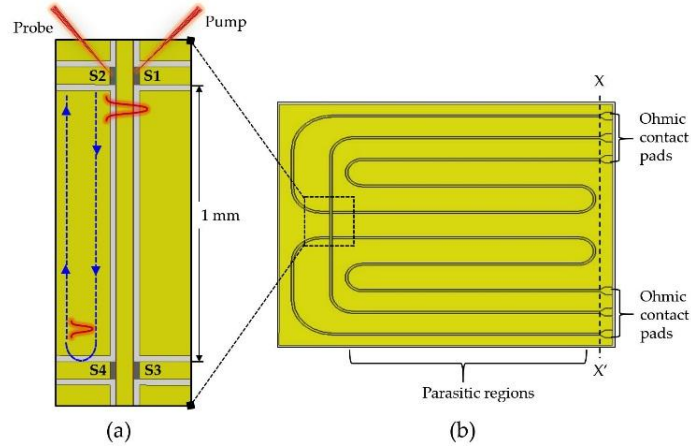


Figure 4.3 IV characteristics of switch S2 and S4 with varying bias and laser power.

#### 4.4.2 Input pulse detection

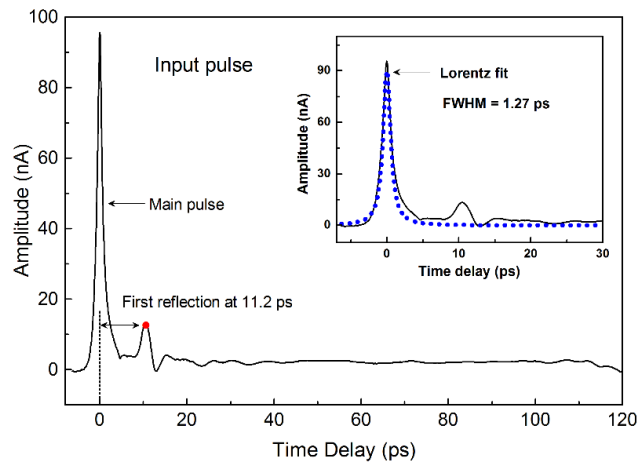
Input pulses were detected at the switch S2 by focusing the pump and probe beams onto the switch S1 and S2 respectively. A bias voltage of 20 V was then applied across the switch S1. In a time-window of 120 ps, traces of input pulses showed the main pulse followed by only a single secondary reflection occurring at 11.2 ps, showing that the other reflections, seen in traces of the input pulse measured in the first-generation

CPW device (see Chapter 3) were indeed being delayed by the long parasitic regions in the second generation CPW as shown in Figure 4.5.



**Figure 4.4** a) Magnified view of transmission region in which a reflection coming from the photoconductive switch region S3-S4 is shown by the blue dashed line. b) Overall schematic of input pulse detection for the second generation CPW device.

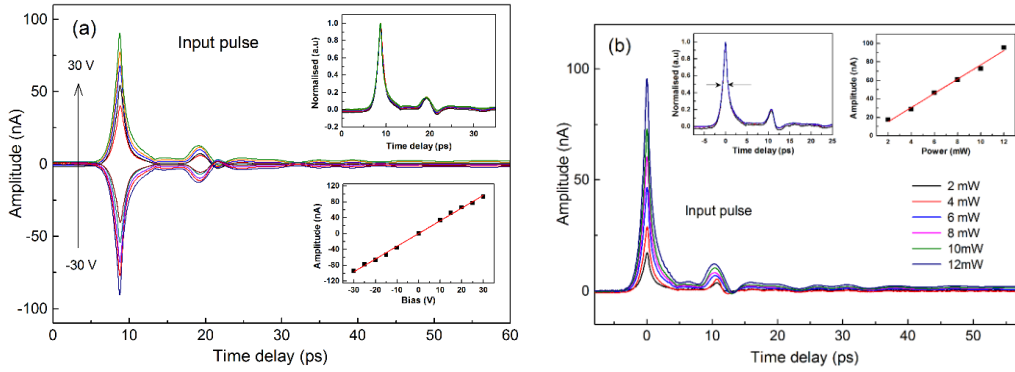
The origin of this single reflection was found to be the photoconductive switch region formed by S3-S4 as those switches were not illuminated while an input pulse was detected at the switch S2. Therefore, switch region S3-S4 offers a higher impedance (compared to switch region S1-S2) to the incoming input pulse, resulting in a pulse reflection (shown in Figure 4.4).



**Figure 4.5** Trace of an input pulse in a time-window of 120 ps, in which the main pulse is followed by a secondary reflection occurring at 11.2 ps after the main pulse and a Lorentz fit to the main pulse is shown in inset graph.

A Lorentz fit to the main pulse revealed a FWHM of  $1.27 \pm 0.02$  ps. The shorter FWHM (compared to that of CPW<sub>LT-GaAs</sub>) in the quartz CPW device is attributed to the higher dark resistance of free standing photoconductive switches on a quartz substrate.

To further characterise the detected input pulse, measurements with varying bias and laser power were performed. The bias and power dependence characteristics of the input pulse are shown in Figure 4.6 a and b respectively. A linear dependence on both the bias and applied power were observed as shown by the linear fit to peak amplitude of the main pulse shown in the inset graphs in Figure 4.6.



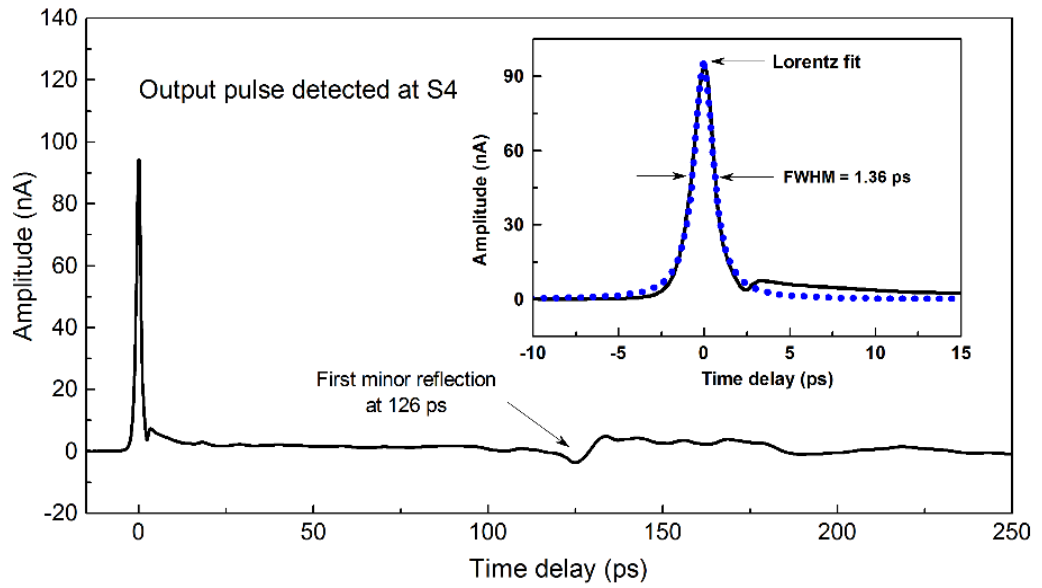
**Figure 4.6** Traces of the input pulse in a time-window of 60 ps a) Amplitude of input pulse as a function of varying bias. b) The amplitude of input pulse as a function of varying the laser power and a Lorentz fit to peak amplitude is shown in inset graphs.

#### 4.4.3 Output pulse detection

Output pulses were detected by focusing a time-delayed probe beam onto the switch S4 while a bias of 20 V was applied across the switch S1. The pump beam was then focused onto the switch S1 in order to generate a THz pulse. As discussed in the previous section reflections could here be potentially delayed, owing to the long parasitic regions. Therefore, a longer scan (250 ps time-window) was performed by time delaying the probe beam using a longer optical delay stage. A trace of the output pulse in a time-window of 250 ps showed the main pulse followed by a secondary reflection with substantially reduced amplitude occurred at 126 ps delay after the main pulse as shown in Figure 4.7. The origin of this reflection was found to be the ohmic contact pad of parasitic region B and (represented as X-X', shown in Figure 4.1).

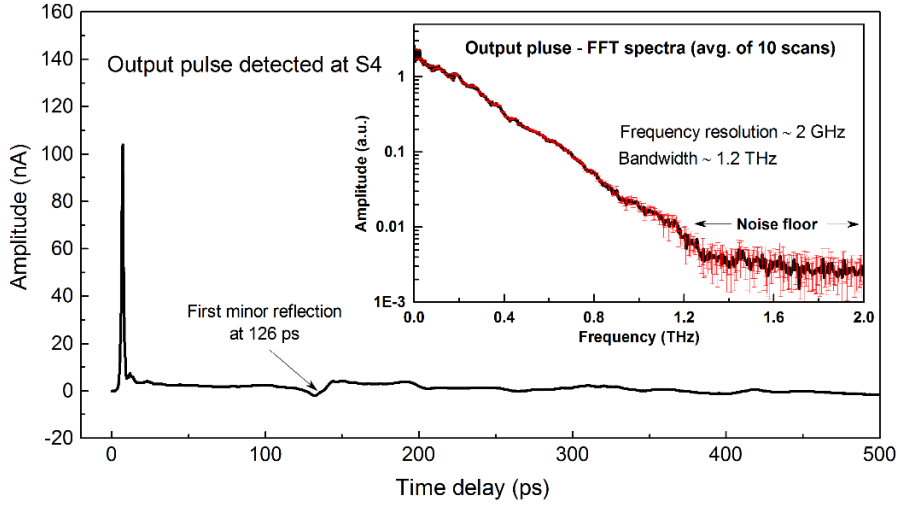


A Lorentz fit to the main pulse revealed a FWHM of  $\sim 1.36 \pm 0.02$  ps, suggesting less broadening of pulse compared to that of measured from the first generation ( $\sim 1.41$  ps) CPW<sub>quartz</sub>. The less broadened pulse width is attributed to the shorter transmission region (1 mm compared to 1.5 mm in first-generation CPW) in second generation CPW devices.



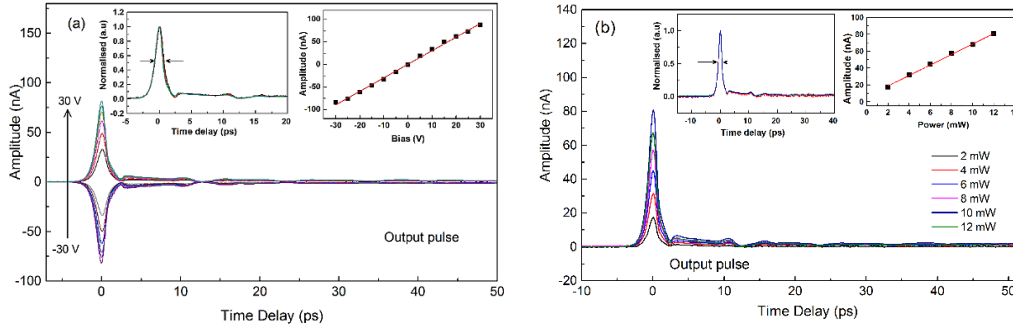
**Figure 4.7** A trace of an output pulse, in which the main pulse is occurring at zero time delay is followed by a minor reflection occurred at 126 ps and Lorentz fit to the main pulse is shown in inset graph.

As no secondary reflections with significant amplitude were observed in the output pulse trace, data points were not truncated before performing the FFT in order to estimate useful bandwidth present in the output pulse. To investigate the useful bandwidth, an FFT was then performed on the output pulses measured across ten consecutive scans. An average of the FFT results was then plotted against standard deviation as shown in Figure 4.8.



**Figure 4.8** A trace of an output pulse detected in a time-window of 500 ps and an average of ten FFT spectra plotted against standard deviation in inset graph.

A useful bandwidth of  $\sim 1.2$  THz was observed in the FFT spectra taken as the point where the signal fell below the level of the noise present in the FFT spectra. As data points were not truncated before performing the FFT, a frequency resolution of  $\sim 2$  GHz was obtained for the 500 ps time-window.



**Figure 4.9** Traces of output pulses a) A linear bias dependence shown by a linear fit to peak amplitude in inset graph. b) A linear power dependence shown by a linear fit to peak amplitude.

Traces of the output pulses measured by varying applied bias ( $-30$  to  $+30$  V) and varying laser power (2 to 12 mW) showed a linear dependence on both applied bias and laser power as shown in Figure 4.9 a and b.

#### 4.4.4 Pulse velocity (quartz substrate)

Traces of two output pulses were detected (in the same time-window) at S2 and S4 by swapping their biasing and probing connections. In Figure 4.10, the relative time difference between two output pulses was found to be 11.48 ps and zero time delay point indicated the origin of generated input pulse. Velocity of pulse was then calculated as,  $V_p = 2l_t/\Delta t = 1.74 \times 10^8 \text{ m/s}$ . Therefore, velocity of THz pulse remains same ( $1.74 \times 10^8 \text{ m/s}$ ) between the first and second generation CPW<sub>quartz</sub> devices, as expected.

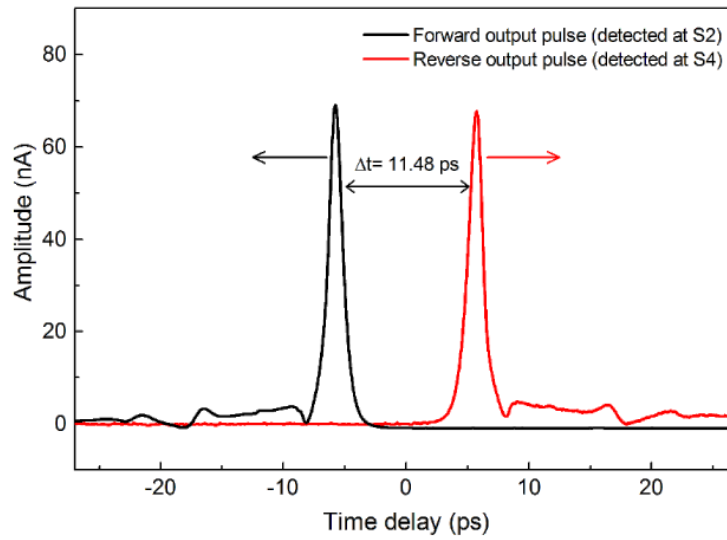
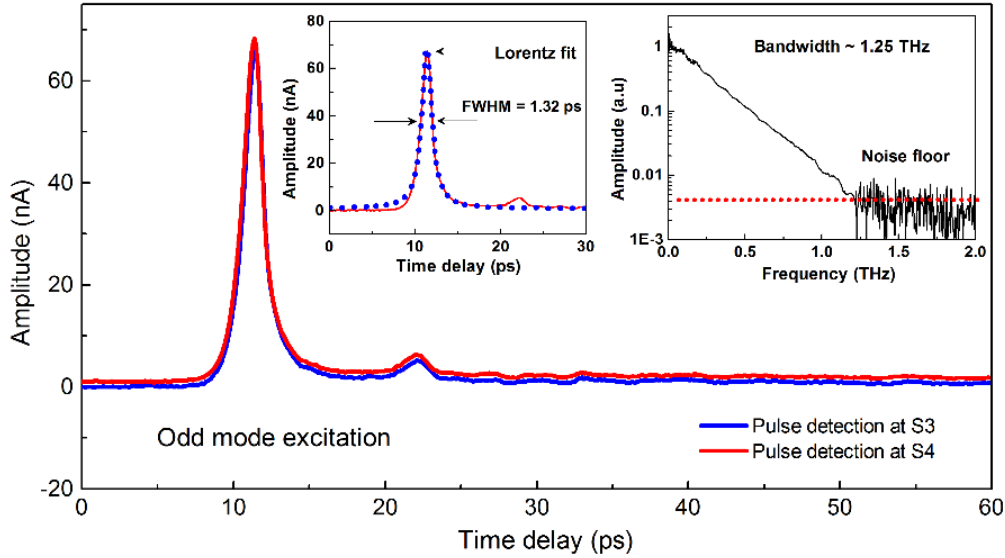


Figure 4.10 Traces of two output pulses detected at switch S2 and S4 respectively, where zero time delay represents the origin of input pulse generation.

#### 4.4.5 Coplanar mode (Odd mode)

“Odd mode” output pulses were detected at the switch S3 and S4 in two consecutive scans by focusing the probe beam onto the switch S3 and S4 respectively. A pair of photoconductive switches S1-S2 were simultaneously illuminated by a defocused pump beam while a bias voltage of 20 V (with the same polarity) was applied across both S1 and S2 in order to excite an odd mode pulse. The detected output pulses were both of the same polarity, indicating propagation of a symmetric field along the CPW.

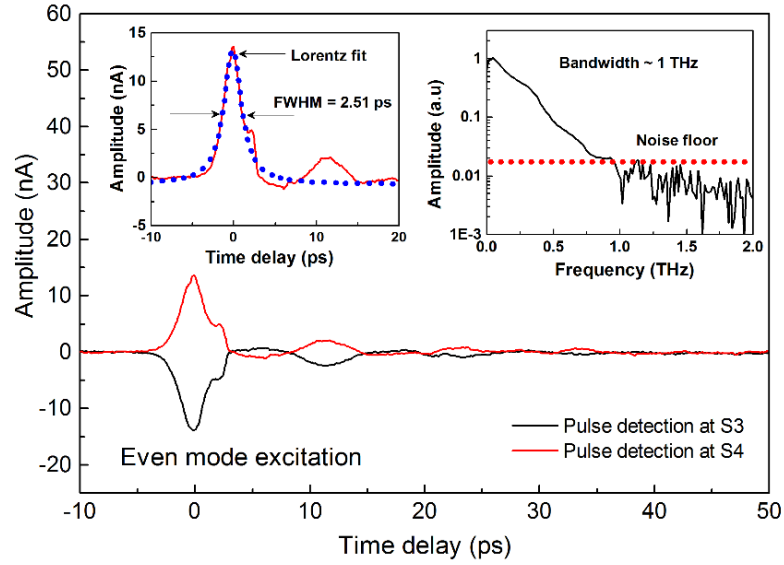


**Figure 4.11** Detection of an output pulse at switch S3 and S4 (in two consecutive scans) in odd mode excitation. Lorentz fit to main pulse and FFT spectra of output pulse are shown in inset graphs.

A Lorentz fit to the main pulse revealed a FWHM of  $\sim 1.32$  ps, slightly shorter than that of measured from hybrid mode-output pulse ( $\sim 1.36$  ps), suggesting dispersive even-mode field components were suppressed. Further, a useful bandwidth of 1.25 THz was observed from FFT performed on “odd mode” output pulse without applying a truncation window.

#### 4.4.6 Slot line mode (Even mode)

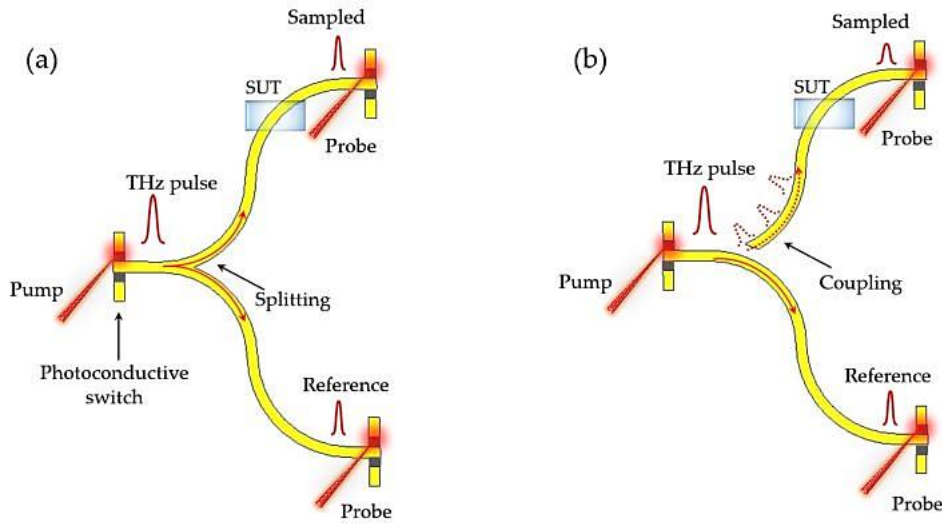
For completeness, the even mode was then excited by reversing the polarity of bias applied across the switch S2, and “even mode” output pulses were then detected at the switch S3 and S4 in two consecutive scans. The detected “even mode” output pulses were of different polarity as was expected from an anti-symmetric field propagating along the CPW. The FWHM was calculated by a Lorentz fit to the main pulse as  $\sim 2.51$  ps, which was broader than that of measured from the “odd mode” output pulse, suggesting even mode pulses were more dispersive in nature. A useful bandwidth of 1 THz was observed from FFT spectra of the “even mode” output pulse.



**Figure 4.12** Detection of an output pulse at switch S3 and S4 (in two consecutive scans) in even-mode excitation. Lorentz fit to main pulse and FFT spectra of output pulse are shown in inset graphs.

## 4.5 THz Y-splitter and coupler

In on-chip THz spectroscopy of polycrystalline materials, it is vital to compare the sampled pulse (interacted with a sample under test) with a reference pulse in order to distinguish their spectral features in frequency-domain. In an on-chip spectroscopy measurement, SUT such as polycrystalline material (lactose) can potentially be overlaid onto the transmission region and the spectral signature of the SUT then extracted from the sampled THz pulses. However, the SUT may need to be removed in order to measure a reference pulse again or to perform spectroscopy of a different material. In doing so, some residue of SUT may remain on the top of the transmission region of the on-chip waveguide, not permitting the reference pulse to be measured correctly. Therefore, an on-chip waveguide with multiple transmission regions is desirable in order to measure the reference and sampled pulses separately. Nevertheless, using a branching waveguide structure such as a Y-splitter or coupler capable of splitting the THz pulses allows pulses to be directed to different branching waveguides. The reference and sampled pulses can then be measured separately as shown in Figure 4.13.



**Figure 4.13** An illustration of THz pulse splitting (sampled and reference pulses) in an on-chip spectroscopy measurement a) Y-splitter loaded with SUT. b) Y-coupler loaded with SUT.

Over the last few decades, a planar Y-splitter design has been used in a variety of applications such as power splitters, Mach-Zehnder interferometers, and photonic crystal splitters [162-165] at a frequency of operation up to few GHz. However, planar Y-splitters operating in the THz frequency range (for broadband applications) have not yet been studied. We, therefore, here investigate a THz Y-splitter engineered in an on-chip CPW, capable of splitting THz pulses. We also investigate a Y-coupler, which can re-direct a THz pulse (by modulating the conductivity of coupling switch using the third beam) from one branching waveguide to another, unlike straight waveguide structures which allow pulse propagation only in one direction. The Y-coupler was engineered in such a way that the two branching waveguides are separated only by a 20  $\mu\text{m}$  gap.

#### 4.5.1 Device Design

In this Y-splitter device design, a low branching angle of  $30^\circ$  was chosen as larger splitting angles would be likely to cause more losses [166, 167], and in order to keep transmission losses low while the THz pulse is being split, as shown in Figure 4.14. Branching waveguides each of 2.18 mm long were engineered by connecting two arcs with a radius of curvatures of 600  $\mu\text{m}$  and 615  $\mu\text{m}$  in series. A symmetric design of Y-splitter ensures the equal splitting of the THz pulse between the two branching

waveguides. On-chip measurements of splitter CPW devices fabricated on both LT-GaAs and quartz substrates were performed.

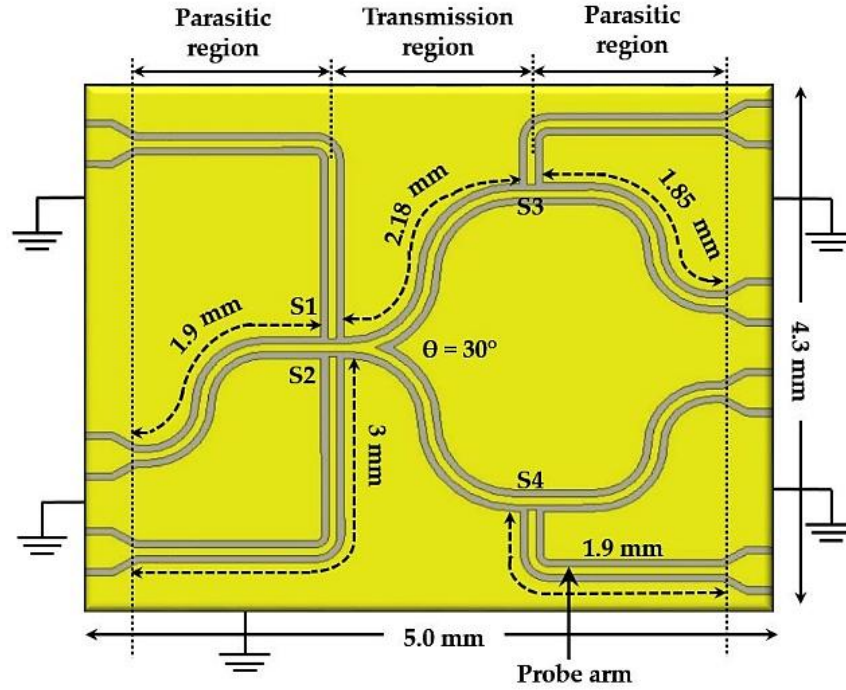


Figure 4.14 A schematic representation of THz Splitter device design.

A Y-coupler was engineered by separating branching waveguides ( $Y_A$  and  $Y_B$ ) by a 20  $\mu\text{m}$  coupling gap as shown in Figure 4.15. The Y-coupler CPW was first fabricated on a quartz substrate in order to incorporate free-standing LT-GaAs switches for THz generation and detection. In this Y-coupler CPW, the waveguide branch  $Y_B$  acts as a continuous CPW, allowing THz pulses to propagate from the generation switch (S1 or S2) to detection switch S4. On the other hand, the branching waveguide  $Y_A$  placed at an angle of  $30^\circ$  with respect to  $Y_B$  acts as a coupler. THz fields propagating along  $Y_B$  may be coupled to  $Y_A$  through the coupling gap (provided the coupling waveguide is properly grounded). The degree of THz field coupling can then be controlled by modulating the conductivity of coupling switch  $S_c$  (fabricated by epitaxial lift-off LT-GaAs layer) using a three-beam on-chip system.

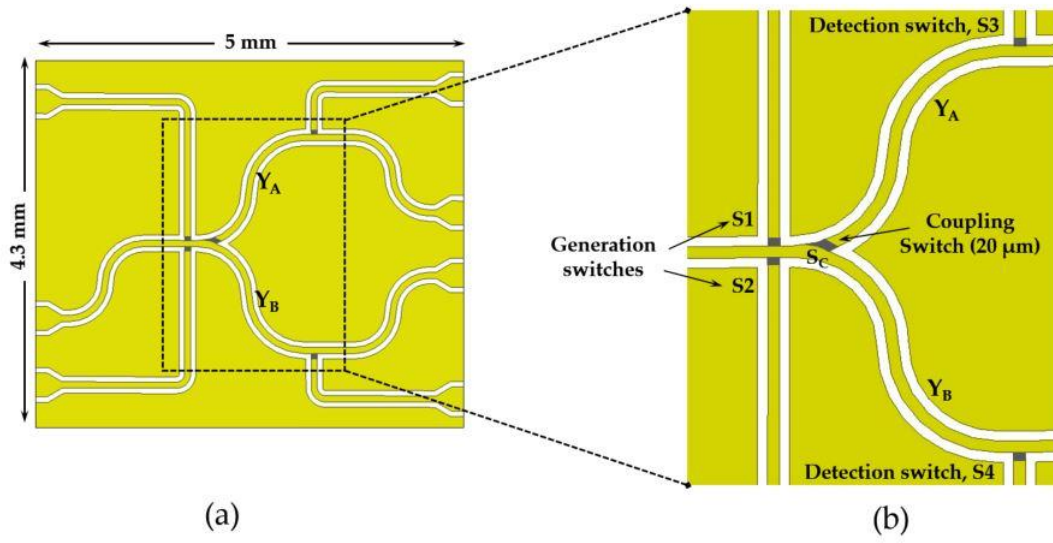
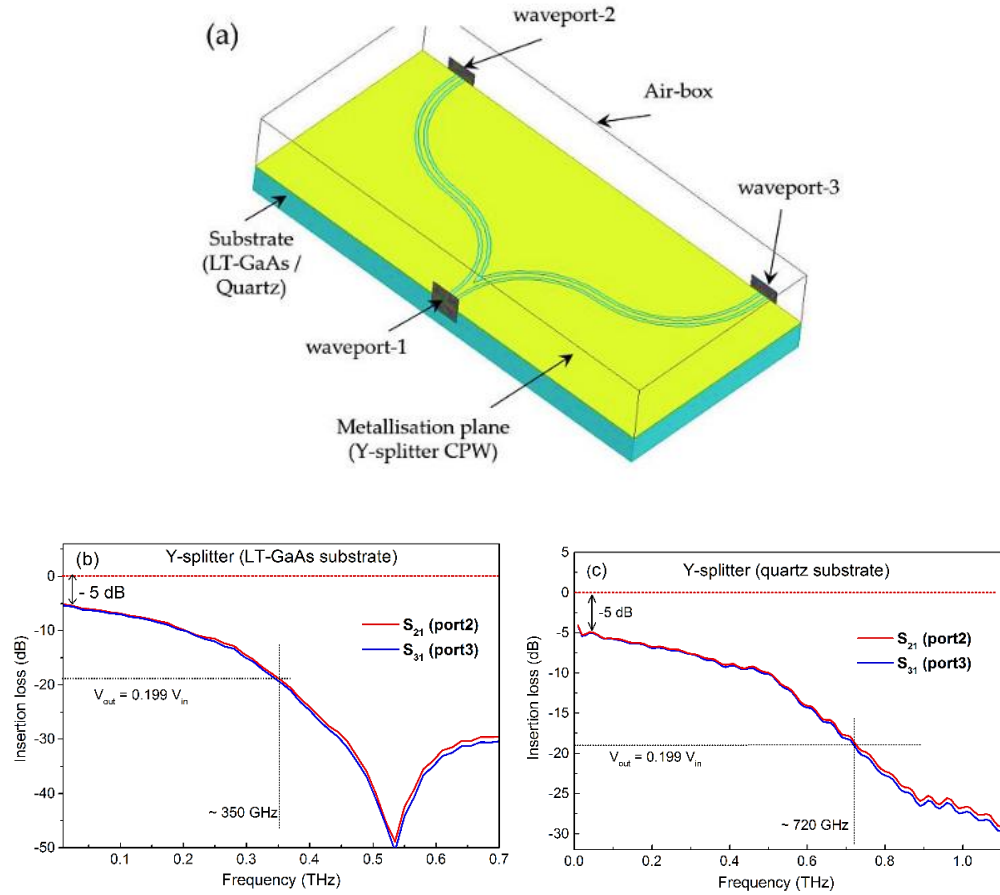


Figure 4.15 a) Schematic representation of a Y-coupler fabricated on a quartz substrate. b) Detail, in which free standing LT-GaAs switches are pointed as S1, S2, S3, S4, and S<sub>C</sub>.

#### 4.5.2 Simulation model of Y-splitter and coupler

Before performing on-chip measurements, electromagnetic simulations (HFSS) were carried out to investigate the frequency response of the Y-splitter and coupler. In doing so, a 3D model of the Y-splitter comprising the centre conductor and ground planes was simulated in HFSS. The Y-splitter dimensions were chosen to align with the proposed device design such that the centre conductor width was 0.03 mm, the slot gap between the centre conductor and ground plane was 0.02 mm wide, and the splitting angle (often called as branching angle) was 30°. Three waveports were assigned to the Y-splitter in order to obtain the scattering parameters from the branching CPWs as shown in Figure 4.16. After defining the design parameters of Y-splitter CPW, simulations were made in the frequency range of 0.01 to 1.1 THz with a solution frequency set to 1 THz. In Figure 4.16 b and c, the transmission and reflection parameters  $S_{21}$  and  $S_{31}$  obtained for both GaAs and quartz substrate are plotted as a function of frequency.



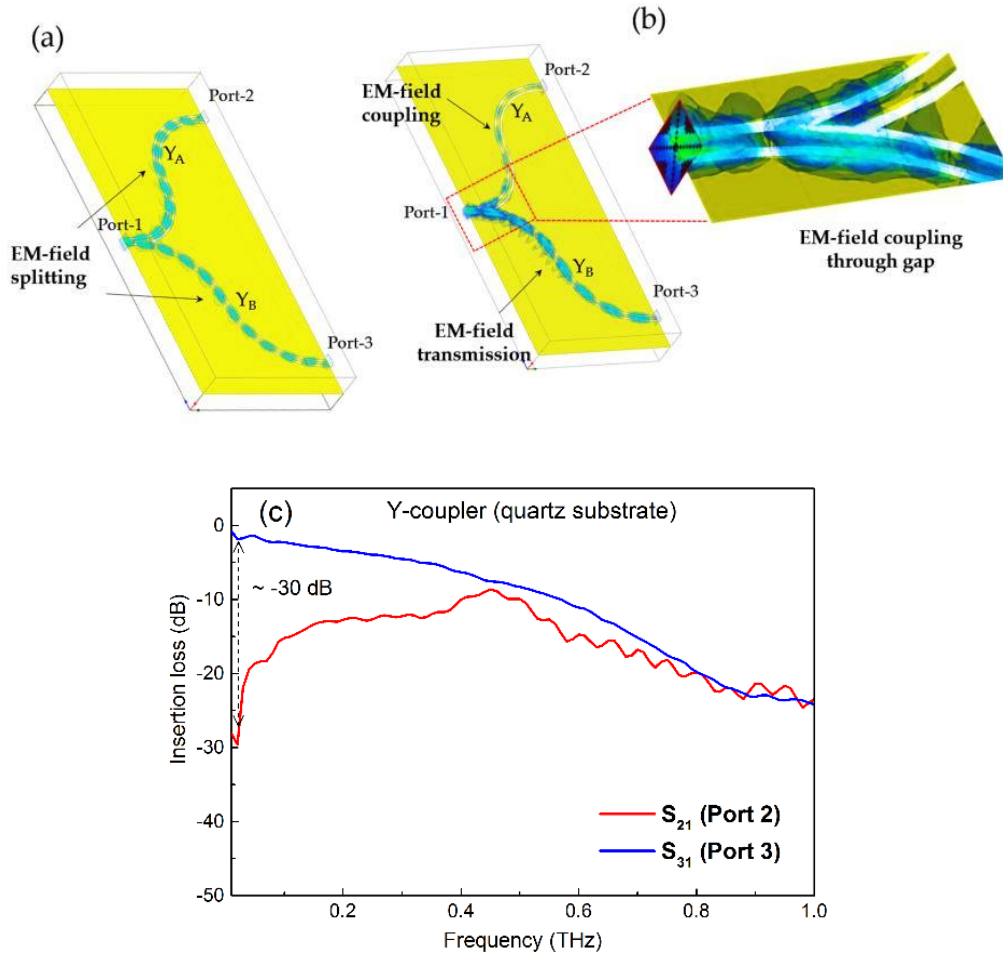


**Figure 4.16** a) 3D simulation model of a Y-splitter. b) Scattering parameters obtained from Y-splitter on a GaAs substrate. c) Scattering parameters obtained from Y-splitter on a quartz substrate.

It is clear from the graph (Figure 4.16) that EM-energy fed on waveport-1 was equally split and transmitted along branching waveguides. Scattering parameters obtained from Y-splitter on GaAs substrate showed higher attenuation compared to that of obtained from the quartz substrate, owing to the higher permittivity of GaAs (12.9). Also, a resonance feature was observed at ~ 530 GHz, owing to excitation of higher-order modes. An insertion loss of ~ 5 dB was observed for both GaAs and quartz substrates, attributed to the splitting angle of  $30^\circ$  in the Y-splitter CPW. The insertion loss could be further minimised by choosing a small branching angle, but this could have the effect of increasing coupling between the two branches. We take the -14 dB roll off (the point at which the signal amplitude falls to 20% of its initial value - see Chapter 2) as a reference to estimate the bandwidth of the Y-splitter on both GaAs and quartz substrate. As shown in the plots in Figure 4.16 b and c, the bandwidths of the Y-splitter

so estimated as 350 and 720 GHz for GaAs and quartz substrates respectively.

Furthermore, a Y-coupler with 20  $\mu\text{m}$  coupling gap was also simulated on a quartz substrate in order to estimate coupling efficiency. Design parameters were similar to that of chosen for Y-splitter except that branching waveguide  $Y_A$  was separated by a coupling gap of 20  $\mu\text{m}$ .



**Figure 4.17** EM-field a) An equal EM-field splitting between  $Y_A$  and  $Y_B$  shown in the Y-splitter, simulation model. b) A weak coupling between straight CPW and  $Y_A$  of EM-field shown in a Y-coupler simulation model. c) Scattering parameters  $S_{21}$  and  $S_{31}$  obtained from port 2 and port 3 respectively in a Y-coupler.

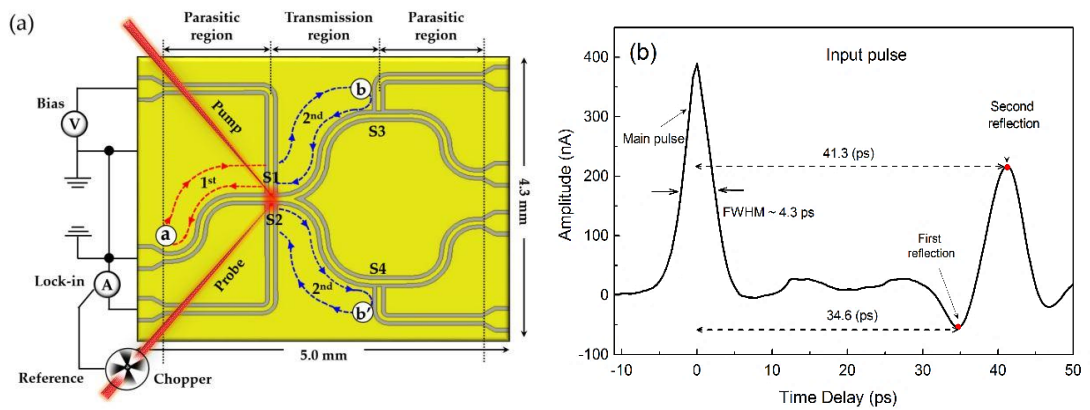
A relatively weak coupling of the EM field (compared to the branching waveguide  $Y_B$ ) with a coupling loss of  $\sim -30$  dB at low frequencies was observed in branching waveguide  $Y_A$  from simulation results as shown in Figure 4.17 c.

## 4.6 On-chip measurements of Y-splitter CPW (LT-GaAs substrate)

On-chip measurements of the Y-splitter were performed using a pump-probe beam on-chip system in order to extract the characteristics of the split THz pulses.

### 4.6.1 Input pulse detection

In the Y-splitter, the input pulse was detected at the switch S2 by focusing pump and probe beams onto the switch S1 and S2 respectively. In doing so, a bias of 30 V was also applied across the switch S1 while the probe arm of the switch S2 was connected in series with the lock-in amplifier in order to measure the generated THz pulses as shown in Figure 4.18 a.

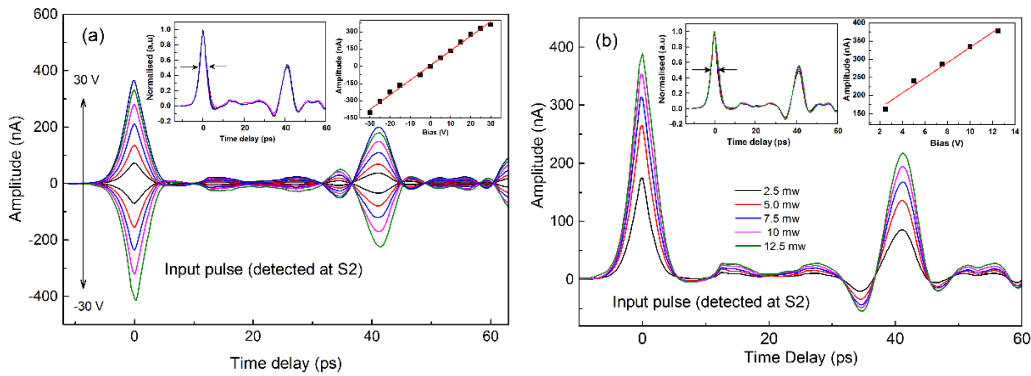


**Figure 4.18 Input pulse detection a) A schematic representation of generation and detection of an input pulse in Y-splitter waveguide. b) Trace of an input pulse, in which the main pulse is followed by two secondary reflections occurring at 34.6 and 41.3 ps after the main pulse.**

A trace of the input pulse measured in the time-window of 50 ps, showed the main pulse followed by two secondary reflections occurred at 34.6 and 41.3 ps after the main pulse, as shown in Figure 4.18 b. The origin of the first reflection was found to be the ohmic contact pad in the parasitic region (marked "a" in Figure 4.18 a). The origin of the second reflection was found to be the high impedance of photoconductive switch regions S3 and S4 (marked as "b" and "b' ") since they were not illuminated while input pulse measurement was performed. Interestingly, the amplitude of the second

reflection was found to be much higher than that of the first reflection in input pulse trace, probably owing to the constructive interference of the reflections coming simultaneously from both switch regions S3 and S4 as shown in Figure 4.18 a. Lorentz fit to the main pulse showed a FWHM of  $\sim 4.3$  ps.

To further characterise the input pulse, the bias across the switch S1 was varied from -30 to +30 V while the laser power was fixed at 10 mW in each set of measurements. A linear fit to the peak amplitude showed a linear dependence on the bias as shown in Figure 4.19 a. A linear dependence on laser power (as it varied from 2.5 to 12.5 mW) was observed in Figure 4.19 b, while a fixed bias of 30 V was applied across the switch S1.



**Figure 4.19** Traces of the input pulse measured from a Y-splitter waveguide a) Traces of input pulse as a function of varying bias. b) Traces of input pulse as a function of varying laser power, a linear fit to peak amplitude is shown in inset graphs.

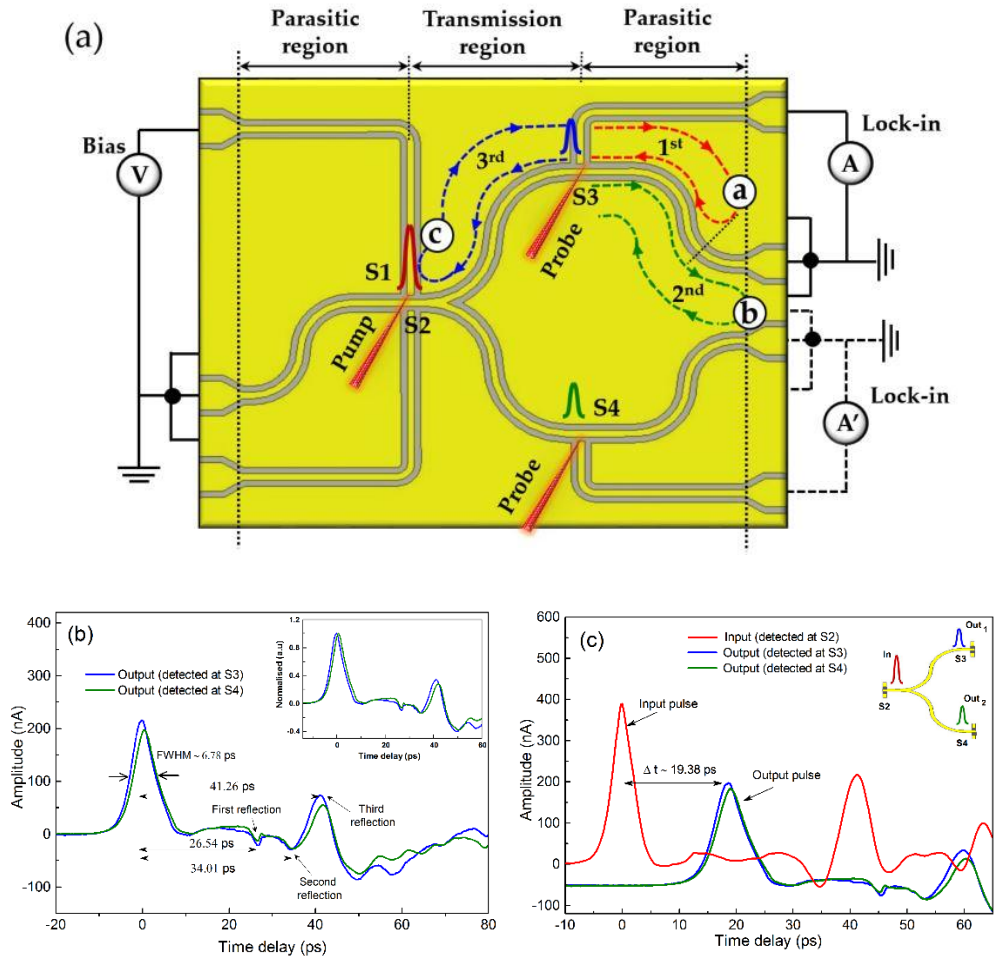
#### 4.6.2 Pulse detection for a split output

Split THz pulses were detected by focusing a time-delayed probe beam onto switches S3 and S4 in two consecutive scans. In doing so, the lock-in amplifier was moved from the switch S3 to S4, (indicated as "A'" in Figure 4.20 a). The detected output pulses were found to be of the same shape and polarity, suggesting that splitting of the input THz pulse did not change its phase, for example.

However, traces of output showed a relative time difference of  $\sim 0.2$  ps, owing to a relative change in path length of the probe beam while moving from the switch S3 to S4. The small difference in amplitude of detected output pulses also observed can be understood as arising from the photoconductive switches S3 and S4 not being identical. In a time-window of 80 ps, traces of the output pulse showed the main pulse followed

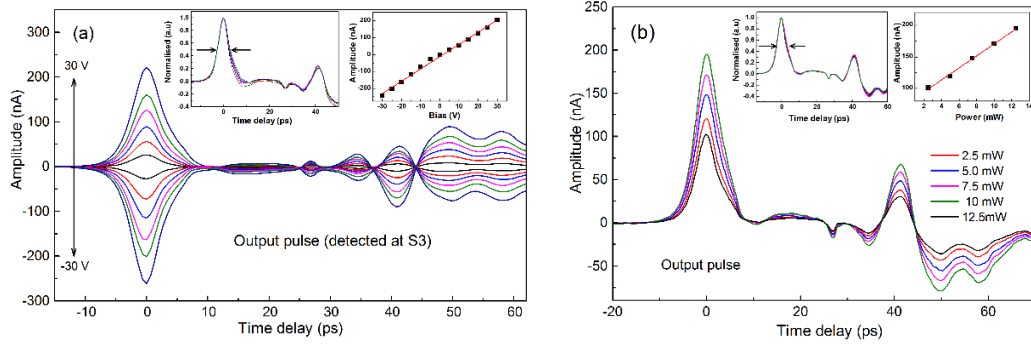
by the secondary reflections occurred at 26.54, 34.01 and 41.26 ps after the main pulse.

The FWHM of the output pulse was calculated as  $6.78 \pm 0.2$  ps by fitting a Lorentz peak function to the main pulse. The FWHM of the output pulse was found to be relatively higher than that measured in the first-generation LT-GaAs CPW devices due to the longer transmission region of 2.18 mm (compared to 1.5 mm long transmission region of the first-generation CPWs) in the Y-splitter CPW, causing additional attenuation to the output pulse. Also, bend discontinuities in the Y-splitter can excite higher-order dispersive modes, causing pulse broadening.



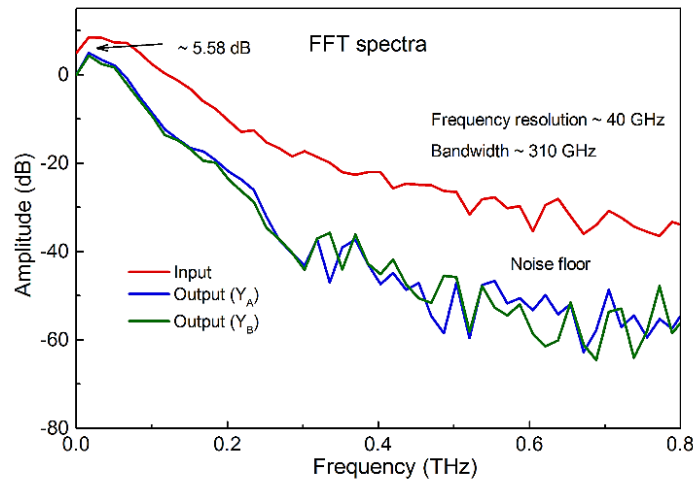
**Figure 4.20** An output pulse detection in a Y-splitter (LT-GaAs substrate) a) A schematic representation of detection of split THz pulses in the Y-splitter waveguide. b) Traces of output pulses, in which the main pulse is followed by secondary reflections occurring at 26.54, 34.01 and 41.26 ps after the main pulse. c) Traces of input and output pulses with a relative time difference of  $\sim 19.38$  ps measured in the same time-window ( $\sim 70$  ps).

The origin of the first reflection was found to be a bend discontinuity (indicated as “a”) in the parasitic region. The second reflection was found to be the ohmic contact pad discontinuity (pointed out as “b”) located in the parasitic region. The origin of the third reflection was found to be the photoconductive switch region S1-S2. In Figure 4.20, traces of the input and output pulses with a relative time-delay of 19.38 ps were detected in the same time-window of 70 ps.



**Figure 4.21** Traces of output pulses measured from a Y-splitter a) As a function of varying bias. b) As a function of varying laser power; a linear fit to peak amplitude is shown in the inset graphs.

Traces of the output pulses measured by varying applied bias (-30 to +30V) and varying laser power (2.5 to 12.5 mW) showed a linear dependence on both the applied bias and laser power as shown in Figure 4.21 a and b.



**Figure 4.22** FFT spectra of input (shown in red) and output pulses (shown in blue and green) measured from the Y-splitter on GaAs substrate.

Furthermore, FFT spectra of the input and output pulses (by performing Fourier transformation on input and output pulses) were compared in order to estimate insertion loss due to the splitting of THz pulse. An insertion loss of  $\sim -5.58$  dB was observed from FFT spectra of the input and output pulse plotted (in dB) as a function frequency. The observed insertion loss of  $\sim -5.58$  dB (at lower frequencies) was found to be in good agreement with the estimated insertion loss of  $\sim -5$  dB from HFSS simulations. A frequency resolution of 40 GHz was obtained by truncating the time-domain output pulses at 25 ps time delay relative to the main pulse. We note that the FFT spectra of the output pulse showed a useful bandwidth of  $\sim 310$  GHz, which is slightly smaller than that estimated ( $\sim 350$  GHz) from the HFSS simulations (shown in Figure 4.16 b).

## **4.7 On-chip measurements of Y-splitter CPW (quartz substrate)**

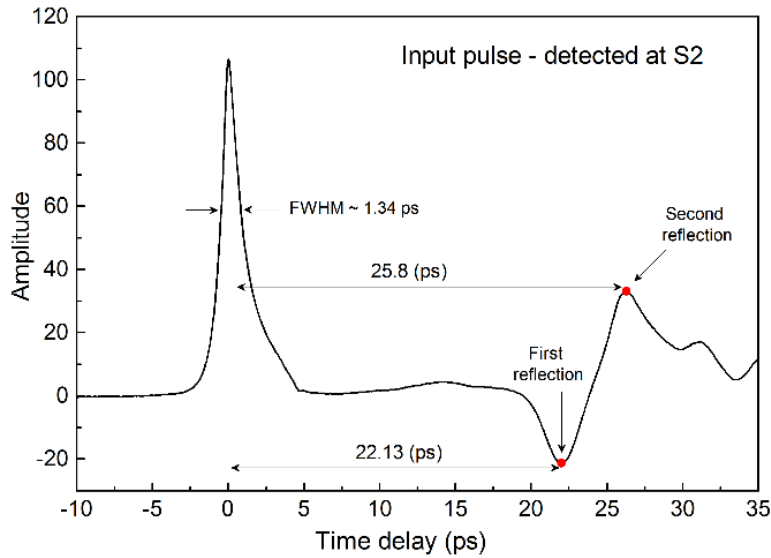
As discussed in Chapter 3, the free-standing LT-GaAs switches fabricated on a quartz substrate by an epitaxial lift-off technique showed a relatively high dark resistance (compared to that of fabricated on bulk LT-GaAs) and therefore, improved the signal-to-noise ratio. Y-splitter CPWs was therefore fabricated on a quartz substrate with free standing LT-GaAs switches embedded as the photoconductive regions of the Y-splitter using epitaxial lift-off. On-chip measurement of Y-splitter on a quartz substrate was then performed, and the results were compared with that of obtained from HFSS simulations.

### **4.7.1 Input pulse detection**

Input pulse was detected at the switch. S2 by focusing a time-delayed probe beam onto the switch S2, and a bias of 20 V was applied across the switch S1. Trace of the input pulse measured in a time-window of 35 ps showed two secondary reflections occurring at 22.1 and 25.8 ps after the main pulse, as shown in Figure 4.23. The origins of reflections were found to be the same as those calculated for the Y-splitter on LT-GaAs



substrate (shown in Figure 4.18 a). FWHM of the input pulse was calculated as  $\sim 1.34 \pm 0.2$  ps, suggesting less broadening of the pulse (compared to that of calculated for LT-GaAs substrate), which is attributed to a lower carrier lifetime in the free-standing LT-GaAs switches on a quartz substrate.



**Figure 4.23** A trace of an input pulse, in which the main pulse is occurring at zero time delay is followed by secondary reflections occurred at 22.13 and 25.8 ps.

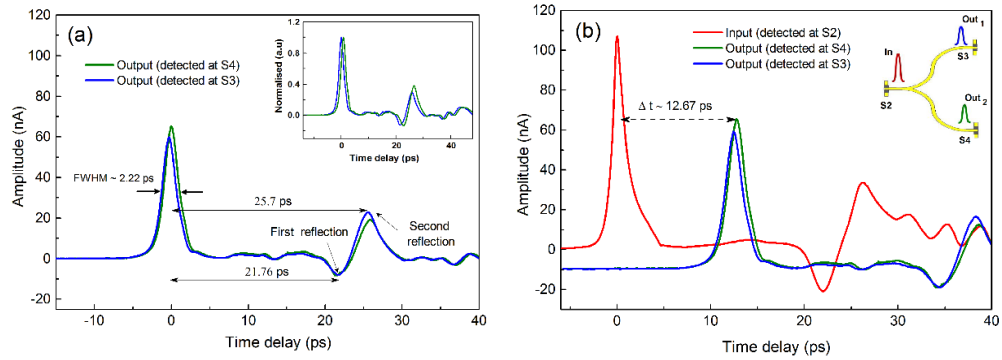
#### 4.7.2 Output (split) pulse detection

Split THz pulses propagating in branching waveguides  $Y_A$  and  $Y_B$  were detected by focusing a time-delayed probe beam onto switches S3 and S4 in two consecutive scans. Output pulses were with a relative time-difference of  $\sim 0.18$  ps, which is again attributed to a relative change in the path length of the probe beam while moving from the switch S3 to S4. In a time-window of 40 ps, traces of output pulse showed the main pulse followed by two secondary reflections occurring at 21.76, and 25.7 ps after the main pulse as shown in Figure 4.24 a.

Interestingly, the first reflection that was observed in the output pulse (occurred at 26.54 ps – shown in Figure 4.20 b) measured from Y-splitter on LT-GaAs somewhat reduced, suggesting bend discontinuities offer less resistance to THz pulses travelling in a waveguide fabricated on a quartz substrate (low permittivity of  $\epsilon_r = 3.78$ ). The origin of the first reflection in output pulse trace was found to be an ohmic contact pad



discontinuity (pointed out as 'b' – shown in Figure 4.20 a) located in the parasitic region. The origin of the second reflection was found to be the photoconductive switch region S1-S2. A Lorentz fit to the main pulse showed relatively higher FWHM of  $\sim 2.22$  ps (compared to that of obtained from the first-generation CPW<sub>quartz</sub>) which is attributed to a long transmission region of branching waveguides  $Y_A$  and  $Y_B$  in Y-splitter. In Figure 4.24 b, traces of the input and output pulses with a relative time-delay of 12.67 ps were detected in the same time-window of 40 ps.



**Figure 4.24** Output pulse detection in a Y-splitter a) Traces of split THz pulses detected at S3 and S4 b) Traces of input and output pulses with a relative time difference of 12.67 measured in the same time-window of 40 ps.

FFT spectra of the input and output pulses obtained from Fourier transformation were then compared in order to estimate insertion loss in Y-splitter (quartz substrate). In doing so, FFT spectra of input and output pulses were plotted on a dB scale. An insertion loss of  $\sim -5.3$  dB was observed from FFT spectra of the input and output pulse plotted as a function frequency.

The observed insertion loss of  $\sim -5.3$  dB was found to be in good agreement with that estimated ( $\sim -5$  dB) from HFSS simulations. The FFT spectra of the output pulse showed a useful bandwidth of  $\sim 750$  GHz, which is in good agreement with that of estimated ( $\sim 720$  GHz) from HFSS simulations (shown Figure 4.16 d). A frequency resolution of 50 GHz was obtained by truncating the time-domain output pulses at 20 ps delay (just before the first reflection) relative to the main pulse.

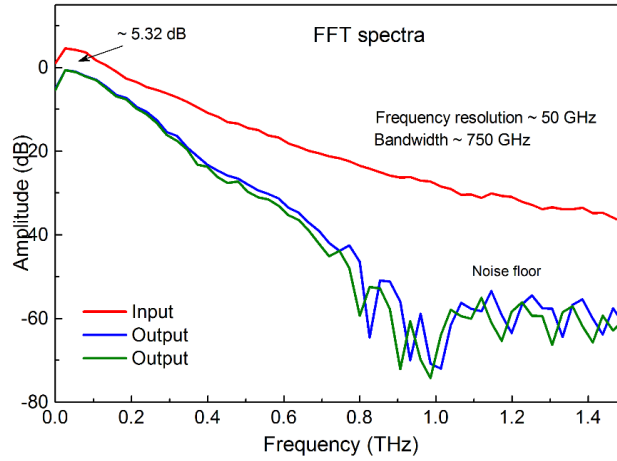


Figure 4.25 FFT spectra of the input and output pulses plotted on a dB scale.

### 4.7.3 Pulse velocity

The velocity of THz pulse in Y-splitter was calculated by knowing the relative time difference between forward and reverse pulses detected at the switch S3 and S4 (located in branching waveguides  $Y_A$  and  $Y_B$ ) and by swapping their bias and probing connections. In doing so, a forward output pulse was detected by focusing the probe beam onto the switch S4, while a bias of 10 V was applied across the switch S3.

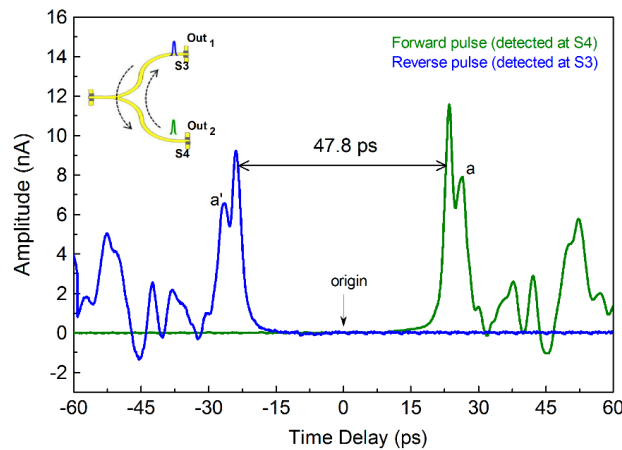


Figure 4.26 Traces of the output pulses detected at S3 and S4 detected in the same time-window of 120 ps, where zero time delay represents the generation of an input pulse.

The THz pulse generated at the switch S3 propagates along branching waveguides  $Y_A$  and  $Y_B$  (passing through Y-junction) before being detected at the switch

S4. Similarly, a reverse output pulse generated at the switch S4 travelled along  $Y_B$  and  $Y_A$  before being detected at the switch S3. It is worth mentioning that a fraction of THz pulse will also propagate along the straight CPW while passing through the Y-junction. A relative time difference of 47.8 was observed between the forward and reverse output pulses. The velocity of pulse was then calculated as,  $V_p = 2(Y_A + Y_B)/\Delta t = 1.71 \times 10^8 \text{ m/s}$ . The calculated pulse velocity of  $1.71 \times 10^8 \text{ m/s}$  was thus slightly smaller than that measured in the first generation CPW<sub>quartz</sub> ( $1.74 \times 10^8 \text{ m/s}$ ), which is attributed to the propagation of THz pulses in the curved transmission regions of  $Y_A$  and  $Y_B$  since the bend discontinuities may slow down the THz pulses. The reflection features observed (pointed out by “a” and “a’” - shown Figure 4.26) in output pulses were originated from the point where the straight transmission region merges into a curved transmission region ( $\sim 250 \mu\text{m}$  away from the switch).).

## 4.8 On-chip measurements of Y-coupler CPW (quartz substrate)

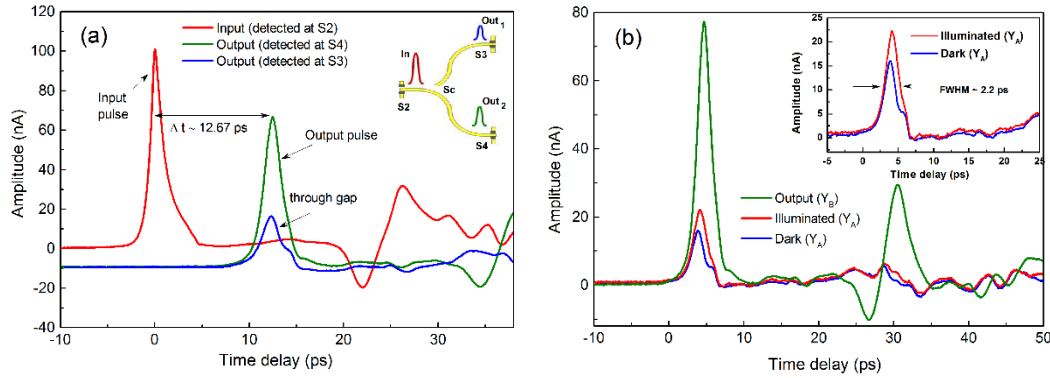
Y-couplers were fabricated on a quartz substrate by the epitaxial lift-off of LT-GaAs and transfer of LT-GaAs to form photoconductive switch regions as discussed earlier. On-chip measurements of Y-coupler were then performed in order to test coupling efficiency of  $20 \mu\text{m}$  coupling switch bridging two branching waveguides  $Y_A$  and  $Y_B$ .

### 4.8.1 Detection of the output (split) pulses

As for the splitter, in the Y-coupler, the output pulses were detected by focusing a probe beam onto the switch S3 and S4 in consecutive scans while a pump beam was focused onto the switch S1. An output pulse of relatively small amplitude (compared to that of detected at S4) was then detected at the switch S3 (under dark conditions for the coupling switch).

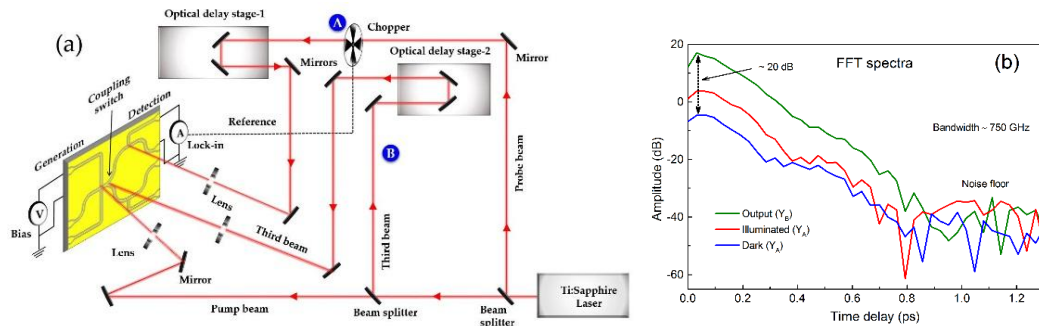
Under dark condition, the coupling switch offered a much higher impedance to the incoming THz pulse. Therefore, a higher proportion of the THz pulse ( $\sim 5$  times higher than that of propagating along  $Y_A$ ) propagated along the continuous branching

waveguide  $Y_B$ , before being detected at S4 as shown in Figure 4.27 a.



**Figure 4.27 a) Detection of the input and output pulses with a relative time difference of 12.67 in the same time-window of 40 ps. b) A comparison of output pulses under dark and illuminated conditions.**

The detected output pulses were of the same polarity but with a slight change in pulse shape, which is attributed to the filtering characteristics of the coupling gap formed between the branching waveguides  $Y_A$  and  $Y_B$ .



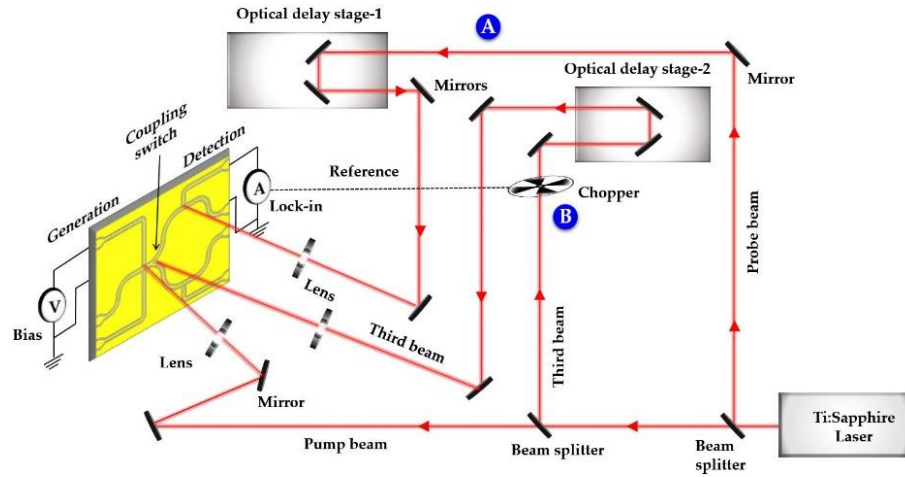
**Figure 4.28 a) Detection of an output pulse in Y-coupler while coupling switch is illuminated by the third beam. b) FFT spectra of input and output pulses plotted on a dB scale.**

However, using a three-beam on-chip system with chopper set at position A (shown in Figure 4.28 a), the shape of the pulse was changed to a Gaussian shape when the coupling switch was illuminated by a third beam (synchronised to the pump beam), and a substantial increase ( $\sim 41\%$ ) in amplitude of the pulse was observed, which is attributed to the higher conductivity of the coupling switch under illumination, which allows the THz field to couple through the gap in a higher proportion (shown in Figure 4.28 b).

FFT spectra of the output pulses were then plotted on a dB scale in order to estimate the coupling loss while the THz pulse was split in branching waveguides. A coupling loss of  $\sim 20$  dB was observed at low frequencies from FFT spectra as shown in Figure 4.28 b. The observed coupling loss was found to be rather smaller than that estimated from HFSS simulations ( $\sim 30$  dB).

#### 4.8.2 THz pulse detection using coupling switch modulation

The modulated THz pulse measurement in a Y-coupler was performed by focusing the pump and probe beams onto the switch S1 and S3 respectively while a third beam (synchronised with pump beam) was focused onto the coupling switch Sc. In doing so, the mechanical chopper was moved from position A to B as shown in Figure 4.29 in order to modulate the coupling switch.



**Figure 4.29** Schematic representation of differential pulse measurement in a Y-coupler using three beams on-chip system, where the mechanical chopper was moved to position B in order to modulate coupling switch Sc.

A modulated differential pulse was generated at the coupling switch which was then detected at the switch S3. A conventional THz pulse (propagating along  $Y_B$ ), split from the generated THz pulse while passing through the Y-junction was then detected at the switch S4.

A Lorentz fit to the modulated pulse revealed a FWHM of  $\sim 1.73$  ps, which is shorter than that of calculated from the “conventional” THz pulse ( $\sim 2.2$  ps) detected at the switch S4 (shown in Figure 4.30 ). However, the amplitude of the modulated differential pulse was found to be relatively smaller (by  $\sim 6$  times) than that of the

conventional pulse, which can be understood as the modulated differential pulse is the result of the difference of two THz pulses ( $S_{\text{on}} - S_{\text{off}}$ ) passing through the coupling switch while the conductivity of switch is modulated by the third beam (i.e. coupling switch acts as an on-off switch - see Chapter 3). A relatively higher bandwidth of  $\sim 1.2$  THz compared to that of conventional pulse  $\sim 0.75$  THz was observed from a comparison of the FFT spectra obtained from the modulated and conventional pulse, as shown in Figure 4.30.

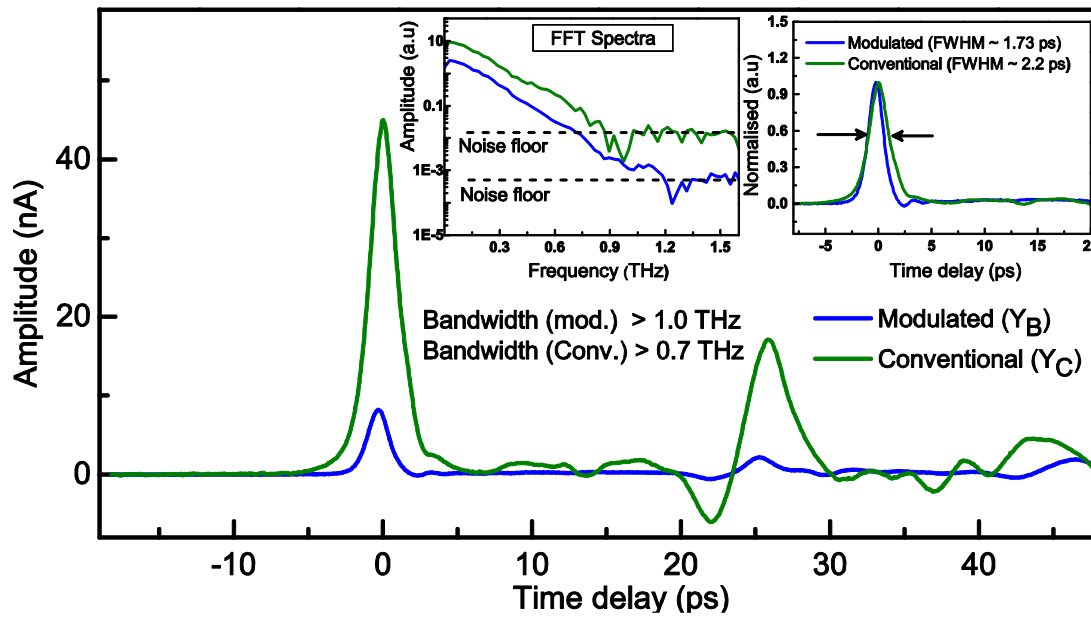


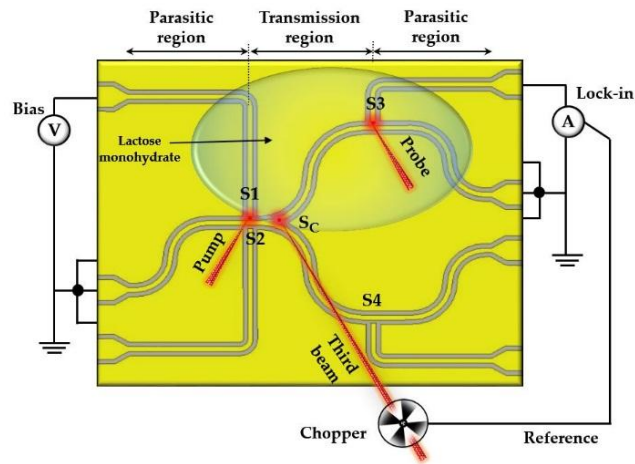
Figure 4.30 Detection of conventional and modulated THz pulses in branching waveguides  $Y_A$  and  $Y_B$  respectively in a time-window of 60 ps. FWHM and FFT spectra of conventional and modulated THz pulses are compared in inset graphs.

### 4.8.3 Initial spectroscopy measurement using Y-coupler CPW device

In the previous section, it was demonstrated that a modulated THz pulse can be generated by modulating the coupling switch in a Y-coupler using a three-beam system. Also, a higher bandwidth of  $\sim 1.2$  THz and shorter FWHM (relative to conventional output pulse) of  $\sim 1.73$  ps was observed from the FFT spectra of the modulated pulse. We, therefore, used a Y-coupler to perform on-chip spectroscopy of lactose monohydrate (a polycrystalline material). In doing so, a highly concentrated solution of lactose monohydrate in DI- $H_2O$  was carefully pipetted onto the device, covering both

the branching waveguide  $Y_A$  and coupling switch  $S_c$ . The device was then left overnight to evaporate off the water left after pipetting. An illustration of the on-chip spectroscopy measurement of lactose monohydrate using the three beams on-chip system is shown in Figure 4.31 in which branching waveguide  $Y_A$  is loaded with lactose monohydrate covering photoconductive switch regions  $S_1$ ,  $S_c$ , and  $S_3$ . Front-side illumination of switches was not feasible in this geometry. A PCB with optical access (a window was milled out - see Chapter 5) was therefore used in order to illuminate the photoconductive switches from the back of quartz substrate.

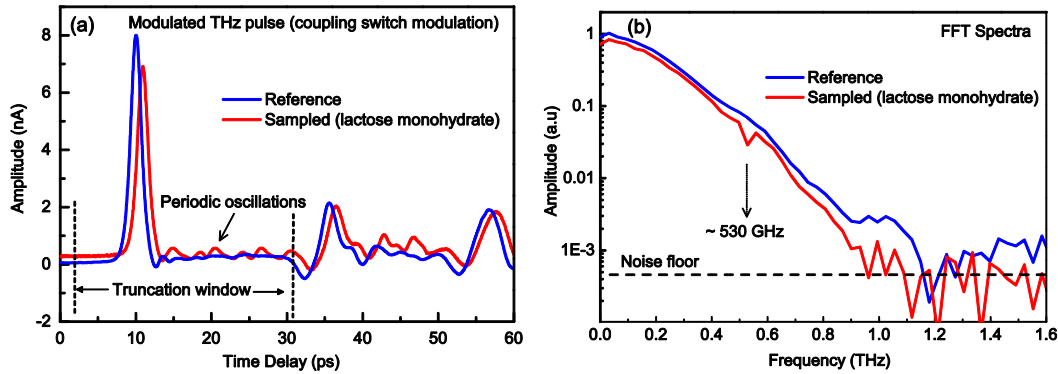
Modulated pulse measurement was then performed by focusing the pump and probe beams onto the switch  $S_1$  and  $S_3$  respectively while a third beam was focused onto the coupling switch  $S_c$ . A differential modulated pulse was generated at the modulating coupling switch  $S_c$ , which then propagates down the branching transmission line  $Y_A$  while interacting with overlaid lactose monohydrate. Modulated pulses then pick up spectral features associated with lactose monohydrate before being detected at the switch  $S_3$ .



**Figure 4.31** A schematic representation of on-chip spectroscopy of overlaid lactose monohydrate on branching waveguide  $Y_A$  in a Y-coupler using three beams on-chip system.

Periodic reflections in the time-domain pulse were observed, which showed an absorption feature, which is referenced in [7, 53, 168], at  $\sim 530$  GHz in FFT spectra of the differential pulse as shown in Figure 4.32 a and b. However, absorption feature observed in FFT spectra was not of high magnitude. Nevertheless, a stronger absorption

feature occurring at  $\sim 1.37$  THz in lactose monohydrate, which is well referenced in the literature [47-50] could further be investigated by using second generation CPW devices (provided a useful bandwidth of  $> 1.4$  THz available in THz pulse).



**Figure 4.32 a) Reference and sampled output pulses in time-domain. b) A comparison of FFT spectra of the reference and sampled pulses.**

The second generation devices were further optimised by reducing the slot gap width ' $W$ ' in order to reduce radiation losses, leading to a significant increase in bandwidth (see Chapter 5).

## 4.9 Conclusion

From on-chip measurements, it was observed that second generation CPW devices yielded a higher useful bandwidth of 1.2 THz. Also, a much higher frequency resolution of  $\sim 2$  GHz was obtained for a time-window of 500 ps, since the secondary reflections were substantially delayed relative to the main pulse.

Furthermore, the splitting of generated THz pulses was also observed from on-chip measurements of Y-splitter. The useful bandwidth and insertion loss observed from on-chip measurements were found to be in good agreement with HFSS results. In pulse velocity measurements, detection of the THz pulses across the Y-junction (making a round trip from the switch S3 to S4), also suggested that Y-splitter design can be used as a multiplexer to combine THz pulses coming from different branched waveguides. Additionally, a THz interferometer could be realised in order to study constructive/destructive interference of THz pulses at a Y-junction.



On-chip measurements of Y-coupler showed that coupling of THz pulse across the coupling gap can substantially be increased under illuminated condition. Differential pulses measured from the Y-coupler, using a three-beam on-chip system, yielded a useful bandwidth of 1.2 THz. On-chip spectroscopy measurements of lactose monohydrate showed periodic oscillation in time-domain differential pulse and showed an absorption feature at  $\sim 530$  GHz in FFT spectra of the differential pulse.

## Chapter 5

# On-Chip THz-TDS of Lactose Monohydrate using Conventional and CGAP-CPW Devices at Low-Temperature

### 5.1 Introduction

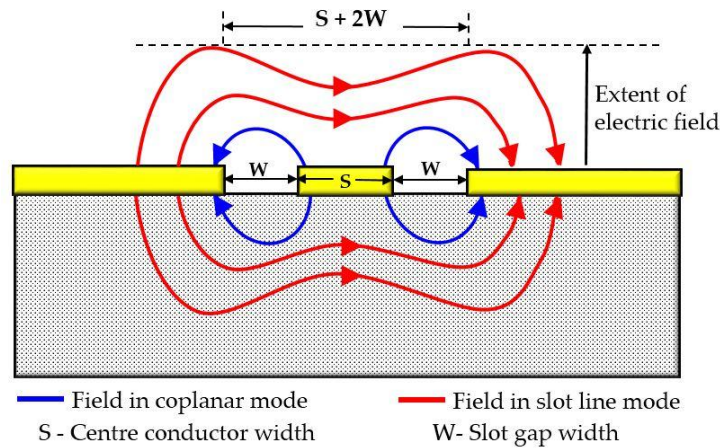
In Chapter 4, it was discussed that extending the parasitic regions of second generation CPW devices improved the frequency resolution when performing a Fourier Transformation by delaying any unwanted reflections from the bond pads. Further optimisation of the second generation CPW design was then needed to achieve higher bandwidth ( $> 1.4$  THz) in order to perform on-chip spectroscopy of polycrystalline materials, such as lactose monohydrate. Spectroscopy of polycrystalline materials allows the observation of molecular vibrations, which resonate at sub-THz and THz frequencies. In the sub-THz regime, it is mainly crystalline phonon vibrations, which are observed, while intermolecular stretching and torsional modes are typically found at THz frequencies [169].

In this Chapter, steps to optimise the second generation CPW device design parameters are discussed, along with electromagnetic (EM) simulations of this system made using HFSS.

## 5.2 Slot gap width optimisation and estimation of extent of evanescent field

In the on-chip THz spectroscopy, the sample under test is overlaid onto the transmission line. The radiation field associated with the THz pulse propagating through the transmission line then interacts with the sample. Hence, it is vital to know the extent of the field above the transmission line to ensure proper interaction between the sample and the electric field. In this section, a theoretical explanation of how optimising slot gap width minimises dispersion and radiation loss is provided. HFSS simulation results are then discussed to support the theoretical modelling.

### 5.2.1 Theoretical modelling of slot gap width $W$



**Figure 5.1** Electric field lines are shown in coplanar mode (blue) and slot-line mode (red).

In Figure 5.1, the two possible fundamental modes of a CPW are shown: a) coplanar mode (also called the “odd” mode) in which ground planes are at equal potential and b) slot-line mode (the “even” mode) in which ground planes have potential of different signs but equal magnitude. The coplanar mode is a quasi-TEM mode with its very low dispersion. The fundamental coplanar mode of a CPW is usually less dispersive than the fundamental mode of microstrip line [99] which makes CPW a potentially promising device for on-chip spectroscopy.

The field distribution around the centre conductor and ground planes mainly

depends on the mode of excitation. In CPW device designs, the width of the centre conductor is termed as  $S$ , and the spacing between the ground planes is termed as  $(S + 2W)$  where  $W$  is slot gap width. The distance  $(S + 2W)$  should then carefully be taken into consideration when designing a CPW, as it will define the extent of the evanescent field. To avoid propagation of higher-order lossy modes, the distance  $(S + 2W)$  should be kept less than  $\lambda_g/2$ , and the ground planes should be wider than  $5(S + 2W)$  on each side [170], where  $\lambda_g = \lambda_0/\sqrt{\epsilon}$  is waveguide wavelength and  $\lambda_0$  is the free space wavelength. If the distance between the ground planes  $(S + 2W)$  is kept much smaller than the dielectric wavelength and the substrate thickness, both radiation and dispersion losses are minimised [80]. If adequate ground to ground plane distance is chosen, interaction between surface wave mode and the coplanar mode is also minimised and tends to become negligible at higher frequencies. Furthermore, at higher frequencies, radiation losses are found to be minimum, since the electric field is more confined within the slot gaps, Rutledge *et al.* [171] relate the attenuation due to radiation loss  $\alpha_r$  with the ground to ground separation distance  $(S + 2W)$  by Equations 5-1 and 5-2:

$$\alpha_r = f(\epsilon_r) \left( \frac{1}{\lambda_d} \right)^3 \frac{(S + 2W)^2}{K(k)K'(k)} \quad 5-1$$

Where,  $k = S/S+2W$ ,  $K$  and  $K'$  are complete elliptical integrals of the first and second kinds.

$$f(\epsilon_r) = \left( \frac{\pi}{2} \right)^5 \frac{1}{\sqrt{2}} \frac{\left( 1 - \frac{1}{\epsilon_r} \right)^2}{\sqrt{1 + \frac{1}{\epsilon_r}}} \quad 5-2$$

From the above Equations, it is clear that the radiation loss is proportional to the square of the distance  $(S + 2W)$  which means that a relatively small increase in gap width can lead to significant radiation loss.

In Figure 5.2 a, attenuation coefficients for different gap widths are calculated using Equations 5-1 and 5-2. The value of the attenuation coefficients gradually decreases with slot gap width decreasing from 40 to 5  $\mu\text{m}$ . In Figure 5.2 b, the characteristic impedance of the transmission line plotted against decreasing slot gap

width shows a strong dependence on slot gap dimensions. It is worth noting that the effective permittivity will be independent of CPW dimensions and can simply be calculated by taking an average of the dielectric constants of air and the substrate.

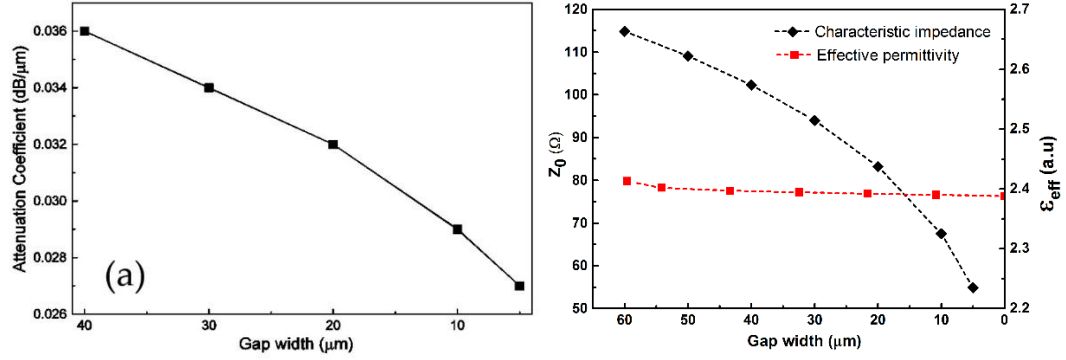


Figure 5.2 a) Attenuation coefficient is plotted w.r.t slot gap width. b) Characteristic impedance and effective permittivity are plotted w.r.t gap width.

We also quote here two useful standard Equations 5-3 and 5-4 taken from [172], which were used to calculate the characteristic impedance and effective permittivity of CPW lines as shown in Figure 5.2 b.

$$Z_o = \frac{30 \pi}{\sqrt{\epsilon_{eff}}} \frac{K(\kappa')}{K(\kappa)} \quad 5-3$$

$$\epsilon_{eff} = \frac{1 + \epsilon_r \frac{K(\kappa')}{K(\kappa)} \frac{K(\kappa_l)}{K(\kappa_l')}}{1 + \frac{K(\kappa')}{K(\kappa)} \frac{K(\kappa_l)}{K(\kappa_l')}} \quad 5-4$$

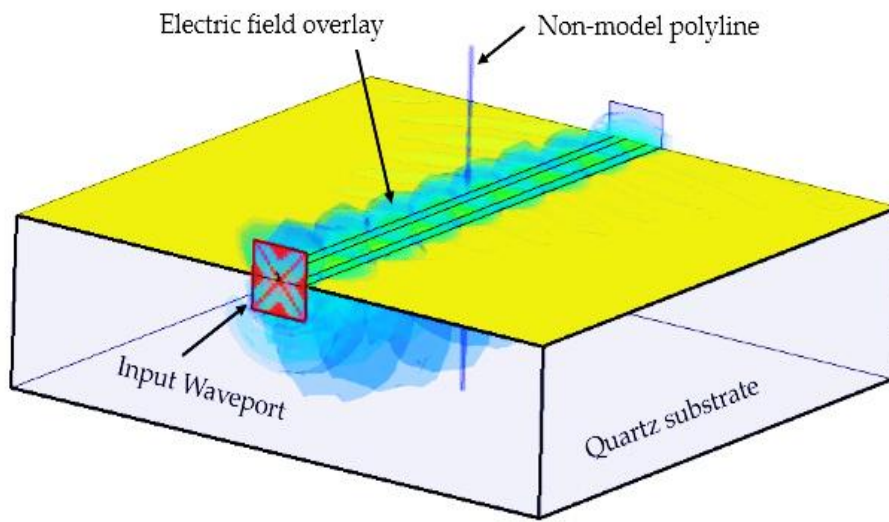
where,  $\kappa = s/s + 2w$ ,  $\kappa = s/s + 2w$ ,  $\kappa = s/s + 2w$  and  $\kappa_l = \tanh\left(\frac{\pi s}{4.0 h}\right) / \tanh\left(\frac{\pi(s+2w)}{4.0 h}\right)$

## 5.2.2 HFSS simulations to find the extent of evanescent field

HFSS breaks down a 3D geometry into many small tetrahedral volume elements forming a mesh and then uses finite-element techniques to calculate the electric field and current in each, using Maxwell's Equations. In Chapter 2, the working principle of the EM simulation tool HFSS was discussed in detail.

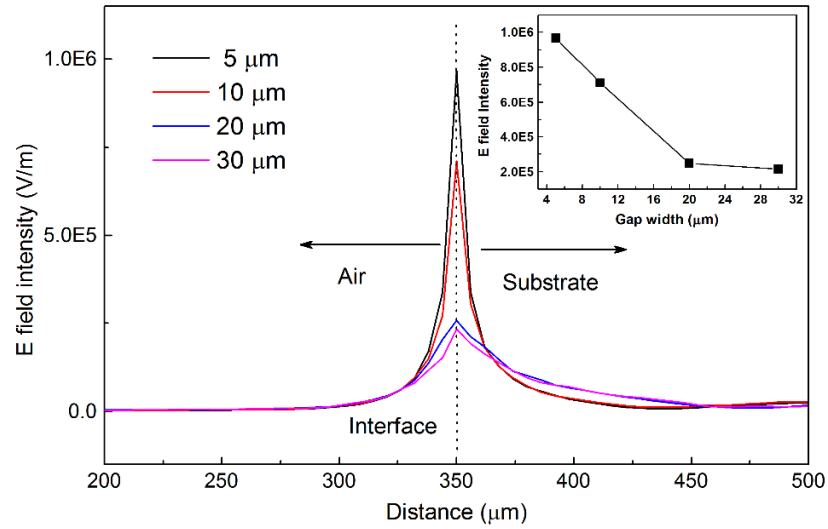
To estimate the extent of the evanescent electric field from HFSS simulations, a

3D model consisting of a 1 mm long CPW comprising a centre conductor and two ground planes sitting on top of the quartz substrate was designed in HFSS as shown in Figure 5.3. The input and output waveports are defined in the model to feed electromagnetic radiation into and out of the structure. First, a reference non-model polyline (excluded from simulation model) which passed through the slot gap was drawn at the centre of the transmission line. The CPW was then simulated at a solution frequency of 1 THz for different slot gap widths. After successful completion of the simulation, the electric field was plotted on the non-model polyline for each gap width.



**Figure 5.3** A 3D model of a CPW in HFSS, where electric field plotted against a polyline in blue.

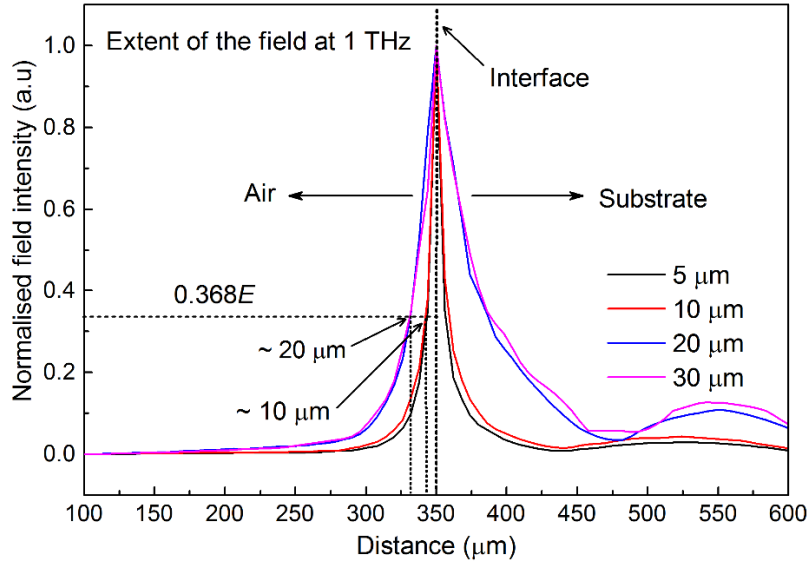
In Figure 5.4, a reference line drawn at 350  $\mu\text{m}$  represents an air-dielectric interface, where metal thickness (200 nm) is neglected. The field extending into the air is shown on the left to the reference line. It is clear from Figure 5.4 that the field intensity for smaller gaps (5 and 10  $\mu\text{m}$ ) is much higher than larger gap dimensions (20 and 30  $\mu\text{m}$ ). The field intensity is plotted against gap widths in inset graph, Figure 5.4 for data clarity.



**Figure 5.4** Electric field intensity for different gap widths is plotted against a polyline in the perpendicular direction, and field intensity also plotted against gap widths for data clarity in inset graph.

To estimate the field extent, all the plots in Figure 5.5 are normalised (0 to 1). It is clear that for larger gaps, more field penetrates into the substrate which is shown on the right to the reference line at 350 μm in Figure 5.5. Another reference line (0.368 E) intersecting plots where field intensity decays to 37% ( $e^{-1} \times E$ ) of its initial value is drawn. These points of intersection give the extent of the field into the air. It is shown that extent of the field into the air for larger gaps (20 and 30 μm) is approximately 20 μm. As the field is more tightly confined within smaller gaps (5 and 10 μm), the extent of field is found to be 10 μm approximately.

This suggests that sample under test should preferably be in direct contact with the transmission line to maximise interaction with the THz field. Regarding the CPW device design optimisation, however, smaller gaps should be preferred to minimise radiation losses. These two considerations offer competing requirements, making careful device design and orientation with respect to samples a necessity.



**Figure 5.5** E-field intensities plots are normalised from 0 to 1 to emphasise the depth of penetration of the field into both air and the substrate.

Another consideration is the manufacturability of devices. CPW devices with a 5- $\mu\text{m}$ -wide gap (or smaller) are at the lower limit of standard optical lithography equipment. Hence, a 10  $\mu\text{m}$  gap width was chosen for optimisation of the second generation CPW devices.

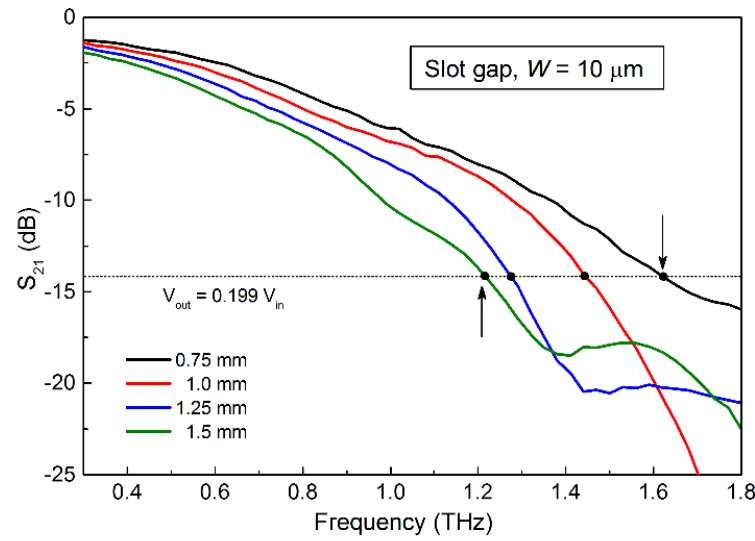
### 5.2.3 Improvements in signal bandwidth by optimising transmission length

The THz signal attenuates as it travels down the transmission line. Therefore, the bandwidth of the signal is limited by the transmission length, which should be taken into account in device optimisation for spectroscopy. Various transmission lengths can be simulated using HFSS to estimate the signal bandwidth to a good approximation.

CPW devices with transmission length ranging from 0.75 to 1.5 mm were simulated with a fixed slot gap width of 10  $\mu\text{m}$  while the  $S_{21}$  scattering parameter was compared for each CPW. In practice, the  $S_{21}$  parameter gives information about how much power is lost during transmission from port1 to port2. In Figure 5.6,  $S_{21}$  parameter extracted from simulation results are plotted with respect to frequency. In the simulations, a solution frequency of 1.4 THz was chosen while a frequency sweep from



0.3 to 1.8 THz was performed.



**Figure 5.6  $S_{21}$  scattering parameter plotted on a dB scale against frequency.**

In scattering parameter analysis, 0 dB indicates lossless transmission, which means 100 % power has transferred from port1 to port2. -20 dB indicates that only 1% power delivered to the load. Using the points at which the -14 dB reference (see Chapter 2) line intersects plots, the bandwidth of various transmission lengths was estimated.

Transmission length (mm)	0.75	1	1.25	1.5
Bandwidth (THz)	1.61	1.45	1.30	1.21

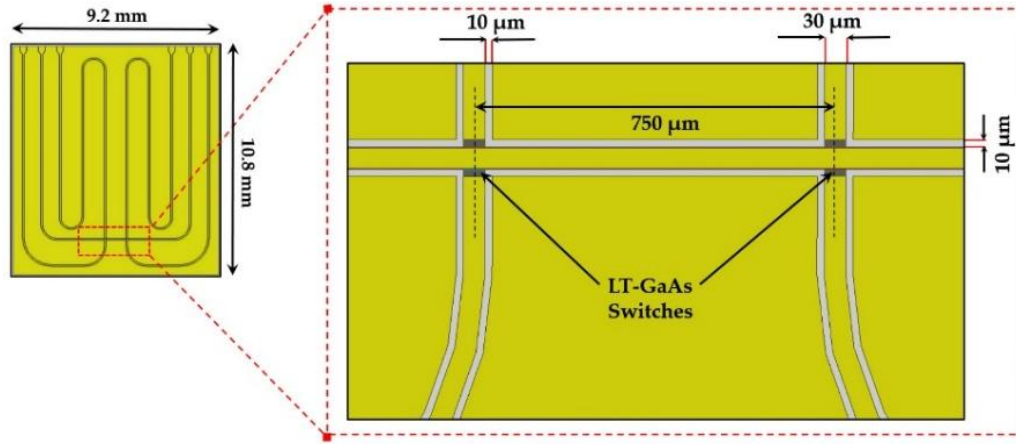
**Table 5-1 Comparing the bandwidth of various transmission lengths.**

Taking theoretical modelling and simulations results into consideration, a slot-gap width of 10  $\mu\text{m}$  and transmission length of 750  $\mu\text{m}$  were chosen for optimisation of the design parameters for the second generation of CPW device.

#### 5.2.4 Experimental Results: Initial testing of optimised CPW device

In Chapter 3, Improvements in a frequency resolution of the second generation CPW (Slot gap width of 20  $\mu\text{m}$ ) devices were demonstrated experimentally. However, the bandwidth of the THz output pulses was found to be 1.2 THz, which was insufficient

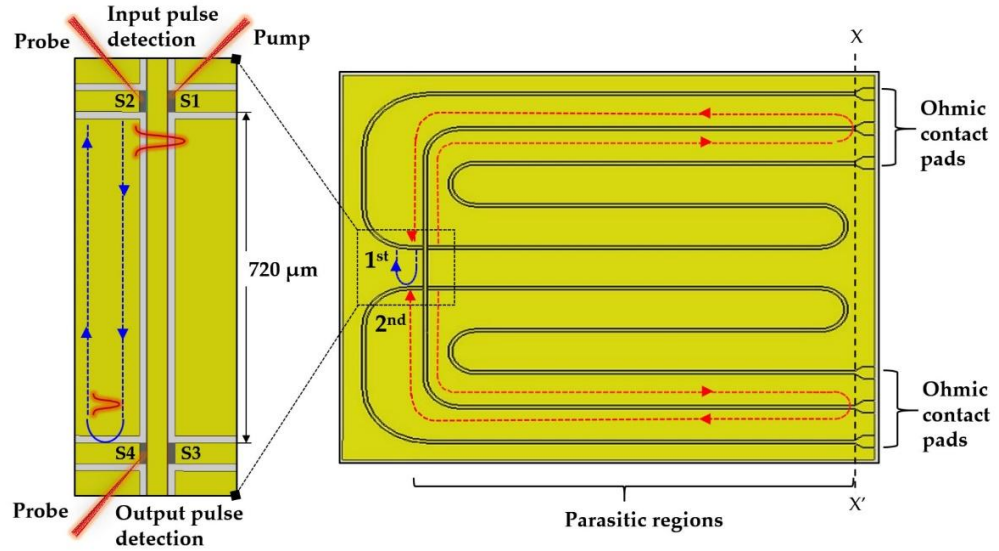
to extract several high-frequency spectral features of lactose monohydrate from the FFT spectra.



**Figure 5.7** A magnification of PC switches region of the second generation CPW device with slot gap width  $10\ \mu\text{m}$  and transmission length of  $750\ \mu\text{m}$ .

For further improvements in the signal bandwidth, a second generation CPW device with optimised slot gap width of  $10\ \mu\text{m}$  and long parasitic region was processed in the cleanroom. CPW device was then tested at room temperature using an on-chip measurement system. A magnified view of PC switches region, slot gap and transmission line, is shown in Figure 5.7.

A time-domain input pulse is detected at the switch S2 using a probe beam while the pump beam illuminates PC switch S1, shown in Figure 5.8. The first reflection appears  $\sim 8.2\ \text{ps}$  after the main pulse, as shown in Figure 5.9. The first reflection in input pulse detection is attributed to the change in impedance at the PC switches S3 and S4 situated on the other end of the transmission line in their dark state (no illumination). The second reflection appears at  $\sim 126\ \text{ps}$  after the main pulse which is attributed to the impedance mismatch due to ohmic contact pads. The total parasitic length travelled (red dotted lines) by the THz pulse, and the origin of the reflections (black dotted line, X-X') are shown in Figure 5.8. Calculations to find origins of reflection were discussed in detail in Chapter 3.

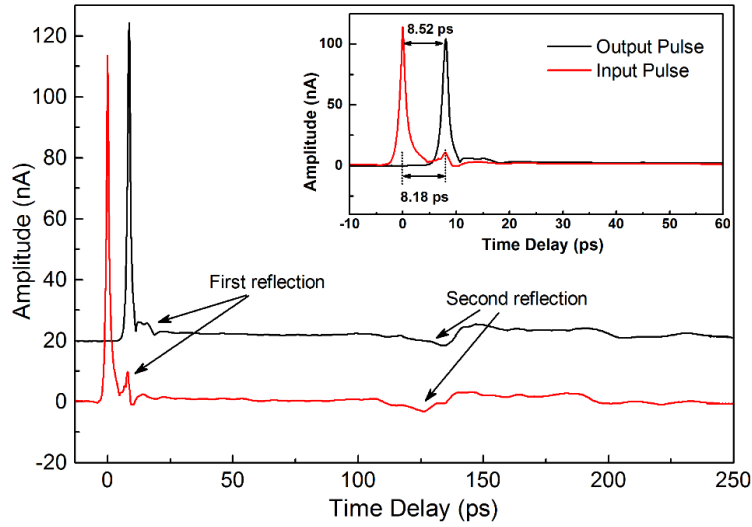


**Figure 5.8** A schematic of the second generation CPW showing the origin of first and second reflections in pulse detection.

The output pulse is detected at the switch S4 using a probe beam while the pump beam is shone onto PC switch S1. It is worth mentioning that the first reflection in the output pulse was found to be relatively much weaker than the first reflection seen in input pulse. This relative difference in magnitude of the reflections is attributed to the lower impedance of PC switches S1 and S4 situated at both ends of the transmission line under illumination of pump and probe laser beams shown in Figure 5.8.

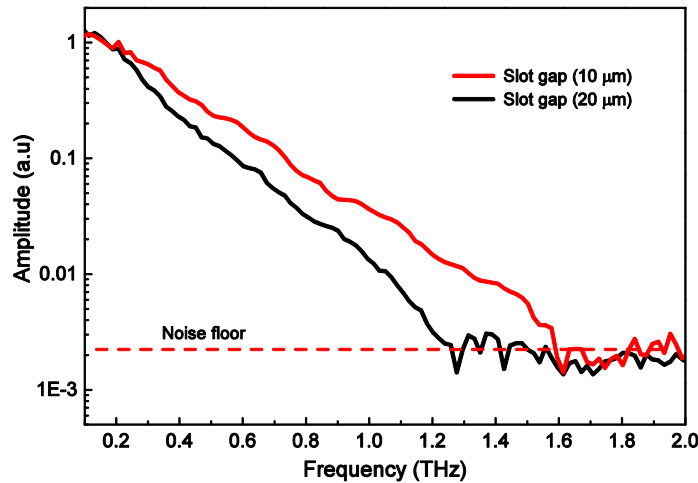
The impedance of PC switches drops drastically when the laser beam is tightly focused onto the switch region. The origin of the second reflection in an output pulse is the same as that discussed above due to symmetric design of the CPW device. Input and output pulses measured using the on-chip system are compared in Figure 5.9.

To determine the bandwidth, a fast Fourier transform (FFT) was performed on the measured time-domain output pulse. In Figure 5.10, FFT spectra from the output pulses measured for CPW waveguides with 10 and 20  $\mu\text{m}$  slot gaps are compared.



**Figure 5.9** Comparison of the input and output THz pulses detected at switches S2 and S4 respectively. The output pulse is offset by 20 nA for clarity.

From the differing slopes of the FFT spectra, it is clear that CPW device with 10  $\mu\text{m}$  slot gap yields greater bandwidth as expected from HFSS simulations. It is also worth mentioning that low-frequency features in the FFT spectra are due to the second reflection present in the time-domain signal.



**Figure 5.10** A comparison of the bandwidth of output pulses measured from CPWs (10  $\mu\text{m}$  and 20  $\mu\text{m}$  slot gaps).

The  $\sim 1.6$  THz bandwidth of the output pulse was found to be promising for use in on-chip spectroscopy, potentially allowing the extraction of high-frequency spectral signatures from lactose monohydrate, for example. Reflections in the output pulse are

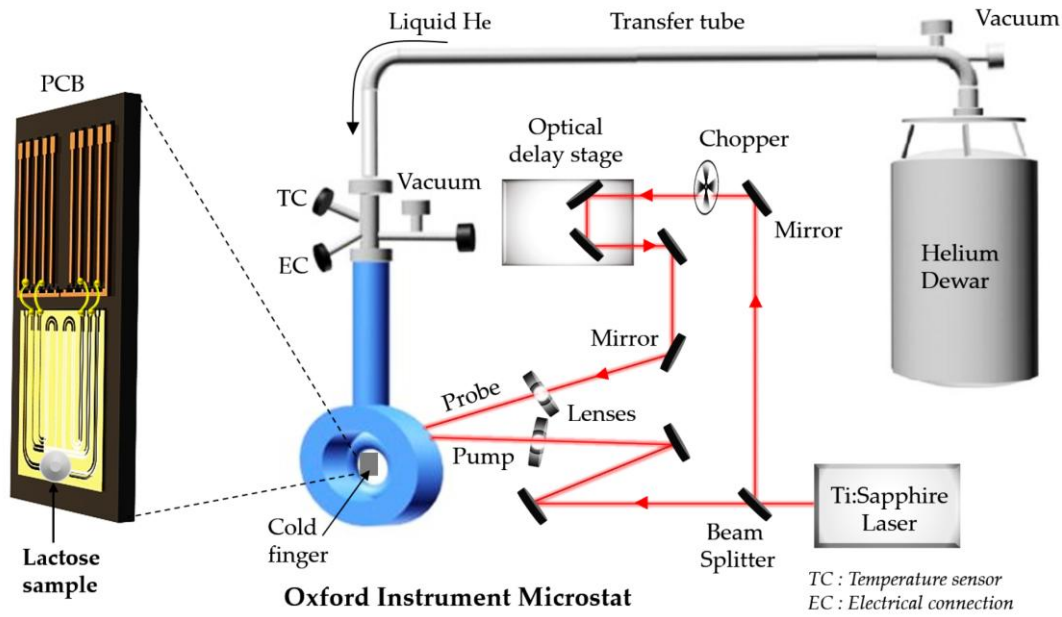
of much smaller magnitude relative to the main pulse. Therefore, the time-domain signal does not need to be truncated while performing Fourier transformation. The resolution of FFT spectra here is mainly limited by the scan length of the time-delay stage. Although high resolution can be achieved by longer scans, it would be time-consuming to do the repeated measurements necessary to reduce noise. Hence, measurement scans were performed at a resolution of 2 GHz.

### **5.3 Variable temperature on-chip measurements using microstat**

Variable temperature on-chip measurements were performed from 6K to 293K using a continuous flow helium microstat, in which the device under test was attached to cold finger (probe) using thermal conducting paste (GE varnish), with electrical connections to the PCB. The Oxford Instruments Microstat system used was fitted with quartz windows to provide optical access for the pump and probe beams. It was noted that about ~ 12% of laser beam power was lost to absorption by the quartz windows (fitted in Oxford instrument microstat for optical access), which is due to multiple reflections coming from sample and window interface. The detailed experimental set-up is discussed in the next section.

#### **5.3.1 Measurement set up**

A lactose sample to be tested was drop-cast onto a CPW device mounted on a PCB before performing measurements. The PCB on which the CPW device was mounted was then attached to a cold finger, and electrical connections to the probe were made using a soldering iron. The probe stick was then placed into the cylindrical chamber of the microstat. To create a vacuum around the sample, the microstat was pumped down using a vacuum pump as shown in Figure 5.11.



**Figure 5.11** A schematic of variable temperature setup consisting of; Oxford Instruments Microstat, Helium Dewar, transfer tube to transfer helium, ports for electrical connection and temperature sensor (EC and TC).

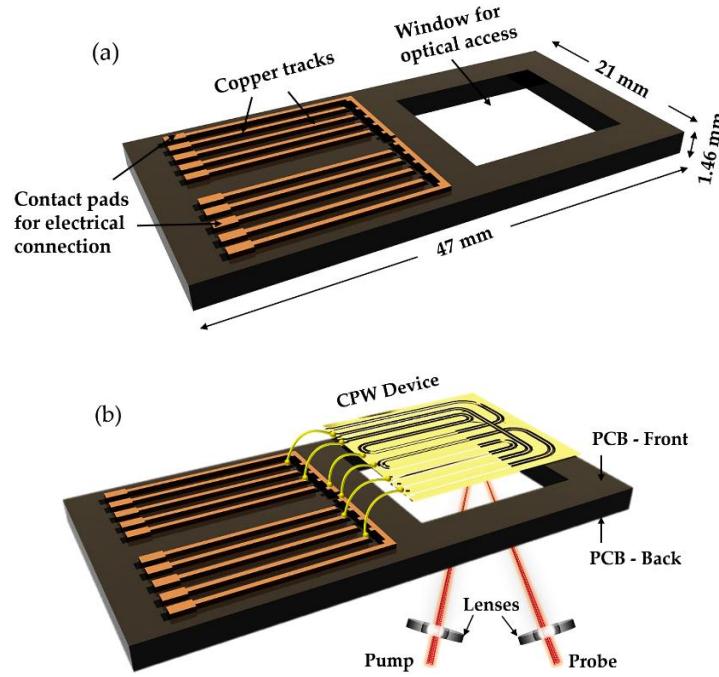
Liquid helium was transferred from a dewar to the cold finger using a vacuum insulated transfer tube. The Microstat cold finger was also fitted with a temperature sensor, and a heater controlled by the external temperature controller to maintain the desired temperature during measurements. A second pump, connected to transfer tube, was used to control the flow of liquid helium. When the desired temperature was achieved, the pump and probe beams passing through the quartz window were aligned to the PC switches on the device. Since the cold finger contracts/expands with temperature, the laser beams had to be re-aligned between each measurement.

The device usually took up to 1.5 hours to thermally stabilise at base temperature. After thermal stabilisation, alignment of PC switches was found not to change with respect to laser beams.

### 5.3.2 PCB Design for back-side excitation of PC switches

One of the key requirements for the realisation of on-chip THz spectroscopy is that PC switches ideally need to be illuminated from the back of the substrate, to allow samples to be aligned as close as possible to the waveguide on the front side; as lactose samples

under test were overlaid onto the entire transmission line covering PC switches, front side illumination was not feasible.



**Figure 5.12 (a) PCB for on-chip spectroscopy with a window for optical access. (b) A CPW device is placed on the top of the optical window for backside illumination.**

To illuminate PC switches from back of the substrate, double side polished (350- $\mu\text{m}$ -thick) quartz material was used as a substrate which had negligible optical attenuation being almost transparent to laser beams. A PCB, which mechanically supported the devices provided electrical connection to the cryostat probe stick, and optical access to illuminate PC switches was first designed and then processed in the cleanroom using standard optical lithography and copper etch solution. A window is milled out from the PCB to obtain optical access as shown in Figure 5.12 a. CPW devices were then glued to the PCB using molten black wax. For PCB connections, the device was bonded to copper tracks using a ball bonder.

### 5.3.3 Sample preparation

Two different sample preparation techniques were used to prepare lactose monohydrate samples prior to their measurement by on-chip THz spectroscopy.

### 5.3.3.1 Lactose pellet method

In this technique, lactose monohydrate was pressed into a pellet using a dedicated hydraulic pellet press. In this process, 35 mg of lactose monohydrate powder was weighed (using an OHAUS Adventure Balance AR0640). Lactose powder was then placed within a copper ring to secure it. Finally, it was pressed into an 8 mm diameter and 0.5 mm thick pellet by applying 8 tons of force.

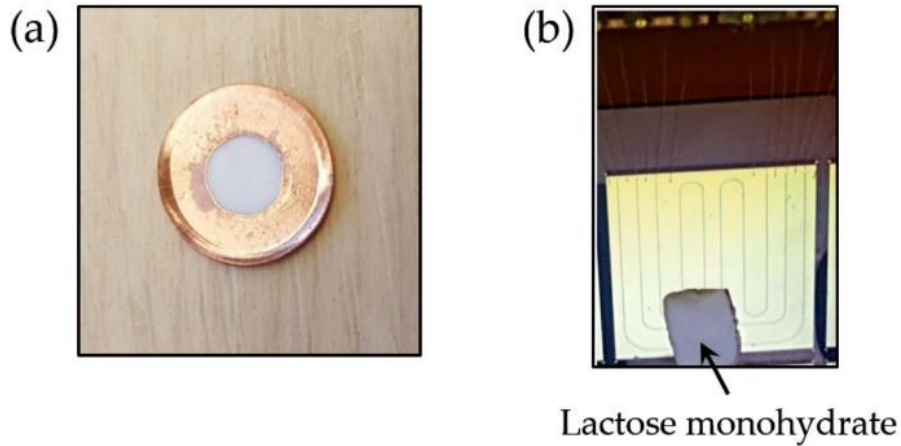


Figure 5.13 a) Compressed lactose pellet in a copper ring. b) Lactose sample overlaid onto a CPW device.

### 5.3.3.2 Drop casting method

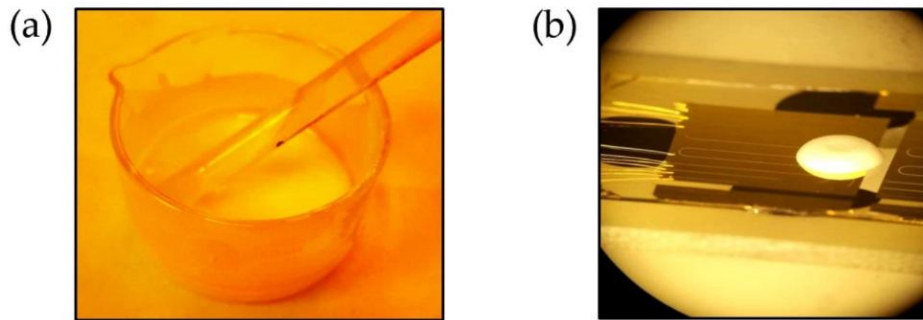


Figure 5.14 a) A concentrated solution of lactose monohydrate in DI water. b) Lactose monohydrate drop cast onto a CPW device.

As an alternative method to the above pellet process, 6 g of lactose monohydrate powder were mixed with 2.5 ml DI water to prepare a highly concentrated solution. A drop of this solution was then pipetted onto the device, covering the transmission line



and photoconductive switch region (the latter on the other side of the substrate) to ensure maximum interaction. The sample was left overnight to dry after pipetting, leaving a lactose mound surrounding the THz waveguide. It is worth noting that the drop casting technique gave much better adhesion between the lactose sample, and the CPW device compared to the lactose pellet method. This technique was therefore, predominantly used to perform on-chip spectroscopy measurements. We note that a similar drop-casting technique was reported previously in the literature to prepare polycrystalline films on a parallel-plate metal waveguide [173].

### **5.3.4 Initial spectroscopy measurement using the first generation CGAP CPW device**

In Chapter 3, it was demonstrated experimentally that the dispersive slot-line mode in a THz CPW can be filtered out by optically modulating a coupling switch in a CGAP-CPW device. It was also discussed how the noise associated with pulse measurements in on-chip systems can be minimised using a differential measurement technique. Experimental results discussed in Chapter 3 showed that a first-generation CGAP-CPW could yield a bandwidth of 1.65 THz judged from the FFT spectra of the differential output pulse.

In this section, the experimental results for an on-chip differential-THz spectroscopy using the first-generation gap CPW are discussed. In Figure 5.15, A CGAP-CPW device is loaded with lactose monohydrate while performing differential spectroscopy measurement.

When the pump beam was focused onto the biased PC switch S1, a THz pulse was generated, which then propagated down the transmission line. The coupling switch Sc, situated in the middle of the transmission line, was optically modulated by the third beam and synchronised with pump beam. When the coupling switch (Sc) is modulated by the third beam, the lock-in amplifier directly measures the part of the signal that is transmitted when Sc is in its “on” state, subtracted by the signal when Sc is “off”, resulting in a differential pulse (see Chapter 3).

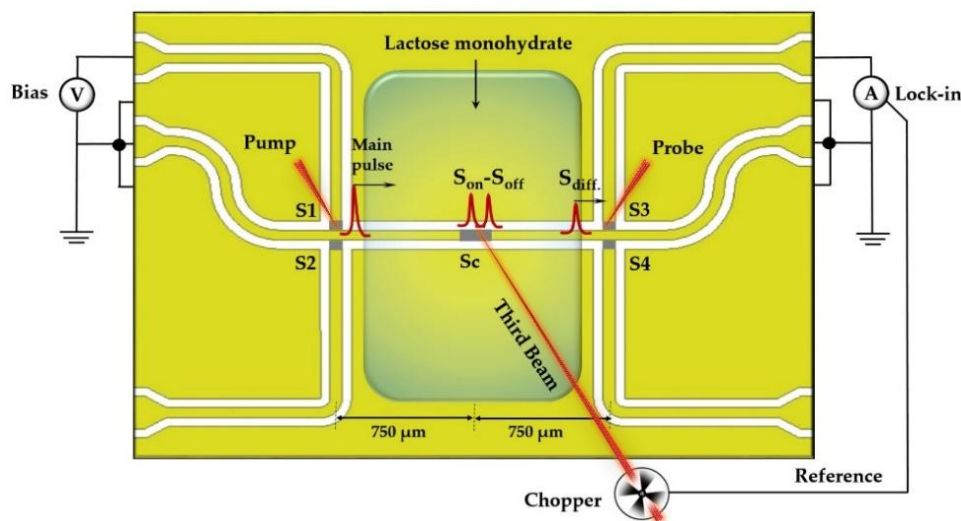


Figure 5.15 A schematic of a first-generation CPW device with gap loaded with lactose monohydrate for differential modulated pulse spectroscopy measurement using the three-beam on-chip system in which coupling switch (Sc) is illuminated by 3<sup>rd</sup> beam.

A differential modulated pulse travelling from the coupling switch Sc was detected at PC switch S2. A reference measurement and lactose spectroscopy measurement are compared in Figure 5.16 a, using the differential configuration.

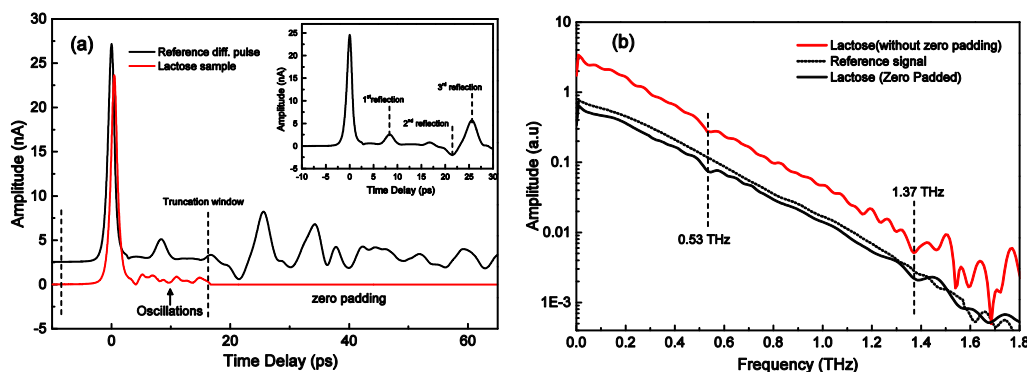


Figure 5.16 a) Time-domain differential (modulated) output pulses (reference and sample). Reflections in the output pulse are shown in inset graph. b) A comparison of FFT spectra of the reference and sample.

Due to the short parasitic regions in the first-generation CPW devices, multiple reflections can be seen in the detected differential output pulse. Periodic oscillations in the output pulse were recorded when the differential signal interacts with a lactose sample. These periodic oscillations reflect absorptions in the FFT spectra of the output pulse. To avoid these large amplitude reflections, the time-domain signal was truncated

at 16.7 ps after the main pulse, yielding a frequency resolution of 60 GHz. To further increase the frequency resolution pulse data were zero padded as shown in Figure 5.16 a. FFT spectra of the reference and the sampled signal are compared in Figure 5.16 b. It is difficult to distinguish lactose absorption features due to the presence of artefacts in the FFT spectra of the raw data. Artefacts are removed by truncating time-domain signal, but absorption features are somewhat smeared when the data is zero padded.

To better resolve lactose absorption features in FFT spectra, the second generation CPW devices were optimised to include longer parasitic regions, offering higher-frequency resolution.

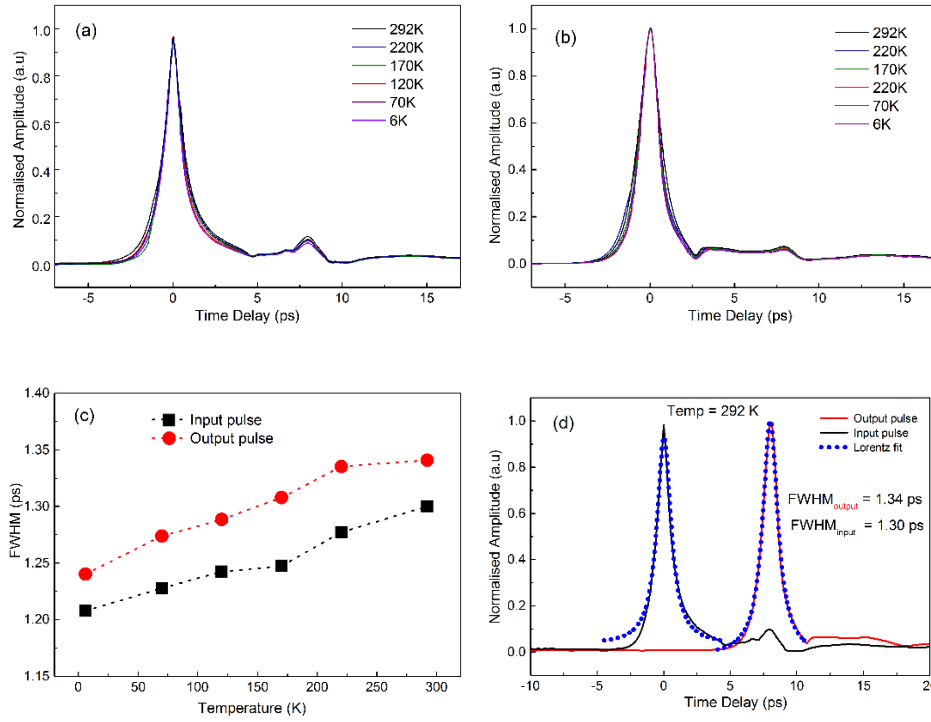
### **5.3.5 Low-temperature measurement using second generation CPW**

To observe higher-frequency resolution and temperature-dependent characteristics, optimised the second generation CPW devices were measured using the microstat system (see Section 5.3.1). The sample under test was then overlaid onto the CPW device to perform variable temperature spectroscopy.

#### **5.3.5.1 Low-temperature characterisation**

Optimised CPW devices were initially characterised at the low temperatures before variable-temperature spectroscopy of lactose monohydrate was performed. Input and output pulses were measured at 30 V bias, and low temperatures ranging from 6 to 292 K temperature in 50 K increments.

The full width at half maximum (FWHM) of the input and output pulses were then compared. Normalised input-output pulses are shown in Figure 5.17 a and b. It was observed that pulse-width decreased at low temperatures. The FWHM of the input and output pulses is plotted against temperature in Figure 5.17 c. Changes in the pulse width are attributed to changes in the carrier concentration at a low temperature. This is because the Fermi energy of the LT-GaAs changes as a function of temperature (see Equation 5-5), decreasing at low temperatures and therefore, the electron density in the conduction band also decreases [174].



**Figure 5.17** a) Normalised time-domain input pulses measured at different temperatures ranging from 6 to 292 K. b) Normalised output pulses measured for different temperatures. c) FWHM of the input and output pulses plotted against temperature. d) Lorentz fit of the input and output pulses (at room temperature), with FWHM of 1.32 ps and 1.41 ps respectively.

In other words, more and more electrons are populated in the valence band. Therefore, reduced carrier concentration results in low recombination time with consequent shortening of FWHM.

$$f_F(E) = \frac{1}{1 + \exp\left(\frac{E - E_F}{K_B T}\right)} \quad 5-5$$

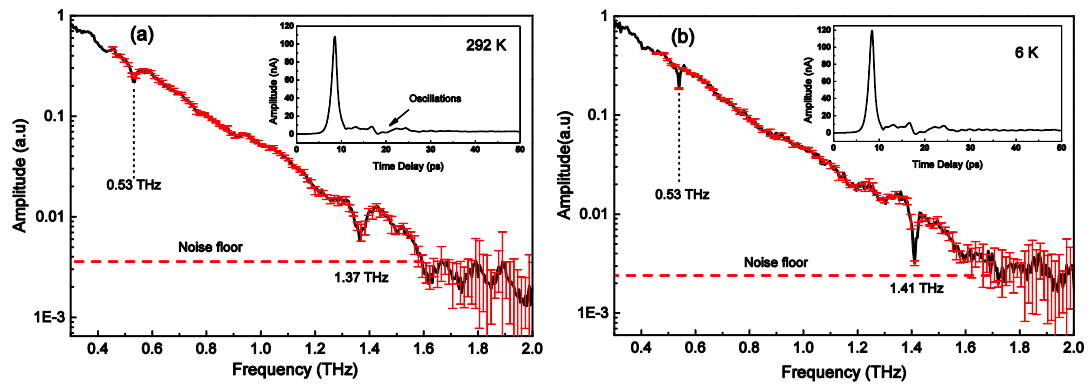
where,  $E_F$  is Fermi energy or Fermi level,  $f_F(E)$  indicates the probability that an energy level  $E$  will be filled by an electron,  $K_B = 8.62 \times 10^{-5}$  eV/K is Boltzmann's constant and  $T$  is the temperature in Kelvin.

### 5.3.5.2 Variable temperature spectroscopy using continuous CPW devices

Initially, lactose samples were measured at room temperature before being cooled down to 6 K using a microstat system. The temperature was then changed before each subsequent measurements using a temperature controller. To assess the actual bandwidth present in the signal, repeat measurements were performed. The standard

deviation of these repeat measurements provides a better estimate of the actual bandwidth present in the signal while the averaging process improves SNR of the FFT spectra.

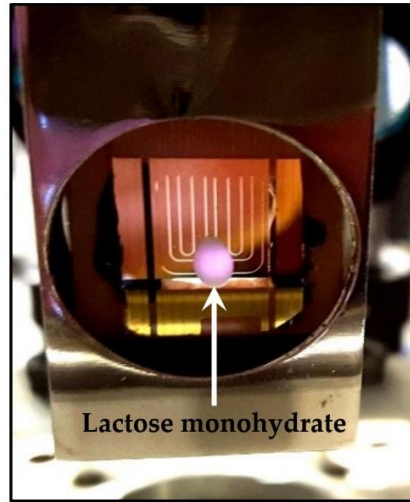
Ten scans of the output pulse transmitting from the switch S1 to S4 were initially measured at room temperature. A fast Fourier transform was then performed on the recorded time-domain pulses, with an average of 10 scans plotted with their standard deviation as shown in Figure 5.18 a. The approximate bandwidth present in the signal (judged from the frequency at which the noise floor is reached) is 1.6 THz. As the resolution of CPW device is only limited by the scan length of the time-delay stage, the time-domain signal is not truncated before taking the Fourier transform.



**Figure 5.18** a) Averaged FFT spectra of 10 scans at room temperature plotted against standard deviation (shown in red). Time-domain signal is shown in the inset graph. b) Averaged FFT spectra of 10 scans at 6 K with standard deviation is shown in red. Time-domain signal is shown in the inset graph.

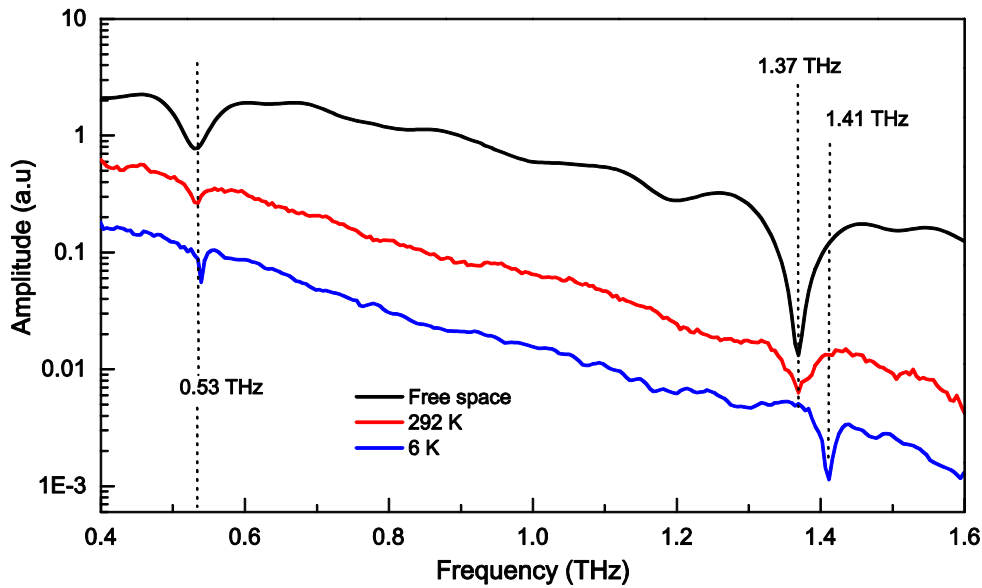
The FFT of the output pulse shows two main absorption features; the first feature is at 0.53 THz while the second at 1.37 THz. To ensure that absorption features are indeed due to overlaid lactose sample, these FFT spectra were compared directly with free space THz-TDS results as shown in the Figure 5.18 b. Similar experimental results regarding these two resonances have also been reported in the literature (see Refs [63, 168, 175-178]).

Although absorption features in lactose were clearly recorded using the second generation CPW device at room temperature, other interesting phenomena such as frequency shifting and narrowing of absorption features (reduction in FWHM) can also be observed as the temperature is reduced.



**Figure 5.19** Image of drop-casted lactose onto the transmission line of the second generation CPW device. The device is mounted on a PCB attached to the cold finger.

The occurrence of these phenomena is due to a change in the vibrational modes of the lactose molecules at lower temperatures [179].



**Figure 5.20** FFT Spectra of lactose monohydrate at the room temperature (red) and low temperatures (6 K, in blue). The temperature result is compared with FFT spectra obtained by free space THz-TDS (black). Plots are offset for clarity.

The sample was cooled down to 6 K by flowing liquid helium to the cold finger. The system was given up to 1.5 hours to reach thermal stabilisation before taking measurements. It is worth noting that photocurrent from the emitter switch S1 stopped

changing when thermal stabilisation was reached, as the position of the laser relative to the device did not change. Ten scans of output pulse transmitting from S1 to S4 were initially recorded at 6 K and then scans at different temperatures in the range of 70 – 220 K in 50 K increments were recorded. Fast Fourier transforms were then performed on time-domain pulses, and an average of ten scans plotted against the standard deviation in Figure 5.18. The magnitude of the error bars is smaller up to 1.6 THz in the FFT spectra, indicating the level of noise rises after 1.6 THz. Figure 5.18 b, Absorption features at 0.53 and 1.41 THz are clearly recorded. Room and low-temperature FFT spectra are compared in the Figure 5.21. It is clear from this graph that absorption features are more pronounced and that the second feature is shifted from 1.37 to 1.41 THz, when the sample is at 6 K. To verify the frequency shift at low temperature, room and low (6 K), temperature FFT spectra are compared with free-space THz-TDS FFT spectra.

The FWHM calculated from the Lorentz fit of the absorption feature at 0.53 THz is compared at room and low (6 K) temperature in the inset graph of Figure 5.21. It is clear from the inset graph that absorption feature at 0.53 has narrowed at the low temperatures.

At the low temperatures, the position of the absorption feature is slightly changed from 0.530 to 0.533 THz, and the FWHM of the absorption feature was reduced from 15 GHz to 9 GHz. In the literature [180], the 0.53 THz absorption feature has been attributed to a hindered rotation of the lactose molecule along the b-axis of the crystal within the hydrogen bond network.

Furthermore, the temperature dependence of the absorption features is explained by the decreased energy spacing due to the population of more molecules in a higher vibrational excited states at room temperature, which results in shifting absorption features to lower frequencies. At low temperatures, more molecules are populated the ground state, which results in an increase in the average frequency of absorption [181].

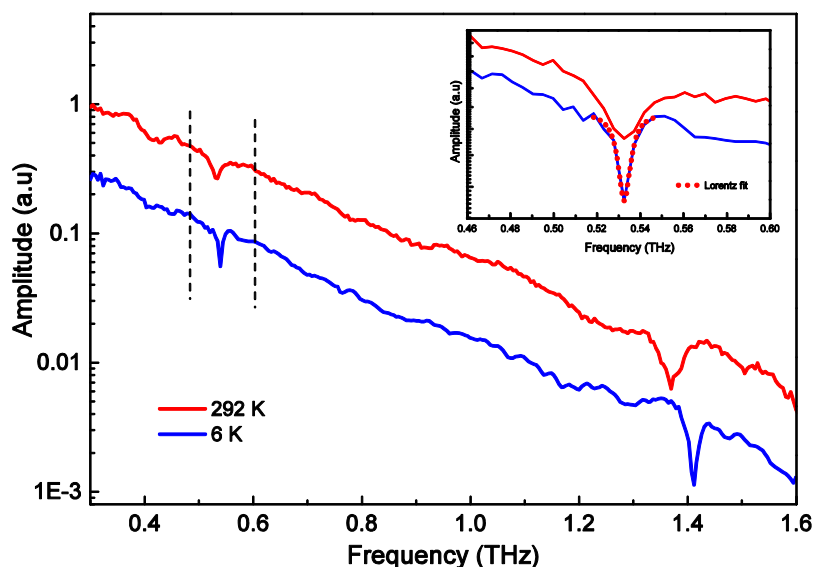


Figure 5.21 FFT Spectra of lactose monohydrate at the room (red) and low (6 K in blue) temperature. FWHM of 0.53 THz absorption feature is compared in the inset graph.

The temperature dependence for polycrystalline materials such as purine, adenine and  $\alpha$ -lactose monohydrate has been studied in the literature [169, 182] where a similar shift towards higher frequencies in the absorption features was recorded, as shown in Figure 5.22 a.

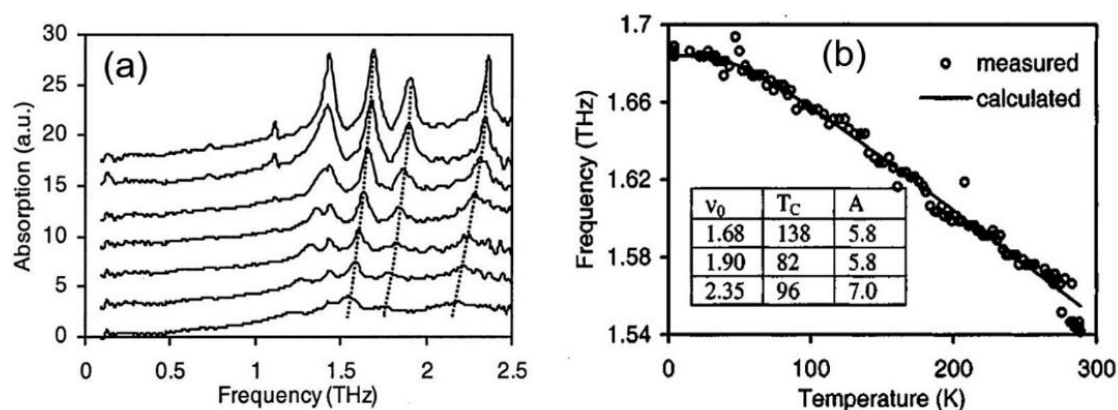


Figure 5.22 a) Absorption spectra of purine at 4, 54, 105, 204, 253, and 295 K (from top to bottom). b) Temperature dependence of the resonance frequency centred at 1.68 THz (at 4K). Open circles are experimental data, and the solid line is calculated by fitting Equation 5-6. The inset shows the best-fitting parameters in units of THz, K. (All plots taken from [182]).



In this Figure 5.22, the frequency shift in the absorption spectra of purine is fitted by empirical expression is given in Equation 5-6 to fit the centre frequency of vibrational mode  $\nu_0$  at different characteristic temperatures  $T_c$ .

$$\nu(T) = \nu_0 - \frac{AT_c}{e^{T_c/T} - 1} \quad 5-6$$

Where,  $\nu_0$  is the centre frequency of vibrational mode at zero K temperature,  $T_c$  is characteristic temperature and A is a constant.

It is clear from Figure 5.22 a and b that the intensities of vibrational modes increase as the temperature is reduced.

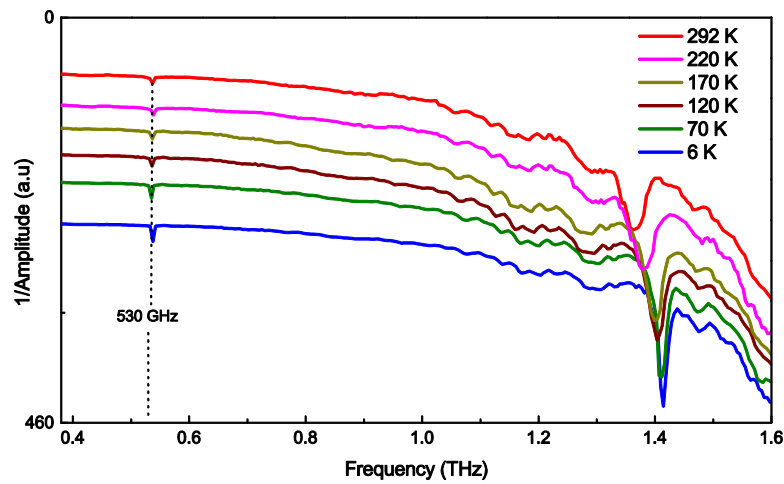
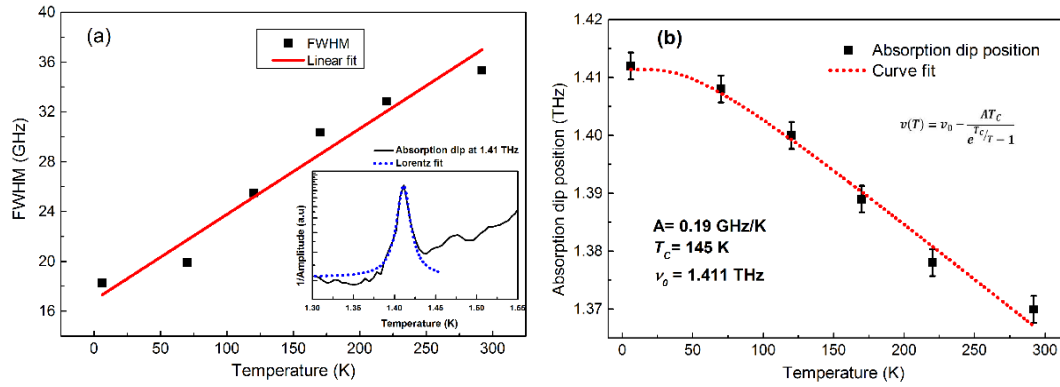


Figure 5.23 FFT spectra of subsequent measurements at room temperature, 6 K and temperatures ranging from 70 – 220 K in 50 K increments are plotted on a reciprocal (1/amplitude) scale against frequency.

In Figure 5.23, FFT spectra of subsequent measurements at different temperatures ranging from 70 – 220 K are plotted in 50 K increments on a reciprocal (1/amplitude) scale against frequency. On this reciprocal scale, high-frequency absorption features are emphasised while the noise floor is flattened. On the reciprocal scale, frequency shift (1.37 to 1.41 THz) and narrowing (reduced FWHM) of the higher-frequency spectral features can easily be seen. There was no significant shift recorded in the lower frequency (0.53 THz) absorption feature, but its relative amplitude decreases with increasing temperature.

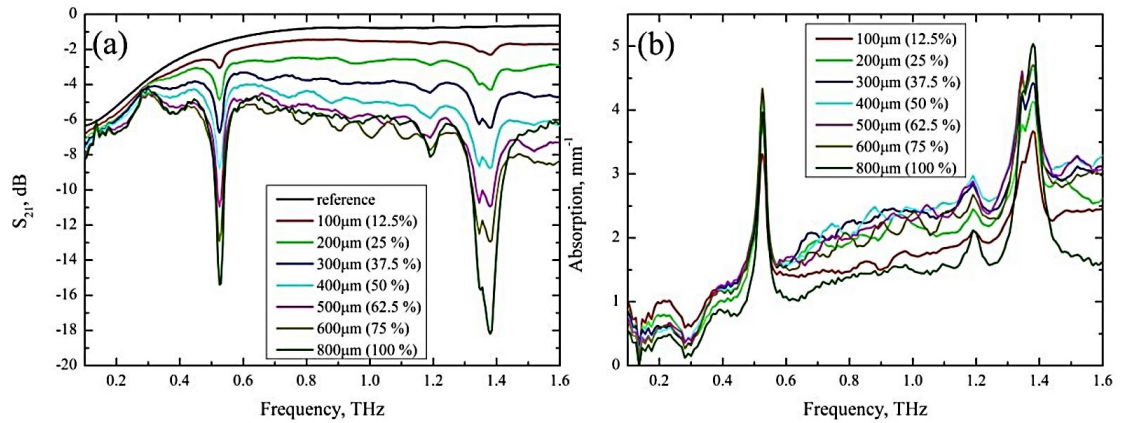


**Figure 5.24 a) The FWHM of the absorption feature at 1.41 THz plotted against temperature. Lorentz fit of the absorption feature is shown in inset graph. b) Shift in absorption dip (1.41 THz) plotted against temperature and centre frequency of the high-frequency absorption feature is determined by curve fitting using Equation 5-6.**

In Figure 5.24 b, the spectral shifting of the higher-frequency absorption (1.41 THz) feature is plotted against temperature. The spectral shifting was then fitted with Equation 5-6 to calculate the centre frequency  $\nu_0$  of the vibrational mode and characteristic temperature  $T_c$  of lactose monohydrate. The calculated values are shown in Figure 5.24 b. The FWHM of the high-frequency absorption feature calculated from Lorentz fitting is plotted against temperature in Figure 5.24 a.

### 5.3.5.3 Low- temperature spectroscopy using the second generation CGAP CPW device

HFSS provides the flexibility to create or edit material files in its material library. By using this feature of HFSS, an absorption model for lactose monohydrate can be developed, if frequency-dependent permittivity and loss tangent parameters (extracted from free-space THz-TDS of lactose monohydrate) are carefully defined. Simulation work by C. Russell *et al.* [90] suggests that the lactose absorption features can be enhanced by increasing the interaction length between the sample under test and the THz field travelling down the transmission line as shown in Figure 5.25.

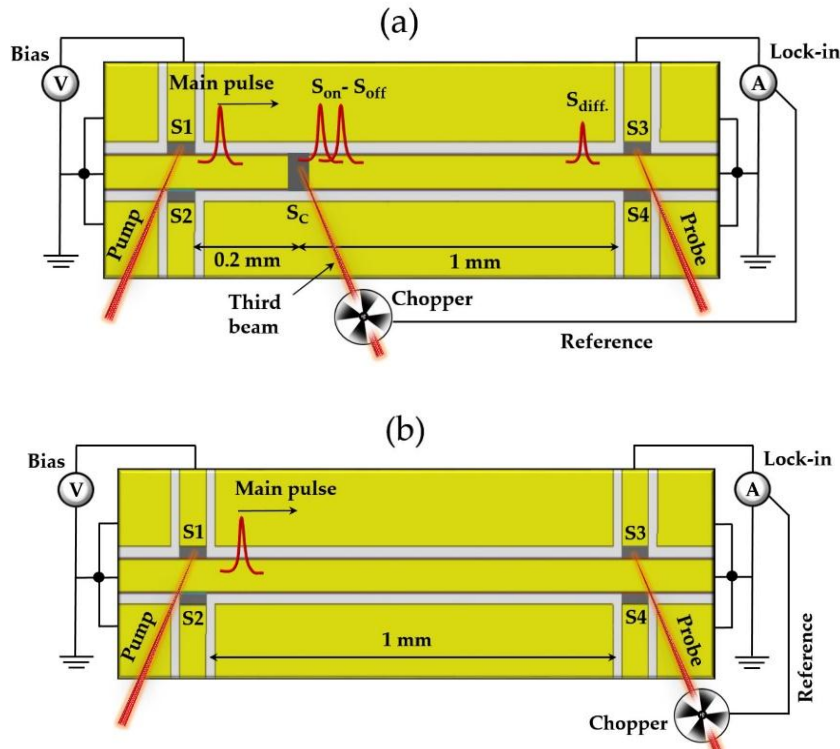


**Figure 5.25 HFSS simulation results for varying interaction lengths (100 – 800  $\mu\text{m}$ ) a)  $S_{21}$  parameters. b) Absorption spectra obtained for a PGL (planar Goubau line) loaded with lactose monohydrate. Simulation results are taken from [90].**

In the previous section, it was experimentally demonstrated that optimised (second generation) CPW device yielded a useful signal bandwidth of 1.6 THz. The interaction length between lactose samples and the THz pulse is limited by length (750  $\mu\text{m}$ ) of the transmission line, however. If the transmission length is further increased, the signal propagating through transmission line will be more attenuated, which will yield low bandwidth. In CPW device optimisation, therefore, there is always a trade-off between signal bandwidth and the interaction length of the transmission line.

To circumvent this issue, a CGAP (centre gap) CPW device was designed to maintain the signal bandwidth while allowing the transmission length to be increased from 750 to 1 mm. In Chapter 3, it was discussed in detail that how a CGAP CPW device filters out the dispersive slot-line mode (even mode) and only allows the coplanar mode (odd mode) to pass through. Furthermore, it minimises the system noise present in the signal by employing the three-beams differential-THz pulse measurement technique, in which a coupling switch is optically modulated to generate a difference signal.

In Figure 5.26 a, the second generation CGAP CPW device is shown in which a coupling switch is embedded lithographically 1 mm away from detection switches S3 and S4. In this scenario, a differential THz pulse propagates down the transmission line (1-mm-long) from the coupling switch Sc to detection switch S3.

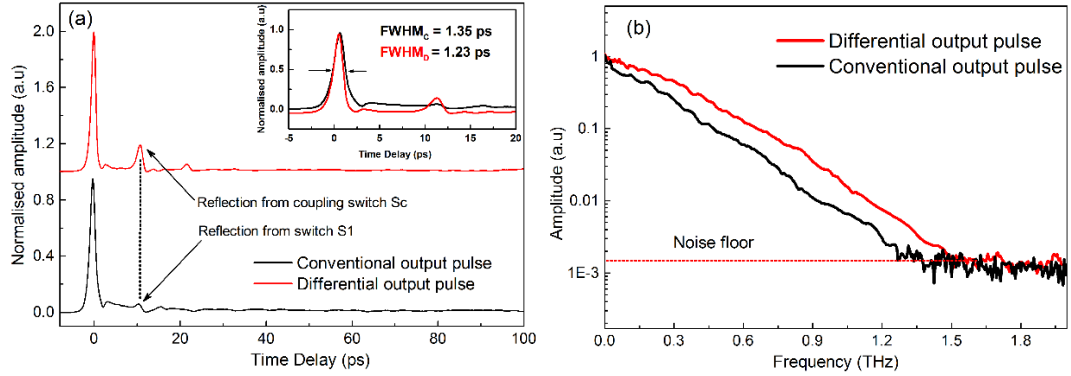


**Figure 5.26** a) Differential-THz output pulse measurement (second generation gap CPW) using the three-beam on-chip system. b) Conventional output pulse measurement (second generation continuous CPW) using the two-beam on-chip system.

The pump beam was focused onto PC switch S1 biased at 30 V and the THz pulse was generated at the switch. S1 propagated down the transmission line and then passed through the coupling switch. The third beam (synchronised with pump beam) and chopped by a mechanical chopper was focused onto the coupling switch S<sub>c</sub>, and the differential signal ( $S_{\text{on}} - S_{\text{off}}$ ) was measured by the lock-in amplifier connected to detector switch S3. Since the coupling switch only supports the less dispersive co-planar mode in the gap CPW, the FWHM of the differential THz pulse is found to be smaller than a conventional (i.e. pulse detected using the two-beam on-chip system) THz pulse. The output pulse from the 1-mm-long conventional CPW device as shown in Figure 5.26 b is measured using two beams in an on-chip system to compare with the differential output signal.

To ensure enhancement in the bandwidth, the FWHM of the differential output signal was measured from the gap CPW device and compared with the FWHM of the

output pulse measured from a continuous 1-mm-long CPW (referred as a conventional pulse) as shown in the inset graph of Figure 5.27 a. It was found that the FWHM (1.23 ps) of the differential signal is smaller than that of measured from the conventional FWHM (~1.41 ps) output pulse.



**Figure 5.27 a) A comparison of output pulses measured using two- and three-beam on-chip systems. Pulses are offset for clarity. FWHM of output pulses are compared in the inset graph. b) A comparison of the FFT spectra of output pulses from the different techniques.**

The first reflection in both conventional and differential output pulses occurs 10.5 ps after the main pulse. The first reflection in a conventional output pulse is due to impedance change caused by switch S1 (1 mm away from S3). The first reflection in a differential output pulse is due to the first discontinuity (the high impedance of the coupling switch) in the transmission line. Both conventional and differential output pulses travel the same distance (1 mm) before being detected at the switch S3 but yield different bandwidths as shown in Figure 5.27 b.

FFT spectra of conventional and differential output pulses have a different roll off slopes, as shown in Figure 5.27 b. The bandwidth of the differential output pulse is found to be 1.5 THz while the conventional output pulse yields a bandwidth of 1.2 THz.

In Figure 5.28, lactose monohydrate is drop-cast onto the transmission line of CGAP CPW devices in order to perform on-chip spectroscopy. PC switches S1, S<sub>c</sub> and S3, were then illuminated from the back of the substrate. The differential output pulses travelling from S<sub>c</sub> to S3 then interact with the overlaid lactose sample.

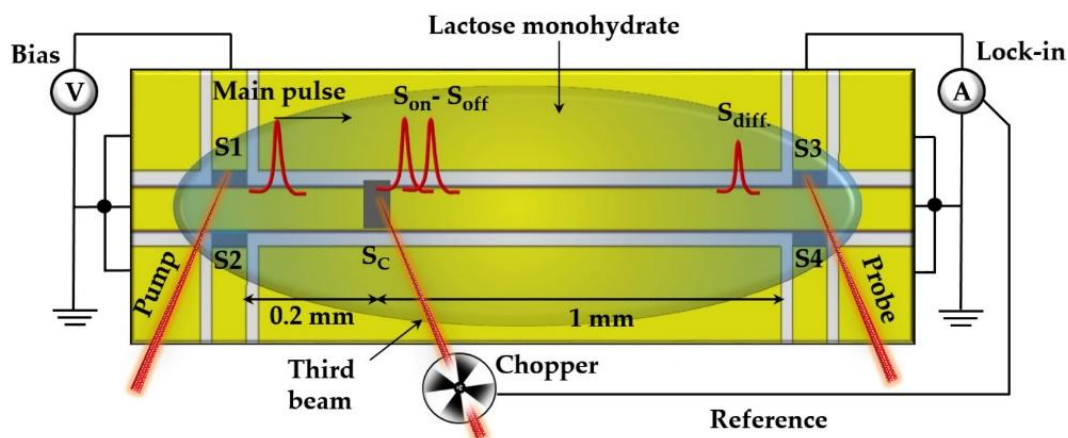


Figure 5.28 A schematic of a second generation gap CPW loaded with lactose monohydrate for differential spectroscopy measurement using the three-beam on-chip system.

Subsequent measurements of differential THz spectroscopy were then performed at room and low temperature ranging from 6 to 220 K in 50 K increments. Periodic oscillations in the time-domain signal shown in Figure 5.29 are more noticeable compared to the previously described on-chip spectroscopy measurements. Prominent oscillations are attributed to longer interaction length between sample under test and THz field. These oscillations correspond to the more pronounced absorption features seen in the FFT spectra.

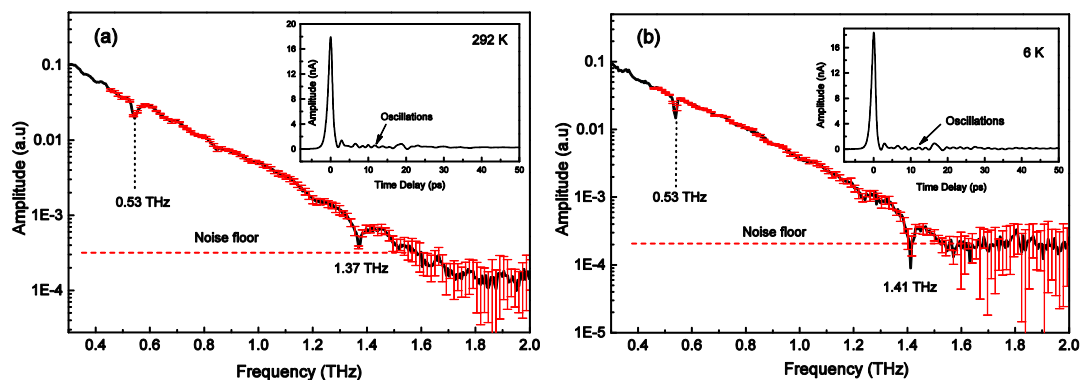


Figure 5.29 a) FFT spectra of 10 scans at room temperature plotted against standard deviation (shown in red). Differential time-domain signal is shown in the inset graph. b) FFT spectra of 10 scans at 6 K with standard deviation is shown in red. Differential time-domain signal is shown in the inset graph.

Ten scans of differential pulse transmitting from switch  $S_c$  to  $S_3$  were initially measured at room temperature. A Fast Fourier transform was then performed on the

recorded time-domain pulses, and the average of 10 FFTs were plotted along with the standard deviation at each frequency, as shown in Figure 5.29 a. The noise floor was reached at  $\sim 1.5$  THz in this data. In Figure 5.29 a, FFT spectra revealed two absorption features at 0.53 and 1.37 THz. A similar shift in the high-frequency absorption feature is recorded at the low temperatures, but features are more pronounced than previously measured, and their magnitudes are relatively higher than previously recorded absorption features.

## 5.4 Conclusion

From the simulation and experimental results, it was observed that dispersion and radiation losses in CPW strongly depend on the ground-to-ground spacing ( $S+2W$ ). Optimised second generation CPW (slot gap of 10  $\mu\text{m}$ ) device demonstrates higher bandwidth than conventional CPW device (slot gap of 20  $\mu\text{m}$ ), which enabled us to extract high-frequency spectral signatures of lactose monohydrate using on-chip spectroscopy technique. It is worth mentioning that CPW design could be further optimised by reducing ground-to-ground spacing, but conductor losses become prominent at a certain limit which imposes a minimum width requirement on the centre conductor line. Furthermore, it is shown how characteristic impedance and effective permittivity change in THz on-chip CPWs with changing slot gap width  $W$  using HFSS modelling. Electric field intensities and attenuation coefficient for the different slot gaps were calculated both from HFSS simulations and mathematical modelling. From these simulations, it is clear that field intensity increases with decreasing gap width, but the extent of field drops because the field is more tightly confined for narrower slot gaps.

Variable temperature characterisation of optimised CPW device was also performed. When the temperature was lowered in the range of from 293 to 6K, a decrease in the FWHM of input and output pulses was observed.

Lactose monohydrate was then loaded onto optimised CPW devices using the drop cast technique. At room temperature, on-chip spectroscopy of lactose monohydrate revealed two spectral features at 0.53 and 1.37 THz. On-chip spectroscopy

results were compared with free-space THz –TDS results to verify the origins of these spectral features, which were confirmed to arise from the lactose monohydrate samples. CPW devices were also cooled down to 6 K using a microstat allowing variable temperature spectroscopy was performed. A shift in the high-frequency spectral feature (1.37 THz) of lactose monohydrate was recorded.



# Chapter 6

## Conclusions and Future Work

### 6.1 Conclusions

The aim of the work discussed throughout this thesis was to optimise on-chip THz coplanar waveguide system as a probing tool in order to extract the spectral signatures of polycrystalline material in the THz regime. A theoretical model of CPW for THz transmission overlaid on different substrates such as GaAs and quartz was first developed from HFSS simulations, in order to estimate the useful bandwidth available from different CPW geometries. THz CPW on-chip devices were then designed and fabricated, and then tested using an on-chip measurement system. A differential on-chip THz-TDS was also developed inspired by the analogy of free-space differential THz-TDS systems. This differential on-chip system allowed us to generate differential THz pulses by modulating the conductivity of a coupling switch embedded in the middle of a CPW, using a three-beam optical setup. The potential use of branching waveguide system (Y-splitter/coupler) capable of splitting THz pulses was also explored, both from HFSS simulation work and on-chip measurements. Spectroscopic measurements of  $\alpha$ -lactose monohydrate overlaid onto on-chip waveguide were performed at both room and low temperature, subsequently revealing the spectral features of lactose monohydrate.

#### 6.1.1 First generation CPW devices

Results obtained from HFSS simulations suggested that a much higher bandwidth of  $\sim 1$  THz can be obtained from CPW<sub>quartz</sub> compared to  $\sim 0.45$  THz in CPW<sub>LT-GaAs</sub>. This was further investigated by on-chip measurements performed on both CPW<sub>LT-GaAs</sub> and CPW<sub>quartz</sub>.

The first-generation devices were then fabricated on both GaAs and quartz substrate. To fabricate CPW on a quartz substrate, an epitaxial lift-off technique was used to transfer thin layer ( $\sim 350$  nm) of LT-GaAs followed by a selective chemical etching to define photoconductive switch regions in CPW<sub>quartz</sub>.

From on-chip measurements, it was demonstrated that CPW<sub>quartz</sub> yields a higher bandwidth of 1.10 THz compared to that of CPW<sub>LT-GaAs</sub> ( $\sim 0.42$  THz). The propagation velocities of THz pulse in CPW<sub>LT-GaAs</sub> and CPW<sub>quartz</sub> were calculated as  $1.13 \times 10^8$  m/s and  $1.74 \times 10^8$  m/s respectively. The difference in pulse velocities was attributed to the different relative permittivities of the GaAs (12.9) and quartz (3.78) substrates. In the first-generation CPW<sub>quartz</sub>, a frequency resolution of 55 GHz was obtained, taking secondary reflections into account, while a Fast Fourier transform was performed on the time-domain pulse.

Differential pulses measured in the first-generation CGAP-CPW<sub>quartz</sub> using the three-beam on-chip system, yielded a much higher bandwidth of  $\sim 1.65$  THz (compared to be continuous CPW<sub>quartz</sub>) while propagating from coupling switch S<sub>c</sub> to S<sub>3</sub>, covering a transmission length of 0.75 mm. It has been demonstrated that a coupling switch embedded in the middle of transmission region acts like a high-pass filter that only allows high-frequency components (i.e. above cut-off frequency) present in a THz pulse passing through the coupling gap. It has also been demonstrated that shape of a THz pulse can potentially be manipulated (Gaussian to monocycle or vice-versa) by illuminating coupling switch with varying laser power.

Initial spectroscopy measurements performed using the first-generation CGAP-CPW<sub>quartz</sub> demonstrated that spectral features seen in FFT spectra (at  $\sim 0.53$  and 1.37 THz) due to lactose monohydrate were of rather a small magnitude and were somewhat smeared when time domain data was zero padded in order to remove artefacts observed in FFT spectra, and therefore, spectral features could not be resolved.

### 6.1.2 Second generation CPW devices

In a second generation of CPW<sub>quartz</sub> devices, a shorter transmission region of 1mm compared to 1.5 mm in the first-generation CPW<sub>quartz</sub> device, was adopted in order to

minimise attenuation loss with a consequent increase in bandwidth (from  $\sim 1.10$  to  $1.2$  THz). Also, the parasitic regions were extended to substantially delay secondary reflections coming from discontinuities located in parasitic regions. With long parasitic regions, a much higher frequency resolution of  $\sim 2$  GHz was obtained from the second generation CPW<sub>quartz</sub> device. The second generation CPW device was further optimised to enhance device bandwidth. HFSS simulations showed that for smaller slot gap width, radiation losses can significantly be minimised with a subsequent increase in bandwidth. Therefore, a slot gap width of  $10\text{ }\mu\text{m}$  and transmission length of  $750\text{ }\mu\text{m}$  was adopted in the second generation CPW devices. On-chip measurements demonstrated an enhanced bandwidth of  $1.6$  THz while the frequency resolution of  $\sim 2$  GHz was obtained. The enhanced bandwidth of the second generation device was then exploited to perform spectroscopy measurements. From spectroscopic measurements performed on optimised second generation device, spectral features of lactose monohydrate (occurred at  $\sim 0.53$  and  $1.37$  THz) were completely resolved. Also, spectroscopic measurements performed over a range of ( $\sim 6$  to  $293$  K) temperatures showed a significant shift in high-frequency spectral feature ( $\sim 1.37$  THz) of lactose monohydrate.

### **6.1.3 Y-splitter/coupler**

From on-chip measurements performed on Y-splitter, it was demonstrated that THz pulse propagating towards Y-junction can be split into two identical THz pulses which further propagate in branching waveguides. A Y-coupler waveguide allowed us to measure differential and conventional THz pulses from the same waveguide. A bandwidth of  $\sim 750$  GHz (quartz substrate) was observed from FFT spectra of split THz pulses. Initial spectroscopic measurements performed on Y-coupler demonstrated that Y-splitter/coupler could potentially be used for on-chip spectroscopy (provided higher bandwidth could be obtained.)

## **6.2 Future Work**

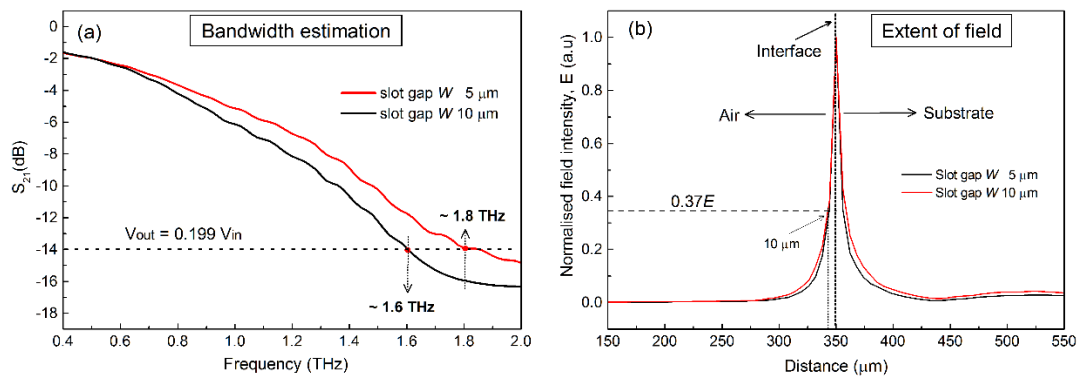
In on-chip spectroscopic measurements, it may be desirable to increase the on-chip system bandwidth in order to probe spectral features of polycrystalline materials occurring at

higher frequencies. Also, it would be useful to fabricate a waveguide system having more than two branching waveguides, allowing spectroscopic measurement of a variety of materials to be performed using the same waveguide.

An example of a Y-splitter having more than two branching waveguides is discussed in the following sections. In Chapter 4, it has been demonstrated that THz pulses can potentially be detected from one branching waveguide to another, and therefore, a Y-splitter can further be investigated as a THz multiplexer/combiner in order to observe interference (constructive or destructive) pattern caused by two THz pulses crossing a Y-junction.

### 6.2.1 Bandwidth enhancement

In Chapter 5, it has been demonstrated that bandwidth of CPW<sub>quartz</sub> can be enhanced by reducing the slot gap width 'W' (separation between centre conductor and ground plane) subsequently reducing radiation loss  $\alpha_r$  (where,  $\alpha_r \propto (S + 2W)^2$ ). A comparison of transmission loss parameters obtained from HFSS simulation for slot gap width 5 and 10  $\mu\text{m}$  is shown in Figure 6.1 a.



**Figure 6.1 a) A comparison of scattering parameters obtained from HFSS simulations performed on CPWs with 5 and 10  $\mu\text{m}$  slot gaps. b) Normalised field intensity for gap widths 5 and 10  $\mu\text{m}$  plotted against a ployline perpendicular to CPW plane.**

On the basis of transmission loss parameters obtained from HFSS, it seems fair to suggest that bandwidth of CPW<sub>quartz</sub> can further be increased from  $\sim 1.6$  to  $1.8$  THz (shown in Figure 6.1 a) by adopting a slot gap width of  $5 \mu\text{m}$  with a consequent increase in design complexity. In Figure 6.1 b, the intensity of evanescent field plotted against distance

perpendicular to CPW geometry, suggests that extent of the field for 5 and 10  $\mu\text{m}$  slot gap CPWs is of the same order ( $\sim 10 \mu\text{m}$ ), therefore, reducing slot gap width should not affect spectroscopic measurements.

## 6.2.2 Implementation of tunable filters in CPW

In Chapter 3, a potential use of coupling gap discontinuity as a high-pass filter has been demonstrated. However, CPW geometry can further be exploited in order to realise fundamental filter elements such as pass-band and stop-band filters (see Chapter 2) which can potentially be tuned (i.e. varying capacitive and inductive reactance) by employing a free-standing LT-GaAs switch underneath the filter element with subsequent laser beam illumination.

Examples of the proposed “stop-band” (centre frequency  $\sim 460 \text{ GHz}$ ) and “pass-band” filter (centre frequency  $\sim 275 \text{ GHz}$ ) designs with their equivalent circuit models are shown in Figure 6.2. Stop and pass-band filters can be realised by introducing “series short” and “series open” stub (lithographically) in the centre conductor of a CPW respectively as shown in Figure 6.2 a and b.

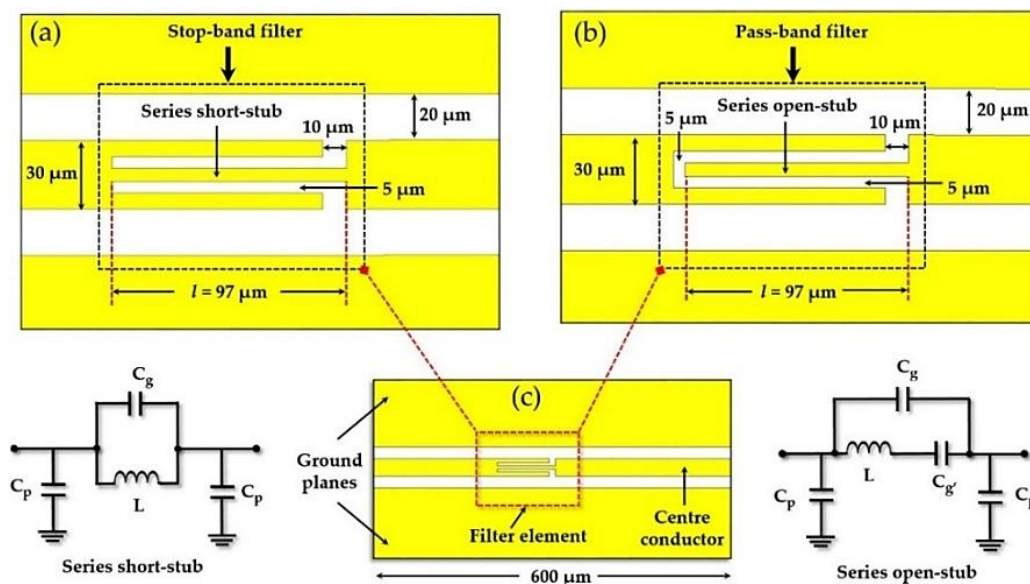
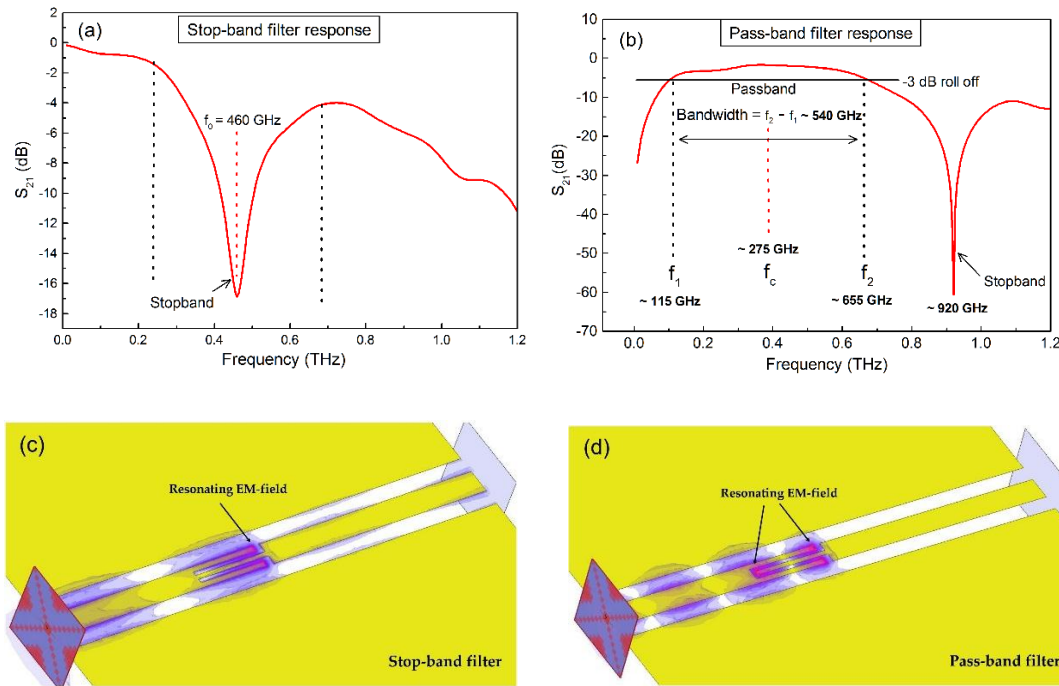


Figure 6.2 Implementation of tunable filters in CPW a) A stop band filter formed by the series short stub b) A pass-band filter formed by the series open stub c) A schematic of proposed CPW device design.

Resonant frequency of filters mentioned above can be obtained as:

$$f_o = \frac{c}{\sqrt{\epsilon_{eff}}} \left( \frac{1}{4l} \right) \quad 6-1$$

Where,  $f_o$  is the resonant frequency,  $\epsilon_{eff}$  is the effective permittivity of dielectric medium and  $l$  is the length of quarter wavelength ( $\lambda_g/4$ ) stub resonator.



**Figure 6.3 a) A stop band with resonant frequency 460 GHz b) A pass band with centre frequency 275 GHz, followed by a stop band with resonant frequency 920 GHz. c) EM field simulation of stop band filter showing resonance field around the stub region d) Em field simulations of pass-band filter shwoing two resonances corresponding to pass-band and stop-band.**

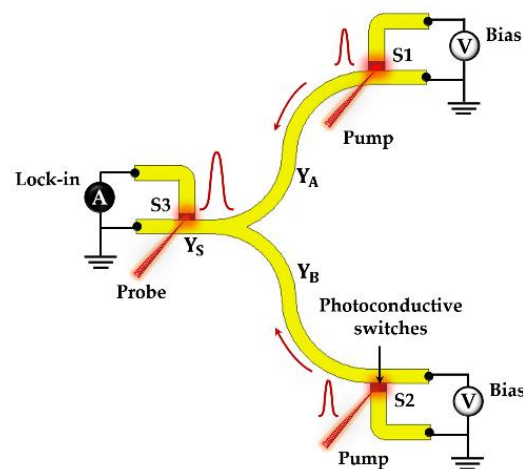
For a series short stub length of  $97 \mu\text{m}$  and width of  $6 \mu\text{m}$ , stop-band filter demonstrated a resonance frequency of  $\sim 460$  GHz while simulations were performed over the frequency range  $0.1\text{--}1.2$  THz, using HFSS. For a series open stub, a pass-band resonance occurred when the resonator length was found to be  $\lambda_g/4$  and subsequent stop-band resonance occurred (as shown in Figure 6.3 b) when resonator length was  $\lambda_g/2$ . In Figure 6.3 b, centre frequency of “pass-band” filter was obtained by taking the geometric mean of lower and upper cut-off frequencies as:

$$f_c = \sqrt{f_1 \times f_2} \quad 6-2$$

In Figure 6.3 d, a closer look at EM-field simulations indicates that two resonances occurring in the series open stub region, correspond to “pass-band” and “stop-band” resonances respectively. These resonating fields can potentially be used as sensing tool in order to probe any significant variation in effective permittivity due to overlaid sample under test [183].

### 6.2.3 Future spectroscopic measurements using Y-splitter/coupler

As discussed earlier, it would be useful to test the functionality of a Y-splitter as a multiplexer/combiner system in order to study interference pattern of THz pulses. An example of Y-splitter is shown in Figure 6.4, in which biasing and probing connections are swapped and a three-beam system is employed in order to generate THz pulse at the switch S1 and S2 simultaneously with a subsequent detection of an output pulse (in straight waveguide,  $Y_S$ ) caused by constructive/destructive interference of THz pulses propagating along branching waveguides  $Y_A$  and  $Y_B$ .

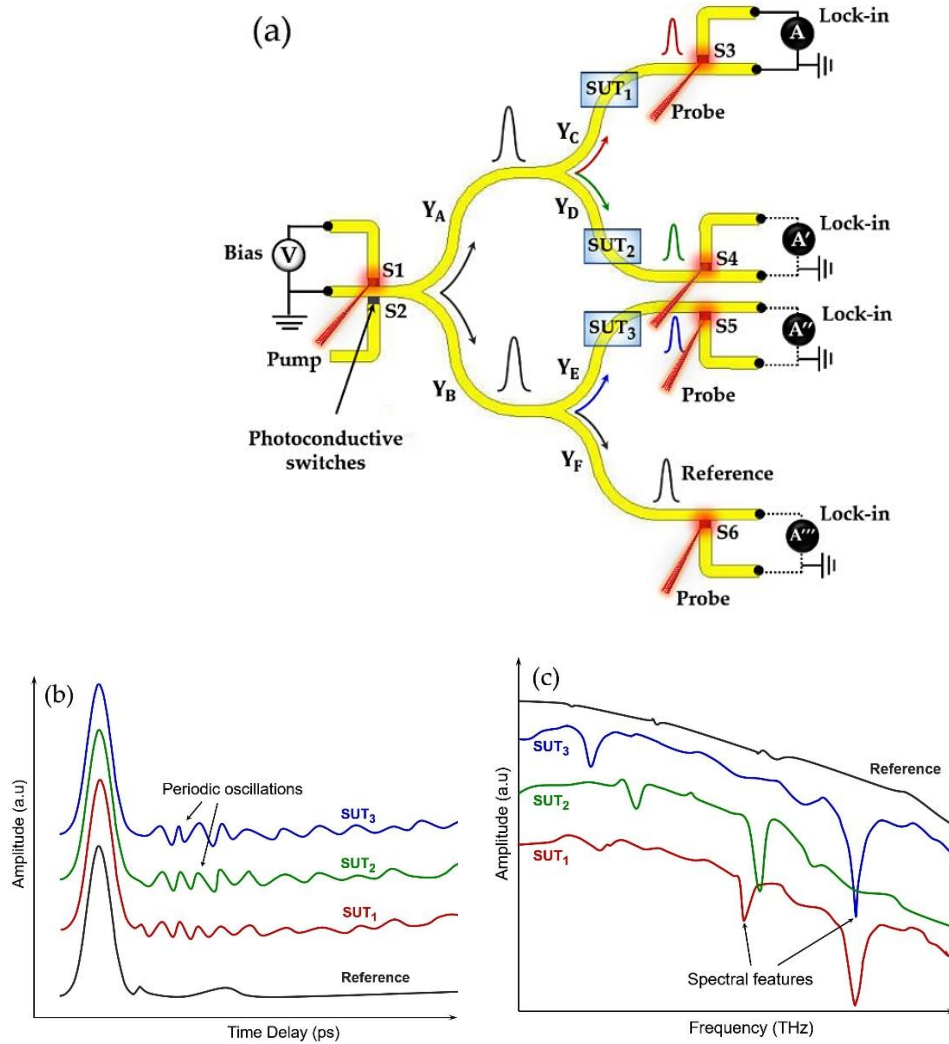


**Figure 6.4** An illustration of Y-splitter used as a multiplexer/combiner in order to study interference pattern.

In this configuration, it is important to note that if relative time delay between THz pulses propagating along  $Y_A$  and  $Y_B$  is varied by means of an optical delay stage, an interference pattern can be observed in the pulse detected at the switch S3.

By employing more than two branching waveguides in a Y-splitter waveguide would allow us to perform spectroscopic measurement on more than one SUT (sample under test) using the same waveguide. An example of 1×4 Y-splitter comprising cascaded

1×2 Y-splitters with arc-shaped branching waveguides is shown in Figure 6.5 a, in which branching waveguides  $Y_C, Y_D$  and  $Y_E$  are loaded with three different test samples  $SUT_1, SUT_2$  and  $SUT_3$  in order to detect sampled THz pulses while unloaded branching waveguide  $Y_F$  can be used to detect a reference THz pulse.



**Figure 6.5** An illustration of 1×4 Y-splitter comprising cascaded 1×2 Y-splitters with arc-shaped branching waveguides in which three branching waveguides are loaded with samples under test and the remaining branching waveguide is used to measure a reference signal.

Spectral features of each test sample then can be extracted by performing furrier transform on time-domain THz pulses. An illustration of sampled and reference THz pulses detected from branching waveguides  $Y_C, Y_D, Y_E$  and  $Y_F$  and spectral features obtained from their respective FFT spectra is shown in Figure 6.5 b and c.



# Conference Proceeding

- S. Chowdhury, J. R. Freeman, M. C. Rosamond, R. A. Mohandas, **M. Kumar**, L. Li, *et al.*, "Study of the effect of annealing temperature on low-temperature-grown-GaAs photomixers," 2015.

## References

- [1] C. Sirtori, "Applied physics: Bridge for the terahertz gap," *Nature*, vol. 417, pp. 132-133, 2002.
- [2] G. P. Williams, "Filling the THz gap—high power sources and applications," *Reports on Progress in Physics*, vol. 69, p. 301, 2005.
- [3] B. S. Williams, "Terahertz quantum-cascade lasers," *Nature photonics*, vol. 1, pp. 517-525, 2007.
- [4] P. H. Siegel, "Terahertz technology," *IEEE Transactions on microwave theory and techniques*, vol. 50, pp. 910-928, 2002.
- [5] P. U. Jepsen, D. G. Cooke, and M. Koch, "Terahertz spectroscopy and imaging—Modern techniques and applications," *Laser & Photonics Reviews*, vol. 5, pp. 124-166, 2011.
- [6] K.-E. Peiponen, A. Zeitler, and M. Kuwata-Gonokami, *Terahertz spectroscopy and imaging* vol. 171: Springer, 2012.
- [7] J. J. Cunningham, M. Byrne, C. D. Wood, and L. Dazhang, "On-chip terahertz systems for spectroscopy and imaging," *Electronics Letters*, vol. 46, pp. s34-s37, 2010.
- [8] J. A. Zeitler, P. F. Taday, D. A. Newnham, M. Pepper, K. C. Gordon, and T. Rades, "Terahertz pulsed spectroscopy and imaging in the pharmaceutical setting—a review," *Journal of Pharmacy and Pharmacology*, vol. 59, pp. 209-223, 2007.
- [9] X. Wang, D. J. Hilton, L. Ren, D. M. Mittleman, J. Kono, and J. L. Reno, "Terahertz time-domain magnetospectroscopy of a high-mobility two-dimensional electron gas," *Optics letters*, vol. 32, pp. 1845-1847, 2007.
- [10] M. Dressel, N. Drichko, B. Gorshunov, and A. Pimenov, "THz spectroscopy of superconductors," *Selected Topics in Quantum Electronics, IEEE Journal of*, vol. 14, pp. 399-406, 2008.
- [11] F. Lewen, R. Gendriesch, I. Pak, D. Paveliev, M. Hepp, R. Schieder, *et al.*, "Phase locked backward wave oscillator pulsed beam spectrometer in the

- submillimeter wave range," *Review of scientific instruments*, vol. 69, pp. 32-39, 1998.
- [12] G. Grüner, "Millimeter and submillimeter wave spectroscopy of solids," *Millimeter and Submillimeter Wave Spectroscopy of Solids*, vol. 1, 1998.
  - [13] S. Martens, B. Gompf, and M. Dressel, "Characterization of continuous-wave terahertz sources: laser mixing versus backward-wave oscillators," *Applied optics*, vol. 48, pp. 5490-5496, 2009.
  - [14] J. Gunn, "Instabilities of current in III-V semiconductors," *IBM Journal of Research and Development*, vol. 8, pp. 141-159, 1964.
  - [15] J. Zhu, "MBE growth, fabrication, and electrical characterisation of terahertz frequency quantum cascade lasers," University of Leeds, 2015.
  - [16] S. Fatholouloumi, E. Dupont, I. C. Chan, Z. R. Wasilewski, S. R. Laframboise, D. Ban, *et al.*, "199.5 K operation of THz quantum cascade lasers," in *CLEO: Science and Innovations*, 2012, p. CTu2B. 1.
  - [17] W. Zouaghi, M. Thomson, K. Rabia, R. Hahn, V. Blank, and H. Roskos, "Broadband terahertz spectroscopy: principles, fundamental research and potential for industrial applications," *European Journal of Physics*, vol. 34, p. S179, 2013.
  - [18] Y. Sakai, I. Kawayama, H. Nakanishi, and M. Tonouchi, "Visualization of GaN surface potential using terahertz emission enhanced by local defects," *Scientific Reports*, vol. 5, p. 13860, 09/09/online 2015.
  - [19] Q. Chang, D. Yang, and L. Wang, "Broadband THz generation from photoconductive antenna," in *Progress in electromagnetics research symposium*, 2005.
  - [20] Z. Piao, M. Tani, and K. Sakai, "Carrier dynamics and terahertz radiation in photoconductive antennas," *Japanese Journal of Applied Physics*, vol. 39, p. 96, 2000.
  - [21] M. Martin and E. Brown, "Critical comparison of GaAs and InGaAs THz photoconductors," in *SPIE OPTO*, 2012, pp. 826102-826102-7.
  - [22] S. Jayaraman and C. H. Lee, "Observation of Two-Photon Conductivity in GaAs with Nanosecond and Picosecond Light Pulses," *Applied Physics Letters*, vol. 20, pp. 392-395, 1972.

- [23] Y. Shen, P. Upadhyaya, E. Linfield, H. Beere, and A. Davies, "Ultrabroadband terahertz radiation from low-temperature-grown GaAs photoconductive emitters," *Applied physics letters*, vol. 83, pp. 3117-3119, 2003.
- [24] K. Sakai and M. Tani, "Introduction to terahertz pulses," in *Terahertz optoelectronics*, ed: Springer, 2005, pp. 1-30.
- [25] C.-S. Kim, J.-H. Kim, K.-J. Yee, D.-H. Youn, and K.-Y. Kang, "Annealing-induced Modifications of Carrier Dynamics and Plasmon-phonon Coupling in Low-temperature-grown GaAs," *Journal of the Korean Physical Society*, vol. 55, pp. 630-635, 2009.
- [26] S. Gupta, M. Frankel, J. Valdmann, J. Whitaker, G. Mourou, F. Smith, *et al.*, "Subpicosecond carrier lifetime in GaAs grown by molecular beam epitaxy at low temperatures," *Applied Physics Letters*, vol. 59, pp. 3276-3278, 1991.
- [27] R. E. Viturro, M. R. Melloch, and J. M. Woodall, "Optical emission properties of semi-insulating GaAs grown at low temperatures by molecular beam epitaxy," *Applied physics letters*, vol. 60, pp. 3007-3009, 1992.
- [28] K. McIntosh, K. Nichols, S. Verghese, and E. Brown, "Investigation of ultrashort photocarrier relaxation times in low-temperature-grown GaAs," *Applied physics letters*, vol. 70, pp. 354-356, 1997.
- [29] A. Bonvalet, M. Joffre, J. Martin, and A. Migus, "Generation of ultrabroadband femtosecond pulses in the mid-infrared by optical rectification of 15 fs light pulses at 100 MHz repetition rate," *Applied Physics Letters*, vol. 67, pp. 2907-2909, 1995.
- [30] J. Zhang, Y. Hong, S. Braunstein, and K. Shore, "Terahertz pulse generation and detection with LT-GaAs photoconductive antenna," in *Optoelectronics, IEE Proceedings-*, 2004, pp. 98-101.
- [31] C. Fattinger and D. Grischkowsky, "Terahertz beams," *Applied Physics Letters*, vol. 54, pp. 490-492, 1989.
- [32] M. Van Exter and D. R. Grischkowsky, "Characterization of an optoelectronic terahertz beam system," *Microwave Theory and Techniques, IEEE Transactions on*, vol. 38, pp. 1684-1691, 1990.
- [33] C. Winnewisser, P. U. Jepsen, M. Schall, V. Schyja, and H. Helm, "Electro-optic detection of THz radiation in LiTaO<sub>3</sub>, LiNbO<sub>3</sub> and ZnTe," *Applied Physics Letters*, vol. 70, pp. 3069-3071, 1997.

- [34] Q. Wu and X.-C. Zhang, "7 terahertz broadband GaP electro-optic sensor," *Applied Physics Letters*, vol. 70, pp. 1784-1786, 1997.
- [35] Q. Wu and X. C. Zhang, "Free-space electro-optic sampling of terahertz beams," *Applied Physics Letters*, vol. 67, pp. 3523-3525, 1995.
- [36] N. C. van der Valk, T. Wenckebach, and P. C. Planken, "Full mathematical description of electro-optic detection in optically isotropic crystals," *JOSA B*, vol. 21, pp. 622-631, 2004.
- [37] A. Tomasino, A. Parisi, S. Stivala, P. Livreri, A. Cino, A. Busacca, *et al.*, "Wideband THz time domain spectroscopy based on optical rectification and electro-optic sampling," *Scientific reports*, vol. 3, 2013.
- [38] M. He, A. K. Azad, S. Ye, and W. Zhang, "Far-infrared signature of animal tissues characterized by terahertz time-domain spectroscopy," *Optics Communications*, vol. 259, pp. 389-392, 2006.
- [39] D. M. Mittleman, R. H. Jacobsen, R. Neelamani, R. G. Baraniuk, and M. C. Nuss, "Gas sensing using terahertz time-domain spectroscopy," *Applied Physics B: Lasers and Optics*, vol. 67, pp. 379-390, 1998.
- [40] A. G. Davies, A. D. Burnett, W. Fan, E. H. Linfield, and J. E. Cunningham, "Terahertz spectroscopy of explosives and drugs," *Materials Today*, vol. 11, pp. 18-26, 2008.
- [41] B. M. Fischer, H. Helm, and P. U. Jepsen, "Chemical recognition with broadband THz spectroscopy," *Proceedings of the IEEE*, vol. 95, pp. 1592-1604, 2007.
- [42] B. Ferguson, S. Wang, D. Gray, D. Abbott, and X.-C. Zhang, "Identification of biological tissue using chirped probe THz imaging," *Microelectronics Journal*, vol. 33, pp. 1043-1051, 2002.
- [43] S. L. Dexheimer and J. Shan, "Terahertz Spectroscopy Principles and Applications," 2007.
- [44] L. Duvillaret, F. Garet, J.-F. Roux, and J.-L. Coutaz, "Analytical modeling and optimization of terahertz time-domain spectroscopy experiments, using photoswitches as antennas," *Selected Topics in Quantum Electronics, IEEE Journal of*, vol. 7, pp. 615-623, 2001.
- [45] L. Duvillaret, F. Garet, and J.-L. Coutaz, "A reliable method for extraction of material parameters in terahertz time-domain spectroscopy," *Selected Topics in Quantum Electronics, IEEE Journal of*, vol. 2, pp. 739-746, 1996.

- [46] W. Withayachumnankul, H. Lin, S. Mickan, B. M. Fischer, and D. Abbott, "Analysis of measurement uncertainty in THz-TDS," in *Microtechnologies for the New Millennium*, 2007, pp. 659326-659326-18.
- [47] C. Russell, C. D. Wood, A. D. Burnett, L. Li, E. H. Linfield, A. G. Davies, *et al.*, "Spectroscopy of polycrystalline materials using thinned-substrate planar Goubau line at cryogenic temperatures," *Lab on a Chip*, vol. 13, pp. 4065-4070, 2013.
- [48] G. M. Png, B. M. Fischer, D. Appadoo, R. Plathe, and D. Abbott, "Double-layered nitrocellulose membrane sample holding technique for THz and FIR spectroscopic measurements," *Optics Express*, vol. 23, pp. 4997-5013, 2015/02/23 2015.
- [49] F. Théberge, M. Châteauneuf, J. Dubois, S. Désilets, and L.-S. Lussier, "Spectral artifacts from non-uniform samples analyzed by terahertz time-domain spectroscopy," *Optics Express*, vol. 17, pp. 10841-10848, 2009/06/22 2009.
- [50] S. Yamauchi, S. Hatakeyama, Y. Imai, and M. Tonouchi, "Nondestructive evaluation of crystallized-particle size in lactose-powder by terahertz time-domain spectroscopy," *Optical Engineering*, vol. 53, pp. 031203-031203, 2013.
- [51] P. Dean, A. Burnett, K. Tych, S. Khanna, M. Lachab, J. Cunningham, *et al.*, "Measurement and analysis of the diffuse reflectance of powdered samples at terahertz frequencies using a quantum cascade laser," *The Journal of chemical physics*, vol. 134, p. 134304, 2011.
- [52] W. Fan, A. Burnett, P. Upadhy, J. Cunningham, E. Linfield, and A. Davies, "Far-infrared spectroscopic characterization of explosives for security applications using broadband terahertz time-domain spectroscopy," *Applied spectroscopy*, vol. 61, pp. 638-643, 2007.
- [53] E. Brown, E. Mendoza, Y. Kuznetsova, A. Neumann, and S. Brueck, "High-Resolution THz Spectroscopy to Measure Strong THz Absorption Signatures of si-RNA in Solution," in *Terahertz and Mid Infrared Radiation*, ed: Springer, 2011, pp. 15-22.
- [54] A. Dobroiu, M. Yamashita, Y. N. Ohshima, Y. Morita, C. Otani, and K. Kawase, "Terahertz imaging system based on a backward-wave oscillator," *Applied optics*, vol. 43, pp. 5637-5646, 2004.
- [55] K. M. Tych, C. D. Wood, and W. Tych, "A Simple Transfer-Function-Based Approach for Estimating Material Parameters From Terahertz Time-Domain Data," *IEEE Photonics Journal*, vol. 6, pp. 1-11, 2014.

- [56] Z. Jiang, M. Li, and X.-C. Zhang, "Dielectric constant measurement of thin films by differential time-domain spectroscopy," *Applied Physics Letters*, vol. 76, pp. 3221-3223, 2000.
- [57] S. P. Mickan, K.-S. Lee, T.-M. Lu, J. Munch, D. Abbott, and X.-C. Zhang, "Double modulated differential THz-TDS for thin film dielectric characterization," *Microelectronics Journal*, vol. 33, pp. 1033-1042, 2002.
- [58] Z. Lu, P. Campbell, and X.-C. Zhang, "Free-space electro-optic sampling with a high-repetition-rate regenerative amplified laser," *Applied Physics Letters*, vol. 71, pp. 593-595, 1997.
- [59] H.-B. Liu, G. Plopper, S. Earley, Y. Chen, B. Ferguson, and X.-C. Zhang, "Sensing minute changes in biological cell monolayers with THz differential time-domain spectroscopy," *Biosensors and bioelectronics*, vol. 22, pp. 1075-1080, 2007.
- [60] K. Wang and D. M. Mittleman, "Metal wires for terahertz wave guiding," *Nature*, vol. 432, pp. 376-379, 2004.
- [61] J. A. Deibel, K. Wang, M. Escarra, N. Berndsen, and D. M. Mittleman, "The excitation and emission of terahertz surface plasmon polaritons on metal wire waveguides," *Comptes Rendus Physique*, vol. 9, pp. 215-231, 2008.
- [62] R. Sprik, I. Duling Iii, C. C. Chi, and D. Grischkowsky, "Far infrared spectroscopy with subpicosecond electrical pulses on transmission lines," *Applied physics letters*, vol. 51, pp. 548-550, 1987.
- [63] M. Walther, M. R. Freeman, and F. A. Hegmann, "Metal-wire terahertz time-domain spectroscopy," *Applied Physics Letters*, vol. 87, p. 261107, 2005.
- [64] M. B. Byrne, "Pulsed imaging and spectroscopy using on-chip THz waveguides," University of Leeds, 2008.
- [65] S. Coleman and D. Grischkowsky, "A THz transverse electromagnetic mode two-dimensional interconnect layer incorporating quasi-optics," *Applied physics letters*, vol. 83, pp. 3656-3658, 2003.
- [66] J. Zhang and D. Grischkowsky, "Adiabatically Compressed THz Waveguides," in *Conference on Lasers and Electro-Optics*, 2005, p. CFD6.
- [67] S. Ramo, J. R. Whinnery, and T. Van Duzer, *Fields and waves in communication electronics*: John Wiley & Sons, 2008.
- [68] R. Mendis and D. Grischkowsky, "Plastic ribbon THz waveguides," *Journal of Applied Physics*, vol. 88, pp. 4449-4451, 2000.

- [69] L.-J. Chen, H.-W. Chen, T.-F. Kao, J.-Y. Lu, and C.-K. Sun, "Low-loss subwavelength plastic fiber for terahertz waveguiding," *Optics Letters*, vol. 31, pp. 308-310, 2006.
- [70] S. Jamison, R. McGowan, and D. Grischkowsky, "Single-mode waveguide propagation and reshaping of sub-ps terahertz pulses in sapphire fibers," *Applied Physics Letters*, vol. 76, pp. 1987-1989, 2000.
- [71] C. Yeh, F. Shimabukuro, and J. Chu, "Ultralow loss dielectric ribbon waveguide for millimeter/submillimeter waves," *Applied Physics Letters*, vol. 54, pp. 1183-1185, 1989.
- [72] E. Yablonovitch, D. Hwang, T. Gmitter, L. Florez, and J. Harbison, "Van der Waals bonding of GaAs epitaxial liftoff films onto arbitrary substrates," *Applied Physics Letters*, vol. 56, pp. 2419-2421, 1990.
- [73] H.-M. Heiliger, M. Nagel, H. Roskos, H. Kurz, F. Schnieder, W. Heinrich, *et al.*, "Low-dispersion thin-film microstrip lines with cyclotene (benzocyclobutene) as dielectric medium," *Applied physics letters*, vol. 70, pp. 2233-2235, 1997.
- [74] D. Auston, "Picosecond optoelectronic switching and gating in silicon," *Applied Physics Letters*, vol. 26, pp. 101-103, 1975.
- [75] R. Urata, L. Y. Nathawad, R. Takahashi, K. Ma, D. A. Miller, B. A. Wooley, *et al.*, "Photonic A/D conversion using low-temperature-grown GaAs MSM switches integrated with Si-CMOS," *Journal of lightwave technology*, vol. 21, p. 3104, 2003.
- [76] F. J. Zutavern, G. M. Loubriel, M. O'Malley, L. Shanwald, W. Helgeson, D. McLaughlin, *et al.*, "Photoconductive semiconductor switch experiments for pulsed power applications," *Electron Devices, IEEE Transactions on*, vol. 37, pp. 2472-2477, 1990.
- [77] D. M. Pozar, *Microwave engineering*: John Wiley & Sons, 2009.
- [78] C. Nguyen, *Analysis methods for RF, microwave, and millimeter-wave planar transmission line structures* vol. 160: John Wiley & Sons, 2003.
- [79] K. Gupta, R. Garg, I. Bahl, and P. Bhartia, "Microstrip Lines and Slotlines. 1996," *Artech House*.
- [80] R. Garg, I. Bahl, and M. Bozzi, *Microstrip lines and slotlines*: Artech house, 2013.



- [81] S. B. Cohn, "Slot line on a dielectric substrate," *Microwave Theory and Techniques, IEEE Transactions on*, vol. 17, pp. 768-778, 1969.
- [82] H. Pahlevaninezhad, B. Heshmat, and T. E. Darcie, "Efficient terahertz slot-line waveguides," *Optics express*, vol. 19, pp. B47-B55, 2011.
- [83] E. A. Mariani, C. P. Heinzman, J. P. Agrios, and S. B. Cohn, "Slot line characteristics," *Microwave Theory and Techniques, IEEE Transactions on*, vol. 17, pp. 1091-1096, 1969.
- [84] D. Grieg and H. Engelmann, "Microstrip-a new transmission technique for the kilomegacycle range," *Proceedings of the IRE*, vol. 40, pp. 1644-1650, 1952.
- [85] N. Marcuvitz, *Waveguide handbook*: Iet, 1951.
- [86] R. K. Hoffmann, "Handbook of microwave integrated circuits," *Norwood, MA, Artech House, Inc., 1987, 544 p. Translation.*, vol. 1, 1987.
- [87] A. Sommerfeld, "Ueber die Fortpflanzung elektrodynamischer Wellen längs eines Drahtes," *Annalen der Physik*, vol. 303, pp. 233-290, 1899.
- [88] G. Goubau, "Surface waves and their application to transmission lines," *Journal of Applied Physics*, vol. 21, pp. 1119-1128, 1950.
- [89] T. Akalin, A. Treizebré, and B. Bocquet, "Single-wire transmission lines at terahertz frequencies," *Microwave Theory and Techniques, IEEE Transactions on*, vol. 54, pp. 2762-2767, 2006.
- [90] C. Russell, "PhD Thesis: Broadband On-Chip Terahertz Spectroscopy ", IMP, University of leeds, leeds, 2013.
- [91] R. M. Barret, "Microwave printed circuits-A historical survey," *Microwave Theory and Techniques, IRE Transactions on*, vol. 3, pp. 1-9, 1955.
- [92] S. H. Hall, G. W. Hall, and J. A. McCall, *High-speed digital system design: a handbook of interconnect theory and design practices*: Citeseer, 2000.
- [93] C. P. Wen, "Coplanar waveguide: A surface strip transmission line suitable for nonreciprocal gyromagnetic device applications," *Microwave Theory and Techniques, IEEE Transactions on*, vol. 17, pp. 1087-1090, 1969.
- [94] R. McGowan, D. Grischkowsky, and J. Misewich, "Demonstrated low radiative loss of a quadrupole ultrashort electrical pulse propagated on a three strip coplanar transmission line," *Applied physics letters*, vol. 71, pp. 2842-2844, 1997.

- [95] H. Cheng, J. Whitaker, T. Weller, and L. Katehi, "Terahertz-bandwidth characterization of coplanar waveguide via time-domain electro-optic sampling," in *Microwave Symposium Digest, 1994., IEEE MTT-S International*, 1994, pp. 477-480.
- [96] G. Ghione and C. U. Naldi, "Coplanar waveguides for MMIC applications: Effect of upper shielding, conductor backing, finite-extent ground planes, and line-to-line coupling," *Microwave Theory and Techniques, IEEE Transactions on*, vol. 35, pp. 260-267, 1987.
- [97] J. Lee, H. Lee, W. Kim, J. Lee, and J. Kim, "Suppression of coupled-slotline mode on CPW using air-bridges measured by picosecond photoconductive sampling," *Microwave and Guided Wave Letters, IEEE*, vol. 9, pp. 265-267, 1999.
- [98] M. Houdart and C. Aury, "Various excitation of coplanar waveguide," in *1979 IEEE MTT-S International Microwave Symposium Digest*, 1979, pp. 116-118.
- [99] I. Wolff, *Coplanar microwave integrated circuits*: John Wiley & Sons, 2006.
- [100] M. Y. Frankel, S. Gupta, J. Valdmann, and G. Mourou, "Terahertz attenuation and dispersion characteristics of coplanar transmission lines," *Microwave Theory and Techniques, IEEE Transactions on*, vol. 39, pp. 910-916, 1991.
- [101] J. Zhang, S. Alexandrou, and T. Y. Hsiang, "Attenuation characteristics of coplanar waveguides at subterahertz frequencies," *Microwave Theory and Techniques, IEEE Transactions on*, vol. 53, pp. 3281-3287, 2005.
- [102] M. S. Islam, E. Tuncer, and D. Neikirk, "Calculation of conductor loss in coplanar waveguide using conformal mapping," *Electronics Letters*, vol. 29, pp. 1189-1191, 1993.
- [103] D. Grischowsky, I. Duling III, J. Chen, and C.-C. Chi, "Electromagnetic shock waves from transmission lines," *Physical review letters*, vol. 59, p. 1663, 1987.
- [104] J. Jelley, "Cerenkov radiation and its applications," *British Journal of Applied Physics*, vol. 6, p. 227, 1955.
- [105] R. N. Simons, G. E. Ponchak, K. S. Martzaklis, and R. R. Romanofsky, "Channelized coplanar waveguide: discontinuities, junctions, and propagation characteristics," in *Microwave Symposium Digest, 1989., IEEE MTT-S International*, 1989, pp. 915-918.

- [106] M. Naghed and I. Wolff, "Equivalent capacitances of coplanar waveguide discontinuities and interdigitated capacitors using a three-dimensional finite difference method," *Microwave Theory and Techniques, IEEE Transactions on*, vol. 38, pp. 1808-1815, 1990.
- [107] J. McLean, A. Wieck, K. Ploog, and T. Itoh, "Fullwave analysis of open-end discontinuities in coplanar stripline and finite ground plane coplanar waveguide in open environments using a deterministic spectral domain approach," in *Microwave Conference, 1991. 21st European*, 1991, pp. 1004-1007.
- [108] R. Stegens, "COPLANAR WAVEGUIDE FET AMPLIFIERS FOR SATELLITE-COMMUNICATIONS SYSTEMS," vol. 9, ed: COMMUNICATIONS SATELLITE CORP 22300 COMSAT DR COMSAT TECHNICAL REVIEW, CLARKSBURG, MD 20871, 1979, pp. 255-267.
- [109] M. Aikawa and H. Ogawa, "2Gb double-balanced PSK modulator using coplanar waveguides," in *Solid-State Circuits Conference. Digest of Technical Papers. 1979 IEEE International*, 1979, pp. 172-173.
- [110] N. I. Dib, M. Gupta, G. E. Ponchak, and L. P. Katehi, "Characterization of asymmetric coplanar waveguide discontinuities," *Microwave Theory and Techniques, IEEE Transactions on*, vol. 41, pp. 1549-1558, 1993.
- [111] R. W. Jackson, "Considerations in the use of coplanar waveguide for millimeter-wave integrated circuits," *Microwave Theory and Techniques, IEEE Transactions on*, vol. 34, pp. 1450-1456, 1986.
- [112] H. Jin and R. Vahldieck, "Full-wave analysis of coplanar waveguide discontinuities using the frequency domain TLM method," *Microwave Theory and Techniques, IEEE Transactions on*, vol. 41, pp. 1538-1542, 1993.
- [113] C.-N. Chang, Y.-C. Wong, and C. H. Chen, "Full-wave analysis of coplanar waveguides by variational conformal mapping technique," *Microwave Theory and Techniques, IEEE Transactions on*, vol. 38, pp. 1339-1344, 1990.
- [114] M. Goano, F. Bertazzi, P. Caravelli, G. Ghione, and T. A. Driscoll, "A general conformal-mapping approach to the optimum electrode design of coplanar waveguides with arbitrary cross section," *Microwave Theory and Techniques, IEEE Transactions on*, vol. 49, pp. 1573-1580, 2001.
- [115] X. Zhang and T. Miyoshi, "Optimum design of coplanar waveguide for LiNbO<sub>3</sub> optical modulator," *Microwave Theory and Techniques, IEEE Transactions on*, vol. 43, pp. 523-528, 1995.

- [116] C. Veyres and V. Fouad Hanna, "Extension of the application of conformal mapping techniques to coplanar lines with finite dimensions," *International Journal of Electronics Theoretical and Experimental*, vol. 48, pp. 47-56, 1980.
- [117] C. Chang, Y.-C. Wong, and C. Chen, "Hybrid quasistatic analysis for multilayer coplanar lines," in *Microwaves, Antennas and Propagation, IEE Proceedings H*, 1991, pp. 307-312.
- [118] M. Abramowitz and I. A. Stegun, "Handbook of mathematical functions," *Applied mathematics series*, vol. 55, p. 62, 1966.
- [119] T. Sporkmann, "The evolution of coplanar MMICs over the past 30 years," *Microwave Journal*, vol. 41, pp. 96-103, 1998.
- [120] T. Sporkmann, "The current state of the art in coplanar MMICs," *Microwave journal*, vol. 41, pp. 60-69, 1998.
- [121] R. N. Simons, *Coplanar waveguide circuits, components, and systems* vol. 165: John Wiley & Sons, 2004.
- [122] M. Riazat, R. Majidi-Ahy, and I. Feng, "Propagation modes and dispersion characteristics of coplanar waveguides," *Microwave Theory and Techniques, IEEE Transactions on*, vol. 38, pp. 245-251, 1990.
- [123] V. Radisic, X. Mei, W. Deal, W. Yoshida, P. Liu, J. Uyeda, *et al.*, "Demonstration of sub-millimeter wave fundamental oscillators using 35-nm InP HEMT technology," *Microwave and Wireless Components Letters, IEEE*, vol. 17, pp. 223-225, 2007.
- [124] A. Rayit and N. McEwan, "Coplanar waveguide filters," in *Microwave Symposium Digest, 1993., IEEE MTT-S International*, 1993, pp. 1317-1320.
- [125] L. Yang and D.-Y. Yang, "High Pass Filter Design Using Folded Coplanar Waveguide CRLH Transmission Line," *International Journal of Contents*, vol. 11, 2015.
- [126] J. S. Hayden and G. M. Rebeiz, "2-bit MEMS distributed X-band phase shifters," *Microwave and Guided Wave Letters, IEEE*, vol. 10, pp. 540-542, 2000.
- [127] M. C. Scardelletti, G. E. Ponchak, and T. M. Weller, "Miniaturized Wilkinson power dividers utilizing capacitive loading," *Microwave and Wireless Components Letters, IEEE*, vol. 12, pp. 6-8, 2002.
- [128] K. Nadaud, H. W. Gundel, C. Borderon, R. Gillard, and E. Fourn, "A new method of dielectric characterization in the microwave range for high-k ferroelectric thin films," in *Applications of Ferroelectric and Workshop on the*

*Piezoresponse Force Microscopy (ISAF/PFM), 2013 IEEE International Symposium on the*, 2013, pp. 9-12.

- [129] H. Skulason, H. Nguyen, A. Guermoune, V. Sridharan, M. Siaj, C. Caloz, *et al.*, "110 GHz measurement of large-area graphene integrated in low-loss microwave structures," *Applied Physics Letters*, vol. 99, p. 153504, 2011.
- [130] R. Bromme and R. Jansen, "Systematic investigation of coplanar waveguide MIC/MMIC structures using a unified strip/slot 3D electromagnetic simulator," in *Microwave Symposium Digest, 1991., IEEE MTT-S International*, 1991, pp. 1081-1084.
- [131] S. Gevorgian, A. Deleniv, T. Martinsson, S. Gal'chenko, P. Linnér, and I. Vendik, "Cad model of a gap in a coplanar waveguide," *International Journal of Microwave and Millimeter-Wave Computer-Aided Engineering*, vol. 6, pp. 369-377, 1996.
- [132] S. Gevorgian, T. Martinsson, P. Linner, and E. Kollberg, "Simple Analytical Approximations for a Gap in Coplanar Waveguide," in *Microwave Conference, 2000. 30th European*, 2000, pp. 1-4.
- [133] W. Hilberg, "From approximations to exact relations for characteristic impedances," *Microwave Theory and Techniques, IEEE Transactions on*, vol. 17, pp. 259-265, 1969.
- [134] J.-F. Lee, D.-K. Sun, and Z. J. Cendes, "Full-wave analysis of dielectric waveguides using tangential vector finite elements," *Microwave Theory and Techniques, IEEE Transactions on*, vol. 39, pp. 1262-1271, 1991.
- [135] G. Hasnain, J. Whinnery, and A. Dienes, "Dispersion of picosecond pulses in coplanar transmission lines," *IEEE Transactions on Microwave Theory Techniques*, vol. 34, pp. 738-741, 1986.
- [136] E. Yamashita and K. Atsuki, "An approximate dispersion formula of microstrip lines for computer aided design of microwave integrated circuits," in *1979 IEEE MTT-S International Microwave Symposium Digest*, 1979, pp. 320-322.
- [137] H. Aouani, J. Wenger, D. Gérard, H. Rigneault, E. Devaux, T. W. Ebbesen, *et al.*, "Crucial role of the adhesion layer on the plasmonic fluorescence enhancement," *ACS nano*, vol. 3, pp. 2043-2048, 2009.
- [138] S. Chowdhury, J. R. Freeman, M. C. Rosamond, R. A. Mohandas, M. Kumar, L. Li, *et al.*, "Study of the effect of annealing temperature on low-temperature-grown-GaAs photomixers," 2015.

- [139] S. Chowdhary, "PhD Thesis: Development of terahertz systems using quantum cascade lasers and photomixers," IMP, University of Leeds, Leeds, 2015.
- [140] F. Ganikhanov, G. R. Lin, W. C. Chen, C. S. Chang, and C. L. Pan, "Subpicosecond carrier lifetimes in arsenic-ion-implanted GaAs," *Applied physics letters*, vol. 67, pp. 3465-3467, 1995.
- [141] R. H. Jacobsen, K. Birkelund, T. Holst, P. U. Jepsen, and S. Keiding, "Interpretation of photocurrent correlation measurements used for ultrafast photoconductive switch characterization," *Journal of applied physics*, vol. 79, pp. 2649-2657, 1996.
- [142] L. Deng, W. zhu Lin, and Z. rong Sun, "Response characteristic of femtosecond LT-GaAs photoconductive switches at different voltage biases," *Journal of Physics D: Applied Physics*, vol. 42, p. 245103, 2009.
- [143] J. Montoya and Q. Hu, "Low-temperature-grown GaAs coplanar waveguide single-photon/two photon absorption autocorrelator," *Journal of applied physics*, vol. 95, pp. 2230-2237, 2004.
- [144] S. E. Ralph and D. Grischkowsky, "Trap-enhanced electric fields in semi-insulators: The role of electrical and optical carrier injection," *Applied physics letters*, vol. 59, pp. 1972-1974, 1991.
- [145] S. Alexandrou, R. Sobolewski, and T. Y. Hsiang, "Time-domain characterization of bent coplanar waveguides," *Quantum Electronics, IEEE Journal of*, vol. 28, pp. 2325-2332, 1992.
- [146] C. Wood, J. Cunningham, P. Upadhy, E. Linfield, I. Hunter, A. Davies, *et al.*, "On-chip photoconductive excitation and detection of pulsed terahertz radiation at cryogenic temperatures," *Applied physics letters*, vol. 88, p. 142103, 2006.
- [147] N. Zamdmer, Q. Hu, S. Verghese, and A. Förster, "Mode-discriminating photoconductor and coplanar waveguide circuit for picosecond sampling," *Applied physics letters*, vol. 74, pp. 1039-1041, 1999.
- [148] L. Dazhang, J. Cunningham, M. Byrne, S. Khanna, C. Wood, A. Burnett, *et al.*, "On-chip terahertz Goubau-line waveguides with integrated photoconductive emitters and mode-discriminating detectors," *Applied Physics Letters*, vol. 95, p. 092903, 2009.
- [149] M. A. de Araújo, R. Silva, E. de Lima, D. P. Pereira, and P. C. de Oliveira, "Measurement of Gaussian laser beam radius using the knife-edge

technique: improvement on data analysis," *Applied optics*, vol. 48, pp. 393-396, 2009.

- [150] H. Jeongwoo and N. Cam, "A new ultra-wideband, ultra-short monocycle pulse generator with reduced ringing," *IEEE Microwave and Wireless Components Letters*, vol. 12, pp. 206-208, 2002.
- [151] R. Slavík, Y. Park, M. Kulishov, R. Morandotti, and J. Azaña, "Ultrafast all-optical differentiators," *Optics Express*, vol. 14, pp. 10699-10707, 2006.
- [152] X. Chen and S. Kiaei, "Monocycle shapes for ultra wideband system," in *Circuits and Systems, 2002. ISCAS 2002. IEEE International Symposium on*, 2002, pp. I-597-I-600 vol. 1.
- [153] N. C. Hunter, "Picosecond pulse measurements of Graphene," IMP, University of Leeds, Leeds, 2015
- [154] D. Li, "PhD Thesis: On-chip pulsed terahertz systems ", IMP, University of Leeds, Leeds, 2010.
- [155] X. Zheng, Y. Xu, R. Sobolewski, R. Adam, M. Mikulics, M. Siegel, *et al.*, "Femtosecond response of a free-standing LT-GaAs photoconductive switch," *Applied optics*, vol. 42, pp. 1726-1731, 2003.
- [156] H. Heiliger, M. Vossebürger, H. Roskos, R. Hey, K. Ploog, and H. Kurz, "THz Signal Generators Based on Lift-Off LT-GaAs on Transparent Substrates," in *Seventh International Symposium on Space Terahertz Technology*, 1996, p. 400.
- [157] H. Cheng, J. F. E. D. S. J. Whitaker, and U. Mishra, "High-Bandwidth Transmission Lines Using Low-Temperature-Grown-GaAs-on Quartz," in *Ultrafast Electronics and Optoelectronics*, San Francisco, California, 1993, p. H1.
- [158] W. Platte and B. Sauerer, "Optically CW-induced losses in semiconductor coplanar waveguides," *Microwave Theory and Techniques, IEEE Transactions on*, vol. 37, pp. 139-149, 1989.
- [159] C. Tripon-Canseliet, S. Faci, A. Pagies, V. Magnin, S. Formont, D. Decoster, *et al.*, "Microwave On/Off Ratio Enhancement of GaAs Photoconductive Switches at Nanometer Scale," *Journal of Lightwave Technology*, vol. 30, pp. 3576-3579, 2012.

- [160] M. Z. Win and R. A. Scholtz, "Ultra-wide bandwidth time-hopping spread-spectrum impulse radio for wireless multiple-access communications," *IEEE Transactions on communications*, vol. 48, pp. 679-689, 2000.
- [161] J. Han and C. Nguyen, "On the development of a compact sub-nanosecond tunable monocycle pulse transmitter for UWB applications," *Microwave Theory and Techniques, IEEE Transactions on*, vol. 54, pp. 285-293, 2006.
- [162] P. Wang, G. Brambilla, Y. Semenova, Q. Wu, and G. Farrell, "Design of an extra-low-loss broadband Y-branch waveguide splitter based on a tapered MMI structure," 2011.
- [163] L. H. Frandsen, P. I. Borel, Y. Zhuang, A. Harpøth, M. Thorhauge, M. Kristensen, *et al.*, "Ultralow-loss 3-dB photonic crystal waveguide splitter," *Optics letters*, vol. 29, pp. 1623-1625, 2004.
- [164] M. Shih, W. Kim, W. Kuang, J. Cao, H. Yukawa, S. Choi, *et al.*, "Two-dimensional photonic crystal Mach-Zehnder interferometers," *Applied physics letters*, vol. 84, pp. 460-462, 2004.
- [165] S.-G. Mao and Y.-Z. Chueh, "Broadband composite right/left-handed coplanar waveguide power splitters with arbitrary phase responses and balun and antenna applications," *Antennas and Propagation, IEEE Transactions on*, vol. 54, pp. 243-250, 2006.
- [166] Y. Zhang, S. Yang, A. E.-J. Lim, G.-Q. Lo, C. Galland, T. Baehr-Jones, *et al.*, "A compact and low loss Y-junction for submicron silicon waveguide," *Optics express*, vol. 21, pp. 1310-1316, 2013.
- [167] H.-B. Lin, R.-S. Cheng, and W.-S. Wang, "Wide-angle low-loss single-mode symmetric Y-junctions," *Photonics Technology Letters, IEEE*, vol. 6, pp. 825-827, 1994.
- [168] E. Brown, J. Bjarnason, A. Fedor, and T. Korter, "On the strong and narrow absorption signature in lactose at 0.53 THz," *Applied Physics Letters*, vol. 90, p. 1908, 2007.
- [169] A. I. McIntosh, B. Yang, S. M. Goldup, M. Watkinson, and R. S. Donnan, "Terahertz spectroscopy: a powerful new tool for the chemical sciences?," *Chemical Society Reviews*, vol. 41, pp. 2072-2082, 2012.
- [170] L. G. Maloratsky, *Integrated Microwave Front-ends with Avionics Applications*: Artech House, 2012.



- [171] D. B. Rutledge, D. P. Neikirk, and D. P. Kasilingam, "Integrated circuit antennas," *Infrared and millimeter waves*, vol. 10, pp. 1-90, 1983.
- [172] B. C. Wadell, *Transmission line design handbook*: Artech House Publishers, 1991.
- [173] N. Laman, S. S. Harsha, and D. Grischkowsky, "Narrow-line waveguide terahertz time-domain spectroscopy of aspirin and aspirin precursors," *Applied spectroscopy*, vol. 62, pp. 319-326, 2008.
- [174] S. M. Sze and K. K. Ng, *Physics of semiconductor devices*: John Wiley & sons, 2006.
- [175] D. G. Allis, A. M. Fedor, T. M. Korter, J. E. Bjarnason, and E. R. Brown, "Assignment of the lowest-lying THz absorption signatures in biotin and lactose monohydrate by solid-state density functional theory," *Chemical Physics Letters*, vol. 440, pp. 203-209, 6/8/ 2007.
- [176] M. B. Byrne, J. Cunningham, K. Tych, A. D. Burnett, M. R. Stringer, C. D. Wood, *et al.*, "Terahertz vibrational absorption spectroscopy using microstrip-line waveguides," *Applied Physics Letters*, vol. 93, p. 182904, 2008.
- [177] M. Walther, B. M. Fischer, A. Ortner, A. Bitzer, A. Thoman, and H. Helm, "Chemical sensing and imaging with pulsed terahertz radiation," *Analytical and Bioanalytical Chemistry*, vol. 397, pp. 1009-1017, 2010.
- [178] D. A. Newnham and P. F. Taday, "Pulsed terahertz attenuated total reflection spectroscopy," *Applied spectroscopy*, vol. 62, pp. 394-398, 2008.
- [179] N. Laman, S. S. Harsha, D. Grischkowsky, and J. S. Melinger, "High-Resolution Waveguide THz Spectroscopy of Biological Molecules," *Biophysical Journal*, vol. 94, pp. 1010-1020, 2/1/ 2008.
- [180] D. Allis, A. Fedor, T. Korter, J. Bjarnason, and E. Brown, "Assignment of the lowest-lying THz absorption signatures in biotin and lactose monohydrate by solid-state density functional theory," *Chemical Physics Letters*, vol. 440, pp. 203-209, 2007.
- [181] Y. Shen, P. Upadhyaya, E. Linfield, and A. G. Davies, "Temperature-dependent low-frequency vibrational spectra of purine and adenine," *Applied Physics Letters*, vol. 82, pp. 2350-2352, 2003.
- [182] Y. C. Shen, P. C. Upadhyaya, E. H. Linfield, and A. G. Davies, "Temperature-dependent low-frequency vibrational spectra of purine and adenine," *Applied Physics Letters*, vol. 82, pp. 2350-2352, 2003.

- [183] M. Byrne, J. Cunningham, S. Khanna, M. Stringer, C. Wood, E. Linfield, *et al.*, "Sub-wavelength imaging of terahertz dielectric permittivity using planar resonant circuits," in *2008 33rd International Conference on Infrared, Millimeter and Terahertz Waves*, 2008.